Gas Flow Field and Collection Efficiency of Cyclone Separators

A. J. Hoekstra

Gas Flow Field and Collection Efficiency of Cyclone Separators

PROEFSCHRIFT

ter verkrijging van de graad van doctor
aan de Technische Universiteit Delft,
op gezag van de Rector Magnificus prof. ir. K.F. Wakker,
voorzitter van het College van Promoties,
in het openbaar te verdedigen op
dinsdag 5 december 2000 om 10:30 uur

door

Arjen Jacco HOEKSTRA

scheikundig ingenieur,
geboren te Leiden.

Dit proefschrift is goedgekeurd door de promotor:
Prof. dr. ir. H. E. A. van den Akker

Samenstelling *promotiecommissie*:

Rector Magnificus, voorzitter
Prof. dr. ir. H. E. A. van den Akker, Technische Universiteit Delft, promotor
Prof. dr. M. Sommerfeld, Martin-Luther Universität Halle-Wittenberg (Duitsland)
Prof. M. P. Escudier FREng, The University of Liverpool (Verenigd Koninkrijk)
Prof. dr. ir. J. J. H. Brouwers, Technische Universiteit Eindhoven
Prof. dr. K. Hanjalić, Technische Universiteit Delft
Prof. dr. ir. P. J. Jansens, Technische Universiteit Delft
Dr. ir. J. J. Derksen, Technische Universiteit Delft

Dr. ir. J. J. Derksen heeft als begeleider in belangrijke mate aan de totstandkoming van het proefschrift bijgedragen.

This study was supported by the Netherlands Foundation for Chemical Research (SON) with financial aid from the Netherlands Technology Foundation (STW).

ISBN 90-90143341-3

Aan mijn ouders

NOMENCLATURE

a	Cyclone inlet height	m
a_{ij}	Anisotropy tensor	–
A_{in}	Cross sectional area at inlet	m^2
A_{out}	Cross sectional area at outlet	m^2
b	Cyclone inlet width	m
c	Speed of light	$m\,s^{-1}$
c_s	Smagorinsky constant	–
C_μ,$C_{\varepsilon,1}$,$C_{\varepsilon,2}$	Constants in $k-\varepsilon$ model	–
C_D	Drag coefficient	–
d_c	Vortex core diameter	m
d_p	Particle diameter	m
d_H	Height of LDA measuring volume	m
d_L	Length of LDA measuring volume	m
d_W	Width of LDA measuring volume	m
d_{50}	Cut-size	m
D	Diameter of cyclone body	m
D_e	Diameter of cyclone exit pipe	m
D_{ij}	Diffusive transport term in RSTM	$m^2\,s^{-3}$
f_D	Doppler shift frequency	s^{-1}
f_{PVC}	Frequency of precessing vortex core	s^{-1}
F_0	Test statistic of regression coefficient	-
h	Height of cyclone body	m
H	Total height of cyclone	m
H_0	Null hypothesis	–
I	Turbulence intensity	–
k	Turbulent kinetic energy	$m^2\,s^{-2}$
l_m	Characteristic turbulent mixing length	m
n	Vortex exponent	–
N_d	Number of delay samples	–
P	Mean pressure	$kg\,m^{-1}s^{-2}$
$P()$	Probability function	–
P_{ij}	Production term in RSTM	$m^2\,s^{-3}$
r	Radial coordinate	m
r_{in}	Cyclone inlet radius	m
R	Radius of cyclone body	m
R^2	Regression coefficient	–

R_{ii}	Auto-covariance function	$m^2\,s^{-2}$
R_{ij}	Cross-covariance function	$m^2\,s^{-2}$
S	Mean rate of strain tensor	s^{-1}
S	Skewness	–
T_L	Lagrangian integral time scale	s
u	Fluctuating axial velocity component	$m\,s^{-1}$
$\tilde{\mathbf{u}}$	Instantaneous fluid velocity	$m\,s^{-1}$
$\tilde{\mathbf{u}}_p$	Instantaneous particle velocity	$m\,s^{-1}$
u_τ	Shear velocity at wall	$m\,s^{-1}$
U	Mean axial velocity component	$m\,s^{-1}$
U_{in}	Linear inlet velocity	$m\,s^{-1}$
v	Fluctuating radial velocity component	$m\,s^{-1}$
V	Mean radial velocity component	$m\,s^{-1}$
w	Fluctuating tangential velocity component	$m\,s^{-1}$
W	Mean tangential velocity component	$m\,s^{-1}$
$\mathbf{W}$	Weight vector of adaptive noise filter	–
x, y, z	Cartesian coordinates	m
x_i	Coded factor in response surface model	–
$Y_{1,k}$	Primary input of adaptive noise canceler	–
$\mathbf{Y}_{2,k}$	Reference input of adaptive noise canceler	–

Greek

α	Correction factor related to cyclone inlet	–
α	Confidence level	–
β	Shape parameter of logistic function	–
β_i,β_{ii},β_{ij}	Coefficients of response surface model	–
Γ	Vortex circulation	$m^2\,s^{-1}$
δ_{ij}	Dirac delta function	–
Δ	Lattice spacing of LES	m
ε	Dissipation rate of turbulent kinetic energy	$m^2\,s^{-3}$
η	Fractional efficiency	–
$\overline{\eta}$	Overall collection efficiency	–
κ	Von Karman constant	–
λ	Wall friction factor	–
λ	Wavelength of laser beam	m
μ	Dynamic viscosity	$N\,s\,m^{-2}$
μ	Stability constant in adaptive filter	–
ν	Kinematic viscosity	$m^2\,s^{-1}$
ρ_g	Density of gas	$kg\,m^{-3}$
ρ_p	Density of particle	$kg\,m^{-3}$
ρ_{ii}	Auto-correlation function	–
ρ_{ij}	Cross-correlation function	–
σ_i	standard deviation in direction i	m
σ_k,σ_ε	Constants in $k-\varepsilon$ model	–

τ_{ij}	Reynolds stress tensor	$kg\,m^{-1}s^{\ 2}$
τ_a	Characteristic macro time scale of the flow	s
τ_K	Kolmogorov time scale	s
τ_p	Particle relaxation time	s
τ_{PVC}	Time scale associated with the PVC	s
τ_ν	Viscous diffusion time scale	s
τ_w	Wall shear stress	$kg\,m^{-1}s^{-2}$
θ	Azimuthal coordinate	–
ϕ	Volumetric particle size distribution	–
Φ	Cumulative particle size distribution	–
ϕ_V	Flow rate	$m^3\,s^{-1}$
Φ_{ij}	Pressure-strain term in RSTM	$m^2\,s^{-3}$
Φ_{ij}^w	Wall-reflection term in RSTM	$m^2\,s^{-3}$
ω	Angular frequency	$rad\,s^{-1}$
∇_k	Gradient of performance surface	–

Dimensionless quantities

Eu	Euler number
Re	Reynolds number
Re_p	Particle Reynolds number
S	Swirl number
S_g	Geometric swirl number
St	Strouhal number
Stk_{50}	Stokes number related to cut-size

Acronyms

ACF	Auto-correlation function
ANOVA	Analysis of Variance
CCF	Cross-correlation function
CFD	Computational Fluid Dynamics
df	Degrees of freedom
FCC	Fluid Catalytic Cracking
LDA	Laser-Doppler Anemometry
LES	Large Eddy Simulation
MS	Mean sum-of-squares
MSE	Mean-square error
PDF	Probability Density Function
PVC	Precessing Vortex Core
RANS	Reynolds Averaged Navier-Stokes
RNG	Re-normalization Group Theory
RSM	Response Surface Model
RSTM	Reynolds Stress Transport Model
SS	Sum-of-squares

CONTENTS

SUMMARY

A.J. HOEKSTRA - GAS FLOW FIELD AND COLLECTION EFFICIENCY OF CYCLONE SEPARATORS

The gas-solids cyclone separator is a dust collection device that has been widely used in industry for more than a century. Due to its industrial relevance, a large number of experimental and theoretical studies have been reported in the literature aimed at understanding and predicting the performance of cyclones in terms of pressure loss and collection efficiency. The currently used (semi-)empirical models for the prediction of cyclone performance, however, exhibit limited accuracy and generality. An alternative approach is to simulate the gas-particle flow field in a cyclone by means of Computational Fluid Dynamics (CFD). As a result of the recent progress of computational power and numerical techniques, CFD has been widely applied to industrial flow problems, although for complex and turbulent flows experimental validation is still required.

The objective of this study is twofold. First, an experimental programme was carried out to properly assess which CFD model should be used to predict the cyclone flow field. CFD simulations of cyclones reported to date generally lack a comparison with detailed gas velocity measurements. The second objective was to explore if this CFD model could be used to sort out an optimal cyclone design, *i.e.* a cyclone that operates most efficiently at a given set of operating conditions. The study was limited to reverse-flow gas-solids cyclone separators operating at low solids loading.

An experimental study on the gas flow field was carried out for two different cyclone geometries, *viz.* a Stairmand high-efficiency cyclone and a tangential swirl tube separator. The tangential and axial velocity components were measured by means of Laser-Doppler Anemometry (LDA). The radial distribution of the mean tangential velocity exhibits the expected shape of a combined vortex, where a solid body rotation prevails in the vortex core, and a free-type of vortex exists between the core boundary and the cyclone wall. The mean axial velocity is characterised by a reverse-flow pattern, where in the core of the flow the axial velocity magnitude is suppressed. A contraction of the exit pipe aperture significantly affects the radial profiles of the tangential and axial velocity components, *i.e.* the size of the vortex core is reduced, which results in a strong increase of the maximum tangential and axial mean velocity.

In the vortex core region, large velocity fluctuations were measured. This is in apparent contradiction to the Rayleigh criterion, which argues that non-axisymmetric disturbances are suppressed by the solid-body rotation in the vortex core. The velocity fluctuations, however, are not related to turbulence, but can be attributed to a coherent, periodic motion known as the precessing vortex core (PVC). Although vortex precession in cyclones has been reported before

in the literature, not much is known about its shape and how it affects LDA measurements of the gas flow field.

Due to the relative motion of the vortex core origin with respect to the measuring volume, the PVC introduces a low-frequency oscillation into the LDA signal. A signal processing technique known as adaptive noise cancellation was used to estimate the contribution of the PVC to the LDA signal. On the basis of the PVC signal and the shape of the auto- and cross-correlation functions, phase-resolved velocity profiles were reconstructed that correspond to the approximate 'apogee' and 'perigee' position of the vortex core origin. These velocity profiles provide an interesting insight in the way that the PVC affects the flow field. For the Stairmand geometries studied, however, the filter technique was less suitable.

Numerical simulations of cyclone flow were carried out by solving the steady-state, axisymmetric Reynolds averaged Navier-Stokes (RANS) equations combined with a closure model for the turbulent stresses. The modelling of cyclone flow by means of Computational Fluid Dynamics (CFD) has been reported before in the literature, but by using the extensive LDA data set obtained in this study, a generic assessment was carried out on a number of turbulence closure models. The Reynolds stress transport model (RSTM) captured the cyclone flow field best compared to the LDA measurements. For cyclones with a small exit pipe diameter, the simulation benefits from disregarding the wall-reflection term in the RSTM. A comparison of a three-dimensional and an axisymmetric RANS simulation of the Stairmand cyclone showed that three-dimensional effects are limited to the inlet section of the cyclone, *i.e.* the flow field in the separation zone of the cyclone can safely be considered as axisymmetric.

An experimental facility was built to study the performance of (modifications of) the Stairmand high-efficiency cyclone at low solids loading. The cyclone pressure drop and overall collection efficiency were measured as a function of the inlet velocity and the exit pipe diameter. The CFD model also predicted the collection efficiency, where the particulate phase was treated in a Lagrangian framework by tracking a large number of particles of different size classes through the computational domain. The stochastic nature of the particle motion due to the fluid turbulence was taken into account by a particle dispersion model. There was a reasonable agreement between the calculated and measured overall efficiencies, but both the experimental set-up and the numerical model could be improved.

The CFD model, validated in terms of the above aspects, was used to predict the pressure drop and the grade efficiency curve of a range of cyclone geometries based on Stairmand's high-efficiency design. These predictions were used to obtain an algebraic equation that relates the performance of a cyclone to its design and a limited set of dimensionless quantities, such as the Reynolds, Euler, and Stokes numbers. This approach towards predicting cyclone performance has not been reported before. By means of a non-linear optimisation procedure, optimal cyclone geometries were determined that yield the lowest particle cut-size at a required flow rate and pressure drop. It is seen that, at a given volumetric flow rate, the collection efficiency of a Stairmand cyclone is improved by reducing simultaneously the exit pipe diameter and the cross-sectional area of the inlet. The application of this optimisation technique for practical engineering purposes is illustrated by an example.

SAMENVATTING

A.J. HOEKSTRA - GASSNELHEIDSVELD EN SCHEIDINGSRENDEMENT VAN CYCLOONSCHEIDERS

De gas-deeltjes cycloonscheider wordt al meer dan een eeuw op grote schaal toegepast in de industrie en is geschikt voor het afvangen van stofdeeltjes. Door het industriële belang van cyclonen is een groot aantal experimentele en theoretische studies gepubliceerd met als doel het voorspellen van de drukval en het scheidingsrendement. Echter, de empirische modellen, die op dit moment in gebruik zijn voor het voorspellen van de prestatie van een cycloon, worden gekenmerkt door een beperkte nauwkeurigheid en algemeenheid. Een alternatieve benadering is het simuleren van het snelheidsveld van gas en deeltjes in een cycloon door middel van Computational Fluid Dynamics (CFD). Ten gevolge van de huidige vooruitgang in computerkracht en numerieke technieken wordt CFD op grote schaal toegepast op industriële stromingsproblemen, hoewel de experimentele validatie voor complexe en turbulente stromingen nog steeds vereist is.

De doelstelling van deze studie is tweeledig. Allereerst is een experimenteel programma uitgevoerd om op een juiste manier te bepalen welk CFD model gebruikt moet worden om het stromingsveld in een cycloon te voorspellen. Tot op heden gerapporteerde CFD simulaties van cyclonen ontberen in het algemeen een vergelijking met gedetailleerde metingen van het snelheidsveld. De tweede doelstelling is te onderzoeken of dit CFD model geschikt is om een optimale cycloongeometrie te selecteren, dat wil zeggen, een cycloon met het hoogste scheidingsrendement onder gegeven procescondities. De studie is beperkt tot zogenaamde 'reverse-flow' cyclonen, die werken bij een lichte stofbelading.

Een experimentele studie van het gassnelheidsveld is uitgevoerd voor twee verschillende cycloongeometriën, te weten een Stairmand hoogrendement cycloon en een zogenaamde 'swirl tube' scheider. De tangentiële en axiale snelheidscomponenten zijn gemeten met behulp van Laser-Doppler Anemometry (LDA). De radiële verdeling van de gemiddelde tangentiële snelheid vertoont de verwachte vorm van een gecombineerde vortex, waar een vast-lichaam rotatie heerst in de vortex kern, en een vrije vortex in het gebied tussen de vortex kern en de cycloonwand. De gemiddelde axiale snelheid wordt gekarakteriseerd door een terugstromingspatroon, waar de axiale snelheid wordt onderdrukt in de kern van de stroming. Het verkleinen van de uitstroomopening heeft een significant effect op de radiële profielen van de tangentiële en axiale snelheidscomponenten: de vortexkern wordt kleiner, waardoor de maximale tangentiële en axiale gemiddelde snelheid sterk toeneemt.

In de vortexkern worden grote snelheidsfluctuaties gemeten. Dit lijkt in tegenspraak met de

Rayleigh voorwaarde, die stelt dat niet-axisymmetrische verstoringen worden onderdrukt door de vast-lichaam rotatie in de vortexkern. Echter, de snelheidsfluctuaties zijn niet gerelateerd aan turbulentie, maar zijn het resultaat van een coherente, periodieke beweging, die bekend staat als de precederende vortexkern (PVK). Hoewel vortexprecessie eerder gemeld is in de literatuur, is er niet veel bekend over de vorm en de manier waarop de LDA metingen van het gassnelheidsveld worden beïnvloed.

Als gevolg van de relatieve beweging van de oorspong van de vortexkern ten opzichte van het meetvolume, introduceert de PVK een laag-frequente oscillatie in het LDA signaal. Een signaalverwerkingstechniek, die bekend staat als adaptief filteren, is toegepast om de bijdrage van de PVK aan het LDA signaal te schatten. Op basis van het PVK signaal en de vorm van de auto- en kruiscorrelatie functies zijn fase-opgeloste snelheidsprofielen afgeleid, die overeenkomen met de uiterste posities van de oorsprong van de vortexkern. Deze snelheidsprofielen leveren een interessant inzicht in de manier waarop het snelheidsveld wordt beïnvloed door de PVK. De filtertechniek bleek echter niet geschikt voor de bestudeerde Stairmand geometriën.

Numerieke simulaties van de stroming zijn gedaan door de axisymmetrische Reynolds gemiddelde Navier-Stokes vergelijkingen op te lossen in combinatie met een sluitingsmodel voor de turbulente spanningen. Het modelleren van cyclonen met behulp van CFD is eerder in de literatuur vermeld, maar door gebruik te maken van de uitgebreide LDA dataset kan een generieke beoordeling plaatsvinden van een aantal sluitingsmodellen. Het Reynoldsspanningsmodel (RSM) voorspelde het snelheidsveld van een cycloon het best vergeleken met LDA metingen. Voor cyclonen met een kleine uitlaatpijp wordt de voorspelling beter door de wandreflectie-term weg te laten. Een vergelijking tussen een drie-dimensionale en een axisymmetrische simulatie van de Stairmand cycloon laat zien, dat 3-D effecten zich beperken tot de inlaatsectie van de cycloon, met andere woorden het stromingsveld in de cycloon kan beschouwd worden als axisymmetrisch.

Een experimentele opstelling is gebouwd om de prestatie van (aanpassingen op) de Stairmand hoogrendementcycloon te meten bij een lage beladingsgraad. De drukval en het scheidingsrendement van de cycloon zijn gemeten als functie van de inlaatsnelheid en de diameter van de uitlaatpijp. Het scheidingsrendement is ook voorspeld door het CFD model, waar de deeltjesfase wordt behandeld in een Lagrangiaans systeem door een groot aantal deeltjes met verschillende grootte te volgen door het rekendomein. De stochastische aard van de deeltjesbeweging als gevolg van de gasturbulentie is meegenomen door een dispersiemodel. De overeenkomst tussen de berekende en gemeten scheidingsrendementen was redelijk, maar er is ruimte voor verbetering van zowel de meetopstelling als het numerieke model.

Het gevalideerde CFD model is toegepast voor het voorspellen van de drukval en de scheidingscurve van een groot aantal cycloongeometriën gebaseerd op Stairmand's hoogrendementcycloon. Deze voorspellingen zijn gebruikt om een algebraïsche vergelijking te krijgen die de prestatie van een cycloon relateert aan zijn ontwerp en een beperkte groep dimensieloze grootheden, zoals het Reynolds, Euler, en Stokes getal. Deze benadering voor het voorspellen van de prestatie van een cycloon is niet eerder gerapporteerd. Door middel van een niet-lineaire optimalisatieprocedure zijn optimale cycloongeometriën bepaald, die de laagste 'cut-size' opleveren bij gegeven waarden van de doorzet en drukval. Bij gegeven doorzet bleek het scheidingsrendement van een Stairmand cycloon verbeterd te worden door gelijktijdig de uitlaatdiameter en het inlaatoppervlak te verkleinen. De toepassing van deze optimalisatie procedure in praktische omstandigheden wordt geïllustreerd met een voorbeeld.

CHAPTER 1

INTRODUCTION

1.1 INDUSTRIAL RELEVANCE OF CYCLONES

"The industrial cyclone is an apparatus that has acquired a unique position among the various forms of equipment available to the present-day engineer as unit in the design of an installation for a chemical or process industry", according to the editors of 'Cyclones in Industry', a collection of papers published in the early sixties (Rietema, 1961). Today, the use of cyclones as an industrial cleaning device is still widespread, and by means of an innovative conversion into a vacuum cleaner (Dyson, 1992) the cyclone is now within reach of the domestic consumer.

The main advantages of the cyclone are its simplicity of construction and the absence of moving parts. Cyclones have been applied for the recovery of product or catalyst particles and for the cleaning of process streams before emission into the environment. Since one disadvantage of most cyclone separators is that the collected particle sizes are relatively coarse, they are often operated in combination with other collectors such as bag filters or electrostatic precipitators. Proper design and operation of a cyclone, however, can result in collecting particles just a few microns in diameter.

The industrial importance of the cyclone has led to many investigations aimed at understanding and improving its operation. The earliest studies on gas cyclones were published during the 1930–40's. Most of these studies were motivated by the lack of data available at the time on the flow pattern and on cyclone pressure drop for various designs and operating conditions. The pressure drop equations presented by Shepherd and Lapple (1939) and Stairmand (1949) were derived by using a (semi-) empirical approach, *i.e.* their models were based on material and energy balances, while experimental data were used to estimate frictional loss and velocity distributions. Significant effort was put into ways of reducing the pressure drop of a cyclone system, *e.g.* by use of internal cyclone modifications (baffles, straightening vanes) or external appendages (extension or expansion of the exit pipe, modified rain cap). Ter Linden (1949) presented a detailed description of the flow pattern in a cyclone that not only is very accurate in view of the experimental technique applied, but which is also in pretty good agreement with our current knowledge of the flow field.

In Germany, a firm basis of cyclone understanding was established by Barth (1956), who

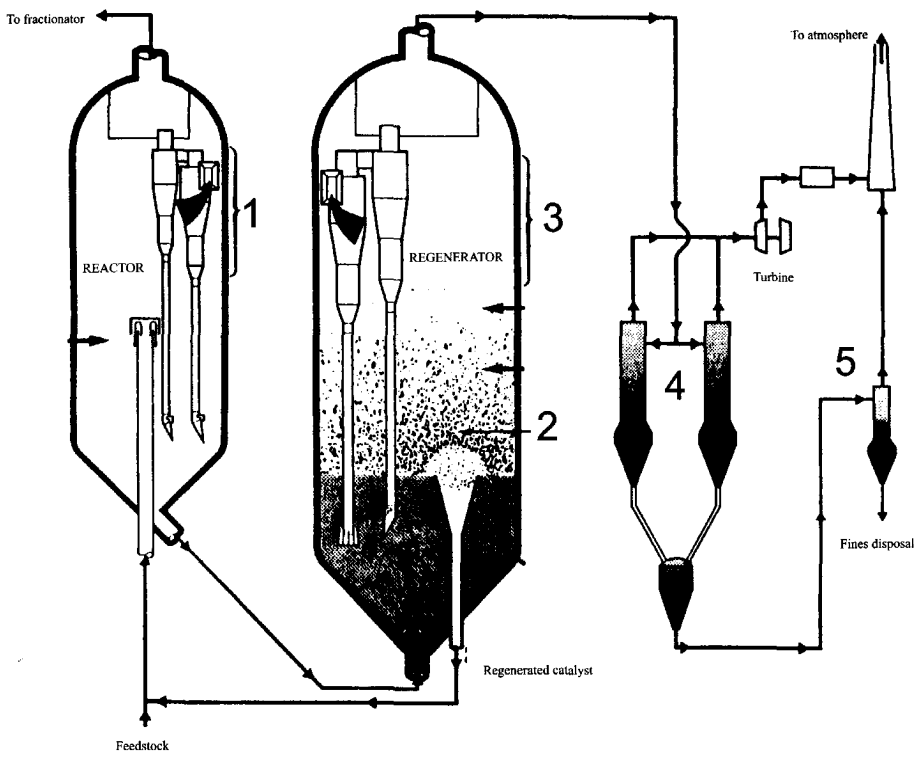

FIGURE 1.1: *Typical Fluid Catalytic Cracking (FCC) system with cyclones for energy recovery (Sowter, 1986): (1) separation of cracked oil gases and carbon-bearing catalyst, (2) burning off carbon coating on catalyst, (3) separation of pure catalyst and combustion product, (4) third stage separator, (5) fourth stage cyclone.*

proposed a series of optimal cyclone designs depending on the collection performance required. Since then, numerous studies have been reported in the literature on different aspects of cyclone operation, *e.g.* at high temperature or at high solids loading, and from different research areas, *e.g.* fluid mechanics, powder technology, or 'Verfahrenstechnik'. Recently, even seminars have been organised that were fully dedicated to cyclone research, such as the one in Essen (Germany) from 29-30 October 1996 organised by the Verein Deutscher Ingenieure (VDI) and that in Warwick (UK) from 31 May-2 June 2000 organised by the BHR Group.

An illustrative example of the application of cyclones in the oil industry is Fluid Catalytic Cracking (FCC). The objective of this process is the cracking of heavy petroleum fractions with the help of a cracking catalyst (nowadays usually zeolite) in a riser reactor (residence times are as short as a few seconds). Fig. 1.1 presents a typical design of a commercial FCC unit as still currently in operation (newer designs refrain from the fluidised bed for the reactor). In the riser reactor, catalyst particles are mixed with the incoming feed, which is steadily converted into lighter products. At the riser exit, the products are separated from the catalyst by means

of a cyclone or a series of cyclones. During the conversion process the catalyst is partially deactivated by coke formation, and needs to be regenerated. The collected catalyst particles flow to the regenerator, which is operated as a conventional bubbling fluidised bed. Inside the regenerator, cyclones are positioned to collect catalyst from the combustion products. The regenerated catalyst particles are then recycled to the riser reactor. Before being supplied to an energy recovery plant, the hot gas stream from the regenerator is dedusted by a number of high-efficiency cyclones in a number of stages. In the last stage, usually a multi-cyclone is applied.

The requirements for the cyclones are different at each stage in the FCC unit. The purpose of the reactor and regenerator cyclones is to separate catalyst from the exiting gas stream. The particle diameter of the catalyst to be separated by these cyclones is roughly in the range 10 to 120 μm with a particle density of around $1400 kg\, m^{-3}$. Subject to a typical solids loading of $4-8 kg\, m^{-3}$, these cyclones can operate at an efficiency of $> 99.99\%$ (Talman, 1998). However, attrition occurs as a result of the high velocities in the riser as well as during transportation of the catalyst from the regenerator to the reactor and vice versa, which causes catalyst fines to be formed. The fines need to be collected by the multi-cyclone to prevent erosive wear of the turbine blades in the energy recovery unit. At this stage, the solids loading is significantly reduced and the collected particles do not need to be recycled into the FCC process. These different requirements on cyclone performance may affect, among other things, the inlet velocity magnitude. The inlet velocity of the internal cyclones should be moderate to prevent attrition of the catalyst particles during collection in the cyclone, whereas the inlet velocity of the multi-cyclone can be much higher due to its dedusting purpose at much lower solids loading. Some basic concepts of cyclone design and performance are discussed in the next section.

1.2 Cyclone design and performance

The cyclone can be considered as a special type of settling chamber with gravity replaced by a much stronger centrifugal force, which accelerates the separation of two phases with different density. Based on this principle, cyclones are usually classified in terms of the physical state of the two phases, *e.g.* gas-solids, gas-liquid, liquid-solids or liquid-liquid cyclone separators. When the carrying fluid is water, the cyclone separator is generally referred to as a hydrocyclone (Svarovski, 1984). The subject of this thesis is limited to the class of gas-solids cyclones.

Another classification scheme is based on the general shape of the flow field, where the main types are the reverse-flow and the straight-through cyclone (Leith and Jones, 1997). In the reverse-flow cyclone, the gas is made to spin by introducing it tangentially at the top of a cylinder. The particles move towards the wall of the cylinder and then towards the base of the cyclone, while the gas spirals upwards towards the gas outlet at the top of the cyclone. The direction of the gas flow is thus reversed in the cyclone. In the straight-through cyclone, the gas is made to spin by a fixed set of swirl vanes, mounted in a circular duct. Dust particles migrate to the wall under the action of the centrifugal forces and, shortly after, pass through a small annulus between two concentric ducts. The cleaned gas flow is passed straight through the inner duct. The advantage of this axial type of cyclone is its limited headroom requirements in contrast to the tangential inlet of the reverse-flow cyclone. However, the centrifugal forces generated by the latter are significantly higher. The cyclones studied in this thesis are all of

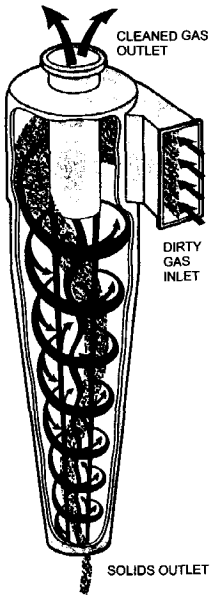

FIGURE 1.2: *Typical high-efficiency cyclone (after Sowter (1986)).*

the reverse-flow type.

An impression of the gas-solids flow in a reverse-flow cyclone separator is shown in Fig. 1.2. The standard cyclone design comprises a tangential or a scroll type of entry that forces the particle laden gas flow to rotate, a cone-under-cylinder body, and a cylindrical exit pipe partly inserted at the top into the cyclone interior. The particles are forced towards the cyclone wall and are ejected into a collection bin at the apex. Their motion in the wall boundary layer is primarily due to the downward component of the gas velocity at the cyclone wall rather than due to gravity. Below the lower end of the gas exit pipe, the spinning gas gradually migrates inward to a central core near the cyclone axis, and from here moves upward to the outlet. Numerous modifications have been proposed based on this generic design. One example is the insertion of a vortex breaker at the apex of the cyclone to prevent re-entrainment of already separated particles from the collection bin by the central vortex core (Muschelknautz and Brunner, 1967).

Cyclone performance is usually described in terms of pressure drop and collection efficiency. Based on the standard cyclone design, Stairmand (1951) proposed two cyclone designs, *i.e.* the high-throughput and the high-efficiency cyclone. The high-throughput cyclone can handle large volumetric flow rates at a moderate pressure drop, while yielding reasonable collection efficiency. The high-efficiency cyclone is capable of obtaining high collection efficiencies and separating micron-sized particles, but at a significant pressure loss. The choice for one of these designs is determined by the operational requirements.

For the prediction of cyclone performance a large number of (semi-) empirical cyclone models

are available in the literature. Most of these models take the effect of the physical properties of the gas and particulate phase on cyclone performance into account as well as the design variables and the operating conditions. However, Leith and Jones (1997) argue that there are a number of limitations related to the practical use of the cyclone models currently available, *i.e.* that they can predict different performances for the same cyclone design, and that generally a larger degree of modelling complexity does not imply a larger predictive accuracy.

1.3 MOTIVATION FOR THIS WORK

Since the pioneering work of Boysan et al. (1982), an alternative approach to (semi-) empirical cyclone modelling is available known as Computational Fluid Dynamics (CFD). The basis of this technique is the numerical solution of the governing equations for fluid flow, *i.e.* the conservation equations for mass, heat and momentum (Ferziger and Perić, 1996). The considerable increase of computing speed and memory during the last two decades has made the study of fluid flow by means of CFD easier and more effective. With respect to the prediction of cyclone performance, CFD can be applied to calculate the gas flow field of a cyclone in great detail as well as predict its pressure drop. For cyclones operated at low solids loading, the collection efficiency is predicted by calculating the trajectories of a large number of particles. However, the complex nature of the fluid flow in cyclones does require a certain level of modelling, which makes the experimental validation of CFD predictions to date still inevitable.

At the Kramers Laboratorium voor Fysische Technologie (Delft University of Technology), the investigation of cyclone separators has received attention since the late 1980's. The focus of this work was on the description of the gas flow field by means of laser diagnostics, such as Laser-Doppler Anemometry (Liem and Van den Akker, 1992) and laser visualisation (Fokke et al., 1994a,b). It was shown that the cyclone flow field exhibits complex flow features that are not likely to be captured easily by a CFD model. This has been the starting-point for the work presented in this thesis. Its objective is to provide an answer to the following questions:

- which CFD approach should be used to predict the cyclone flow field in a sufficiently accurate way?
- could this CFD model be used to define an *optimal* cyclone design, *i.e.* a cyclone that operates most efficiently at a given set of operating conditions (pressure drop)?

The study was limited to reverse-flow gas cyclone separators operating at low solids loading.

1.4 OUTLINE OF THE THESIS

The thesis is organised as follows:

In **Chapter 2**, the basic concepts and models of cyclone separators are discussed. The flow pattern is characterised by use of dimensionless quantities. Several (semi-) empirical models are discussed that predict cyclone pressure drop and collection efficiency. In addition, an overview is presented of work reported in the literature on the application of CFD in cyclone modelling.

In **Chapter 3**, experimental results are presented on the gas flow field of a number of cyclone geometries. Velocity and turbulence distributions are measured by means of Laser-Doppler Anemometry (LDA). Analysis of the LDA data reveals the existence of a low-frequency instability, which is related to a phenomenon known as the precessing vortex core (PVC).

Chapter 4 is dedicated to the description and reconstruction of the PVC signal. The LDA time series are analysed by means of a filtering technique known as adaptive signal processing. The spatial characterisation of the PVC is done using laser visualisation. Results of this study are used to assess the prediction of the PVC obtained by means of a Large Eddy Simulation (LES).

In **Chapter 5**, the experimental data on the gas flow field are used to assess the performance of different CFD models. The performance of turbulence models is studied for (modifications of) the Stairmand cyclone and a comparison is made of 2D and 3D calculations. In addition, the predictions of the flow field in a laboratory-scale cyclone are compared with LES results.

In **Chapter 6**, experimental and numerical results are presented as to the particle collection by the Stairmand cyclone and modifications thereof. A regression model is used to describe the collection efficiency measurements, and a comparison is made with the results obtained by means of CFD.

In **Chapter 7**, a response surface model is presented that is based on CFD predictions. By means of this model the pressure drop and cut-size of (modifications) of the Stairmand cyclone can be predicted. The model can also be applied to find optimal cyclone designs.

The thesis is concluded by **Chapter 8**, which summarises the conclusions and gives recommendations for further work.

CHAPTER 2

REVIEW OF CONCEPTS AND MODELS

The reader is introduced to the general concepts of cyclone design and performance. The focus will be on cyclones for gas-solids separation of the reverse-flow type. First, the operating principle and basic flow pattern are discussed. A number of dimensionless quantities are defined to characterise the flow field. Next, a review is presented on the modelling of the pressure drop and the collection efficiency of cyclone separators. Finally, recent advances in cyclone modelling by means of Computational Fluid Dynamics (CFD) are summarised.

2.1 CYCLONE FLOW CHARACTERISATION

An impression of the gas flow pattern in a cyclone may be obtained from the velocity and pressure measurements presented by Ter Linden (1949) (see Fig. 2.1). The tangential velocity profiles exhibit the typical shape of a combined vortex. The central region or vortex core is described by a rigid-body rotation; the tangential velocity increases linearly with increasing radial distance. In the outer region, limited by the core edge and the wall boundary layer, a free-type of vortex prevails resulting in a decrease of the tangential velocity with increasing radial distance. The tangential velocity distribution in the two vortex regions is characterised by:

$$W r^n = \text{constant} \tag{2.1}$$

where n represents the vortex exponent, which is equal to -1 for a forced vortex, and equal to 1 for a free or potential vortex. For the tangential velocity distribution in cyclones the outer region of the flow is generally described by Eq. 2.1 with a vortex exponent that varies between 0.4 and 0.7 (Gupta et al., 1984).

The axial velocity profiles presented in Fig. 2.1b confirm the reverse flow character of the cyclone. Near the wall, the mean flow is directed downwards, while in the central region the gas flows upwards. A complicated flow pattern exists in the core region with low axial velocities near the centreline. The radial velocity is smaller than the tangential and axial velocity components by an order of magnitude. The measurements of Ter Linden (1949) show

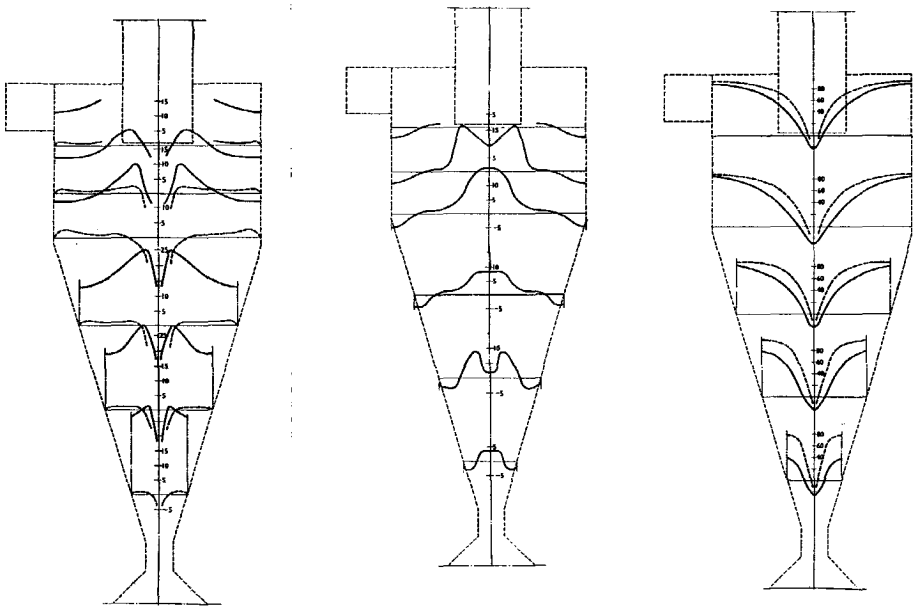

(a) (b) (c)

FIGURE 2.1: *Pitot tube measurements of the flow field and pressure distribution at several axial stations in a cyclone separator (Ter Linden, 1949), with (a) tangential (–) and radial (- -) velocity components, (b) axial velocity component, and (c) static (–) and total (- -) pressure.*

an inward radial velocity in the outer vortex region that is almost constant with radial position, and approximately equal at all vertical positions within the cyclone.

The pressure distribution in the cyclone is presented in Fig. 2.1c, where the total pressure is defined as the sum of the static and dynamic pressure. The static pressure decreases from a maximum value at the cyclone wall to a minimum value near the cyclone axis, which is due to the strong coupling between the tangential velocity component and the radial pressure distribution. This directly results from the Navier-Stokes equation in the radial direction by assuming that turbulent and viscous stresses are small and that the tangential velocity component, W, dominates the other two velocity components. The steady-state Navier-Stokes equation for the radial direction is then simplified to:

$$\frac{\partial P}{\partial r} = \rho_g \frac{W^2}{r} \tag{2.2}$$

Due to the strongly swirling flow field in the cyclone, the static pressure at the centreline may fall below atmospheric pressure. This zone of negative pressure can extend into the dust collection bin, and cause re-entrainment into the cyclone of particles already separated.

Swirling flow is a result of an impartation of a tangential velocity component on a flowing medium by means of a swirl generator. For swirl burners, the degree of swirl is usually characterised by the swirl number, S, which is a non-dimensional quantity representing axial flux of swirl momentum, G_ϕ, divided by axial flux of axial momentum, G_x, times the nozzle radius, R_x (see Gupta et al. (1984)):

$$S = \frac{G_\phi}{G_x R_x} \tag{2.3}$$

G_ϕ includes the $x - \theta$ directed turbulent shear stress; the term G_x includes the normal Reynolds stress in the x direction and the axial pressure gradient. Definition of the swirl number for cyclones is complicated due to the reverse-flow character of the flow field. The swirling flow in a cyclone is therefore usually characterised by a *geometric* swirl number defined by (Gupta et al. (1984)):

$$S_g = \frac{\pi}{4}\frac{D_e D}{A_{in}} \tag{2.4}$$

where D_e is the exit pipe or vortex finder diameter, D is the cyclone body diameter, and A_{in} is the inlet cross sectional area. For industrial cyclones, the geometric swirl number usually varies between 1 and 5.

The hydrodynamic stability of swirling flow is usually considered in terms of the Rayleigh criterion (see *e.g.* Chanaud (1965), Sloan et al. (1986) and Escudier (1987)). The criterion was derived by considering the general problem of the stability of inviscid two-dimensional swirling flows to non-axisymmetric disturbances, and proposes that a system is: (1) stable if $\rho W r$ increases locally with r, which is the case for a forced vortex rotation, (2) neutrally stable if $\rho W r$ is constant with r, which is valid for a free vortex, and (3) unstable if $\rho W r$ decreases with r. This implies that flow disturbances are suppressed in the vortex core region of the flow field in a cyclone.

In spite of its stability in terms of the Rayleigh criterion, the turbulent vortex core in cyclone flow is associated with low frequency oscillations. This three-dimensional, time-dependent coherent structure is often referred to as the precessing vortex core (PVC). Smith (1962) observed the PVC in gas cyclones by means of a smoke visualisation study, and Chanaud (1965) used a dye injection technique in a laboratory-scale hydrocyclone. Both authors observed a periodic motion with a frequency proportional to the flow rate through the device. Ito et al. (1983) measured the periodically fluctuating pressure with a pressure transducer, and observed that the PVC frequency is linearly dependent on the supplied flow rate. The frequency of the PVC is typically $10 - 200Hz$ (Sloan et al., 1986). A way to relate the PVC frequency to the macro time scale of the flow in a cyclone is by defining the Strouhal number, St, as the ratio of an overall time scale, $\tau_a = D/U_{in}$, and the time scale of the PVC, $\tau_{PVC} = 1/f_{PVC}$. This yields:

$$St = f_{PVC}\frac{D}{U_{in}} \tag{2.5}$$

Chanaud (1965) suggested that the precessing vortex core is closely related to a phenomenon known as vortex breakdown, which is described as a spatial transition via a stagnation point

from a steady axisymmetric vortex to a periodic spiral motion and then downstream to an irregular turbulent motion. This transition is generally considered one between a supercritical upstream state and a subcritical downstream state (Escudier, 1987). A vortex flow is defined as subcritical if it can support upstream propagation of waves and disturbances. A rule of thumb is that for a flow to be subcritical the ratio of the maximum tangential velocity to the axial velocity exceeds one, which is generally valid for the flow in the exit pipe of an industrial gas cyclone. Sloan et al. (1986) argues that inertial waves accumulate at the transition point, which is finally manifested as vortex breakdown.

Although there is no general agreement on the physical mechanism of vortex breakdown or the precessing vortex core, Sloan et al. (1986) asserts that an adequate theory must eventually describe the periodic, asymmetric oscillations by utilisation of the full three-dimensional, time-dependent Navier-Stokes equations. This will be reconsidered while discussing experimental and numerical results on the precessing vortex core in cyclones (see Ch. 4).

The turbulent flow in cyclone separators of industrial scale is usually characterised by a Reynolds number, Re, which may be interpreted as the ratio of a characteristic overall time scale, τ_a, and a viscous diffusion time, τ_ν (Tennekes and Lumley, 1972). These time scales are defined by means of characteristic length scale, L, and a characteristic velocity, U, of the flow. For some applications the choice for these flow scales is straightforward (*e.g.* the bulk velocity and the pipe diameter for turbulent pipe flow), but for cyclones a number of definitions are used in the literature.

One approach is to define the Reynolds number at the inlet by choosing the linear inlet velocity and the width of the inlet box as characteristic velocity and length scales (see *e.g.* Rietema (1961)). A similar approach is based on the flow in the exit pipe by taking the exit pipe diameter and the average axial velocity (Muschelknautz, 1972; Bohnet, 1995).

Alternative definitions of the Reynolds number are efforts to characterise the flow in the cyclone itself by choosing the cyclone diameter as a length scale and a superficial axial velocity (Chanaud, 1965; Liem and Van den Akker, 1992; Ontko, 1996) or a 'wall' circumferential velocity (Rumpf et al., 1968; Broer, 1961; Beeckmans and Kim, 1977; Bohnet, 1995) as the characteristic velocity of the flow. As the subject of study is the swirling flow in a cyclone itself, the latter approach appears to be favourable. In addition, the thickness of a turbulent wall-boundary layer and the friction factor are related to a Reynolds number based on the typical bulk velocity of the flow adjacent to the boundary layer, and a typical length scale of the flow field (Tennekes and Lumley, 1972). For the boundary layer at the cyclone wall, the characteristic scales would be the cyclone diameter and the 'wall' tangential velocity, because the tangential wall shear stress is predominant (Rumpf et al., 1968). Provided that the tangential velocity component at the cyclone wall is approximately equal to the linear inlet velocity, the Reynolds number is defined by:

$$Re = \frac{\rho_g U_{in} D}{\mu} \tag{2.6}$$

where ρ_g and μ represent the density and the molecular viscosity of the gas. For industrial gas cyclones, the Reynolds number varies between 10^5 and 10^6.

Since the Reynolds number of the flow in cyclones is quite large, viscous effects are limited to the wall region. Bloor and Ingham (1987) derived an analytical solution for the flow field

based on the inviscid, axisymmetric momentum equations and simplified boundary conditions. Although of a mathematical charm, the approach is not capable of taking into account more realistic boundary conditions.

For turbulent flows, a statistical approach is applied to the equations of motion by decomposing the instantaneous velocity and pressure into a mean and fluctuating component (Reynolds decomposition). After time averaging this substitution yields the following equations of motion for the mean flow of an incompressible, Newtonian fluid (Tennekes and Lumley, 1972):

$$\frac{\partial U_i}{\partial x_i} = 0 \tag{2.7}$$

$$\frac{\partial U_i}{\partial t} + U_j \frac{\partial U_i}{\partial x_j} = -\frac{1}{\rho_g}\frac{\partial P}{\partial x_i} + \frac{1}{\rho_g}\frac{\partial}{\partial x_j}\left[\mu \frac{\partial U_i}{\partial x_j} + \tau_{ij}\right] \tag{2.8}$$

where Eq. 2.7 is the continuity equation, and Eq. 2.8 is known as the Reynolds averaged Navier-Stokes (RANS) equation in the i-direction. In these equations, U_i is the mean velocity component, $\partial P/\partial x_i$ is the mean pressure gradient, and τ_{ij} represents the Reynolds stress tensor:

$$\tau_{ij} = -\rho_g \overline{u_i u_j} \tag{2.9}$$

where u_i is the fluctuating velocity in the i-direction. The diagonal components of τ_{ij} are normal stresses, and their sum is used to define the turbulent kinetic energy, $k = \frac{1}{2}(\overline{u_i u_i})$. The off-diagonal components of τ_{ij} are shear stresses; they play a dominant role in the theory of mean momentum transfer by turbulent motion (Tennekes and Lumley, 1972).

Compared to the original Navier-Stokes equations, Eq. 2.8 contains six additional unknowns (*i.e.* the Reynolds stress tensor). This is known as the closure problem of turbulence modelling. A number of closure models have been proposed in the literature with varying degrees of sophistication and computational complexity (see *e.g.* Hanjalić (1994) for an overview of advanced closure models). The complicated flow field in cyclones poses additional constraints on the application of a turbulence closure model. Some results of turbulence modelling applied to cyclones are discussed in Sec. 2.4.

In the literature, a large variety of reverse-flow gas cyclone separators have been studied. All cyclone designs have common geometry characteristics, but most of them were adjusted to serve a specific operating purpose. Stairmand (1951) recommends two standard designs of the gas-solids cyclone, *i.e.* the high-efficiency and the high-throughput cyclone. Their typical dimensions are schematically presented in Fig. 2.2.

The high-efficiency cyclone has a tangential inlet, whereas the high-throughput design has a scroll type of inlet to accommodate a large flow rate while avoiding the inlet flow to impact on the exit pipe wall in the interior of the cyclone.

For both cyclone designs, Stairmand (1951) measured the grade efficiency curve, which represents the fractional collection efficiency as a function of particle size. Scaling rules are presented to adjust the measured grade efficiency curves for different flow rates, particle density, gas viscosity and cyclone diameter. These scaling rules are based on the assumption of a constant Stokes number. The Stokes number, Stk, is a dimensionless parameter used to characterise the motion of a particle in a flow field. It is defined as the ratio of a macro time scale of the flow, $\tau_a = D/U_{in}$, and the Stokesian particle relaxation time, $\tau_p = \rho_p d_p^2/18\rho_g\nu$, yielding:

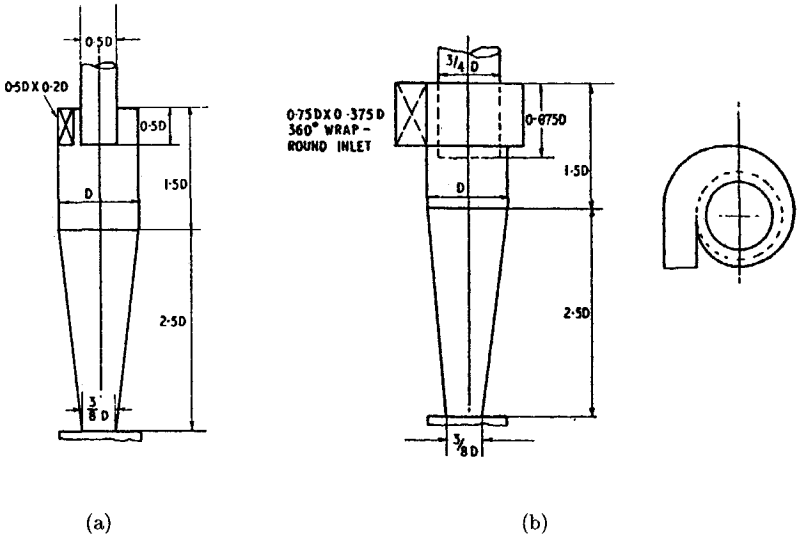

FIGURE 2.2: *Typical proportions of the (a) high-efficiency cyclone, and (b) high-throughput cyclone after Stairmand (1951). All dimensions are given relative to the cyclone body diameter, D.*

$$Stk = \frac{\rho_p}{\rho_g} \frac{d_p^2}{18\nu} \frac{U_{in}}{D} \tag{2.10}$$

where ρ_p and ρ_g denote the particle and gas density, respectively, ν is the kinematic viscosity of the gas, and d_p is the particle diameter.

The cyclone separator designs shown in Fig. 2.2 are defined by a limited number of geometrical dimensions such as the cyclone internal diameter, the exit pipe diameter and the cyclone length. Several cyclone geometries of different geometrical dimensions may result in the same collection efficiency for a given composition of the gas-particle flow. If the cyclone designs are compared on the basis of an equivalent total volume, *i.e.* cyclones of comparable weight and, hence, manufacturing costs, the optimal cyclone design corresponds to the one operating at lowest pressure loss. This approach towards estimating the 'optimal' cyclone geometries was pursued in particular by Barth (1956), Rumpf et al. (1968) and Muschelknautz (1972). We will return to the subject of optimised cyclone design in Ch. 7. First, models from the literature are discussed that deal with cyclone performance in terms of pressure drop and collection efficiency.

2.2 PRESSURE DROP

Many investigators have developed expressions to predict cyclone pressure drop; some are empirical, some theoretical, and most a mixture of both. Phenomena that are considered to contribute to the pressure drop of a cyclone separator include (Barth, 1956):

- pressure losses due to the tangential injection of gas by the inlet section,
- the formation of a vortex,
- energy losses due to wall friction and at the exit.

Based on these pressure loss contributions and assumptions with respect to the flow field, *e.g.* on the vortex shape and the wall friction coefficient, several authors have presented expressions that relate pressure drop to cyclone dimensions and operating conditions.

Most authors provide experimental data to support their pressure drop models. Nevertheless, calculated values for cyclone pressure drop may give results in error by 50 % or more according to Leith and Jones (1997). Part of the discrepancies between (semi-)empirical expressions and experimental data presented in the literature may be attributed to the different definitions of pressure drop. To compare experimental data and expressions, Leith and Jones (1997) define the overall cyclone pressure drop as the static pressure differential across the cyclone. This definition is also used in most experimental work presented in the literature, where the pressure drop is measured at the cyclone inlet and outlet by means of pressure tabs inserted in the cyclone wall (see *e.g.* Muschelknautz and Krambrock (1970) and Hoffmann et al. (1992)). Also by Bohnet (1995) the cyclone pressure drop is measured as the difference in static pressure at the inlet and outlet, but here a flow straightener was situated in the outlet duct. Note that in the presence of swirl the static pressure at the wall is increased as a result of the radial pressure distribution.

In contrast to the experimental work presented on cyclone pressure drop, most (semi-) empirical expressions consider *energy* losses at different locations in the cyclone as mentioned earlier. Using this approach, Barth (1956) defines the cyclone pressure drop by subtracting the total pressure averaged on an axial plane at the outlet from that at the inlet. The total pressure at the inlet is made up of a static and a dynamic pressure component, which is determined by the magnitude of the inlet velocity. At the outlet, a superficial exit velocity is used to calculate the velocity head.

A similar approach was used by Stairmand (1949). Here, the total energy dissipated by the flow of fluid through the cyclone is calculated by summing the velocity head at the inlet, the centrifugal head of the cyclone vortex, and energy losses related to the velocity head at the exit. The differences in defining the pressure drop imply that some caution is needed when calculated and measured cyclone pressure drops are compared.

In both the pressure drop models of Stairmand (1949) and Barth (1956), the maximum circumferential velocity needs to be estimated to calculate the centrifugal head of the vortex. Based on different assumptions with respect to the velocity distributions, both authors arrive at an expression that relates the maximum circumferential velocity to the inlet velocity, the wall friction factor, and geometrical dimensions of the cyclone.

The pressure drop due to wall friction is determined by the wall shear stress, τ_w, which can be modelled by

$$\tau_w = \lambda \frac{1}{2} \rho_g U_{in}^2 \tag{2.11}$$

where the wall friction factor, λ, is a function of Re. Stairmand (1949) as well as Barth (1956) use a wall friction factor, λ, equal to 0.02. This value was chosen by considering the analogy with friction loss in hydrodynamically smooth pipes at Reynolds numbers corresponding to those obtained for cyclones.

Muschelknautz and Krambrock (1970) estimated the wall friction factor from measurements of the maximum circumferential velocity for a range of Reynolds numbers and three different values for the relative wall roughness. The results show that at low Reynolds numbers the wall friction factor strongly decreases with increasing Reynolds number as a result of the decreasing thickness of the laminar boundary layer. In the turbulent regime, the wall friction factor still depends on the Reynolds number, but to a smaller extent in agreement with turbulent boundary layer theory. Similar considerations on the relation of wall friction and Reynolds number were taken into account in the theoretical analysis of cyclone flow by Rumpf et al. (1968).

The magnitude of the wall friction factor has a considerable effect on the predicted pressure drop. This is demonstrated in Fig. 2.3, where the cyclone pressure drop is presented as a function of the linear inlet velocity for the Stairmand high-efficiency cyclone geometry (see Fig. 2.2). The models of Stairmand (1949) and Barth (1956) predict similar values for the pressure drop. The pressure drop is larger for lower values of the wall friction factor, which is related to higher velocity head of the vortex, *i.e.* the ratio of the maximum tangential velocity to the inlet velocity increases for lower values of the wall friction factor.

The pressure drop is usually normalised by the velocity head at the inlet, $\frac{1}{2}\rho_g U_{in}^2$, and known as the Euler number or pressure drop coefficient (Ontko, 1996). Measurements on the wall friction factor presented by Bohnet (1995) show an effect of the Reynolds number on the pressure drop coefficient, although few measurements were done for the turbulent regime. In the field of hydrocyclones, Rietema (1961) also presented a non-linear increase of the pressure drop coefficient with increasing Reynolds number.

In contrast to these experimental and theoretical results on the Reynolds number dependency of the cyclone pressure drop, no straightforward conclusions could be drawn from a comparison of measurements and models as presented by Ogawa (1984). A large number of models does not predict an effect of the Reynolds number on the pressure drop coefficient, and the experimental data presented show a scatter too large to draw definite conclusions.

The centrifugal head of the cyclone vortex as calculated by Stairmand (1949) depends on the shape of the vortex, and the spinning speed of the vortex at the inlet radius. This spinning speed may be greater than, equal to, or less than the magnitude of the linear inlet velocity depending on the balance between the rate of supply of angular momentum to the vortex, and the frictional losses due to wall friction. Based on a momentum balance, Stairmand (1949) presented an expression that relates the ratio of the spinning speed at the inlet radius and the linear inlet velocity to the ratio of the inlet and exit pipe radius. The loss of momentum due to wall friction is taken into account by an additional parameter, which is determined by the wall friction factor and the cyclone dimensions. Two issues need to be considered if this model is

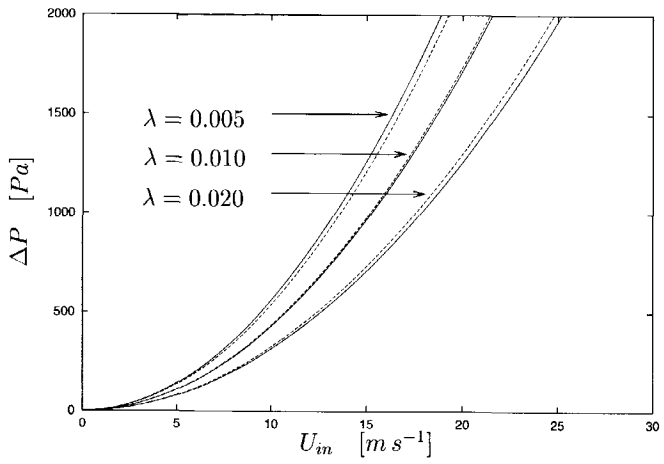

FIGURE 2.3: *The pressure drop, ΔP, of a Stairmand high efficiency cyclone ($D = 0.290\,m$) versus the linear inlet velocity, U_{in} at ambient conditions according to the models of (–) Stairmand (1949) and (- -) Barth (1956).*

applied, *viz.* it is strictly spoken only valid for cyclones with a tangential inlet, and the spinning speed at the inlet radius is assumed to be constant along the cyclone length.

Instead of the spinning speed at the inlet radius, Barth (1956) and Muschelknautz (1972) consider the average circumferential velocity component, W, at the cyclone radius, R, where $R = D/2$, and its deviation from the linear inlet velocity, U_{in}, depending on the inlet configuration. The effect of different inlet configurations is expressed in terms of a correction factor, α, defined as:

$$\alpha = \frac{U_{in}\, r_{in}}{W\, R} \tag{2.12}$$

where r_{in} is the inlet radius. The magnitude of the inlet radius depends on the shape of the inlet section. The effect of three different inlet sections on the correction factor, α, is shown in Fig. 2.4.

Inlet A shown in Fig. 2.4 is also known as a scroll type of inlet, whereas inlet B is a tangential inlet used in the Stairmand high-efficiency cyclone (Fig. 2.2a). For inlet B it has been shown that the correction factor is a function of the ratio of the inlet to outlet area and also depends on the inlet width (see Muschelknautz (1972) and Bohnet (1984)). Configuration C with its fixed inlet vane extending into the cyclone was used in the cyclones studied by Shepherd and Lapple (1939).

Barth (1956) arrives at an expression for the maximum circumferential velocity depending on cyclone dimensions and wall friction in a similar way as was modelled by Stairmand (1949). The cyclone pressure drop relation proposed by Barth (1956) is adopted in a modified form in the papers of Muschelknautz (1972) and Bohnet (1984). In this discussion of the pressure drop

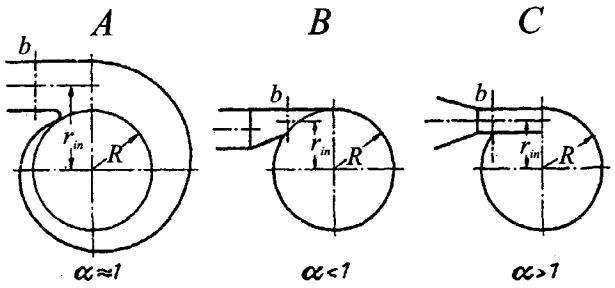

FIGURE 2.4: *Different inlet configurations for cyclone separators and their effect on the correction factor α used in Eq. 2.12.*

models of Stairmand (1949) and Barth (1956), some weaknesses were already revealed, which are mainly related to the postulated velocity field in the cyclone separator, in particular the radial swirl distribution.

The gas that is exhausted through the exit pipe still has a strong swirling flow component. To reduce the cyclone pressure loss several measures have been proposed in the literature to convert the high kinetic energy of the flow into pressure (see *e.g.* Bohnet (1982) and Greif (1996)). An important issue on the application of these types of de-swirlers is whether they affect the vortex in the cyclone itself. Stairmand (1951) performed a visualisation study of the vortex flow in a cyclone by using a dye tracer, and unequivocally showed that the vortex is strongly disturbed and the core is almost completely absent when an internal obstruction is fitted in the exit pipe. This may obviously reduce the cyclone pressure drop significantly, but at the same time destroy the cyclone's separation capability.

Cyclone pressure drop is also affected by the solids loading of the gas flow, which is defined as the ratio of solids to gas mass flow rate. Muschelknautz (1972) proposed an expression that relates the wall friction factor to the solids loading. The model predicts a decrease of the cyclone pressure drop for increasing solids loading. This is the result of two opposite effects, *i.e.* increasing the concentration of particles results in a larger wall friction and a reduction of the maximum circumferential velocity of the vortex at the same time. The reduction of the velocity head, being the dominant contribution, results therefore in a decreased cyclone pressure drop. The same trend was observed experimentally by Hoffmann et al. (1992), although at a much stronger rate, and by Comas et al. (1991).

Ontko (1996) studied the effect of solids loading on cyclone pressure drop by means of a response surface technique. The pressure drop coefficient was found to be a function of both the Reynolds number and the dust loading, and their combined effect over the experimental region. This combined effect could be explained by the damping effect of the solids on the fluid turbulence at higher concentrations. An unusual effect of the solids loading on the pressure drop coefficient was demonstrated by Molerus and Glückler (1996). For their new cyclone design, the pressure drop coefficient showed an approximately linear *increase* with growing solids loading. Due to the low circumferential velocities in the cyclone, the solids loading hardly affected the vortex, but instead resulted in a higher pressure drop similar to the effect of the solids

concentration on the flow in for instance pneumatic conveying. However, for most conventional cyclones the vortex contributes significantly to the total pressure drop.

2.3 COLLECTION EFFICIENCY

The collection capability of cyclone separators is based on a simple physical mechanism, *i.e.* particles injected into the cyclone are submitted to a strong centrifugal force field, and, due to their inertia, drift radially to the wall, where they are transported to the catch bin by the wall boundary layer. However, despite this straightforward operating principle, considerable effort has been put into developing cyclone models that are capable of predicting the (grade) collection efficiency for a specific cyclone geometry and a wide range of operating conditions.

In addition to the modelling approach, a large number of experiments have been reported in the literature. Part of this experimental work is carried out for the assessment of collection efficiency models, and part of it is used to demonstrate the effect of proposed cyclone modifications or even new designs. The experimental work presented in the literature generally shows a wide variety with respect to operating conditions, *e.g.* temperature, pressure, flow rate, and solids loading, as well as the applied cyclone geometrical lay-out. Hence, a genuine comparison of experimental data and models is complicated. To identify a common ground for several models widely applied in cyclone design, the basic concepts and simplifications are discussed here.

Cyclone collection performance is generally described by its overall particle collection efficiency, $\overline{\eta}$, reflecting the fraction of particulate mass entering the cyclone that is captured. Since the overall collection efficiency is related to the particle size distribution of the solids fraction injected into the cyclone, a more favourable parameter is the fractional or grade efficiency, η. The grade efficiency describes the variation of collection efficiency with particle size, and is related to the overall efficiency by

$$\overline{\eta} = \int_0^\infty \eta(d_p)\ \phi(d_p)\ \mathrm{d}\, d_p \tag{2.13}$$

where ϕ is the size distribution function of the incoming particulate mass, and η is assumed to be independent of ϕ. This assumption was tested by Ontko (1996) by means of an experimental regression analysis of two batches of test particles with different particle size distributions, and no relation was found between η and ϕ.

Some cyclone models presented in the literature aim at predicting the complete grade efficiency curve as a function of the cyclone dimensions and operation, whereas other models estimate the collection efficiency by means of a characteristic particle diameter, *viz.* the critical particle diameter, or the cut-size. The theoretical grade efficiency curve is characterised by a critical particle diameter; the cyclone has zero efficiency for all particles smaller than the critical diameter, and 100% efficiency for all particles larger. In practice, this sharp transition between maximum and minimum collection efficiency does not occur, and the critical particle diameter is replaced by the cut-size representing the particle size that corresponds to 50 % collection efficiency. An extensive summary of the cyclone models for cut-size prediction is given by both Bernard (1992) and Leith and Jones (1997).

The cyclone models presented in the literature are derived from two different approaches. Based on the *static particle* approach, equations for the critical particle diameter were developed by Stairmand (1951) and Barth (1956). This approach involves determining the particle diameter for which the centrifugal force on the particle is exactly balanced by the inward (Stokesian) drag force. It is assumed that larger particles drift towards the cyclone wall and become collected, whereas smaller particles flow into the vortex core and are exhausted.

For the calculation of the critical particle diameter, the gas flow field in the cyclone is characterised by the maximum circumferential velocity of the gas and the average inward radial velocity. These variables depend on the inlet velocity and the geometrical dimensions of the cyclone. In addition, the critical diameter is related to physical properties of the gas and the particles, *i.e.* the gas density and dynamic viscosity, and the particle density. In the equations proposed by Stairmand (1951) and Barth (1956), the relation between cyclone design and gas flow field is derived theoretically. A practical approach was followed by Iozia and Leith (1989, 1990), who proposed empirical equations for flow field variables based on an experimental programme with laboratory-scale cyclones. The static particle approach may be considered rather crude, because the cyclone flow field is reduced to two variables only.

The *time of flight* approach is another way to calculate the critical particle diameter. It considers the time it takes for a particle to travel to the cyclone wall from its initial position. The particle residence time is sometimes defined in terms of an empirical 'number of turns' that the gas stream makes within the cyclone. Since the initial position of the critical particle diameter is assumed to be the midpoint of the gas entry, information is required on the shape of the free vortex type of flow in this region. This vortex region is usually described in terms of a vortex exponent (see Eq. 2.1). Compared to the static particle approach, more information on the flow field is taken into account, although knowledge is needed of the vortex exponent and the number of rotations of the gas flow.

To obtain a genuine efficiency classification of a gas cyclone, it is necessary to estimate the full grade efficiency curve, as was argued earlier. Most modelling efforts of recent years have been focussed on describing the gas flow field in a cyclone, and on defining an equation that represents the radial component of the trajectory of an individual particle moving in the gas. One of the first models was proposed by Leith and Licht (1972). In this model, the equation of motion for a particle is simplified, *i.e.* there is no acceleration of the particle in the radial direction, the gas has zero radial velocity, and there is no slip velocity between the two phases in the circumferential direction. Other assumptions are related to the particle itself, *e.g.* the particle is spherical in shape, the radial drag force on the particle is given by Stokes' law, and the particle trajectory is not affected by the presence of other particles. The gas flow field is taken into account by assuming the quasi-free vortex outside the vortex core, and estimating an average residence time of the gas in the cyclone. The average residence time depends on the geometrical dimensions of the cyclone, and the fraction of collected particles is related to it. In this way, a full grade efficiency curve may be calculated.

The model assumptions of Leith and Licht (1972) have been the starting point for a number of models presented in the literature with increasing sophistication and complexity. In the model of Dietz (1981), the cyclone flow field was subdivided into three compartments to take the existence of varying residence times into account, and to comply more with the reverse-flow characteristics. An improved description of the process of particle exchange between the core and the outer vortex region was proposed by Mothes and Löffler (1984), who introduced a

particle diffusivity between the regions by means of an effective particle dispersion coefficient. In a model by Enliang and Yingmin (1989), turbulent diffusion was only considered in the wall region together with a particle bounce or re-entrainment coefficient. Gottschalk and Bohnet (1998) extended the Dietz model with four more cyclone flow regions, including a blow-down region at the bottom of the cyclone in case part of the gas flow is removed here, and proposed a relation for the particle dispersion coefficient as a function of the Reynolds number and a volumetric ratio depending on the blow down flow rate.

Improvements of the models due to Leith and Licht (1972) as well as Dietz (1981) were proposed by Clift et al. (1991). Especially a modification of the Leith & Licht model considering the particle removal resulted in a dramatic improvement of the calculated grade efficiency curve compared to other models, and experimental data. A recent collection efficiency model proposed by Kim and Lee (1997) is an extension of the model by Mothes and Löffler (1984). The importance of boundary-layer effects on particle deposition in cyclones is taken into account by considering the wall boundary layer as an additional region in the model.

In Fig. 2.5, the grade efficiency curve for a Stairmand high-efficiency cyclone is presented according to a number of cyclone models discussed here. All predicted curves exhibit the characteristic S-shape. The mutual comparison of the model calculations of the grade efficiency reveals that they differ quite strongly with respect to the predicted cut-size and the curve shape. Dirgo and Leith (1985) performed grade efficiency measurements of the standard Stairmand geometry at varying inlet velocity magnitude, and compared their experimental results with some of the models discussed here. All models failed to predict the correct cut-size, and only the grade efficiency curve due to Barth (1956) exhibited the correct slope. A similar study by Griffiths and Boysan (1996) showed that only the empirical model of Iozia and Leith (1989) was useful in reproducing the experimental performance.

The concise description of collection efficiency models given here reveals that models are expected to benefit from an improved description of the gas flow field. The reverse side of this development is the increasing complexity of the models, and the introduction of additional variables that need experimental validation. As the inclusion of more and more details of the flow field in the collection efficiency models may result in improved predictions, an alternative approach to the empirical models discussed here becomes more attractive. This approach is the prediction of the flow field by means of Computational Fluid Dynamics.

2.4 THE COMPUTATIONAL FLUID DYNAMICS APPROACH

A field of research that has gained increasing interest from engineers during the last decade as a result of the advancement of computer power and numerical methods is Computational Fluid Dynamics (CFD). By means of CFD, the partial differential equations that describe flow phenomena are approximated by a system of algebraic equations, which can then be solved numerically. In this way, not only overall parameters such as pressure drop are estimated, but it is also possible to study *e.g.* the presence of recirculation zones. A more general introduction on the principles and capabilities of CFD is given by Ferziger and Perić (1996).

Some of the first results on modelling the gas-particle flow of cyclone separators by use of CFD were obtained by Boysan et al. (1982). To reduce the computational effort for solving the Reynolds averaged Navier-Stokes equations (Eq. 2.8), the gas flow field was solved in an

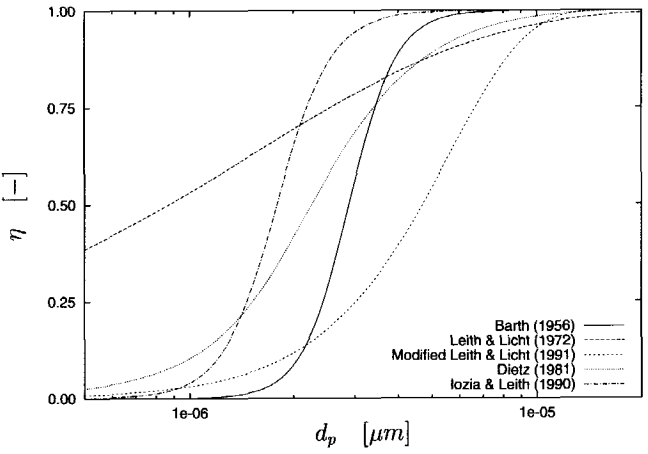

FIGURE 2.5: *Model predictions of the grade efficiency curve of the Stairmand cyclone studied experimentally in this thesis with* $D = 0.290\,m$, $\rho_g = 1.185\,kg\,m^{-3}$, $\rho_p = 2,740\,kg\,m^{-3}$, $\mu = 1.85\ 10^{-5}\,N\,s\,m^{-2}$, *and* $U_{in} = 20\,m\,s^{-1}$.

axisymmetric, rather than the full 3D, Eulerian framework. The particle flow was solved by means of a Lagrangian method. An additional closure model is required to relate the Reynolds stresses to the mean quantities. This approach has been applied since then in several CFD studies on cyclone separators, and most of the simulations presented in this thesis were done in a similar way.

Two interesting conclusions from the paper of Boysan et al. (1982) are worth mentioning here. First, turbulence closure models based on the assumption of isotropy (*e.g.* the $k-\epsilon$ model) are inapplicable in the case of highly swirling flow. Second, it is permissible to ignore all the derivatives with respect to the tangential direction, because the flow loses its three-dimensional character at a short distance from the tangential inlet. These model assumptions will be discussed in more detail in this thesis while comparing experimental data and numerical predictions.

The CFD calculations on cyclone flow available in the literature show a wide variety of modelling frameworks and geometries studied. Bernard et al. (1989) applied the model of Boysan et al. (1982) to predict the gas flow field and pressure drop of a Lapple type of gas cyclone operating at high temperatures. The turbulence model employed here was the algebraic stress model (ASM), which is an algebraic approximation of the full Reynolds stress transport model (RSTM). Predictions of the grade efficiency curve corresponding to a Stairmand cyclone were presented by Hoffmann et al. (1996) by using the same model, and were compared to empirical model calculations and experimental data.

Other CFD calculations of cyclone flow published more recently employed (versions of) the $k-\epsilon$ model, which is remarkable in view of the first conclusion of Boysan et al. (1982) mentioned earlier. The axisymmetric simulations done by Zhou and Soo (1990) were obtained with the

standard $k-\epsilon$ model, and are compared with LDA data presented by the same authors. It is shown that the $k-\epsilon$ model is even capable of predicting the combined vortex. A modified $k-\epsilon$ model was used by Dyakowski and Williams (1993) for axisymmetric CFD calculations of the flow in a hydrocyclone. The simulation results show a reasonable agreement with LDA measurements, however, the amount of experimental data is rather limited.

Hsieh and Rajamani (1991) modelled the fluid flow in a hydrocyclone in an axisymmetric vorticity-streamfunction formulation. Turbulent transport was modelled by means of a modified Prandtl mixing-length model, where the mixing length was estimated as a function of the cyclone radius and the ratio of water to slurry viscosities. The predictions are compared to LDA measurements of the mean axial and tangential velocity components at a large number of axial measurement stations. This model predicted the experimentally observed vortex correctly, too.

The approach of Boysan et al. (1982) was applied to calculate the pressure drop and grade efficiency curve for a number of cyclone geometries by Griffiths and Boysan (1996). They modelled the complete cyclone geometry in a three-dimensional structured grid, and solved the 3D RANS equations by using the RNG-$k-\epsilon$ model. In the RNG-$k-\epsilon$ model, the effect of rotation is included in the calculation of the turbulent viscosity. Again, this is an approach to account for the relation between the strongly swirling flow field and turbulent stress anisotropy. The predicted pressure drops as well as the calculated grade efficiency curves were in reasonable agreement with the experimental data.

A three-dimensional calculation of a gas cyclone separator using the Reynolds stress transport model was carried out by Viollet et al. (1992). Particle trajectories were predicted by means of a Lagrangian method. It was shown that there is a significant effect of turbulent dispersion and wall adhesion on the calculated grade efficiency curves. An alternative approach to Lagrangian modelling of particle trajectories is the two-fluid approach used by Kitamura and Yamamato (1999), where the particulate phase is treated as a continuum of mono-dispersed particle size distribution. Particle-particle interactions are assumed to be negligible, but two-way interactions between the phases are taken into account. The grade efficiency curve was computed by estimating the mass flux of particles that leave the cyclone through the exit pipe for different particle sizes.

This summary of papers on CFD applied to cyclones demonstrates at least two issues of concern: (1) special care should be taken at employing a turbulence closure model, and (2) accurate experimental data of velocity profiles and collection efficiency are inevitable to assess the CFD predictions. These issues will be the main focus of this thesis.

2.5 Closure

The literature review presented in this chapter was intended to get the reader acquainted with the concepts and principles of gas-particle flow in a cyclone separator. It reveals that considerable effort has been put into this subject by the research community during a number of decades starting from different points of departure and knowledge, and a variety of both theoretical and experimental techniques. The interpretation of numerical and experimental data provided by different authors on cyclone flow is hampered by the non-uniformity in operating conditions and geometries. In addition, velocity measurements obtained by LDA are available particularly

in the field of hydrocyclones, whereas the experimental data on gas-particle cyclones generally consist of just collection efficiency measurements. For the assessment of CFD calculations, both kinds of experimental information are demanded.

Despite its limitations, CFD has an advantage over traditional collection efficiency models due to the increasing availability of affordable computer power. The detailed information on the flow field provided by CFD calculations may in principle yield a more accurate prediction of the performance of gas-particle cyclone separators related to their operation and design. The approach in this thesis will be based on these considerations by starting with an experimental study of the gas flow field by means of laser diagnostics. These experimental data will then be used to assess different turbulence models and numerical approaches. Finally, the relation between cyclone performance and its design and operation will be discussed by means of collection efficiency measurements and CFD predictions.

CHAPTER 3

EXPERIMENTAL STUDY OF THE GAS FLOW FIELD

Experimental results are presented on the gas flow field and the pressure drop of two different cyclone geometries, viz. a Stairmand high-efficiency cyclone and a tangential swirl tube separator. Measurements of the tangential and axial velocity components were obtained by means of Laser-Doppler Anemometry (LDA). First, the basic concepts and operation principles of the LDA technique are discussed. Next, a description is given of the experimental set-up and the cyclone geometries studied. It is shown that a contraction of the exit pipe significantly affects the radial profiles of the mean tangential and axial velocity components in the separation zone of the cyclone. High levels of velocity fluctuation were measured in the vortex core. In addition, the velocity distribution in this region deviates from a Gaussian probability density function. These characteristics are due to a flow phenomenon known as the precessing vortex core, which is the subject of the next chapter.

3.1 INTRODUCTION

The literature review on cyclone models (Ch. 2) revealed that the assessment of cyclone performance predictions necessitates experimental investigation of the gas flow field. Early measurements of the flow pattern in a gas cyclone were done by Ter Linden (1949), who measured the static pressure and gas velocity components by means of a pitot probe (Fig. 2.1). A similar probe was used by Alexander (1949) to study a number of cyclones with different internal diameter. More recent examples of velocity measurements in a cyclone are provided by Reydon and Gauvin (1981) and Patterson and Munz (1996). In these studies, a five-channel pressure probe, 6.4 mm in diameter, was used for simultaneously measuring all velocity components and the static pressure.

A disadvantage of the pitot probe is that it might disturb the flow field due to its finite size, and hereby introduce a significant experimental error. In addition, knowledge of the main direction of the flow is necessary for the proper positioning of the probe, and prior to employment, the probe needs to be calibrated. To a lesser extent these considerations also apply to a hot-wire anemometer. In particular the intrusive nature of these types of anemometers

reduces their suitability for the accurate measurement of the mean velocity components as well as turbulence characteristics in gas cyclones.

A well-known, non-intrusive measuring technique for fluid flow applications is Laser-Doppler Anemometry (LDA). LDA does not require calibration, and is capable of determining the direction of the flow. Early measurements of the flow field in a cyclone by means of LDA were done by Mothes (1982), who studied the effect of solids loading on the radial distribution of the tangential velocity. Bernard (1992) used LDA measurements to determine the effect of temperature on the mean tangential and axial velocity components. The effect of geometry modifications on the flow field in a cyclone was studied by Liem and Van den Akker (1992). By means of LDA signal analysis, the presence of (quasi-) periodical fluctuations in the flow field was revealed, and a procedure was proposed to separate these fluctuations from the turbulent signal (see also Fokke et al. (1994a)). Other examples of the application of LDA to cyclone flow were reported by Fraser and Abdullah (1995), Gorton-Hülgerth and Staudinger (1996), Hoffmann et al. (1998), and Slack and Boysan (1998).

In this work, LDA measurements were carried out in two different cyclone geometries. Both geometries were modified with respect to the exit pipe diameter. The obtained experimental data set was used to validate numerical flow predictions obtained with Computational Fluid Dynamics (CFD).

3.2 Laser Doppler Anemometry

Since its introduction a few decades ago, Laser Doppler Anemometry (LDA) has evolved in a well-established experimental technique used to study a wide range of fluid flow applications. A general overview of the theory and practice of the Laser Doppler technique may be found in a number of textbooks, *e.g.* Durst et al. (1976) and Watrasiewicz and Rudd (1976). A recent and elaborate discussion of LDA applied to aerodynamic turbulent flow may be found in Absil (1995).

Here, a short introduction of the LDA technique and its physical principles is presented along with a description of the actual measurement system used. Some practical issues concerning the specific application of LDA for studying the gas flow field in cyclone separators will be discussed in more detail.

3.2.1 Principles of operation

The principle of LDA is based on using the Doppler shift of laser light to measure the velocity of a fluid. The Doppler shift is the change in frequency that is observed when light is scattered by a moving object, *e.g.* a tracer particle transported by the fluid flow. In Fig. 3.1, a particle moving with velocity $\mathbf{v}$ is illuminated by a laser beam of frequency f_i and wavelength λ along unit vector $\mathbf{i}$. A detector, located in the direction of unit vector $\mathbf{s}$, will receive scattered light with a frequency f_s, which can be written as

$$f_s = \left(\frac{c - \mathbf{v} \cdot \mathbf{i}}{c - \mathbf{v} \cdot \mathbf{s}} \right) f_i \tag{3.1}$$

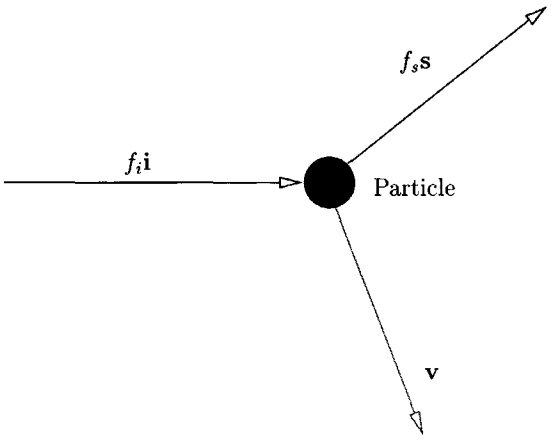

FIGURE 3.1: *Schematic representation of the Doppler shift.*

where c is the velocity of light, and $f_i = c/\lambda$. The term $(c - \mathbf{v} \cdot \mathbf{i})$ is the velocity difference between the particle and the illuminating wave. In a similar way, $(c - \mathbf{v} \cdot \mathbf{s})$ represents the velocity difference between the moving particle and the scattered light.

The Doppler shift f_D is defined as the difference between the frequency of the scattered and incident radiation, and can be approximated by:

$$f_D = \frac{\mathbf{v} \cdot (\mathbf{i} - \mathbf{s})}{\lambda} \tag{3.2}$$

where it is assumed that $|\mathbf{v}| << c$. It follows from Eq. 3.2 that the Doppler shift depends linearly on the velocity of the scattering particle.

Since the Doppler frequency is much smaller than the incident light frequency, an indirect method has to be used to measure the frequency difference. In LDA systems, this method is based on the concept of optical mixing. If two coherent light waves of slightly different frequency f_1 and f_2 fall on a photodetector, optical mixing will occur. The output signal of a photodetector being a square-law device will contain contributions with sum-frequencies $2f_1$, $2f_2$, and $f_1 + f_2$, and a contribution which oscillates with the frequency difference $f_1 - f_2$. This last contribution provides information on the Doppler shift, and is the only oscillating component present in the output signal, as the frequencies of the other contributions are too high for detection.

The optical arrangement used in this study is based on the dual beam or differential method. Its principle of operation is shown in Fig. 3.2. Scattered light from a particle moving through the crossing region of two laser beams of equal wavelength is focussed onto a detector. According to Eq. 3.2 both beams will be Doppler shifted. The frequency difference in the photodetector signal is then equal to

$$\Delta f = f_{s1} - f_{s2} = \frac{\mathbf{v} \cdot (\mathbf{s_1} - \mathbf{s_2})}{\lambda} = \frac{2v_\perp \sin(\theta/2)}{\lambda} \tag{3.3}$$

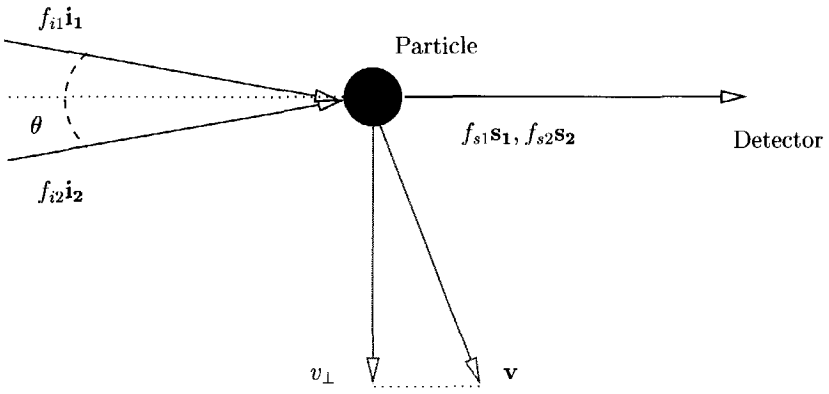

FIGURE 3.2: *The dual beam or differential method.*

where θ denotes the crossing angle of the beams and $v_\perp$ is the velocity component lying in the plane of the crossing beams and perpendicular to their bisector. Eq. 3.3 shows that the frequency difference in the dual beam mode is independent of the detector's location.

The oscillating component in the detector's output signal provides information on the velocity *magnitude* of the scattering particle, but not on its *direction*. This directional ambiguity is removed by applying a frequency pre-shift, f_{shift}, to one of the laser beams. A zero velocity will then yield a frequency difference equal to the pre-shift frequency. Accordingly, negative velocities will generate frequencies below f_{shift}, and positive velocities frequencies higher than f_{shift}. This implies that the pre-shift must be selected larger than the frequency difference corresponding to the largest negative velocity appearing in the flow.

3.2.2 Set-up and signal processing

A 4W Argon-ion laser of Spectra Physics generates light that is directed into the TSI Colorburst model 9201. The Colorburst produces pairs of laser beams with three different colours. In this study, the colours green ($\lambda = 514.5\,nm$) and blue ($\lambda = 488\,nm$) were used for the simultaneous measurement of the tangential and axial velocity components, respectively. One beam of each pair is directed into an acousto-optic modulator or Bragg cell to give it a pre-shift frequency of 40 MHz. The laser beams are then coupled into mono-mode optical fibers for transportation to the measurement probe.

The laser beams are emitted from the measurement probe and focussed into a measuring volume. In the measurements, two different lenses were used with a focal distance of 250 and 350 mm, respectively. Using the 350 mm lens, it was possible to traverse the LDA measurement volume along the whole cyclone diameter. During some measurements, the quality of the blue channel was not good enough to measure both velocity components simultaneously. In these cases, the LDA probe was effectively used as a 1D probe.

The lens was also used for the collection of light scattered by tracer particles (on-axis backscatter mode). The TSI Colorlink model 9230 separates the light into a green and a blue component. The optical signal is converted into an electrical signal by means of photo-multiplier

$\lambda[nm]$	$f[mm]$	$d_W[mm]$	$d_H[mm]$	$d_L[mm]$
514.5	350	0.218	0.219	3.06
488	350	0.207	0.208	2.91
514.5	250	0.156	0.157	1.57
488	250	0.148	0.149	1.49

TABLE 3.1: *Dimensions of the LDA measuring volume for the two wavelengths and focal distances used in the measurements. The beam spacing and beam diameter are 50 mm and 2.1 mm, respectively.*

tubes. Since it could be difficult for the signal processor to resolve small Doppler frequencies relative to the 40 MHz pre-shift, downmixing of the electric signal is commonly used. For the blue channel measuring the axial velocity component a downmixed pre-shift frequency of 10 MHz was sufficient. In most measurements, downmixing was not applied to the green channel measuring the tangential velocity component due to the high velocities encountered.

Detected light originating from a scattering particle in the measuring volume results in an output signal known as a Doppler burst. A Doppler burst consists of a pedestal (DC) and a fluctuating (AC) component. The Doppler signal is directed into the TSI Intelligent Flow Analyser (IFA model 750), which uses a bandwidth filter to eliminate the pedestal and the high frequency noise. The IFA is a so-called Doppler Burst Correlator that estimates the frequency difference by computing the auto-correlation function of the Doppler burst and dividing the number of zero-crossings by their time span (TSI Inc., 1988). The data are sent from the signal processor to the TSI software program FIND, which is also used to define processor settings. *e.g.* pre-shift frequency, threshold voltage and band-pass filter frequencies. The FIND program controls the saving of the data on a hard-disc to enable post-processing.

For all measurements, the data were acquired in the random mode where each channel operates independently. An alternative acquisition mode is using a coincidence time window: only those scattering particles are taken into account that result in a Doppler burst on both channels within a pre-set time interval. This would only be meaningful if the measuring volumes of both pairs of laser beams coincide. As is discussed hereafter, the overlap of measuring volumes is not always assured through the presence of the cylindrical cyclone wall.

The spatial resolution depends on the dimensions of the LDA measuring volume, which can be calculated from the relations given by *e.g.* Absil (1995). In Table 3.1 the width d_W, height d_H, and length d_L of the measuring volume are summarised for the two wavelengths and two lenses used. The position of the measuring volume in the cyclone separator is affected by the presence of the cyclone wall. In the measurements, the green laser pair was focussed in a horizontal plane to measure the tangential velocity component. The cyclone wall affects the position of the measuring volume due to its finite thickness and curvature. The blue laser beams were used to measure the axial velocity component, and in this case the cyclone wall acted as a flat interface. By means of geometrical relations and Snell's law of refraction, the optical path of the green and blue laser beams could be traced from the LDA probe to the actual position of the measuring volume in the cyclone. Due to the different interfaces that are encountered by the two laser pairs, the measuring volumes of both pairs of laser beams do no coincide at all positions along the cyclone diameter. At the geometric centre of the cyclone the

radial distance between both measuring volumes reaches a maximum equal to $1.6\,mm$.

3.2.3 Tracer particles

In general, liquid flows are naturally seeded with sufficient amounts of scattering particles, whereas for aerodynamic applications additional seeding of the flow is necessary. The choice of tracer particles for LDA measurements is a compromise between their light scattering properties, and their ability to track the flow accurately. It is also important that a seeding system is capable of producing clean particles at sufficient quantities in a cheap and easy way.

The size of the tracer particles has a large effect on the signal quality. A considerable reduction of the Signal-to-Noise-Ratio (SNR) occurs if the particle has a size comparable to or larger than the fringe spacing (Absil, 1995). Hence, it is important to remove over-sized particles to reduce noise. The scattering power of a particle strongly depends on its diameter. The scattering properties of particles of diameters greater than the wavelength of the incident light obey Mie's theory. For larger Mie particles of around 1 μm the scattering cross section is roughly proportional to the geometrical cross section ($\sim d^2$). However, it goes down much more steeply for smaller particles ($\sim d^6$), making it difficult to obtain useful Doppler bursts from particles of 0.1 to 0.3 μm.

The fluid dynamic behaviour of spherical particles suspended in a moving flow depends on the particle diameter, d_p, which affects drag, and the density ratio of the particle and the fluid, ρ_p/ρ_f. For liquid tracer particles in air, the density ratio is approximately 10^3. If drag is given by Stokes' Law and no external body forces act on the particle, the equation of motion may be approximated by:

$$\frac{dU_p}{dt} + \frac{1}{\tau_p}(U_p - U_f) = 0 \tag{3.4}$$

where τ_p is known as the particle relaxation time defined as:

$$\tau_p = \frac{\rho_p}{\rho_f}\frac{d_p^2}{18\nu} \tag{3.5}$$

with ν the kinematic fluid viscosity (for air $\nu \approx 15\ 10^{-6} m^2\, s^{-1}$). The ability of a tracer particle to track a turbulent flow may be estimated by modelling turbulent fluctuations by means of a periodical flow motion with an amplitude $U_{f,0}$ and a frequency f. Solving Eq. 3.4 then results in (Drain, 1980):

$$\frac{U_p}{U_{f,0}} = \frac{1}{\sqrt{1 + (2\pi f \tau_p)^2}} \tag{3.6}$$

To follow frequencies in air up to 1 kHz and 10 kHz, the maximum acceptable diameters for a water droplet are $2.5\,\mu m$ and $0.8\,\mu m$, respectively, within 1% accuracy according to Eq. 3.6. This range of frequencies is typical for turbulent gas flows.

A point of concern for LDA measurements in cyclone separators is whether there will be tracer particles present in the vortex core, and whether the tangential velocity component can be measured accurately. Provided that the vortex core may be described as a solid body rotation with an angular velocity ω and zero radial velocity, the radial velocity of the particle, V_p, at position r in the vortex may be estimated by (Durst et al., 1976):

$$V_p = r\omega^2\tau_p \tag{3.7}$$

Here, the term $r\omega^2$ is the centrifugal acceleration and τ_p is the particle relaxation time. Dividing both sides of Eq. 3.7 by the tangential velocity, $W = r\omega$, the following expression is obtained:

$$\frac{V_p}{W} = \omega\tau_p \tag{3.8}$$

For a particle 1 μm in diameter the velocity ratio V_p/W is very small, $O(10^{-4})$, for industrial cyclone separators. Nevertheless, the particles tend to move away from the vortex core centre, which implies that low data rates will be obtained in this region.

Given these considerations with respect to the tracer particle diameter, a seeding system was developed based on liquid atomisation to produce droplets of appropriate size. Droplets were produced by atomising a 10% solution of glycerol in water by means of an industrial paint spray gun. Air is supplied to the blast atomiser at a pressure of 6 bar absolute. The particle size distribution of the produced tracer droplets was measured with a Malvern 2600 Particle Sizer. It appeared that a considerable part of the droplets produced was larger than 10 μm in diameter. To reduce this over-sized amount of tracers, the droplets were blown into a small cyclone separator before they were injected into the main flow line of the experimental set-up. Air was injected into this small cyclone to control the seeding flow rate.

Analysis of the particle size distribution at the exit pipe of the seeding cyclone showed that the number of droplets larger than 10 μm in diameter is reduced. The cumulative particle size distributions (PSD) measured at the atomiser and after separation by the seeding cyclone are presented in Fig. 3.3. After leaving the pre-separator, the cut-size of the PSD is reduced by a factor of two.

3.3 Experimental set-up

3.3.1 General description

The operation of a Laser-Doppler Anemometer demands optical access to the interior of the cyclone. Geometry modifications are easy to make due to the modular construction of the cyclone by using cylindrical elements. To facilitate visual observation most cyclone parts were constructed of acrylate (perspex). The conical section of one of the cyclone geometries was made of steel. At several axial positions, small rectangular windows were inserted in the conical wall to provide access to the cyclone interior. The measuring windows were made of conventional overhead sheet with a thickness of approximately 80 μm, and attached to the inner side of the

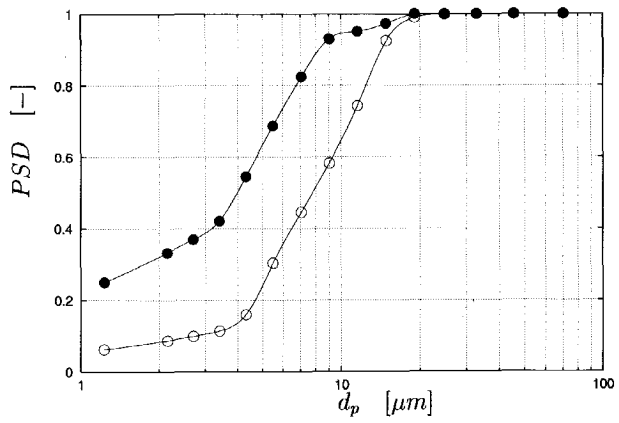

FIGURE 3.3: *Cumulative particle size distribution of the seeding obtained with (•) and without (○) pre-separator.*

wall. The diameter of the cylindrical body of the cyclones is of an industrial scale and equal to $0.290\,m$.

The cyclone under investigation is attached to a metal frame together with a traversing system for the LDA probe. Two pairs of laser beams are transmitted by the LDA probe and focussed into the cyclone flow field. Reflections at the opposite cyclone wall are absorbed by a black, thin sheet of copper attached to the inner side of the wall. This proved to boost the signal quality in the LDA measurements.

Air at ambient pressure and temperature is supplied to the cyclone by a compressor. The flow rate is manually controlled by a valve, and monitored by a flow sensor. The seeding particles for the LDA measurements are injected into the main air line at approximately two metres before entering the cyclone. The transition from the air-supplying pipe to the rectangular inlet box has a length of one meter to prevent large flow disturbances at the inlet. The air is exhausted through the exit pipe, which is approximately two metres long outside the cyclone separator. An impression of the upper part of the cyclone and the air supply is shown in Fig. 3.4.

At the inlet section, an orifice was made to introduce a probe for measuring the temperature and relative humidity of the flow. During the LDA measurements, the probe is removed. Pressure taps are positioned in the wall of the inlet section, and in the exit pipe wall $0.145\,m$ above the top of the cyclone. These pressure taps are used to measure the cyclone pressure drop by means of a differential pressure sensor. The maximum pressure drop allowed by the membrane is $20\,cm$ water column. Higher pressure drops were measured by means of a conventional U-tube. Due to the additional flow of air with tracer particles produced by the seeding system, the flow rate was somewhat increased. To estimate the total volumetric flow introduced into the cyclone, a calibration curve of the cyclone pressure drop versus flow rate was measured for every cyclone geometry under investigation.

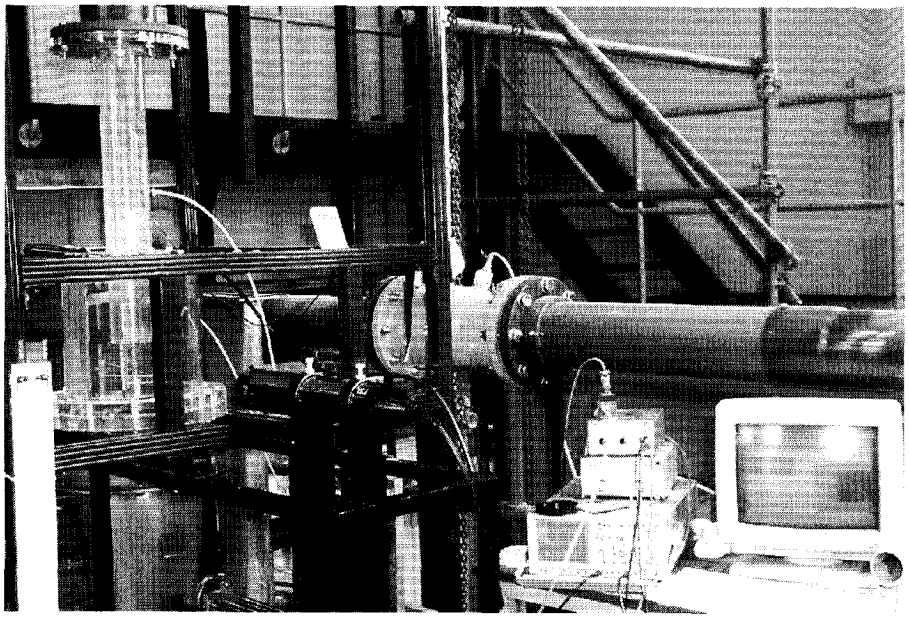

FIGURE 3.4: *Impression of experimental set-up used for LDA measurements. The cyclone and the traversing system for the LDA probe are attached to the metal framework on the left side of the picture. On the right side, the flow rate and cyclone pressure drop are monitored.*

3.3.2 Cyclone geometries

As was discussed in the introduction (Sec. 3.1), a large number of cyclone geometries have been designed, modified, and studied in the literature. Most designs emanate from the high efficiency cyclone separator introduced by Stairmand (1951) or the cyclone designs studied by Barth (1956). In this study, LDA measurements were done of the flow field in a Stairmand geometry as well as in a cyclone geometry known as a tangential swirl tube separator. This swirl tube separator resembles the Barth geometries, and was studied as an axial reverse-flow cyclone by Van den Akker and De Kort (1989). Both geometries were modified with respect to the diameter of the exit pipe.

The geometry of the Stairmand high efficiency cyclone separator is described in terms of geometrical design ratios, *e.g.* the height (a) and width (b) of the inlet box, and the diameter of the exit pipe (D_e) normalised with the cyclone body diameter (D). The geometrical lay-out and dimensions of the Stairmand cyclone used in this study are shown in Fig. 3.5(a). In the experiments a collection bin was attached to the cone of the cyclone having a diameter equal to the cyclone body diameter and a height twice the cyclone diameter. The collection bin did not have a specific purpose in the LDA experiments, but is used in Ch. 6 for the efficiency measurements.

Compared to the Stairmand cyclone, the geometry of the swirl tube separator mainly differs with respect to the inlet configuration and the absence of a cone as is shown in Fig. 3.5(b). The

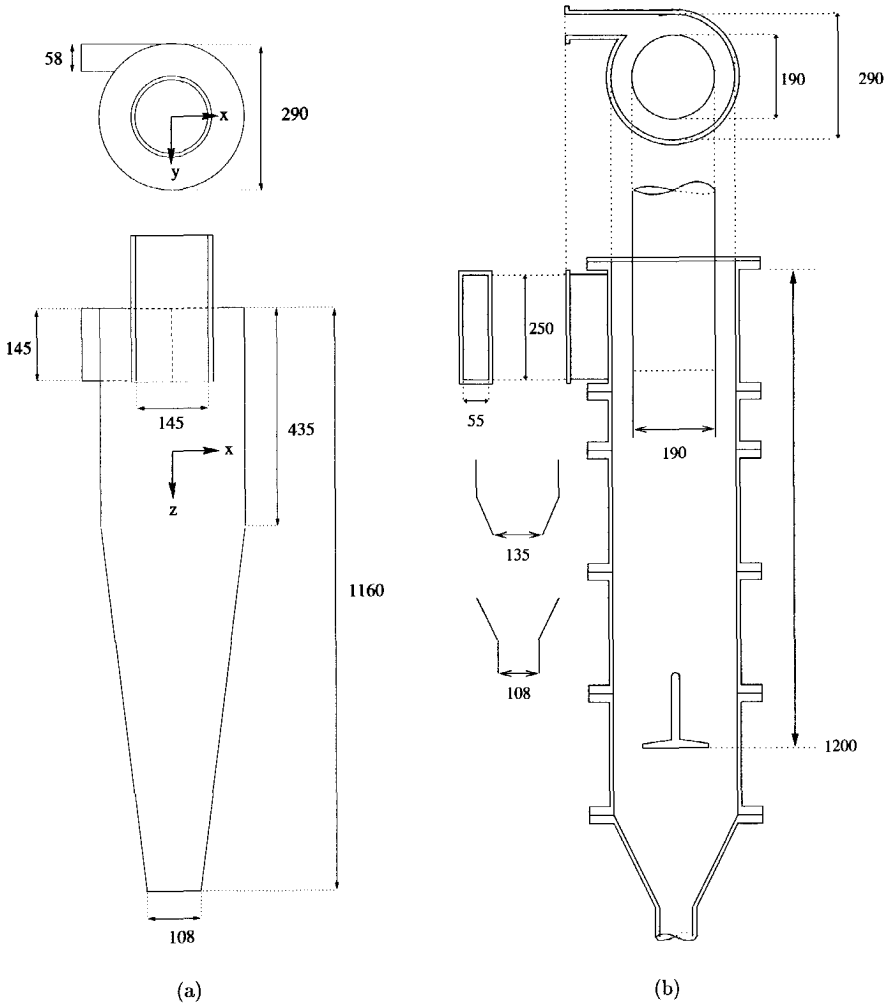

FIGURE 3.5: *Schematic representation of (a) the high efficiency cyclone separator (Stairmand, 1951), and (b) the swirl tube separator with characteristic dimensions in millimetres. The coordinate system was the same for both geometries. The LDA measuring volume was traversed along the x-axis.*

flow is introduced tangentially into the separator by means of a scroll inlet section to prevent collision of the flow with the exit pipe wall. In the Stairmand cyclone a scroll inlet is not necessary, because the diameter of the exit pipe is sufficiently small. In the lower part of the cyclone a cylindrical section develops into a short cone and a so-called vortex stabiliser. The rationale of this design is that the vortex stabiliser forces the particles to travel to the solids outlet along the wall, hereby inhibiting re-entrainment. It is also expected to enhance stability by capturing the vortex core (Liem and Van den Akker, 1992).

The geometries were modified by reducing the diameter of the exit pipe. For the Staimand cyclone, three different exit pipes were used with a diameter of 0.145, 0.116 and 0.086 m, corresponding to a design ratio D_e/D of 0.50, 0.40 and 0.30, respectively. The length of the exit pipes in the interior of the cyclone was equal to the height of the inlet section, and extended 1.5 times the cyclone diameter outside of the cyclone. At this position, a transition element was present to direct the flow from the exit pipe into the exhaust pipe of diameter 0.150 m. The exit pipe diameter of the swirl tube separator was modified by fitting conical sections to the exit pipe entrance (see Fig. 3.5(b)). Three different cyclone design were studied, where the aperture of the exit pipe diameter was 0.108, 0.135 and 0.190 m. In terms of the design ratio D_e/D these values are equal to 0.37, 0.47 and 0.66, respectively.

3.3.3 Accuracy and bias

The LDA set-up enables the simultaneous measurement of two velocity components. There are two practical reasons for studying the *tangential* and *axial* velocity components of the flow field in a cyclone separator. First, cyclone flow is dominated by the axial and tangential velocity components; the mean radial velocity is at least one order of magnitude smaller. LDA measurements of the radial velocity component are prone to error due to misalignment of the measuring volume, because the measured velocity would contain contributions of both the radial and the tangential velocity components. Second, traversing the measuring volume along the cyclone diameter for the measurement of the radial velocity component is complicated by the presence of a cylindrical cyclone wall. At an off-centre position of the LDA probe during the traverse the emitted laser beams enter the flow field at different points in the cylindrical wall. This results in a measuring volume that is slightly rotated with respect to the bisector of the laser beams. For applications where the flowing medium is water, *e.g.* stirred vessels or hydrocyclones, this effect is usually circumvented by surrounding the geometry with a rectangular box filled with water.

The measuring volume is traversed along the x-axis through the geometric centre of the cyclone (see Fig. 3.5 for the definition of the coordinate system). It is known that the vortex centre of swirling flows does not always coincide with the geometrical centre, although the eccentricity is generally small (see, *e.g.* Escudier et al. (1980)). The measuring volume is manually traversed, and its position could be determined with an accuracy of 0.5 mm. The origin of the z-axis is located at the cover plate of the cyclone. The separation zone of the cyclone usually extends from the entrance of the exit pipe at $z/D = 0.5$ to the bottom of the cone at $z/D = 4.0$ for the Stairmand cyclone. Most of the velocity profiles were measured in this zone.

The data rate, which is the number of measurements per unit time, depends on the radial position of the measuring volume. This is due to the migration of seeding particles towards the

wall by the centrifugal force field in the cyclone (see Sec. 3.2.3). Near the wall, data rates of 800 Hz were obtained, while at the centreline it was still possible to obtain data rates of some 50 Hz per channel. Reduction of the exit pipe diameter resulted in a significant decrease of the data rate at measuring positions in the core region. The flow statistics were derived from approximately 10,000 to 30,000 data points per channel depending on the mean data rate.

Scattering particles with high velocities are more likely to cross the measuring volume than particles with low velocities, and consequently are more frequently detected. This effect is called *velocity bias*, because it results in a bias towards higher velocities when calculating velocity distributions. There are several methods for correcting velocity statistics for velocity bias (see *e.g.* Absil (1995)). The most common approach is known as inverse-velocity weighting. This method obtains a bias-free estimate of the mean velocity by weighting each sample by the inverse of the magnitude of the instantaneous velocity. This would require knowledge of three velocity components at the same time. In practice, a 2D weighting factor may be applied when the measuring volume is considered an ellipsoid. For this 2D-estimator two velocity components are needed simultaneously. This is usually obtained by setting a small coincidence window. In the current LDA set-up, a coincidence window was not set, because the measuring volumes did not overlap at every position along the traversing axis (see Sec. 3.2.2).

3.4 Results and discussion

3.4.1 Pressure drop measurements

For both the Stairmand high-efficiency cyclone and the tangential swirl tube separator the pressure drop was measured as a function of the inlet velocity. The cyclone pressure drop is estimated by measuring the static pressure difference between two pressure taps inserted in the cyclone wall. One pressure tap was located at half the inlet height of the tangential inlet, and the other at the exit pipe wall outside the cyclone. For the Stairmand cyclone the measurements of the pressure drop were done with a differential pressure sensor, while for the other cyclone geometry a conventional U-tube manometer was used. Both cyclones were modified with respect to the exit pipe diameter (see Fig. 3.5). The measurement results are shown in Fig. 3.6.

The results show a non-linear increase of the cyclone pressure drop for increasing inlet velocity and decreasing exit pipe diameter. In Sec. 2.2, an overview was given of the various pressure drop models presented in the literature. The empirical model derived by Stairmand (1949) is compared to the pressure drop measurements shown in Fig. 3.6a. Since the tangential swirl tube separator resembles the cyclones studied by Barth (1956), the measurements in Fig. 3.6b are compared to his pressure drop model.

As was mentioned in Sec. 2.2, Stairmand (1949) and Barth (1956) considered the total energy loss of the cyclone, *i.e.* the sum of static and dynamic pressure components averaged at the inlet and exit plane. However, the pressure drop measurements presented here are defined as the difference of static wall pressure at the cyclone inlet and exit. The model equation can be corrected for the difference in velocity head of the mean flow at the inlet and outlet plane by subtracting an amount

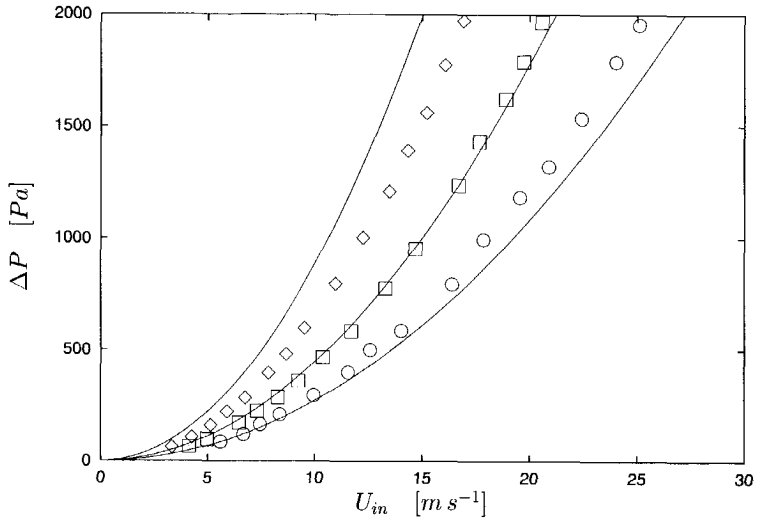

(a) Stairmand cyclone

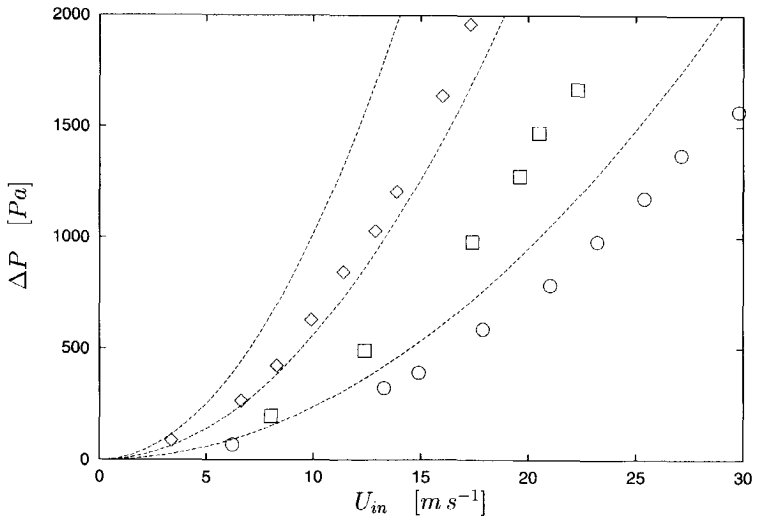

(b) Tangential swirl tube separator

FIGURE 3.6: *Measurements of the cyclone pressure drop versus inlet velocity for the (a) Stairmand cyclone with D_e/D equal to (○) 0.50, (□) 0.40, and (◇) 0.30, and the (b) tangential swirl tube separator with D_e/D equal to (○) 0.66, (□) 0.47, and (◇) 0.37. The pressure drop models of Stairmand (1949) and Barth (1956) are represented by (–) and (- -), respectively.*

$$\frac{1}{2}\rho U_{in}^2 \left[1 - \left(\frac{A_{in}}{A_{out}}\right)^2\right] \tag{3.9}$$

where A_{in} and A_{out} are the cross sectional areas at the inlet and exit plane, respectively. Eq. 3.9 corrects for the different cross sectional areas at the inlet and outlet of the cyclone.

Due to the absence of swirl, the static pressure measured at the wall of the inlet box is equal to its averaged value at the inlet cross section. To obtain an averaged static pressure at the exit plane, the distribution of the static pressure needs to be known along the exit pipe radius. Assuming a linear radial profile, Hoffmann et al. (1992) argue that the average static pressure across the section of the exit pipe equals the static pressure at the wall. Following this argument, no correction for the static pressure was applied to the pressure drop models.

The model curves shown in Fig. 3.6 correspond to the pressure drop equations derived by Stairmand (1949) and Barth (1956) with a correction for the velocity head. The friction factor, λ, is equal to 0.02. It is shown that the calculated pressure drop deviates from the experimental data especially for the tangential swirl tube separator. This could be explained by the magnitude of λ, *i.e.* the wall friction factor strongly affects the relation between the inlet velocity and the pressure drop (see Fig. 2.3). Another explanation could be found in the postulated distribution of the tangential velocity component, which determines the velocity head of the vortex.

3.4.2 Mean velocity profiles

Stairmand cyclone

In Fig. 3.7, the mean tangential and axial velocity components are shown as a function of the radial coordinate. The LDA measurements were done along the cyclone diameter at $z/D = 0.75$, which is located in the cylindrical section of the cyclone close to the aperture of the exit pipe. Three velocity profiles were measured that correspond to a Stairmand high-efficiency cyclone with D_e/D is equal to 0.50, 0.40, and 0.30, respectively. The exact radial position of the measuring volume was determined by calculating the path of the laser beams through the respective flat or cylindrical interface.

The velocity profiles show a small but significant axi-asymmetry with respect to the cyclone centreline. This could be due to the relative close location of the measurement station to the tangential inlet section, and its axi-asymmetric injection of the gas. Both the axial and swirl velocity distribution shows the dominant influence on the flow of the exit pipe contraction. For all exit pipe diameters, the radial distribution of the mean tangential velocity component exhibits the expected shape of a combined vortex, consisting of an outer free-type of vortex and a rigid-body rotation in the vortex core. Nevertheless, the profiles differ quite strongly with respect to the size of the core region and the magnitude of the maximum tangential velocity. A reduction of the exit pipe diameter results in a sharp increase of the maximum tangential velocity as a result of the decreasing vortex core size.

The reverse-flow character of the Stairmand cyclone becomes evident from the axial velocity distributions. The flow is directed downwards near the cyclone wall, while in the central region of the flow the axial velocity is directed towards the exit pipe. The upward directed flow exhibits

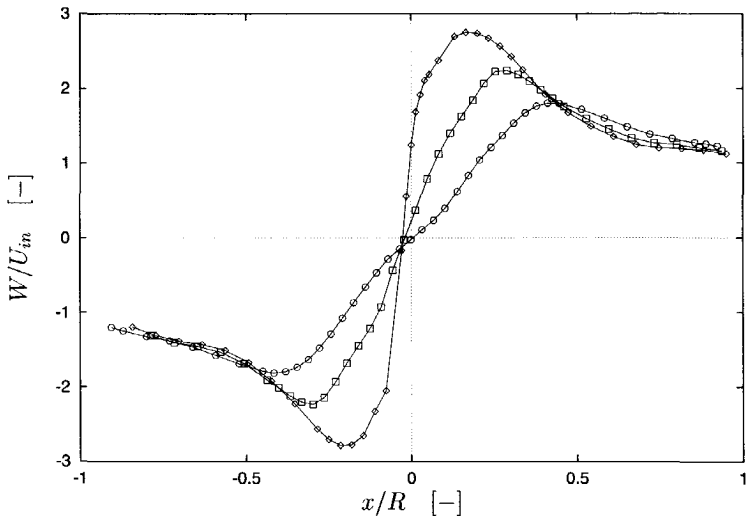

(a)

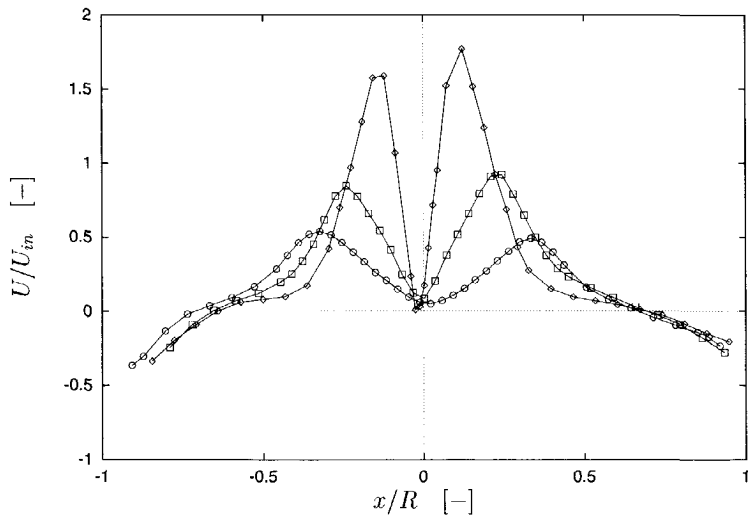

(b)

FIGURE 3.7: *Radial profiles of the mean tangential (a) and axial (b) velocity components normalised with the inlet velocity (Re = 2.8 10^5) at z/D = 0.75 for the Stairmand cyclone with exit pipe diameter D_e/D equal to (○) 0.50, (□) 0.40, and (◇) 0.30.*

D_e/D	W_{max}/U_{in}	$r_{W_{max}}/R$	d_c/D_e	U_{max}/U_{in}	$r_{U_{max}}/R$
0.50	1.81	0.42	0.83	0.52	0.33
0.40	2.24	0.30	0.74	0.89	0.24
0.30	2.75	0.19	0.63	1.68	0.12

TABLE 3.2: *Characteristic values for the maximum tangential and axial velocity normalised with the inlet velocity and their relative radial positions for the Stairmand cyclone with three different exit pipe diameters. The values are averaged over both sides of the vortex core. The core diameter d_c is defined by the radial position of the maximum tangential velocity at the core edge.*

a velocity maximum for all three cyclone geometries. Due to the contraction of the exit pipe this maximum axial velocity increases significantly to provide for an equivalent throughput. Near the centreline a region exists of axial velocity deficit for all cyclones. Although the axial velocity magnitude near the centreline is very small, on average flow reversal is not present at this position in the cyclone.

The pressure drop models of Stairmand (1949) and Barth (1956) characterise the swirl distribution by means of the vortex core size and the magnitude of the maximum tangential velocity (see the discussion on cyclone models in Chapter 2). From the velocity profiles presented in Fig. 3.7 characteristic values can be derived for these parameters. The results are summarised in Table 3.2 for the Stairmand geometries studied.

It is shown that the maximum tangential velocity increases from 1.81 to 2.75 times the inlet velocity due to the contraction of the exit pipe from 0.50 to 0.30. The vortex core diameter, which is usually defined by the radial position of the maximum tangential velocity, decreases both in absolute and relative terms due to the contraction. The values for d_c/D_e clearly show that the core diameter is not equal to the exit pipe diameter or half the exit pipe diameter as was assumed by Barth (1956) and Stairmand (1949). The radial position of the maximum axial velocity does not coincide exactly with the edge of the vortex core, but is somewhat smaller for all cyclone geometries.

LDA measurements were also done at other axial stations in the Stairmand cyclone. These results are discussed in Ch. 5, where they are compared to numerical predictions of the gas flow field.

Swirl tube separator

Mean velocity profiles were measured at four axial stations in the separation zone of the tangential swirl tube separator. These LDA measurements were done using a lens with a focal length of $250\,mm$, as a result it was not possible to traverse the measuring volume along the whole cyclone diameter. The mean velocity distribution along the cyclone radius is presented in Fig. 3.8 and Fig. 3.9 for three different values of the exit pipe diameter. The flow field in these cyclone geometries may be described in a similar way as was done for the Stairmand cyclone. The radial profiles of the tangential velocity component exhibit the combined vortex distribution, although the outer region appears to deviate more strongly from a free vortex than in the Stairmand cyclone. This is in particular valid for the cyclone with $D_e/D = 0.66$.

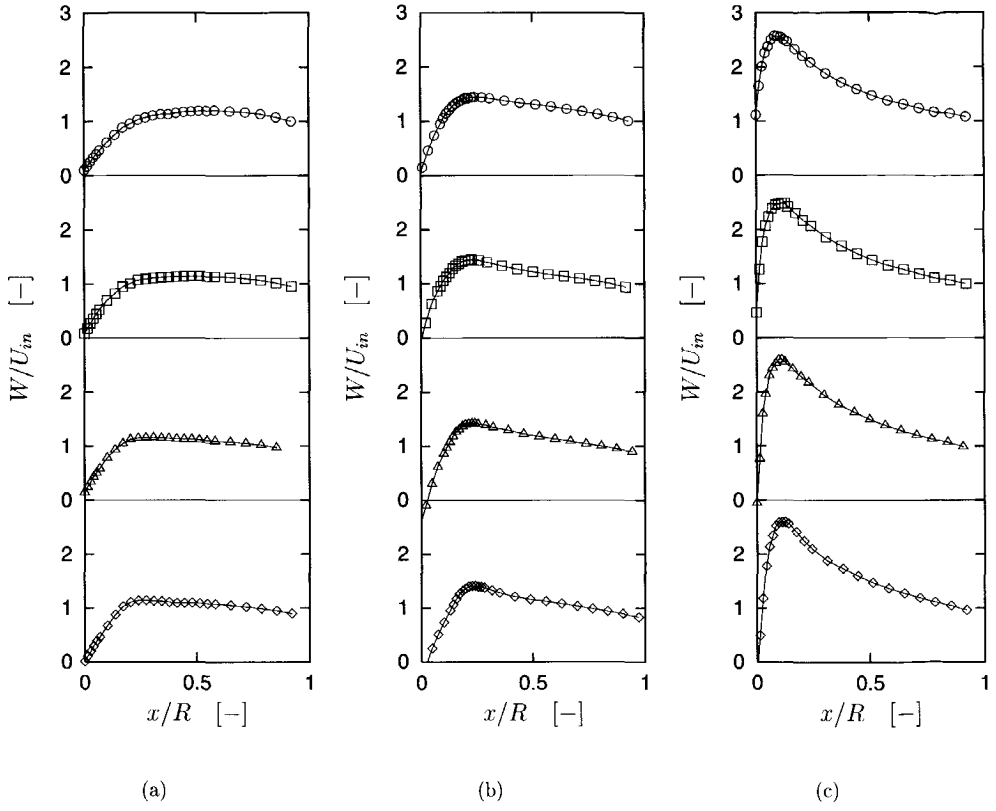

FIGURE 3.8: *Radial profiles of the mean tangential velocity with* $Re = 1.2\ 10^5$ *at four axial measurement stations of the swirl tube separator with* z/D *equal to* (○) *1.75,* (□) *2.25,* (△) *2.75,* (◇) *3.10. The exit pipe diameter is normalised with the cyclone diameter and equal to (a) 0.66, (b) 0.47, and (c) 0.37, respectively. The velocity magnitude is normalised with the inlet velocity.*

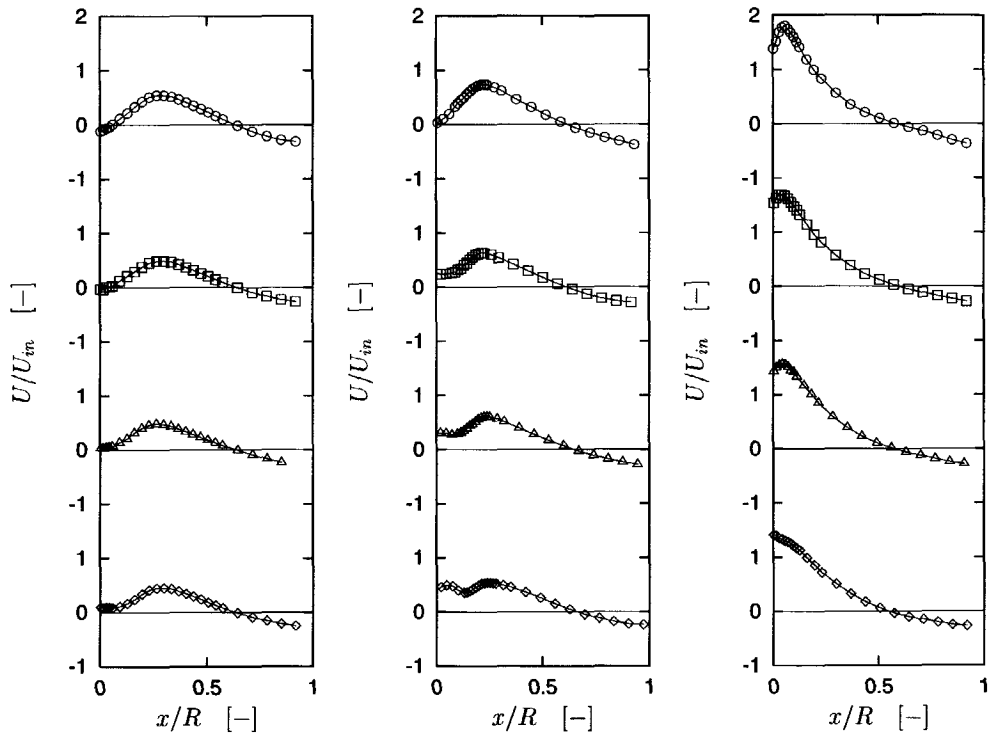

FIGURE 3.9: *Radial profiles of the mean axial velocity with* $Re = 1.2\ 10^5$ *at four axial measurement stations of the swirl tube separator. For details see caption Fig. 3.8.*

Again, contraction of the exit pipe strongly affects the vortex core size, which results in an increase of the maximum tangential velocity from 1.2 to 2.5 times the inlet velocity. The axial velocity distribution shows a strong resemblance to the measurement results for the Stairmand cyclone, where the core region is characterised by an axial velocity deficit and, incidently, even flow reversal. The cyclone geometry with $D_e/D = 0.37$ is an exception in this respect; the axial velocity profile in the core region exhibits a jet-like behaviour.

In general, there is a strong similarity between the mean axial and tangential velocity distributions in the axial direction. At all axial levels, a small residual asymmetry remains with respect to the geometric centreline. Following the axial development of the velocity profiles, some specific flow features can be recognised that are characteristic for cyclone flow. Due to wall friction, there is a decrease of the 'wall' circumferential velocity while proceeding from the inlet to the lower cyclone section. This wall circumferential velocity is defined as the bulk velocity of the flow just outside the turbulent boundary layer. It is combined with a decreasing axial downflow near the cyclone wall, which is due to the radial inflow of fluid towards the vortex core.

Fig. 3.9 shows that for each cyclone design the axial velocity near the centreline decreases while approaching the exit pipe. This is due to the existence of an adverse (positive) pressure gradient, which results from the strong coupling between the radial pressure distribution and the mean tangential velocity. Fluid entering the exit pipe will exhibit loss of swirl due to wall friction, and as a result a positive pressure gradient exists in the axial direction. In this way, fluid with less swirl will be drawn back into the cyclone. This is clearly observed for the swirl tube separator with $D_e/D = 0.66$ near the exit pipe aperture.

Instead of the cone used in the Stairmand cyclone, the tangential swirl tube separator has a reduction of the cross sectional area in the lower cyclone section by means of a vortex stabiliser inserted on a circular disk. The vortex stabiliser prevents the vortex core from extending into the catch bin. It also appears to inhibit flow reversal at the centreline. This effect is clearly demonstrated in Fig. 3.9(b), where a small jet exists near the centreline in the lower part of the cyclone.

A comparison of the measured flow field in the Stairmand cyclone and the tangential swirl tube separator is hampered by the mutual differences in Reynolds number and Swirl number. A closer inspection of the flow field in terms of these dimensionless flow numbers is done in Chapter 5, where the LDA measurements are used to assess numerical predictions of cyclone flow.

3.4.3 Fluctuating velocity profiles

Rms velocity profiles

The experimental set-up as discussed in Section 3.3 allowed for the measurement of the tangential and axial velocity components only. The magnitude of velocity fluctuations is usually expressed in terms of its standard deviation or root-mean-square (rms) velocity. The axial and tangential rms velocity are related to the normal Reynolds stresses by $u_{rms} = (\overline{u^2})^{1/2}$ and $w_{rms} = (\overline{w^2})^{1/2}$. In Fig. 3.10, radial profiles of the tangential and axial rms velocity are shown for the Stairmand cyclone with different values for the exit pipe diameter. The rms velocity profiles for the tangential swirl tube separator are not presented as they are quite similar to

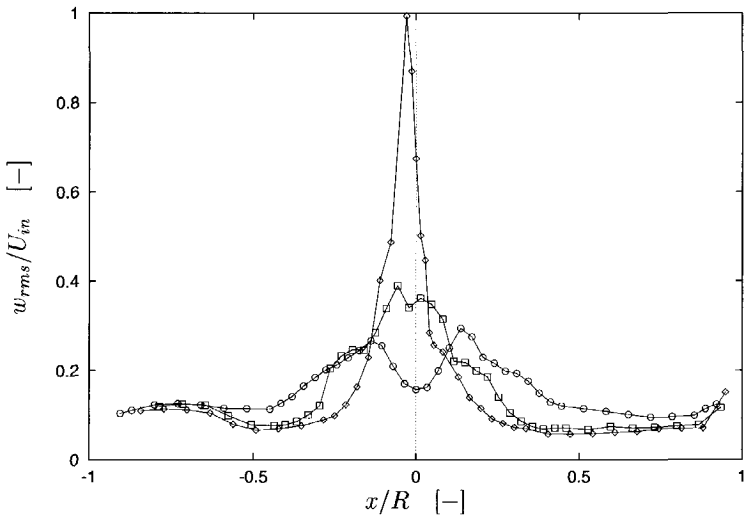

(a)

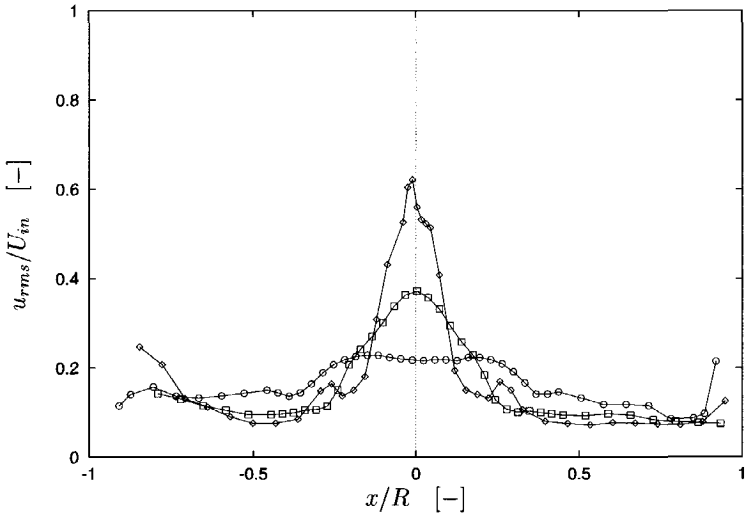

(b)

FIGURE 3.10: *Radial profiles of the tangential (a) and axial (b) rms velocity normalised with the inlet velocity ($Re = 2.8\ 10^5$) at $z/D = 0.75$ for the Stairmand cyclone with exit pipe diameter D_e/D equal to (○) 0.50, (□) 0.40, and (◇) 0.30.*

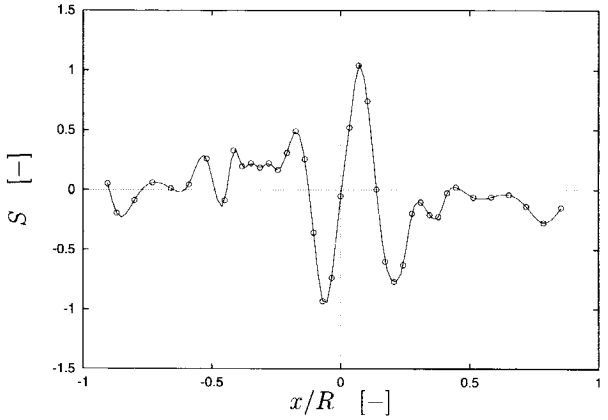

FIGURE 3.11: *Skewness factor of the tangential velocity distribution at $z/D = 0.75$ for the Stairmand cyclone with $D_e/D = 0.50$.*

the profiles shown for the Stairmand cyclone (see Hoekstra et al. (1999b)).

Both the tangential and axial fluctuating velocity distributions can be described in terms of a wall region, an annular region, and a core region. In the wall region ($|y/R| > 0.9$), the axial and tangential rms velocity shown in Fig. 3.10 tend to increase with decreasing distance to the wall for all three cyclone lay-outs. This could be explained by the presence of large velocity gradients in the radial direction of the mean tangential and axial velocity components in the vicinity of the wall. These large velocity gradients cause an increased production of axial and tangential normal stresses. In addition, it is known that an increased stress anisotropy close to the wall exists due to the selective damping of the radial normal stress.

The annular region extends from the wall region to the radial position that corresponds to the velocity extremes in the respective mean axial and tangential velocity distributions. The tangential rms velocity is approximately constant in this region, whereas the axial fluctuations exhibit a small increase for decreasing radius. The contraction of the exit pipe results in a suppression of the level of both the axial and tangential fluctuations.

In the core region, there is a sharp increase of the axial and tangential velocity fluctuations for decreasing exit pipe diameter. At the centreline, except for the standard Stairmand geometry, the rms velocity reaches a maximum value. For $D_e/D = 0.30$ the tangential velocity fluctuations near the cyclone axis are of the same order of magnitude as the inlet velocity. Th large values of the rms velocity in the vortex core appears to be in contradiction with the Rayleigh criterion, which attributes a stabilising effect to a solid-body rotation (see Section 2.1).

Velocity histograms

Additional information on the distribution of the instantaneous velocity is provided by the skewness factor. The skewness, S, or third moment is a non-dimensional quantity that characterises the degree of asymmetry of a distribution around its mean. As an illustrative ex-

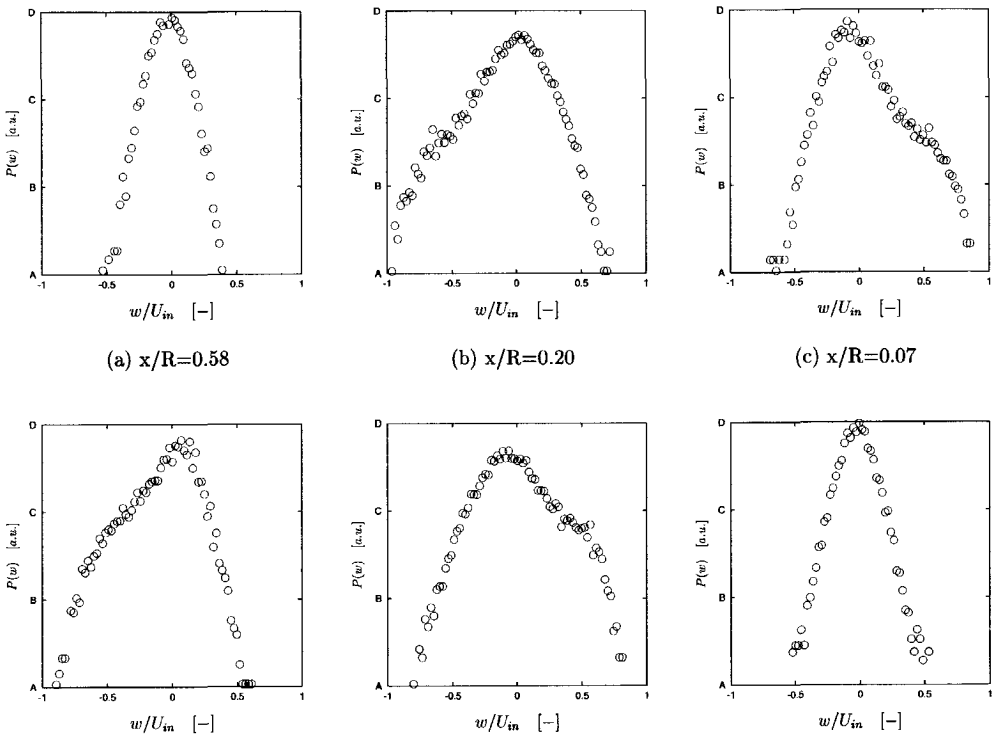

(a) x/R=0.58 (b) x/R=0.20 (c) x/R=0.07

(d) x/R=-0.07 (e) x/R=-0.17 (f) x/R=-0.59

FIGURE 3.12: *Probability density function of the fluctuating tangential velocity component normalised with the inlet velocity at $z/D = 0.75$ for the Stairmand cyclone with $D_e/D = 0.50$. The skewness factor, S, of the PDF's is equal to (a) -0.1, (b) -0.8, (c) 1.0, (d) -0.9, (e) 0.5, and (f) 0.0.*

ample, the skewness factor of the tangential velocity distribution is shown in Fig. 3.11 for the standard Stairmand cyclone. The profile exhibits an approximate point symmetrical shape ($S(x) = -S(-x)$) with respect to the geometric centre of the cyclone. In the core region a strong variation of the skewness factor exists with maximum and minimum values located at $x/R = \pm 0.07$. At the geometric centre the tangential velocity distribution is nearly symmetrical (has zero skewness). At the other two positions in the vortex core where the skewness factor is close to zero the rms velocity profile reached its maximum value (see Fig. 3.10).

A closer look at the probability density function (PDF) of the fluctuating velocity elucidates the meaning of the skewness factor. In Fig. 3.12, velocity histograms are presented of the fluctuating tangential velocity component for six typical positions along the cyclone diameter. In the outer region of the vortex at $x/R = 0.58$ and $x/R = -0.59$ the skewness factor is small and the velocity distribution is nearly symmetrical. The other velocity histograms correspond to measurement positions in the core region with a significant negative or positive skewness. The PDF's at $x/R = \pm 0.07$ exhibit two smoothed peaks located on both sides of $w/U_{in} = 0$. The histograms of the velocity measurements at $x/R = 0.20$ and $x/R = -0.17$ show an asymmetric distribution, whose tail extends towards negative and positive values of w/U_{in}, respectively.

Part of the measured velocity fluctuations is due to the finite size of the measuring volume, which accounts for additional signal variance especially in the core region where large gradients prevail. It can be shown that, to the first order, this contribution to the signal variance depends in a quadratic way on the mean velocity gradient and the length of the measuring volume. For the PDF's shown in Fig. 3.12 the variance due to the finite spatial resolution amounts to only $\sim 2\%$ of the measured variance. Hence, an additional source of measurement dispersion is present.

The explanation may be found in a flow phenomenon known as the precessing vortex core (PVC). The PVC is defined as the three dimensional, time dependent, coherent motion of the vortex core (see Gupta et al. (1984)). Vortex core precession introduces low-frequency oscillations in the LDA signal due to relative motion of the core centre with respect to the measuring volume. The PVC contribution to the measured velocity fluctuations is especially high in the region close to the vortex core and in the vortex core itself. This explains qualitatively the high levels of rms velocity in the vortex core. Furthermore, the local extremes in the radial distribution of the tangential and axial rms velocity profiles (see Figs. 3.10) are also attributed to vortex precession; the signal variance due to the PVC is proportional to the local mean velocity gradient. In this way, the low tangential rms velocity near the centreline for the Stairmand cyclone with $D_e/D = 0.50$ is explained by the smaller mean velocity gradient at $x/R = 0$ (see Fig. 3.7). A more elaborate discussion of the PVC and its effect on the flow field in a cyclone separator is the subject of the next chapter.

3.5 CLOSURE

The experimental results presented in this chapter demonstrate the significant effect of cyclone design on the mean and fluctuating velocity distribution. The LDA measurements quantitatively show to what extent the contraction of the exit pipe results in a reduction of the vortex core size and in an increase of the maximum circumferential velocity. These data could be used to assess the validity and suitability of the assumptions on the flow field used in (semi-)

empirical cyclone models as discussed in Ch. 2.

Another application of the LDA data is the validation of numerical predictions of the flow field in a cyclone separator. The measurements provide great detail on the flow field, which facilitates the assessment of turbulence models. The effect of the precessing vortex core on the velocity measurements needs some additional attention. In the LDA measurements, no distinction is made between the turbulent velocity fluctuations and the low-frequency oscillation resulting from the spatial motion of the vortex core. The next chapter reports on efforts to circumvent the limitations of the LDA measurements in this respect by means of advanced signal analysis and an additional optical technique.

CHAPTER 4

VORTEX CORE PRECESSION

The gas flow field in a cyclone exhibits an unsteady, coherent oscillation known as the precessing vortex core (PVC). The effect of the PVC is most notable by its introduction of additional velocity fluctuations in the velocity measurements as a result of its relative motion with respect to the LDA measuring volume. By means of an analytical model, the effect of the PVC motion on the velocity signal is illustrated qualitatively. A signal processing technique known as adaptive noise cancellation is used to estimate the contribution of the PVC to the LDA signal, and to reconstruct phase-resolved velocity profiles. Spatial information on the PVC motion is obtained from a quantitative visualisation study of the cyclone flow field. Finally, the experimental results are compared to a Large Eddy Simulation (LES) of the flow field in a laboratory scale cyclone.

4.1 INTRODUCTION

The first indications of unsteady flow behaviour in a cyclone separator emanated from visual observations of the flow field, *e.g.* by means of a dye tracer injected into a hydrocyclone (Stairmand, 1951; Chanaud, 1965), and by smoke visualisation of the flow in a gas cyclone (Smith, 1962). The smoke patterns at high flow rates studied by Smith (1962) revealed the presence of a core region, which was clear of smoke, and the deformation of the core to an indistinct wave pattern. Smith (1962) presumed that the clear core region is a result of the actual separation of the smoke from the air due to the low mean velocity near the cyclone axis. It was also concluded that the unsteady flow behaviour of the vortex core does *not* enhance mixing of the flow.

The three-dimensional, time dependent motion of the vortex core in a cyclone is known as *precession*. In the field of rigid body dynamics, precession is defined as the motion of the axis of rotation about a fixed axis due to an external torque (see Alonso and Finn (1980)). If the torque is perpendicular to the angular momentum, the angular momentum changes in direction but not in magnitude. One example of this situation is found in a toy known as the spinning top. The top is spinning about its own principle axis with a certain angular velocity. At the same time due to an external torque on the top provided by the gravity, the gyroscope axis of the top is precessing about the axis of the inertial frame of reference. The angular velocity of

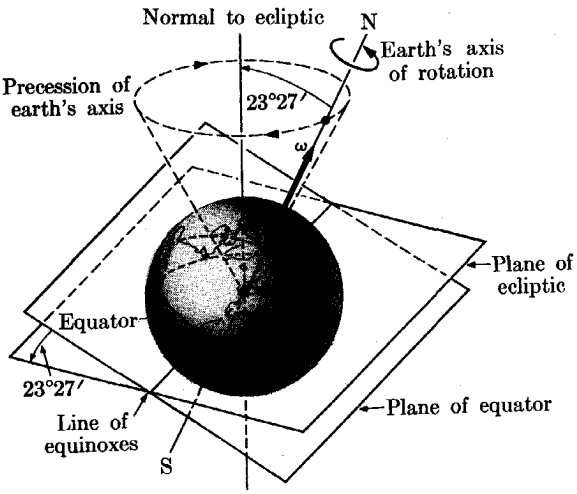

FIGURE 4.1: *Precession of earth's axis of rotation (after Alonso and Finn (1980)).*

the precession is usually much smaller than of the spinning top itself.

Another example is the precession of the earth's axis of rotation. This is schematically shown in Fig. 4.1. The plane of the equator makes an angle of 23°27′ with the plane of the earth's orbit or its ecliptic. The earth's axis of rotation essentially is the line passing through the north and south poles. This axis is precessing in the east-west direction around the normal to the plane of the ecliptic, *i.e.* opposite to the earth's rotation as indicated in Fig. 4.1. The angular velocity of the precession is equal to 7.19 $10^{-12}\,rad\,s^{-1}$, which is small compared to the angular velocity of the earth's rotation of 7.29 $10^{-5}\,rad\,s^{-1}$. The torque that drives the earth's precession is due to forces exerted by the sun and the moon.

Since these examples of precession are related to the dynamics of a rigid body, their analysis is not directly applicable to the precessing vortex core in a fluid. The approach applied in this study focuses on the interpretation of LDA data obtained from the cyclone flow field. As was mentioned in the previous chapter, the precessing vortex core induces large velocity fluctuations in the core region due to the relative motion of the vortex centre with respect to the LDA measuring volume. This hampers the assessment of Computational Fluid Dynamics (CFD) simulations that apply turbulence closure models. The conventional CFD modelling approach towards cyclone flow does not resolve the unsteady behaviour of the flow field as a result of the precessing vortex core. Hence, techniques were developed to study the effect of the PVC on the flow field in cyclones, and to estimate its contribution to the LDA signal.

First, a simple analytical model of the PVC is presented that is used to clarify the characteristics of the measured LDA signal. Two experimental techniques were used, *viz.* LDA signal analysis by means of adaptive signal processing, and quantitative visualisation of the precessing vortex core. It also was possible to resolve the PVC motion in a laboratory scale

cyclone numerically by means of a time-dependent, three-dimensional Large Eddy Simulation (LES). A comparison is made between the LES and the experimental results.

4.2 A DESCRIPTIVE MODEL

The vortex flow in cyclones is usually described in terms of a core region dominated by a forced vortex near the centreline and an outer region with a free-vortex type of swirl distribution. Several authors used the Burgers' vortex for a comparison of swirl-velocity measurements (see, for example, Garg and Leibovich (1979) and Escudier et al. (1980)):

$$W(r) = \frac{\Gamma}{2\pi r}\left[1 - e^{-\beta r^2}\right] \tag{4.1}$$

where Γ is the circulation and β is related to the size, r_c, of the vortical core; $r_c = 1.12/\beta^{1/2}$. In case of cyclone flow, these two parameters can be estimated by performing a least-squares fit on swirl-velocity measurements. For the LDA measurements of the Stairmand cyclones presented in Fig. 3.7, it appears that more than two fit parameters are required for an accurate analytical description of the tangential velocity profile. A modification to the Burgers' vortex for cyclone flow will be discussed in Sec. 4.3.

The effect of the precessing vortex core on the velocity signal as measured by the laser Doppler anemometer may be described as follows. Assume the PVC is a circular motion of the vortex centre with constant angular frequency, $\omega = 2\pi f_{PVC}$, about the axis of symmetry of the cyclone body, and a constant radius, r^*, which is smaller than the vortex core radius r_c. The swirl distribution is defined by the Burgers' vortex (Eq. 4.1), which is a function of the radial distance, r', from the vortex centre. The LDA measuring volume is located at a fixed radial position, r, relative to the geometrical axis of the cyclone.

In Fig. 4.2, a graphical representation is given of the position of the measuring volume and the vortex centre. The PVC rotates in the same direction as the main flow (see *e.g.* Wunenburger et al. (1999)). The position of the measuring volume relative to the rotating vortex centre is defined by $\mathbf{r}'$, where $\mathbf{r}' = \mathbf{r} - \mathbf{r}^*$. Because the LDA measuring volume, M, is directed and traversed along the x-axis, the measured velocity component, W_{meas}, is perpendicular to this axis. This implies that the anemometer only measures the y-projection of the velocity vector W given by the Burgers' vortex.

The measured velocity component, W_{meas}, can now be expressed as a function of the radial co-ordinate r, and the PVC phase $\phi = \omega t$ as follows:

$$W_{meas}(r,\phi) = \left[\frac{r - r^*\cos\phi}{r'}\right] W(r') \tag{4.2}$$

In Fig. 4.3, the effect of the PVC according to this model is illustrated for an arbitrary Burgers' vortex. The size of the vortex core, r_c, is equal to $0.2R$, where R is the radius of the cyclone, and the PVC is assumed to move in a circular orbit with radius $r^* = 0.05R$. The Burgers' vortex is shown for two extreme positions of the vortex core origin with respect to the measuring volume. Taking the PVC motion into account, the time averaged velocity

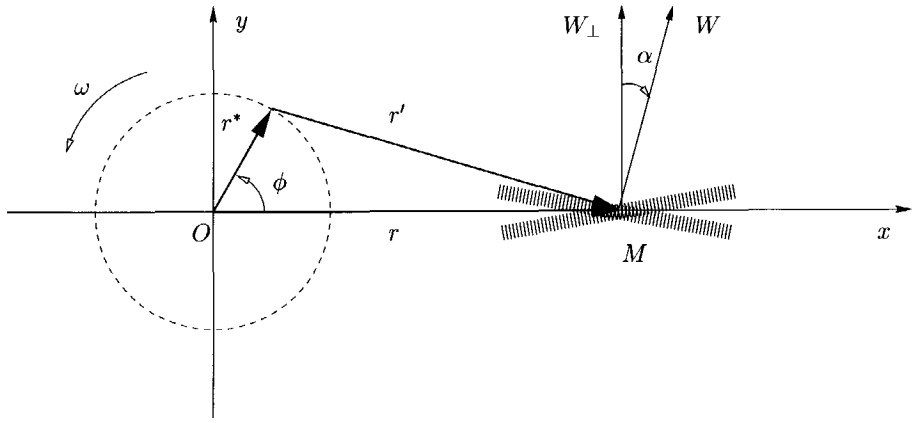

FIGURE 4.2: *Graphical representation of the PVC motion and its effect on the measured velocity component. The LDA measuring volume is located at M and is traversed along the x-axis.*

distribution measured by the LDA exhibits a reduction of the maximum tangential velocity compared to the imposed Burgers' vortex.

It is also shown that the PVC introduces a signal variance. Note that this variance is not due to turbulent velocity fluctuations. The root-mean-square (rms) velocity profile shown in Fig. 4.3 exhibits a large increase in the core region, while in the outer region its magnitude is rather small, and decays towards the wall. At the wall the rms velocity is not equal to zero, because no wall effects were taken into account in Eq. 4.2. The magnitude of the rms velocity is related to the mean velocity gradient, which results in a local minimum in the rms profile at the edge of the vortex core. At this position, the mean tangential velocity obtains a maximum value, whereas the mean velocity gradient locally approaches zero.

The effect of precession on the LDA signal is illustrated in Fig. 4.4. In this figure, simulated velocity traces are shown for different radial positions at the Burgers' vortex versus the PVC phase. The PVC induces a periodical component in the measured velocity signal with decreasing amplitude for larger radii. An exception being the velocity trace at $r/R = 0.2$, where there is a strong attenuation of the PVC component. The signal in the vortex core exhibits a phase lag of π radians with respect to the velocity traces in the outer region. The phase jump occurs at the edge of the vortex core where $r = r_c$. At this position the mean velocity gradient changes sign: from positive in the vortex core region, to negative in the outer region with its free vortex type of swirl distribution. In the next section, it will become evident that this phase jump needs to be taken into account for the reconstruction of phase-resolved velocity profiles.

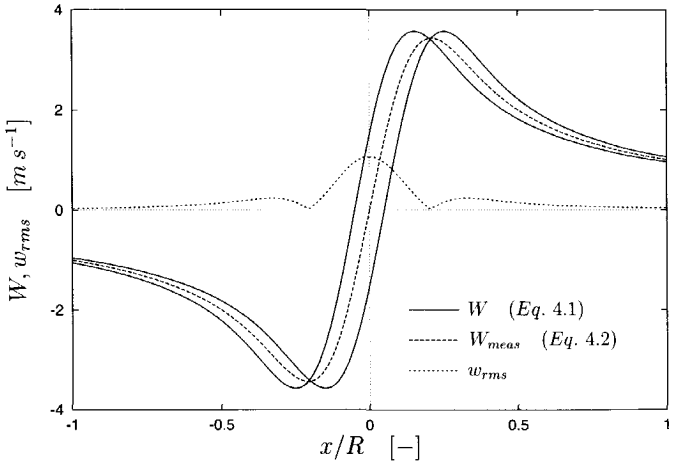

FIGURE 4.3: *Effect of precession on a Burgers' vortex with* $(\Gamma/2\pi) = 1.0\,m^2\,s^{-1}$ *and* $\beta = 31.4\,m^{-2}$. *The amplitude of the PVC with respect to the geometric centre is set to* $0.05R$.

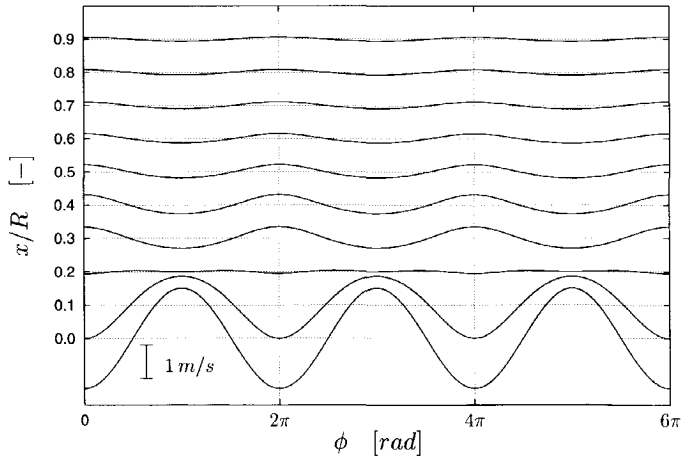

FIGURE 4.4: *Simulated LDA velocity traces at different positions along the cyclone radius. The fluctuating velocity component is shown for three revolutions of the vortex core about the geometric centre.*

4.3 LDA SIGNAL ANALYSIS AND PROCESSING

4.3.1 Time series and auto-correlation

Turbulent flows are characterised by the simultaneous existence of large and small scales of motion. The largest eddy sizes are determined by the size of the geometry, whereas the smallest turbulent scales are related to the dissipation rate ε, and the kinematic viscosity ν, and are referred to as the Kolmogorov microscales. The Reynolds number, Re, for the flow in a cyclone is characterised by the inlet velocity U_{in}, and the cyclone diameter D (see Eq. 2.6).

Accordingly, an appropriate choice for the macro turbulent time scale is $T = D/U_{in}$. The typical time scale associated with the smallest eddy size is then proportional to $TRe^{-1/2}$ following Kolmogorov's scale relations (Tennekes and Lumley, 1972). For the Stairmand gas cyclone studied in Ch. 3 with $U_{in} = 15\,m\,s^{-1}$ and $D = 0.290\,m$ the turbulent eddies correspond to frequencies varying between 50 Hz and 27 kHz. It is clear that the range of turbulent scales widens as the Reynolds number increases.

A way to study the time scales in a flow is to estimate the auto-correlation function (ACF) of the measured fluctuating velocity, $u(t)$. Provided that the signal is stationary, the auto-correlation function $\rho_{uu}(\tau)$ is defined by

$$\rho_{uu}(\tau) = \frac{R_{uu}(\tau)}{R_{uu}(0)} = \frac{\overline{u(t)u(t+\tau)}}{\overline{u^2}} \tag{4.3}$$

where τ is the time lag, and $R_{uu}(\tau)$ is the auto-covariance function. The auto-correlation function can be interpreted as a measure for the similarity between the signal $u(t)$, and the time-shifted signal $u(t+\tau)$. Quasi-periodical phenomena in the velocity signal due to, for example, the precessing vortex core, can be detected by means of the auto-correlation function, where they are visible as sinusoidal continuations of $\rho_{uu}(\tau)$ for long lag times. This is demonstrated in Fig. 4.5.

In this figure, a fraction of the fluctuating tangential velocity time series recorded near the cyclone centreline is shown together with its auto-correlation function. The ACF was obtained by means of the slotting technique using local normalisation (Tummers et al., 1994) [1]. The velocity trace and auto-correlation function clearly show the presence of a low-frequency, periodic component, which can be attributed to the precessing vortex core. It is possible to estimate the PVC frequency from the spectral estimate of the LDA time series. The power spectral density can be obtained directly by a cosine transformation of the discrete auto-correlation function. For the LDA signal presented in Fig. 4.5, the dominant PVC frequency was equal to 12.0 Hz, which corresponds to a Strouhal number of 0.60 (see Eq. 2.5). In Fig. 4.6, the precession frequency is shown versus the linear inlet velocity for the tangential swirl tube separator. The cyclone geometry was modified by contraction of the exit pipe diameter (see for details Sec. 3.3).

The fundamental frequency of the precessing vortex core is proportional to the inlet velocity or flow rate. This observation agrees with earlier reported results on the PVC in cyclone flow

[1] The advantage of this ACF estimator is that it uses the non-equidistant LDA time series directly; it is not necessary to first re-sample the signal.

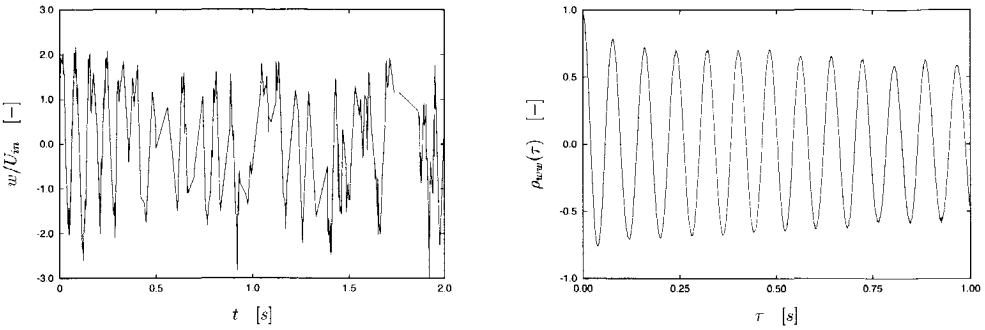

FIGURE 4.5: *(a) Measured part of LDA time series and its (b) estimated auto-correlation function of the fluctuating tangential velocity component recorded at* $x/R = -0.014$. *The data were measured at* $z/D = 1.75$ *of the tangential swirl tube separator (see Fig. 3.5b) with* $D_e/D = 0.37$ *and* $Re = 1.2\ 10^5$.

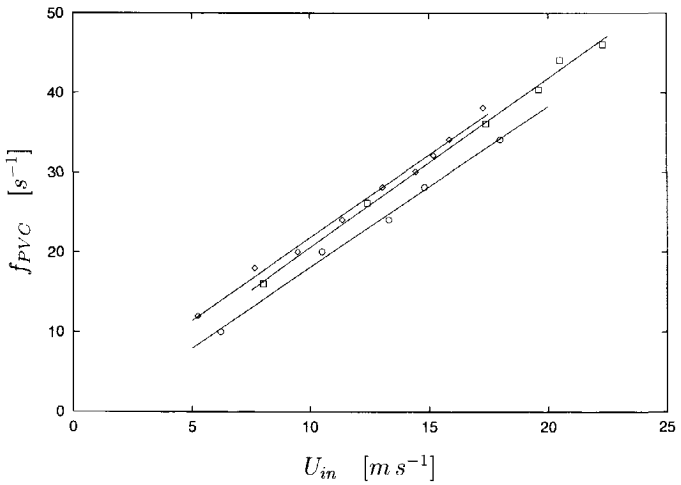

FIGURE 4.6: *The PVC frequency versus the linear inlet velocity for the tangential swirl tube separator at* $r/R = 0.0$ *with* D_e/D *equal to (○) 0.66, (□) 0.47, and (◇) 0.37. The solid lines represent a linear fit of each data set.*

(Gupta et al., 1984). In addition, the figure shows an increase of the PVC frequency with decreasing exit pipe diameter.

There are a number of fluid flow applications where the measured LDA signal is affected by a periodically unsteady motion. A well-known example is the periodic motion of the impeller in a stirred tank reactor, which introduces pseudo-turbulent fluctuations in the LDA signal as a result of the trailing vortices, attached to the impeller blades. Phase-resolved LDA measurements are capable of distinguishing turbulent and non-turbulent velocity fluctuations by use of an external trigger signal originating from the impeller motion (see, for example, Derksen and Van den Akker (1999)). It is, however, not possible to apply this approach to the precessing vortex core in cyclone flow, because no natural triggering signal is available. In addition, the PVC is internally driven, and, hence, can exhibit irregularities such as phase jumps, and non-constant amplitude.

Yazdabadi et al. (1994) were able to derive a sinusoidal PVC signal from the gas flow in the exhaust of a cyclone using a hot wire probe. The probe was used as a triggering unit for the LDA system. A similar approach was applied by Dirkzwager (1996), who used a second LDA system to obtain a trigger signal from the PVC in the flow field of an axial hydrocyclone. Although the triggered velocity profiles confirmed the smoothing effect of the PVC on the mean velocity profiles as well as its significant contribution to the signal variance, the results appeared to be rather sensitive to the irregular motion of the PVC. Contrary to these methods based on external triggering, Fokke et al. (1994a) estimated the PVC motion from the LDA signal itself by means of a double moving average filter. Since the LDA measurements were done in a hydrocyclone, the filtering technique could benefit from the high data rates. For a gas cyclone where the data rates are generally much lower, it was felt that a more advanced filtering technique was required to estimate the effect of the PVC on the LDA measurements. This technique is discussed in the next section.

4.3.2 Adaptive signal processing

Adaptive signal processing is a technique regularly applied in noise cancellation problems. For an extensive discussion on the subject of adaptive signal processing, the reader is referred to Widrow and Stearns (1985). A schematic diagram of the adaptive noise cancellation system applied in this study is given in Fig. 4.7.

Adaptive noise cancelling is capable of estimating the periodical interference from the LDA signal by inserting a fixed delay in a reference input drawn directly from the primary input. The delay chosen must be of sufficient length to cause the turbulent velocity fluctuations in the reference signal to become de-correlated from those in the primary input. The interference component resulting from the PVC motion will remain correlated due to its periodic nature (*cf.* the auto-correlation function in Fig. 4.5 for large time lags). The 'noise' or filtered reference input, η_k, is subtracted from the primary input, $Y_{1,k}$, and the resulting 'error', ϵ_k, is used to adapt the filter coefficients. The adaptive nature of the filter is very suitable for estimating the interference in the LDA signal as a result of the (pseudo-) periodic PVC motion. Adaptive noise cancelling generally does a better job than a classical filter because the noise here is subtracted from rather than filtered out of the primary signal.

The adaptive filter used in the noise cancellation is a linear combiner or finite impulse response filter (Widrow and Stearns, 1985). The input of the filter, $\mathbf{Y}_{2,k}$, consists of $L + 1$

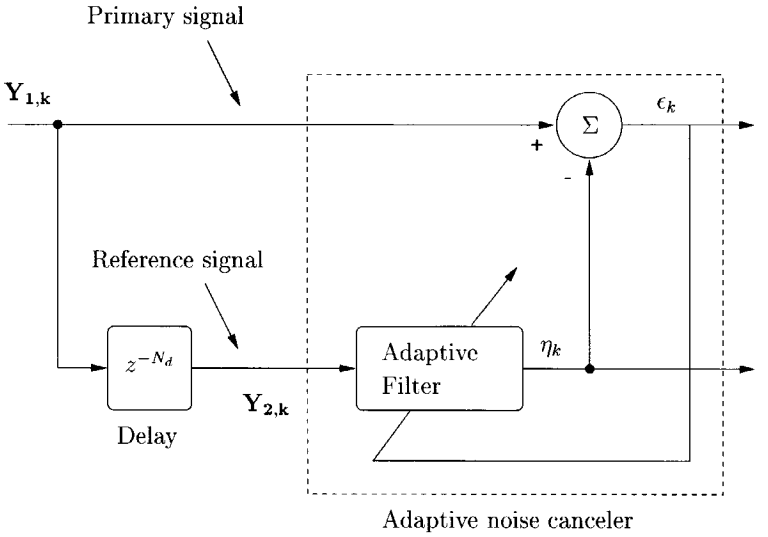

FIGURE 4.7: *Schematic representation of adaptive noise cancellation. The reference input is a delayed version of the primary input. The coefficients of the linear filter are adapted continuously to minimise the mean square error.*

sequential samples taken at points $k, k-1, ...$, going back in time. This reference input is a delayed version of the primary input, which is represented in Fig. 4.7 by a delay element of N_d samples. The filter output, η_k, now is a linear combination of the filter weight vector, $\mathbf{W}_k$, and the reference input, $\mathbf{Y}_{2,k}$, given in vector notation:

$$\eta_k = \mathbf{W}_k^T \mathbf{Y}_{2,k} \tag{4.4}$$

where T stands for transpose. Note that the weight vector consists of $L+1$ elements, and η_k is a scalar.

In the adaptation process, the weight vector of the linear combiner is adjusted to cause the output, η_k, to agree as closely as possible with the primary input, $Y_{1,k}$. This is accomplished by minimising the mean square error (MSE), $E[\epsilon_k^2]$, where $\epsilon_k = Y_{1,k} - \eta_k$. It can be shown that the expression for the MSE is a quadratic function of the weight elements if the input components and the desired response are stationary stochastic variables. Because the MSE performance surface has a single global minimum, an optimal weight vector can be obtained (Widrow and Stearns, 1985).

However, this optimal weight vector requires the knowledge of the auto-covariance matrix of the reference input, and the cross-covariance vector between the primary and reference input. This information is usually not available *a priori*. In addition, the periodical interference does not need to be stationary, *i.e.* the environment in which the filter is operating is changing slowly. These limitations necessitate the use of an *iterative* method capable of searching the performance surface and finding the optimal weight vector.

An algorithm that has proven its value in a wide variety of practical applications is the method of steepest descent. It is a method of gradient search that causes all components of the weight vector to change in the direction of the negative gradient of the performance surface:

$$\mathbf{W}_{k+1} = \mathbf{W}_k + \mu(-\nabla_k) \tag{4.5}$$

where ∇_k denotes the gradient of the performance surface $E[\epsilon_k^2]$ at $\mathbf{W}_k$, and the parameter μ is a constant that governs stability and rate of convergence.

Eq. 4.5 requires the gradient vector at each iteration. In most applications, an estimator is based on a limited statistical sample. A special estimate that is valid for the adaptive linear combiner η_k discussed in this set-up, is known as the least-mean-square (LMS) algorithm. The LMS algorithm takes ϵ_k^2 itself as an estimate of the performance surface $E[\epsilon_k^2]$. In the adaptive process we then have a gradient estimate of the form

$$\hat{\nabla}_k = \begin{bmatrix} \frac{\partial \epsilon_k^2}{\partial w_0} \\ \vdots \\ \frac{\partial \epsilon_L^2}{\partial w_L} \end{bmatrix} = 2\epsilon_k \begin{bmatrix} \frac{\partial \epsilon_k}{\partial w_0} \\ \vdots \\ \frac{\partial \epsilon_L}{\partial w_L} \end{bmatrix} = -2\epsilon_k \mathbf{Y}_{2,k} \tag{4.6}$$

which is an unbiased estimator of the true gradient ∇_k. Substitution of the gradient estimate in Eq. 4.5 then results in the adaptive algorithm. It is expected that the gradient components of Eq. 4.6 contain a large component of noise. However, the noise is attenuated with time by the adaptive process (Widrow and Stearns, 1985). The pseudo-code of the adaptive noise cancellation with the LMS algorithm is listed below.

Algorithm 1 Adaptive noise cancellation

Choose μ, L, and N_d
$k = k_0 = L + N_d$
$\mathbf{Y}_{2,k_0} = \mathbf{Y}_{1,k_0-N_d} = [Y_{1,L} Y_{1,L-1} \ldots Y_{1,0}]^T$
$\mathbf{W}_{k_0} = 0$
$\epsilon_{k_0} = Y_{1,k_0}$
for $k = k_0, k+1, \ldots$ **do**
  $\eta_k = \mathbf{W}_k^T \mathbf{Y}_{2,k}$
  $\epsilon_k = Y_{1,k} - \eta_k$
  $\mathbf{W}_{k+1} = \mathbf{W}_k + 2\mu\epsilon_k \mathbf{Y}_{2,k}$
end

The adaptive process of Algorithm 1 is determined by three parameters, *i.e.* the gain factor, μ, the number of filter coefficients, $L+1$, and the number of delay samples, N_d. The magnitude of the gain factor, μ, determines the adaptation time of the filter, and is bounded to assure convergence of the LMS algorithm. Widrow and Stearns (1985) provide the following expression for choosing the gain factor:

$$0 < \mu < \frac{1}{(L+1)\sigma_{11}^2} \tag{4.7}$$

where σ_{11}^2 represents the signal power of the primary input. Typical values for μ are of the order of a tenth of the upper bound given by Eq. 4.7 (Widrow and Stearns, 1985).

As was mentioned earlier, the delay used in the reference input must be chosen such that the turbulent signal becomes de-correlated, while the PVC signal remains correlated. The minimum delay is determined by the time scale of the largest turbulent eddies. On the other hand, the correlation coefficient of the PVC motion decreases for large lag times. For the LDA signal traces presented in Fig. 4.5, a delay of $1.0\,s$ was used, which corresponds to approximately 20 times the macro scale of the flow. The adaptive process did not prove to be very sensitive to the exact magnitude of the delay as long as it exceeded the maximum turbulent time scale.

To apply the adaptive process of Fig. 4.7 to the measured time series, re-sampling of the LDA signal is necessary. The mean data rate of the non-equidistant LDA signal generally varied between 200 and 800 Hz, and re-sampling of the time series was obtained by means of linear interpolation at a mean frequency of 1,000 Hz. The delay of the reference signal was 1,000 velocity samples of the re-sampled primary input corresponding to a time lag of $1.0\,s$. The number of filter coefficients was set to 3,000, which was estimated empirically by evaluating the filter output variance. The learning curve of the LMS algorithm is characterised by a time constant of adaptation, T_{mse}. It was shown by Widrow and Stearns (1985) that the time constant of the adaptive process is given by $T_{mse} = 2.5(L+1)$ in terms of the number of data samples. During the adaptation time the data were not taken into account for the velocity statistics of the filtered LDA signal.

4.3.3 Results and discussion

Adaptive filter

The adaptive filter is used to estimate the PVC component in the LDA time series for each measurement position in a similar way as was achieved by Yazdabadi et al. (1994) using an external triggering technique. The limitation of the adaptive filter technique is that the exact PVC phase is not known *a priori*, but it may be obtained deviously from the velocity signal. The relation between the PVC motion and the periodical component in the LDA signal was elucidated by the PVC model and demonstrated in Fig. 4.3. In this study, the adaptive filter is combined with the concepts of the PVC model to reconstruct phase-resolved velocity profiles corresponding to the extreme positions of the PVC centre with respect to the measuring volume, *i.e.* $\phi = 0$ and $\phi = \pi$ (see Fig. 4.2). Since these positions are located at the traversing axis of the LDA probe, the tangential velocity, W, is equal to its projected component, $W_\perp$.

The filter output at each measurement position represents the periodical interference in the velocity signal, and is used to estimate the maximum and minimum velocity magnitude during a PVC cycle. The extremes of the filter output are determined by comparing each data sample with an interval of neighbouring samples (typically corresponding to one third of a PVC cycle). The velocity measurements at these points are labelled in the re-sampled LDA signal and collected. An example of this procedure is shown in Fig. 4.8. Velocity statistics for the phase-resolved velocity profiles were based on $300 - 500$ labelled LDA data per radial position.

As an illustrative example of adaptive signal processing, the LDA measurements of the flow field in a tangential swirl tube separator will be analysed here. The velocity profiles for $D_e/D = 0.37$ presented in Fig. 3.8 and Fig. 3.9 exhibit strong velocity gradients in the radial

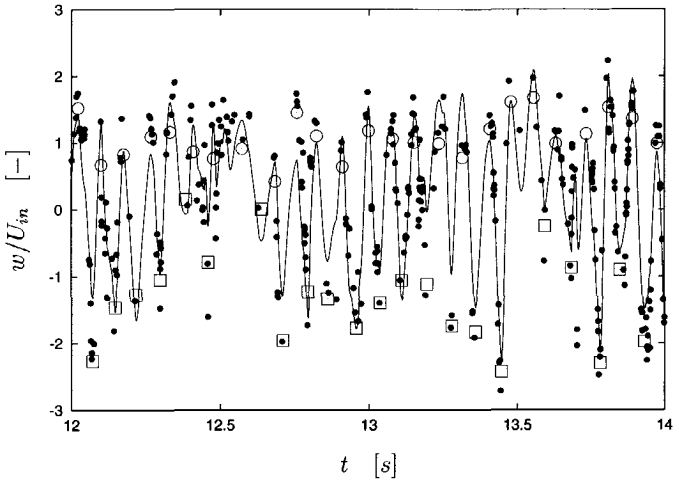

FIGURE 4.8: *Adaptive processing of an original LDA time series (•) recorded at the cyclone centreline. The filter output (–) is used to estimate the (□) minimum and (○) maximum of a PVC cycle from the re-sampled LDA signal.*

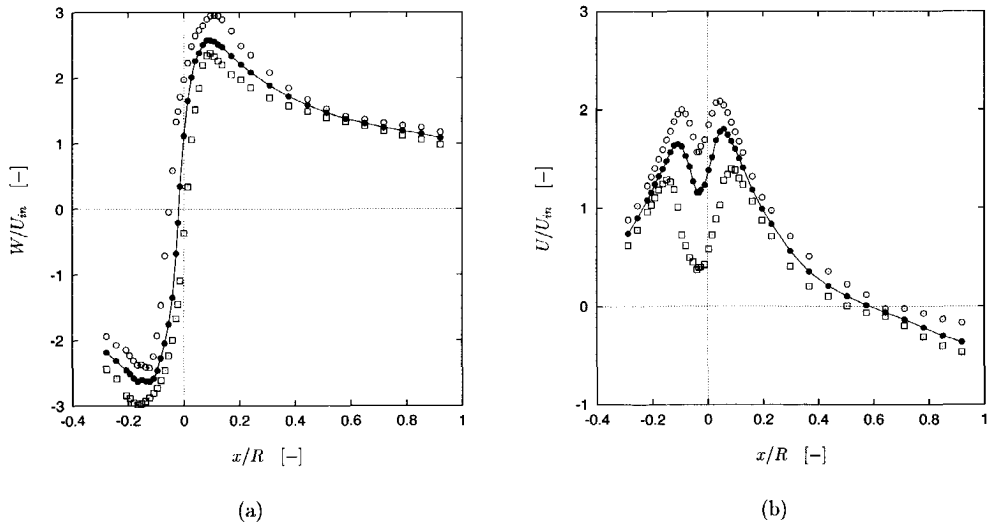

(a) (b)

FIGURE 4.9: *Radial distribution of the measured mean (•) and the estimated averaged values of the minimum (□) and maximum (○) velocity for the tangential (a) and axial velocity (b) component, respectively. The LDA measurements were done of the flow in a tangential swirl tube separator at* $z/D = 1.75$ *with* $D_e/D = 0.37$ *and* $Re = 1.2\ 10^5$.

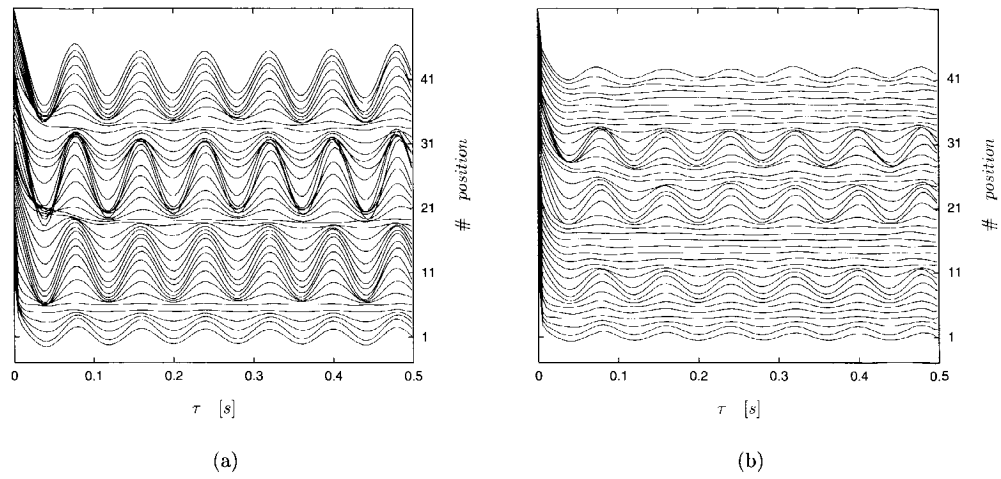

FIGURE 4.10: *Auto-correlation function of the fluctuating (a) tangential velocity, ρ_{ww}, and (b) axial velocity, ρ_{uu}, along the cyclone diameter. The ACF's are smoothed by means of a Bezier function.*

direction due to the limited core diameter. Hence, it is expected that the effect of the PVC on the LDA signal will be considerable.

In Fig. 4.9a, radial profiles of the *tangential* velocity are shown that correspond to the maximum and minimum of the PVC cycle, respectively. The data were recorded at measurement station $z/D = 1.75$. The mean tangential velocity estimated from the complete set of velocity samples is also presented as a reference. The results show that especially in the core region the minimum and maximum values differ significantly from the mean tangential velocity. Using the interpolated zero-crossings of the minimum and maximum tangential velocity profiles the approximate amplitude of PVC is equal to $0.03R$.

The time-dependent radial displacement of the vortex core also affects the radial distribution of the mean *axial* velocity. Fig. 4.9b shows that the difference in magnitude between the minimum and maximum values of the axial velocity component is considerable, especially in the core region. The axial velocity maximum, which is located at the edge of the vortex core, varies between 1.3 and 2.1 times the inlet velocity. Due to the spatial averaging effect of the PVC the local minimum near the centreline is 1.1 normalised by the inlet velocity for the mean axial velocity, whereas it is approximately 0.4 at the minimum of the PVC cycle.

Tangential velocity profile

The reconstruction of phase-resolved velocity profiles from the data displayed in Fig. 4.9 is not straightforward. Our aim is to obtain the phase-resolved velocity profiles corresponding to $\phi = 0$ and $\phi = \pi$ (see Fig. 4.2), *i.e.* to the 'apogee' and the 'perigee' of the vortex trajectory following the nomenclature of Wunenburger et al. (1999). These positions of the swirl centre

result in a minimum or maximum value in the LDA signal, which depends on the direction of the local mean velocity gradient (see Fig. 4.4). Hence, information on the shape and behaviour of the PVC is only obtained indirectly through its effect on the measured LDA signal.

The presence of a periodical component in the LDA signal is properly determined by means of the auto-correlation function (ACF). An example was given earlier in Fig. 4.5. In Fig. 4.10a, the ACF of the fluctuating tangential velocity is shown for each radial measurement position used for the velocity profile at $z/D = 1.75$. Note that the measurement positions are not distributed at equal intervals along the cyclone diameter. Each auto-correlation function has been shifted vertically with respect to its predecessor.

A first analysis reveals that each auto-correlation function displayed in Fig. 4.10a exhibits a sinusoidal shape due to the precessing vortex core, except those located at three intermediate radial positions, where the periodical component is virtually absent. Six periods of the sinusoidal can be identified within a time lag of $0.5s$, which agrees with the fundamental frequency of the PVC equal to 12 Hz. Starting at the first four measuring locations, it is shown that the PVC affects the fluctuating tangential velocity component close to the cyclone wall, although its contribution to the signal variance is rather limited. The periodical interference in the LDA signal is attenuated at measurement positions 5, 19 and 33 corresponding to the radial coordinates $x/R = 0.65$, 0.069, and -0.11. The latter two positions characterise the edge of the vortex core, *i.e.* at these radial coordinates the mean tangential velocity obtains its maximum value, while the direction of the mean velocity gradient changes sign concurrently (see Fig. 4.9a).

The attenuation of the PVC in the velocity signal at the edge of the vortex core was already demonstrated by the PVC model discussed in Sec. 4.2. In addition, it was shown that there exists a phase shift of π radians between the velocity traces recorded at the core region and the outer region, where a free-vortex type of swirl distribution prevails (*cf.* Fig. 4.4). Although all phase information is lost in the auto-correlation, it is expected that the absence of the PVC component at $x/R = 0.65$ is associated with a similar phase shift.

Based on this assumption, the phase-resolved tangential velocity profiles have to cross at the edge of the vortex core. This is shown in Fig. 4.11a. At the 'apogee' ($\phi = 0$) of the PVC, the mean tangential velocity in the vortex core is equal to the values corresponding to the minimum ($\square$) of the PVC cycle, whereas outside the core region it is equal to the maximum ($\circ$) values. For the 'perigee' ($\phi = \pi$), it is the other way round. In the analytical PVC model discussed in Sec. 4.2, the same Burgers' vortex is applied for each PVC phase. However, the experimental results show that the vortex depends on the position of the swirl centre due to the confinement of the flow by the cyclone wall.

The radial displacement of the core origin hardly affects the vortex core *itself*, because both the angular velocity and the diameter of the vortex core are the same for the two PVC phases. Instead, the strongest influence is exercised on the outer region of the vortex. At $\phi = 0$, the maximum mean tangential velocity is located at $r/R = 0.11$ and its magnitude is approximately equal to 3.0 times the inlet velocity. At $\phi = \pi$, the maximum mean tangential velocity is shifted towards $r/R = 0.028$, and its magnitude is reduced to 2.5 times the inlet velocity. As a result, the swirl distribution in the free vortex type of region is adapted in terms of its vortex exponent. This could be an explanation for the absence of the PVC component in the auto-correlation function at $x/R = 0.65$. Using the concept of a phase shift at similar positions in the velocity profile, another crossing of the 'apogee' and 'perigee' velocity profiles

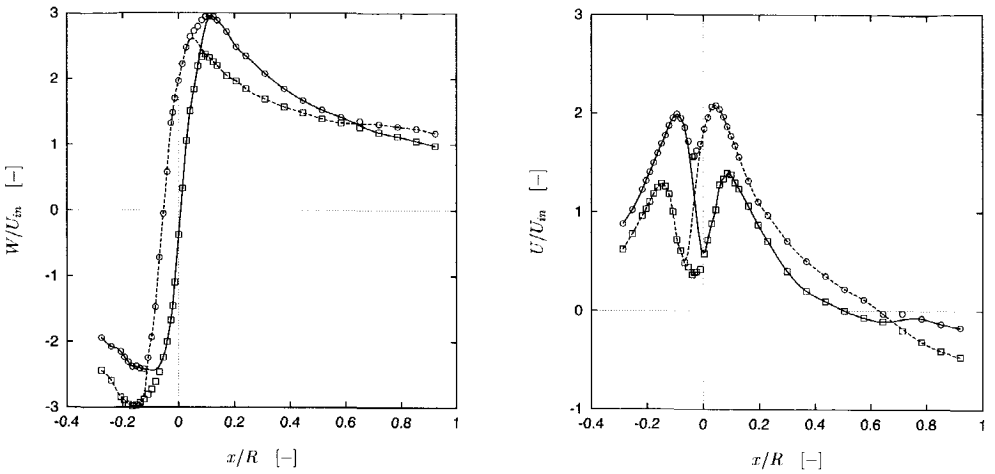

FIGURE 4.11: *Radial distribution of mean tangential (a) and axial (b) velocity profiles, where the 'apogee' ($\phi = 0$) of the PVC is represented by (–) and the 'perigee' ($\phi = \pi$) by (- -). The minimum (□) and maximum (○) values of the velocity components are related to the extremes of the periodical component in the LDA time series.*

occurs. A physical argument for this crossing is the conservation of angular momentum on both sides of the displaced vortex centre (Yazdabadi et al., 1994).

Axial velocity profile

The auto-correlation function of the axial velocity component, presented in Fig. 4.10b, also exhibits a sinusoidal component due to the precessing vortex core. Although its frequency is equal to the fundamental frequency of the PVC, the contribution of the periodical component to the signal variance is less than observed for the tangential velocity component. Four locations along the cyclone diameter can be identified, where the PVC component is virtually absent. Starting from the cyclone wall, the first measuring position where the periodical interference is attenuated is #4 located at $r/R = 0.71$. The meaning of this position will be addressed later. A similar location is measuring position #25, which corresponds to the local minimum in the mean axial velocity profile near the cyclone centreline (see Fig. 4.9b). The other two positions, where the periodical component is absent in the ACF, correspond to an interval of several measurement points, *viz.* points $13 - 17$ and $35 - 39$. The profiles of the maximum and minimum values of the mean axial velocity presented in Fig. 4.9b show that these measurement points are associated with the outer edge of the vortex core, where the mean axial velocity approaches its maximum value.

Following the characteristics of the PVC model, a phase shift needs to be applied at each (local) minimum or maximum, because at these positions the direction of the local mean velocity

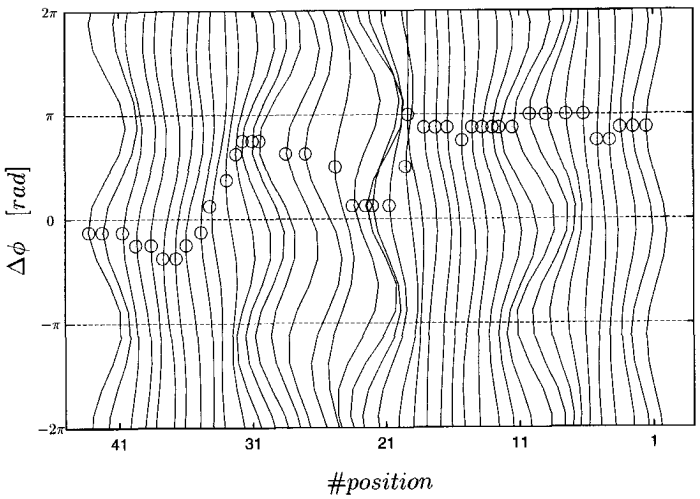

FIGURE 4.12: *Cross-correlation function, ρ_{uw}, of 2D LDA signal recorded along the cyclone diameter and smooth by means of a Bezier function. The time lag τ is converted to a phase shift $\Delta\phi$ related to the fundamental period of the PVC. At each measurement position the maximum correlation peak is indicated (○).*

gradient changes sign. Before the reconstructed axial velocity profiles can be assigned to the 'apogee' and 'perigee' position of the PVC, it is necessary to determine the phase lag between the periodical components in the tangential and axial velocity signal. Since a 2D LDA measurement set-up was used, this phase lag could be estimated from the cross-correlation function, ρ_{uw}, defined as

$$\rho_{uw}(\tau) = \frac{\overline{w(t)u(t+\tau)}}{\sqrt{\overline{w^2}}\sqrt{\overline{u^2}}} \tag{4.8}$$

where the tangential leads the axial velocity component. Provided that the measuring volumes of both channels overlap and that a proper coincidence time window is set, the cross-covariance coefficient at $\tau = 0$ is related to the Reynolds shear stress $\tau_{uw} = -\rho\overline{uw}$.

In Fig. 4.12, the cross-correlation function is presented for each measuring position along the traversing axis. Since the fundamental period of the PVC cycle is equal to $0.080\,s$, the time shift τ of the CCF is easily converted to a phase lag $\Delta\phi$ of the PVC cycle. The cross-correlation function exhibits a periodical continuation if the periodical interference due to the PVC is present in both velocity channels. Accordingly, a maximum in the cross-correlation function corresponds to the phase shift between the PVC components in the tangential and axial velocity signal.

The correlation peaks labelled in Fig. 4.12 exhibit a complicated development while traversing along the radial coordinate. By means of a simplification, the phase characteristics can be used for the reconstruction of the 'apogee' and 'perigee' axial velocity profiles. A maximum

in the CCF exists at approximately π radians for the measuring positions #1 – 19, *i.e.* the tangential leads the axial velocity component by half a PVC cycle. These locations represent the outer region of the vortex located at the positive x/R axis. The phase lag of π radians implies that the phase-resolved axial velocity exhibits a minimum value if the tangential velocity reaches a maximum value in the PVC cycle (see Fig. 4.11). In other words: high tangential velocities are associated with low axial velocities and vice versa.

These arguments also hold for the outer vortex region at the negative part of the x-axis. From the cross-correlation function it follows that the phase lag between the tangential and axial velocity components is approximately zero for the measuring positions in this region (#33 – 42), *i.e.* both the tangential and axial velocity component exhibit a minimum value in the PVC cycle. However, the tangential velocity magnitude hits a maximum, because it has negative values at the negative part of the x/R axis. This is clearly shown in Fig. 4.11.

In the core region, the phase lag of the axial velocity component gradually varies between 0 and π radians. These values are obtained at measuring positions #23 and #29, respectively. On the other hand, no min-max transition occurs in the vortex core for the phase-resolved *tangential* velocity component. By use of the phase shift transitions in the cross-correlation function, the phase-resolved axial velocity profile may be reconstructed according to Fig. 4.11b. A closer inspection of this figure reveals that the axial velocity profiles associated with the 'apogee' and 'perigee' of the PVC cross at the local minimum in the mean axial velocity profile near the centreline, and in the outer region close to the axial zero-crossing coordinate. Note that at these radial locations the PVC component is absent in the auto-correlation function of the axial velocity component (see Fig. 4.10b). An explanation for the crossing of the velocity profiles in the outer vortex region is the conservation of mass; there is a balance of downward and upward directed fluxes at each side of the displaced vortex centre.

Rms velocity

Next to an estimate of the periodical interference, the adaptive filtering technique provides us with an 'error' or filtered LDA signal. When the adaptation time of the LMS algorithm has passed, the filtered LDA signal is cleaned from velocity fluctuations due to vortex core precession. The variance of the filtered signal is only due to turbulence, and represents the tangential or axial normal stress.

In Fig. 4.13, the filtered tangential and axial rms velocity components are compared to the original rms velocity. The profiles show that especially in the core region a significant part of the rms velocity is due to vortex precession. Near the centreline, the non-turbulent velocity fluctuations contribute to at least 80% and 70% of the total signal variance for the tangential and axial velocity component, respectively. In the outer vortex region, the contribution of the PVC to the rms velocity is limited.

Other velocity profiles

For the swirl tube separators with a larger exit pipe diameter, the effect of the precessing vortex core on the mean and fluctuating velocity profiles is less pronounced. The reconstructed velocity profiles for these geometries exhibit similar flow characteristics, *e.g.* the absence of a low-frequency oscillation in the LDA signal at radial positions where the phase-resolved velocity

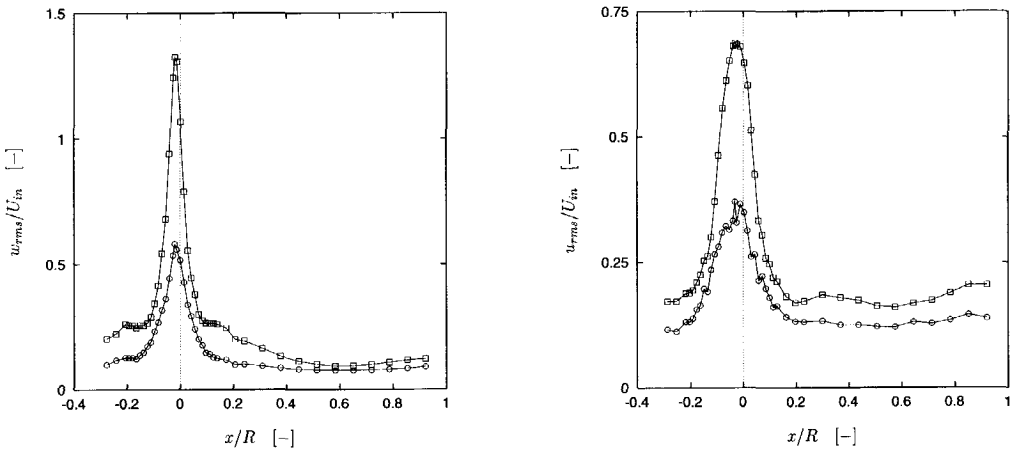

FIGURE 4.13: *Radial distribution of the original (□) and filtered (○) rms velocity of the tangential (a) and axial (b) velocity component.*

profiles cross, the vortex core being displaced by the PVC, and the contribution to the signal variance in the core region. The application of adaptive processing to the Stairmand velocity measurements, however, proved to be more complicated.

First, the LDA time series for the Stairmand cyclone were not dominated by the low-frequency oscillation of the PVC in the extent observed for the swirl tube separator (see Fig. 4.8). Although the existence of a precessing vortex core was confirmed by spectral analysis, its contribution to the auto-correlation function was small for larger time lags. Hence, a smaller delay had to be used for the reference signal of the adaptive filter. Second, the data rate of the LDA signal in the core region of the Stairmand cyclone was generally lower than obtained for the swirl tube separator. This affected the re-sample frequency of the LDA signal, and, subsequently, the number of filter coefficients. For the Stairmand cyclone studied, the phase-resolved velocity profiles could not be clearly discriminated from the time-averaged profiles.

4.4 FLOW FIELD VISUALISATION

4.4.1 Experimental set-up

It has been demonstrated that LDA, being a one-point measuring technique, needs additional signal analysis to describe a flow phenomenon such as vortex core precession. A more favourable optical technique would record a single realisation of the complete flow field, hereby providing information on the *spatial* character of the flow. A popular whole-field laser technique is Particle Image Velocimetry (PIV). For a basic description of this technique, the reader is referred to

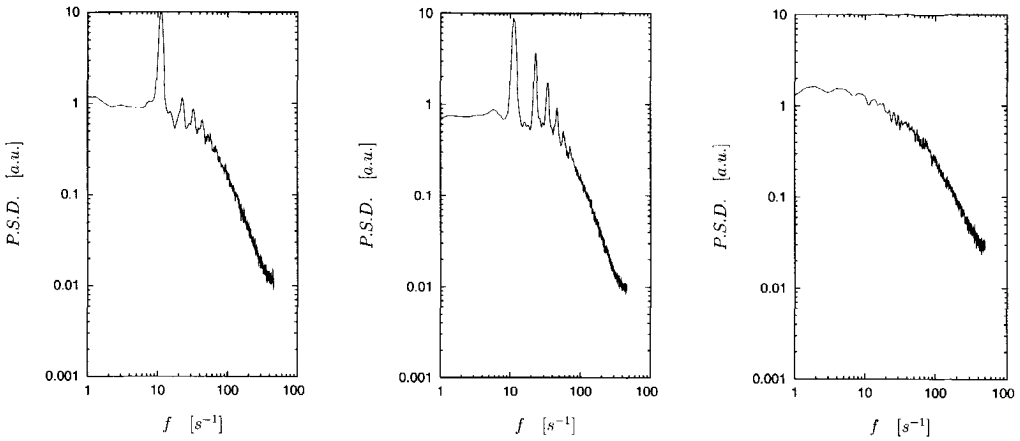

FIGURE 4.14: *Power spectral estimates at $x/R = 0.5$ and $z/D = 1.5$ of the (a) tangential, and (b) axial fluctuating velocity component, and (c) at the inlet section.*

Adrian (1991). The operating principle of PIV is based on recording the displacement of tracer particles in a cross-section of the flow during a small time interval. By estimating the magnitude of the particle image displacements at several positions in the recording, a cross section of the flow field is obtained at a moment in time. This way, spatial information is provided on coherent flow structures such as the PVC.

An example of the application of PIV for studying vortex precession is provided by Volkert et al. (1996) and Grosjean et al. (1997). They used PIV in combination with LDA to examine the strongly swirling flow in a combustion engine. The trajectory of the PVC was estimated by interpolation of the velocity vectors at each PIV recording. Next, the time-dependent character of the swirl centre was expressed as a joint probability function in Cartesian co-ordinates. In this study, a similar approach was applied to the PVC in a cyclone separator.

To comply with the experimental facilities available, a perspex laboratory scale cyclone or vortex chamber with an internal diameter of $100\,mm$ was constructed, resembling a downscaled version of the tangential swirl tube separator studied in Ch. 3. The geometry was cylindrical in shape with a flat bottom plate to facilitate visual observation of an illuminated horizontal plane. The vortex flow was generated by a tangential inlet at a flow rate of $16.3\,m^3\,h^{-1}$. The flow rate corresponds to a linear inlet velocity of $2.26\,m\,s^{-1}$, and a (moderate) Reynolds number of 15,000 according to Eq. 2.6. The geometric swirl number was equal to 2.1. LDA measurements of the tangential and axial velocity components were carried out along the radius at four axial stations. At one measurement station, an additional visualisation experiment was performed that will be discussed in this section. A schematic description of the geometry is presented in Sec. 5.3.5, where the measured velocity profiles are compared to numerical predictions of the flow field.

The existence of a precessing vortex core is revealed in Fig. 4.14. In this figure, normalised spectral estimates are presented of the fluctuating velocity components recorded at the inlet and at a position in the vortex. The spectral estimates were obtained by a fast Fourier transform of the re-sampled LDA time series using linear interpolation. The time series for each spectral estimate consisted of $\approx 10^5$ data points. Both the tangential and axial velocity components show a distinct low-frequency peak at 11 Hz, which can be attributed to the PVC, along with some higher harmonics. A peak frequency and its harmonics was also observed by Garg and Leibovich (1979) for the two velocity components they measured with LDA in the wake of vortex breakdown flow fields. That the PVC is driven internally is confirmed by the absence of a low-frequency oscillation in the inlet flow (see Fig. 4.14c).

At $z/D = 3.0$ a horizontal slice of the flow was illuminated by a sweeping laser beam from a CW $4W$ Ar^+ laser. To improve light scattering, fluorescein was added to the seeding droplets. It was observed that near the centreline of the cyclone a region exists where seeding particles were virtually absent. This region is associated with the vortex core. As a result of the low seeding concentration in this part of the flow, the circular motion of the vortex core could easily be recorded by a digital video camera. Hence, it was possible to estimate the approximate swirl centre as a function of time. This will be discussed in the next section.

4.4.2 Distribution of the vortex centre

The vortex core motion was recorded by use of a CCD camera with a spatial resolution of 256^2 pixels at an image acquisition rate of 40 Hz. As spectral analysis pointed out, the PVC moves at ≈ 11 cycles per second; this implies that the sample rate obeys the Nyquist criterion for resolving the fluctuations. The total number of samples obtained was $1,200$. The PVC was visualised by sweeping an Ar^+ laser beam through the measurement plane at high frequency (typically 3 kHz) to obtain a pseudo-sheet of light. The light sheet was formed at the axial station $z/D = 3.0$.

The data were processed by the image processing software Scil-Image. The quality of the recorded grey-value images was improved by background removal and smoothing. A dynamic threshold level was used to separate the vortex core structure from the image, and to convert the image to a binary format. Finally, the centre of mass was determined of the remaining object. Images consisting of multiple structures were rejected. In Fig. 4.15, the measured positions of the PVC centre are shown in a 2D scatter plot together with the corresponding 2D probability density function. The figures show that the PVC is not rotating about the geometric centre at a constant amplitude, and the time-averaged PVC centre does not coincide with the geometric centre, in contrast to the model assumptions of Sec. 4.2.

The 2D PDF of the swirl centre can now be used in the method described by Volkert et al. (1996) and Grosjean et al. (1997) in order to estimate the contribution of the PVC to the LDA signal variance. Their starting point is to express the PDF of the swirl centre (Fig. 4.15) in analytical form. For the position of the swirl centre, a Gaussian distribution is postulated. The 2D PDF can then be written in a Cartesian co-ordinate system as follows:

$$p(x,y) = \frac{1}{2\pi\sigma_x\sigma_y} \exp\left[-\frac{1}{2}\left(\frac{(x-\mu_x)^2}{\sigma_x^2} + \frac{(y-\mu_y)^2}{\sigma_y^2}\right)\right] \tag{4.9}$$

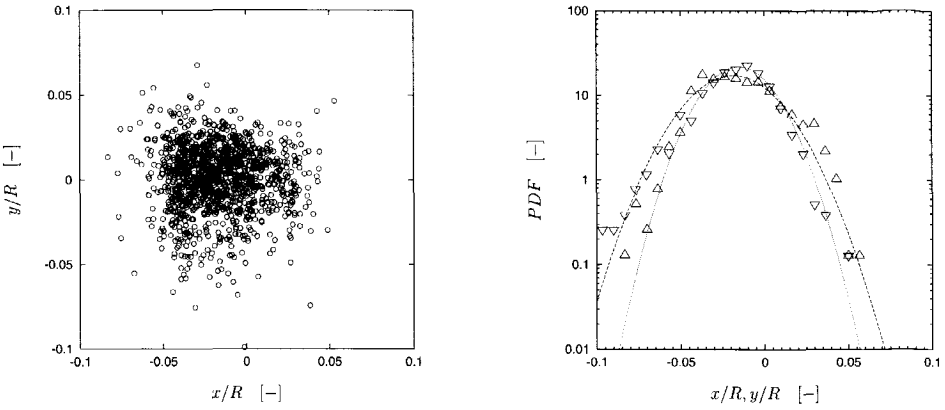

FIGURE 4.15: *(a) Scatter plot of the position of the processing vortex core centre as derived from the visualisation experiment. (b) Corresponding probability density function of the x-coordinate (△) and the y-coordinate (▽), and Gaussian fits (–) and (- -), respectively.*

where $p(x, y) = p(x)p(y)$, and $p(x)$ and $p(y)$ are 1-dimensional probability density functions. The mean position of the vortex origin (μ_x, μ_y) and the variances (σ_x^2, σ_y^2) were estimated from a Gaussian fit of the 1D PDF's presented in Fig. 4.15b. The mean swirl centre position normalised with the vortex chamber radius was located at $(-0.018, -0.015)$ relative to the geometric centre. The normalised standard deviation σ_x and σ_y was equal to 0.023 and 0.018, respectively.

The strategy of Volkert et al. (1996) to estimate the velocity fluctuations due to the PVC is to first describe the mean velocity field around the measurement point, and then to use the 2D PDF of Eq. 4.9 to 'sample' this field. Similar to the PVC model described in Section 4.2, it is assumed that the shape of the instantaneous velocity profile is only weakly affected by boundary conditions and pressure effects. The phase-resolved mean velocity presented in Fig. 4.11 showed that this assumption is questionable, because the radial displacement of the vortex centre affects the velocity profile in particular near the core edge. However, it seems reasonable to assume that a considerable contribution to the velocity fluctuations is due to the combined effect of PVC motion and mean velocity gradient.

This effect is estimated as follows. The swirl centre probability function is traversed along the traversing axis of the LDA measuring volume, while the mean velocity profile moves about the measurement point accordingly. The probability function of the PVC motion with respect to the position of the measuring volume, (x_0, y_0), is now given by:

$$P_W(x', y', x_0, y_0) = \frac{1}{2\pi\sigma_x(x_0)\sigma_y(y_0)} \exp\left[-\frac{1}{2}\left(\frac{x'^2}{\sigma_x^2(x_0)} + \frac{y'^2}{\sigma_y^2(y_0)}\right)\right] \tag{4.10}$$

where the co-ordinates x' and y' are relative to the measurement position (x_0, y_0) (*i.e.* $x' = x - x_0$ and $y' = y - y_0$). Volkert et al. (1996) use a damping function for the standard

deviations to include wall effects (the values of σ_x and σ_y ultimately become zero at the wall). The measured variance of the fluctuating tangential velocity component due to the PVC motion can now be evaluated as:

$$\overline{w^2_{PVC}}(x_0, y_0) = \iint (W_y(x, y) - W(x_0, y_0))^2 P_W(x', y', x_0, y_0) dx dy \tag{4.11}$$

where W_y is the tangential velocity component projected on the y-axis, since this is the velocity component measured by the LDA. The integral of Eq. 4.11 can be estimated using a 2D extended trapezoidal rule or a similar numerical integration technique. For this purpose, the measured mean velocity profile is first approximated by an analytical expression.

4.4.3 Results and discussion

The PDF methodology of Volkert et al. (1996) was applied to the LDA measurements obtained at $z/D = 3.0$. First, the mean tangential velocity profile needs to be described analytically. An obvious candidate is the Burgers' vortex (Eq. 4.1). It is known, however, that a vortex exponent equal to 1.0 does not accurately describe the outer region of the cyclone's vortex. The Burgers' vortex was modified as follows:

$$W(r) = \frac{\Gamma}{2\pi r^n} \left[1 - e^{-\beta r^{1+n}}\right] \tag{4.12}$$

where n is the vortex exponent. For large radial distances, Eq. 4.12 approaches $(\Gamma/2\pi)r^{-n}$. The vortex exponent is also included in the exponential part of Eq. 4.12 to ensure a linear decay of the velocity near the axis of symmetry; the fraction $\Gamma\beta(1+n)/(2\pi)$ represents the angular velocity of the vortex core. The measured radial distribution of the mean tangential velocity component at $z/D = 3.0$ is shown in Fig. 4.16a together with a three parameter fit of Eq. 4.12. Because of the small deviation from axi-symmetry, the velocity profile was re-normalised with respect to the cyclone radius, and the time-averaged position of the swirl centre was traversed to the geometric centre.

The analytical expression for the mean tangential velocity component, and the x- and y-variances of the swirl centre PDF (Eq. 4.9) derived from the visualisation experiment were used to estimate the rms velocity as a result of vortex precession. For the numerical integration of Eq. 4.11 the limits were fixed at $\pm 3\sigma_x$ and $\pm 3\sigma_y$. The solution was not significantly affected by choosing larger integration limits. The result is shown in Fig. 4.16b. Volkert et al. (1996) investigated two different damping functions for the standard deviation used in Eq. 4.10, *viz.* a linear and a polynomial decay function. In this study, a linear damping function was used.

Inspection of Figs. 4.16b and 4.3 shows that the results obtained by use of the PDF method described in this section and the analytical PVC model of Sec. 4.2 are similar. Both models predict a large contribution of the PVC motion to the tangential velocity fluctuations in the vortex core, a local minimum at the edge of the core region, and a decaying effect while proceeding towards the wall. For most of the cyclone radius, the mean tangential velocity exhibits a higher local mean velocity gradient than the axial velocity component, which results in a larger contribution of the PVC to the rms velocity. The local minimum in the rms velocity

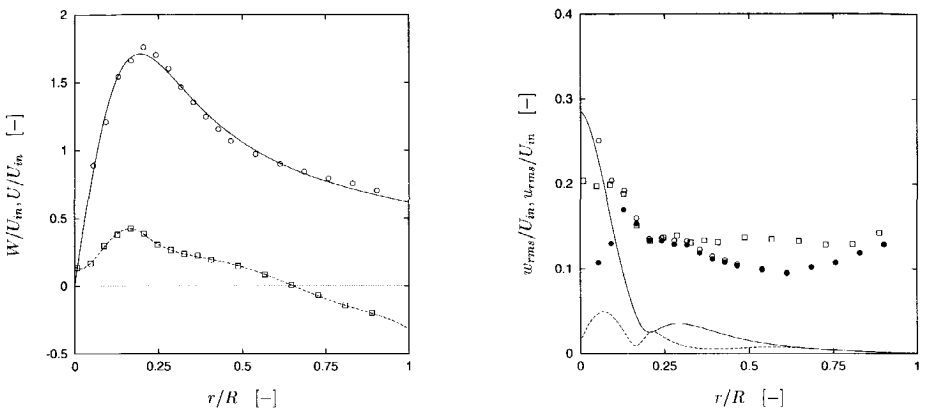

FIGURE 4.16: *(a) Radial profile of the mean tangential (○) and axial (□) velocity at $z/D = 3.0$. The tangential velocity profile was fitted to a modified Burgers' vortex (see Eq. 4.12), where $\Gamma/(2\pi) = 0.62\,s^{-1}$, $\beta = 27.2\,m^{-2}$, and $n = 0.79$. A polynomial fit was used for the axial velocity distribution. (b) Radial distribution of the rms velocity and the contribution of the PVC to the tangential (–) and axial (- -) rms velocity as obtained by Eq. 4.11. The 'corrected' rms velocity for the tangential component is represented by (●).*

corresponds to the maximum velocity at the edge of the vortex core present in the radial profile of both velocity components (see Fig. 4.16a). The local minimum in the mean axial velocity at the cyclone centreline results in a reduced contribution of the PVC to the rms velocity at this position.

The corrected rms velocity is now estimated by subtracting the variances of the LDA signal and the PVC contribution obtained with the PDF approach. In Fig. 4.16b the radial profile of the corrected tangential rms velocity is presented. For the axial rms velocity the original and corrected profiles did not significantly differ.

For the tangential rms velocity near the centreline, approximately 80% of the signal variance can be attributed to the PVC. At the edge of the vortex core, the corrected rms velocity profile reaches a maximum value. This is explained by the model assumption that was used in the PDF approach, *i.e.* the mean velocity field is not affected by the precession (Volkert et al., 1996). The phase-resolved velocity profiles obtained with adaptive noise cancellation, however, demonstrated that the vortex is modified by the radial displacement of the swirl centre in particular at the edge of the core region as is shown in Fig. 4.11. With respect to the axial component, the phase resolved velocity profiles showed that, especially in the vortex core, the PVC considerably affects the mean axial velocity profile. This could explain for the small contribution of the PVC to the signal variance as predicted by the PDF approach.

In general, the results of the PDF approach provide a rather crude estimate of the signal variance due to vortex precession. According to the model, the outer region of the vortex is

hardly affected by the PVC, whereas the results presented in Sec. 4.3 clearly prove otherwise. For the axial velocity component, the PDF approach fails to predict the expected contribution of the PVC to the signal variance. The study of Volkert et al. (1996) and Grosjean et al. (1997) showed that the model is quite sensitive to the value of σ_x and σ_y assigned to the PDF of the swirl centre.

4.5 Comparison of experiment and simulation

The conventional modelling approach to cyclone flow simulation is based on solving the steady-state, Reynolds averaged Navier-Stokes (RANS) equations in combination with a closure model for the Reynolds stresses. This approach was also chosen for the main part of the computations presented in this thesis (see Ch. 5 and 7). In contrast to RANS modelling, a large eddy simulation (LES) is capable of explicitly resolving the time and length scales associated with the PVC. Since a large eddy simulation requires a three-dimensional, time dependent numerical framework, its demands are considerable in terms of computer memory and processor speed. Hence, large eddy simulations of industrial applications such as the cyclone separator are still rarely reported in the literature.

Recently, Derksen and Van den Akker (1999) simulated the turbulent flow in a stirred tank reactor by means of a LES with lattice-Boltzmann discretisation. They were capable of predicting the coherent non-turbulent flow structure attached to the impeller blades known as the trailing vortex. The same modelling approach was used for the simulation of the flow in the vortex chamber studied experimentally in the previous section (Derksen and Van den Akker (2000) and Hoekstra et al. (1999c)). The LES prediction is assessed in Sec. 5.3.5, where the mean and rms velocity distributions are compared to LDA measurements. Some results on the unsteady flow characteristics of the vortex flow are discussed here; they are compared to the experimental results on the precessing vortex core presented in Sec. 4.4.

Both the artificial time series derived from the analytical PVC model shown in Figure 4.4, and the measured LDA time series presented in Figure 4.5, demonstrate the sinusoidal contribution of the PVC motion to the velocity signal. This effect is also predicted by the LES as is shown by the *simulated* velocity signal of Figure 4.17a. The LES time series was recorded at the geometrical centre. It is shown that the velocity signal consists of a superposition of turbulent velocity fluctuations onto a periodic low-frequency component. The corresponding power spectral density function shown in Figure 4.17b, exhibits a distinct peak at $f_{PVC} = 12$Hz, which is close to the experimentally observed frequency of 11 Hz (see Sec. 4.3).

The amplitude of the velocity trace shown in Fig. 4.17a appears to vary with time, which is supported by the experimental observation that the vortex centre is not rotating at a fixed radius. In Fig. 4.18, the trajectory of the vortex core centre is presented in the x, y-plane at $z/D = 2.0$. The origin of the vortex centre is associated with the minimum static pressure in the axial plane, and a line joins the consecutive positions. The probability density function of the swirl centre projected on the x- and y-axis is shown in the same figure. Both figures show resemblance to the experimentally obtained PDF's presented in Fig. 4.15b, although the vortex core appears to avoid the geometrical centre in the simulation.

At this axial position, both PDF's have a time-averaged vortex origin close to the geometric centre, and a standard deviation of $0.070R$ and $0.068R$, respectively. It is shown in Fig. 4.19a

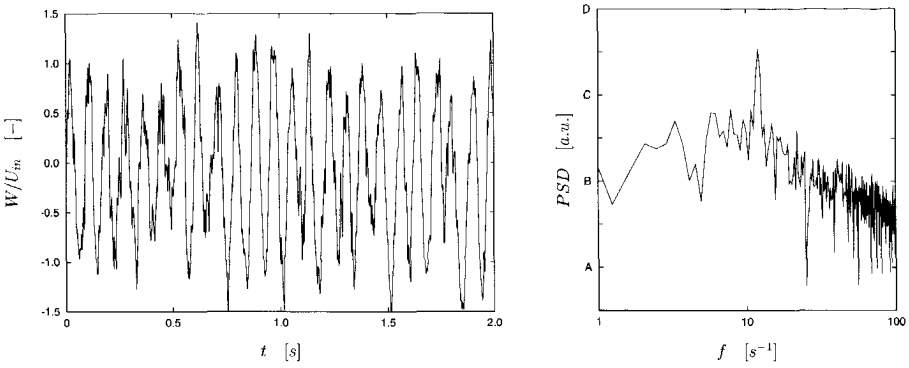

(a) (b)

FIGURE 4.17: *(a) Time series of the velocity component in the $z-$ direction at $x/D = 1.89, y = 0, z = 0$. (b) Corresponding power spectral estimate.*

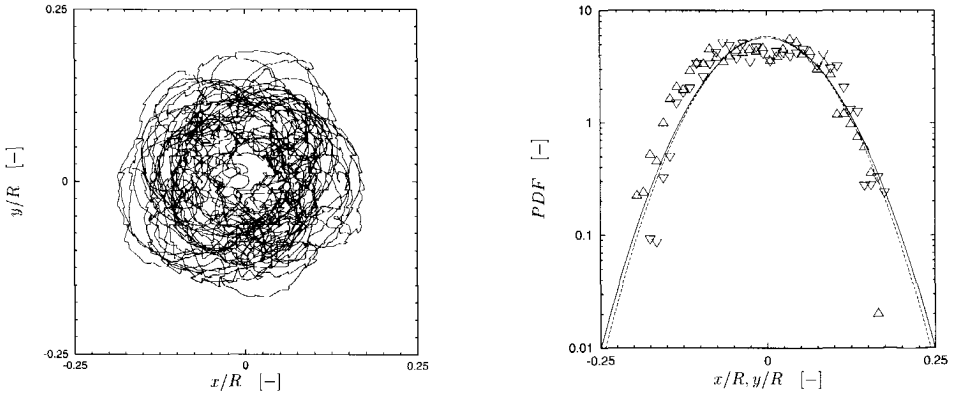

(a) (b)

FIGURE 4.18: *(a) Position of the vortex core origin at $z/D = 2.0$ during a time interval of $80D/U_{in}$. (b) Corresponding probability density functions of the ($\triangle$) x- and ($\triangledown$) y-projected vortex centre co-ordinates with Gaussian fits (-) and (- -), respectively.*

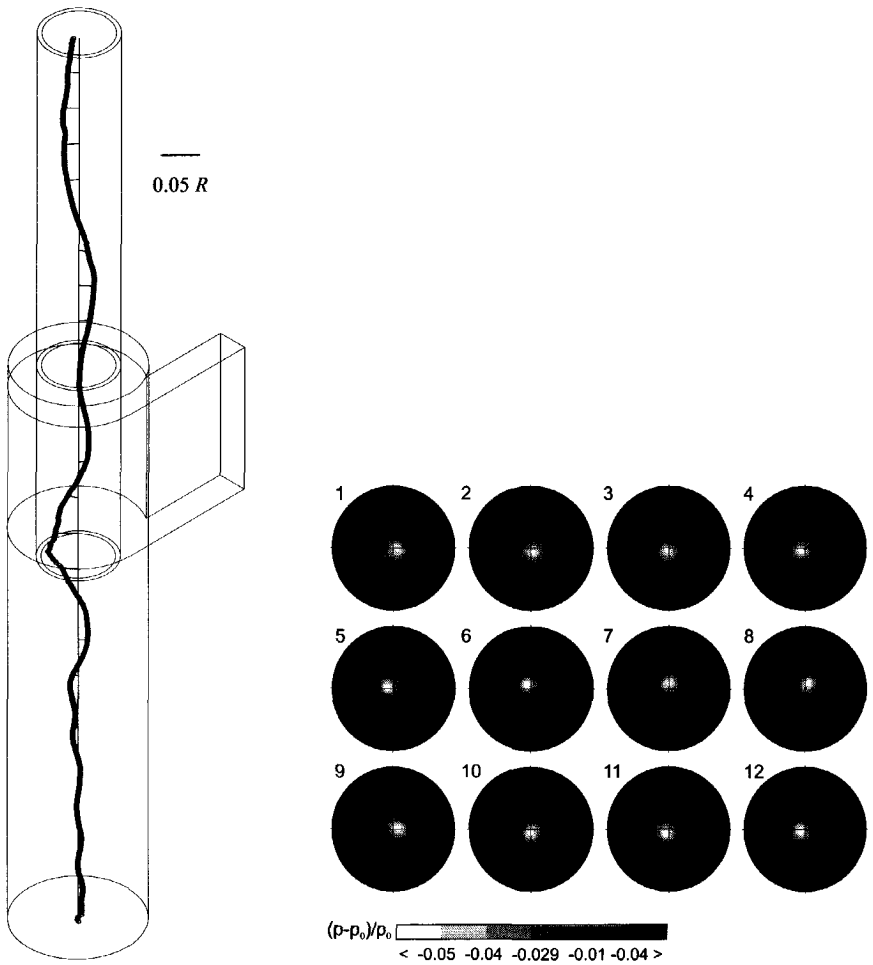

(a) (b)

FIGURE 4.19: *(a) Time-averaged position of the vortex core origin along the geometric centreline of the vortex chamber. Radial position of core centre and geometry not to scale. (b) Twelve realisations of the pressure field in a horizontal plane at $z/D = 2.0$. The time separation between the subsequent images is $0.19D/U_{in}$, which corresponds to approximately one tenth of the average PVC period.*

that the time-averaged position of the swirl centre depends on the axial location. In the lower part of the vortex chamber the time-averaged position of the vortex hardly deviates from the geometric centreline. Near the entrance of the exit pipe, the eccentricity of the vortex origin reaches its maximum at $\overline{r}_{PVC} = 0.03R$. This could be caused by the vicinity of the tangential inlet, since this region is associated with the a geometrically imposed axi-asymmetry. The spiral shape of the vortex core and its eccentricity become more pronounced in the exit pipe outside the vortex chamber.

The standard deviation of the swirl centre PDF varies along the cyclone axis in a similar way as the time-averaged position, with a maximum value found near the vortex finder entrance. The x- and y-projected standard deviations were mutually equal at all axial locations, hence there was no directional preference of the PVC (Derksen and Van den Akker, 2000). At $z/D = 3.15D$ the probability distribution of the swirl centre was estimated from the visualisation experiment (see Sec. 4.4). The LES predicted a σ_{PVC} equal to $0.031R$, which is only slightly larger than the experimentally found values of $\sigma_{x,PVC} = 0.024R$ and $\sigma_{y,PVC} = 0.018R$.

The precessing vortex core can be visualised by using the simulated pressure field. In Fig. 4.19b, a sequence of computed contour plots of the static pressure is presented for an axial plane approximately halfway the vortex chamber. The vortex core centre can be associated with the point of least pressure, and is clearly rotating about the geometric centre. Furthermore, in the contour plots two clearly different flow regions can be distinguished: the inner forced vortex region, and the outer free-vortex region. The outer region exhibits large-scale turbulent structures that are formed from time to time in a seemingly erratic manner. The inner region behaves much more deterministically: the shape of the contour lines changes gradually.

This observation is consistent with the Rayleigh criterion, described in Ch. 2. The forced vortex region is *stable* to non-axisymmetric disturbances caused by the PVC, whereas the vortex in the outer region, where $W \sim 1/r^n$, is *unstable*. Experimental evidence for this phenomenon can be found in the study of Fokke et al. (1994a). They demonstrated in a joint LDA and LIF study of the flow in a hydrocyclone that turbulent mixing in the radial direction is almost absent in the vortex core, whereas it is very strong in the free vortex.

4.6 Closure

Several approaches have been discussed that deal with the issue of the precessing vortex core in cyclone flow and its effect on LDA velocity measurements. It was argued that the vortex precession hampers the interpretation of LDA measurement results, because it affects the flow field and contributes to the signal variance. It was shown that this effect is especially significant in the vortex core region of the flow.

The adaptive signal processing of LDA time series was used to estimate the periodical interference in the LDA signal, and to obtain filtered velocity samples. Due to its adaptive nature, the filter is capable of capturing the irregular spatial characteristics of the PVC. A disadvantage of the technique compared to an external triggering method is that the exact position or phase of the PVC is not known *a priori*, which complicates the reconstruction of phase-resolved velocity profiles. The application of adaptive filtering was illustrated for one particular velocity profile in the separation zone of a swirl tube separator. For the Stairmand geometries studied, the technique proved to be less suitable.

The experimental study on the motion of the vortex core in a laboratory scale cyclone confirmed the spatial irregularity of the PVC. Hence, the position of the PVC origin is described more realistically by means of a 2D probability density function than by defining a constant PVC amplitude. It was shown that the PDF could be used to estimate the contribution of the PVC to the signal variance. Since the PDF needs experimental input on the distribution of the swirl centre, the PVC contribution to the signal variance is not readily estimated in case of industrial sized cyclones.

CHAPTER 5

MODELLING AND SIMULATION OF THE GAS FLOW FIELD

In this chapter, results are presented on the modelling and simulation of the gas flow field in a cyclone separator. First, the numerical framework is discussed that was used to solve the Reynolds averaged Navier-Stokes (RANS) equations, and the associated turbulence closure model. Next, Laser-Doppler measurements presented earlier (see Ch. 3) were used for the assessment of cyclone predictions of three different turbulence models. The effect of the inlet section on the flow field was studied by means of a three-dimensional simulation of the Stairmand cyclone. Finally, results are presented on the flow field of a laboratory scale vortex chamber. The predictions of a Large Eddy Simulation and a RANS simulation are compared both mutually and to Laser-Doppler measurements.

5.1 INTRODUCTION

Swirling flows have been subject to extensive numerical and experimental study because of their industrial relevance. Some practical examples are the swirl-stabilised combustion in furnaces and engines, exit-chambers for axial-flow turbo-machinery, and the pneumatic convection of gas through pipes. The swirl in these applications is either induced by rotation or imparted on the flow by a swirl generator. In addition, the flow is turbulent, and the interaction between swirling motion and turbulent transport is generally considered complex (Sloan et al., 1986).

The cyclone separator flow field exhibits flow features that have also been observed for other swirl flow applications, *e.g.* strong streamline curvature and anisotropy of the Reynolds stresses. Although several modelling efforts have been dealt with in the literature (see Sec. 2.4), a generic assessment of CFD models for cyclone flow is hampered by the lack of quantitative experimental data on the distribution of mean and fluctuating quantities. However, a considerable experimental data set on the cyclone flow field was collected during the course of this project (see Ch. 3). These data are used to assess the numerical models and calculation results presented in this chapter.

5.2 Theory

The literature review on CFD modelling of cyclone separators (Sec. 2.4) revealed that the modelling approach for cyclones operating at low solids loading is generally based on an Eulerian-Lagrangian formulation. The gas flow field is approximated by using the continuity equation and the Reynolds averaged Navier-Stokes (RANS) equations, which need an additional turbulence closure model, whereas the motion of particles is treated by calculating their individual trajectories. In this section, the 2D computation of the gas flow field is addressed using the RANS approach.

5.2.1 Modelling framework

The conventional way of modelling strongly swirling flow in cyclones is to assume incompressible, steady, and axisymmetric flow. These assumptions facilitate the mathematical formulation of the problem by simplifying ($\partial/\partial\theta = 0$) the continuity equation and the averaged Navier-Stokes equations for transport of momentum (Eq. 2.8), which may be written in cylindrical coordinates as:

$$\frac{\partial}{\partial x}U + \frac{1}{r}\frac{\partial}{\partial r}rV = 0 \tag{5.1}$$

$$\rho\left(U\frac{\partial}{\partial x}U + V\frac{\partial}{\partial r}U\right) = -\frac{\partial}{\partial x}P + \frac{\partial}{\partial x}\tau_{xx} + +\frac{1}{r}\frac{\partial}{\partial r}r\tau_{xr} \tag{5.2}$$

$$\rho\left(U\frac{\partial}{\partial x}V + V\frac{\partial}{\partial r}V - \frac{W^2}{r}\right) = -\frac{\partial}{\partial r}P + \frac{\partial}{\partial x}\tau_{xr} + +\frac{1}{r}\frac{\partial}{\partial r}r\tau_{rr} - \frac{\tau_{\theta\theta}}{r} \tag{5.3}$$

$$\rho\left(U\frac{\partial}{\partial x}W + V\frac{\partial}{\partial r}W + \frac{VW}{r}\right) = \frac{\partial}{\partial x}\tau_{x\theta} + \frac{1}{r^2}\frac{\partial}{\partial r}r^2\tau_{r\theta} \tag{5.4}$$

where the velocity components (U, V, W) are ensemble averaged through Reynolds decomposition, and the stress terms τ_{ij} are the sum of viscous and turbulent (Reynolds) stresses. The presence of the Reynolds stresses in the momentum equations means that the latter are not closed, *i.e.* they contain more variables than there are equations. Closure requires some approximations, which usually take the form of prescribing the Reynolds stress tensor in terms of the mean quantities. The approximations introduced are called turbulence models.

Turbulence models commonly applied to industrial applications are based on the concept of a turbulent or eddy viscosity, a well-known example being the $k-\varepsilon$ model. The $k-\varepsilon$ model is a two-equation model, since two additional transport equations are solved that relate the turbulent kinetic energy, k, and its dissipation, ε, to the mean quantities. The turbulent viscosity is obtained by assuming that it is proportional to the product of a turbulent velocity scale and a length scale. Defining these scales by $k^{1/2}$ and $k^{3/2}/\varepsilon$, respectively, the eddy viscosity is expressed as:

$$\mu_t = \rho_g C_\mu \frac{k^2}{\varepsilon} \tag{5.5}$$

where $C_\mu = 0.09$. The $k-\varepsilon$ model contains four additional parameters; the most commonly used values are $C_{\varepsilon_1} = 1.44$, $C_{\varepsilon_2} = 1.92$, $\sigma_k = 1.0$, and $\sigma_\varepsilon = 1.3$ (Ferziger and Perić, 1996).

The model equations of the Renormalisation Group (RNG) $k-\varepsilon$ model are quite similar to the standard $k-\varepsilon$ model, except for the values of the model constants. The RNG approach yields a model for the turbulent viscosity that varies with the effective Reynolds number or eddy scale, and, hence, can deal with low-Reynolds number and near-wall flows. The effects of swirl or rotation are accounted for by modifying the constant C_μ using a characteristic swirl number (Fluent Inc., 1996).

The eddy-viscosity approach presumes a linear relationship between the Reynolds stresses and the mean velocity gradients (Boussinesq hypothesis), which may be inappropriate for complex flows. A way to avoid this deficiency is to solve the transport equations for the individual Reynolds stresses. These transport equations can be derived from the momentum equations and contain triple order velocity correlations and pressure-velocity correlations that must be modelled to obtain closure. This approach is known as the Reynolds Stress Transport Model (RSTM).

In symbolic form, the equation describing the transport of the Reynolds stress may be written as

$$\frac{\partial \overline{u_i u_j}}{\partial t} + U_k \frac{\partial \overline{u_i u_j}}{\partial x_k} = D_{ij} + P_{ij} + \Phi_{ij} - \varepsilon_{ij} \tag{5.6}$$

The term D_{ij} represents the diffusive transport term, which is usually modelled by means of the generalised gradient diffusion hypothesis proposed by Daly and Harlow (1970). A simplified form of this model is obtained by assuming isotropic stress diffusion, which has been found to yield better agreement with experimental data (Lien and Leschziner, 1993). The generation of stress, P_{ij}, only involves mean velocity gradients and Reynolds stresses, and thus is exactly determinable at second-moment level. This is the main reason that second moment closure is considered a *more generic approach than eddy-viscosity models.*

The modelling of the pressure-strain correlation Φ_{ij}, is considered of decisive importance for determination of the Reynolds stresses from their transport equations Launder (1991); Hadzić (1999). The pressure-strain term is usually modelled as a linear combination of three parts, *e.g.* a turbulence-turbulence interaction or slow term, Φ^1_{ij}, a turbulence-mean flow interaction or rapid term, Φ^2_{ij}, and a surface contribution or wall-reflection term, Φ^w_{ij}. The approach towards Φ^1_{ij} is to adopt Rotta's return-to-isotropy model, where its magnitude is proportional to the local level of anisotropy. The term Φ^2_{ij} can be modelled in a similar way: where Rotta's term acts to diminish the anisotropy of the stress field, this term tends to isotropise the turbulence production tensor (Launder et al., 1975).

The wall-reflection term, Φ^w_{ij}, in the model for the pressure strain correlation is included to account for the highly inhomogeneous flow in the near-wall region of wall-bounded flows. The most common practice is to decompose the wall reflection term into a slow and a rapid contribution, which are both inversely proportional to the wall distance normal to the wall (Gibson and Launder, 1978). In this way the Reynolds stress component normal to the wall is effectively damped.

The dissipative eddies are usually assumed to be isotropic, $\varepsilon_{ij} = \frac{2}{3}\delta_{ij}\varepsilon$. The energy dissipation rate is then found from the same transport equation used in the $k-\varepsilon$ eddy-viscosity model. The model formulation discussed here is also known as the basic RSM or LRRG-model (see for a survey of advanced second moment closure, *e.g.* , Hanjalić (1994)).

A gas cyclone operating at industrial conditions is usually characterised by a high Reynolds number, and consequently a large number of computational points have to be used to resolve the turbulent boundary layer. This problem can be avoided by using the wall function approach, where the viscosity affected near-wall region is not resolved. Instead, wall functions are used to 'bridge' the viscosity-affected region between the wall and the fully-turbulent region. The velocity profile in the logarithmic region of the turbulent boundary layer, or inertial sublayer, is described by the law-of-the-wall:

$$u^+ = \frac{\overline{v}_t}{u_\tau} = \frac{1}{\kappa} \ln y^+ + B \tag{5.7}$$

where $\overline{v}_t$ is the mean velocity parallel to the wall, u_τ is the shear velocity, $u_\tau = \sqrt{\tau_w/\rho}$, τ_w is the shear stress at the wall, κ is the so-called von Karman constant, B is an empirical constant related to the thickness of the viscous sublayer and y^+ is the dimensionless distance to the wall ($y^+ = yu_\tau/\nu$). The inertial sublayer is known to be valid if $y^+ > 30$.

Close to the wall the velocity fluctuations do not contribute much to the total stress because of the dominating effect of the viscosity (Tennekes and Lumley, 1972). This region is called the viscous sublayer, where the velocity profile is linear ($u^+ = y^+$) up to about $y^+ = 5$. In between the viscous and inertial sublayers both the viscous and Reynolds stresses are important. In CFD calculations this buffer layer is usually disposed of by linking the velocity profiles of the viscous and inertial sublayers at their intersection ($y^+ \approx 11$). The turbulent quantities at the wall-adjacent control volume are computed by balancing turbulent production and dissipation on the basis of a local equilibrium hypothesis.

5.2.2 Flow solver and numerical aspects

The RANS simulations presented in this chapter were done by use of the finite volume flow solver Fluent v.4.4 (Fluent Inc., 1996). This general purpose CFD solver employs a non-orthogonal, body-fitted mesh for the discretisation of the transport equations. The meshing flexibility was limited due to the structured, one-block approach, which did not permit local grid refinement. The grid generator Gcomesh was used for meshing the flow domain and defining the boundary conditions. The implementation of the Reynolds stress transport model in Fluent v.4.4 was verified by means of a swirling flow benchmark case from the literature. The quality of the simulations was assessed by studying grid dependency, numerical accuracy, and the influence of boundary conditions. These issues will be treated accordingly.

A recent study on rotating and swirling flow was done by Jakirlić (1997) to assess the performance of several eddy viscosity and second moment closure models. Three test cases were chosen that have been well-reported in the literature both experimentally and numerically, *viz.* axially rotating pipe flow, annular swirling flow in a combustion chamber, and the decay of swirl in long pipes. All three cases illustrate certain aspects of swirling flow that are related to turbulence and swirl intensity as well as geometrical complexity. The swirling flow in a combustion chamber is treated here, because it exhibits a strong similarity to cyclone flow due to its high Reynolds and Swirl numbers. The flow geometry consists of a uniform-diameter chamber, in which a confined strongly swirling outer flow is directed together with a small central non-swirling jet. So et al. (1985) measured the tangential and axial velocity components

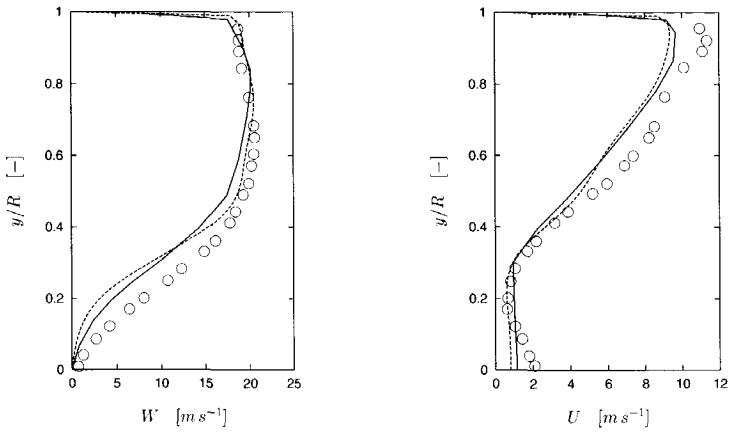

FIGURE 5.1: *Confined swirling flow in a combustion chamber: radial distribution at $x/d = 10$ of the (a) tangential and (b) axial velocity component. Measurements (○) and calculations according to Hogg and Leschziner (1989) (–) and Fluent v.4.4 (- -)*

at several downstream positions by means of Laser-Doppler Anemometry. Hogg and Leschziner (1989), Jones and Pascau (1989), and Wong and Sharif (1995) studied this case numerically to assess the performance of several closure models, *e.g.* versions of the $k-\varepsilon$ model, the algebraic stress model and the Reynolds stress model.

Benchmark study

The numerical study of Hogg and Leschziner (1989) was used to verify the code implementation of the Reynolds stress transport model in Fluent v.4.4, because the authors discuss the numerical accuracy and boundary conditions in great detail. The model equations and empirical constants used in Fluent v.4.4 and the code of Hogg and Leschziner (1989) are identical, except for the Daly & Harlow approximation of the diffusive transport term used by the latter. The inlet flow conditions were imposed by interpolation of measurement data available at $x/d = 1$, where x represents the downstream direction and d the diameter of the central non-swirling jet. Other properties, of which no experimental data were available, were estimated or assumed. Hogg and Leschziner (1989) demonstrated that a grid-independent solution could be obtained at a mesh of 48×48 non-uniformly distributed grid nodes. The convective fluxes were approximated by the quadratic upstream-weighted scheme (QUICK). The same approach was applied in the Fluent simulation.

In Fig. 5.1, the radial profiles of the mean tangential and axial velocity components are shown for a characteristic downstream position ($x/d = 10$). The velocity profiles predicted by Fluent and the code of Hogg and Leschziner (1989) are quite similar, and they correspond reasonably well with the LDA data. The Reynolds stress model clearly mimics the existence

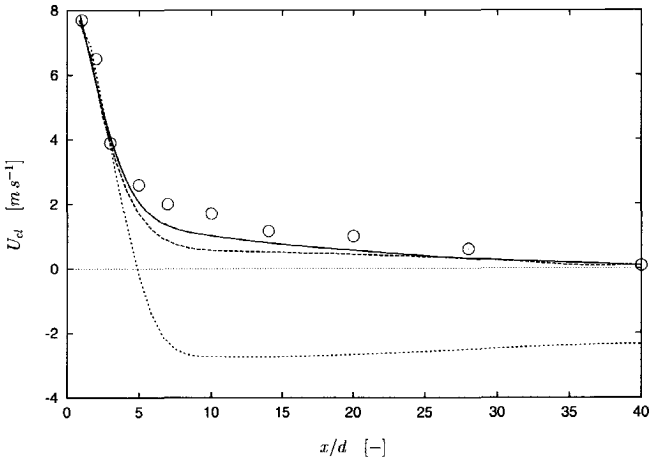

FIGURE 5.2: *Decay of centreline velocity: measurements (o) and calculations according to Hogg and Leschziner (1989) ( ), Fluent v.4.4 with fixed axial velocity profile at the exit plane (- -) and with zero gradient boundary condition (...).*

of two rotational regimes, *i.e.* a forced and free vortex type of swirl distribution in the inner and outer regions, respectively. In contrast, eddy viscosity based models are generally not capable of predicting a combined vortex. The measured and predicted tangential velocity profiles deviate most significantly near the centreline, where the simulation predicts a stronger effect of the central non-swirling jet on the downstream swirl distribution than was observed experimentally.

A characteristic flow feature is the rapid decay of the mean axial velocity at the centreline due to diffusion of the central jet. This is shown in Fig. 5.2. Hogg and Leschziner (1989) pointed out that the flow is likely to be subcritical in spite of the absence of flow reversal. A vortex flow is defined as subcritical if it can support or guide, upstream (and downstream) propagation of waves, even though the source of wave energy is substantially removed from the region of interest (Sloan et al., 1986). Since it is not likely that the flow is fully established at $x/d = 40$, a zero gradient boundary condition for all quantities in the streamwise direction is likely inappropriate. This was avoided by prescribing the mean axial velocity profile at the exit plane explicitly using the experimental data. The decay of the centreline velocity was predicted by both calculations as is shown in Fig. 5.2. Using the zero gradient boundary condition at the outlet plane a reverse flow region is predicted near the centreline, which extends towards the exit.

Boundary conditions

The proper application of boundary conditions is also relevant for the simulation of cyclone flow. An obvious issue here is the conversion of the prevailing flow conditions at the cyclone inlet towards boundary conditions for the axisymmetric flow geometry. For the three-dimensional cyclone model a linear inlet velocity, U_{in}, is imposed normal to the cross sectional area of the

inlet duct. This is a natural way of defining the flux of angular momentum, $\dot{m}\,\mathbf{r} \times \mathbf{v}$, at the cyclone inlet.

For the axisymmetric cyclone model, the mean velocity components U, V, and W at the inlet are set as follows. The volumetric flow rate is imposed by defining the mean radial velocity directed inwards at the cyclone radius, V_R, along the inlet height, a, given by:

$$V_R = \frac{abU_{in}}{2\pi Ra} = \frac{b}{2\pi R}U_{in} \tag{5.8}$$

where b represents the inlet width (see Fig. 3.5a). The mean axial velocity component at the inlet is set equal to zero. The angular momentum is set by imposing a tangential velocity component at the cyclone radius equal to the linear inlet velocity ($W_R = U_{in}$) .

In general, the tangential inlet velocity is not equal to the linear inlet velocity, but is a function of the shape of the inlet configuration. This was discussed in more detail by Barth (1956) and Muschelknautz (1972) (see also Sec. 2.2). The tangential velocity component is estimated from the linear inlet velocity , the dimensions of the inlet section and the annulus, and a correction factor α (see Eq. 2.12).

The effect of the correction factor α on the velocity predictions was studied for all three Stairmand geometries. The magnitude of α was estimated using a correlation given by Bohnet (1984). For the standard Stairmand geometry, the predicted radial profiles of the mean tangential velocity were very similar, because the inlet tangential velocity is nearly equal to the linear inlet velocity ($\alpha = 0.82$). Clearly in this case no correction factor is needed. For the other cyclone geometries ($D_e/D = 0.30$ or 0.40) different velocity profiles were obtained depending on the inclusion of a correction factor. Compared to the LDA measurements, however, the use of a correction factor was not favourable (*cf.* results of Van der Velde (1996)). Unless stated differently the axisymmetric cyclone simulations presented in this chapter were performed without using a correction factor.

Another important modelling issue is the choice of outlet or downstream boundary conditions. The gas flow in the cyclone exit pipe exhibits similar flow characteristics as the benchmark flow case described earlier, in particular its subcritical behaviour. As a rule-of-thumb a vortex flow is likely to be subcritical if the ratio of maximum swirl velocity to mean axial velocity exceeds unity (Hogg and Leschziner, 1989); in case of cyclone flow, this ratio is at least 2. Hence, it is expected that a zero gradient boundary condition is also inappropriate as an outlet condition for cyclones (see Fig. 5.2). The suitability of the zero gradient boundary condition was assessed by modifying the length of the exit pipe outside the cyclone geometry. For the standard Stairmand cyclone it was seen that the length of the exit pipe did not affect the velocity profiles in the separation zone. Using a radial outflow condition at the exit pipe outlet also did not significantly affect the cyclone flow field. This suggests that the flow field in the cyclone itself is not very sensitive to the outlet conditions applied at the exit pipe outlet, as long as these boundary conditions are imposed at several cyclone diameters away from the domain of interest.

However, for the cyclones with $D_e/D = 0.40$ and $D_e/D = 0.30$ the experimental set-up exhibits an expansion of the exit pipe approximately 1.5 cyclone diameters downstream (see Fig. 3.4). This expansion does affect the upstream flow field due to the subcritical character of the flow, particularly the core region of the flow, *i.e.* the magnitude of the axial velocity deficit

and the maximum mean tangential velocity. Hence, the downstream exit pipe expansion was incorporated in the cyclone model.

Although no outlet boundary condition needs to be applied, the geometrical boundary at the lower side of the cyclone also affects the cyclone flow field. The inclusion of the particle collection hopper enables the vortex core to extend out of the cyclone body, which reduces the magnitude of the flow reversal in the core centre. Hoffmann et al. (1996) noticed that the inclusion of the dust collection system has a considerable effect on the flow pattern in the gas cyclone as well as the collection efficiency. This has serious implications for the number of grid cells employed, in particular in case of one-block flow solvers such as Fluent V4.4. Without the extended exit pipe and the collection bin the standard Stairmand cyclone takes only $\approx 3,300$ grid cells to model the geometry, whereas the full model needs $\approx 14,000$ grid cells and only 56% of these cells are functional. Grid dependency was studied by increasing the grid resolution in both directions; especially the radial node density affected the mean flow field. Beyond $\approx 14,000$ cells used for the model the solution did not benefit from a higher node density.

Since Fluent V4.4 applies an iterative procedure to solve the discretised conservation equations, convergence is usually assumed when the numerical error has decreased to a required value. For engineering accuracy a normalised discretisation error of 10^{-3} is considered acceptable. However, it was noted that most cyclone flow field predictions were not fully converged at this level for the grid sizes employed. Converged solutions were obtained at normalised error levels smaller than 10^{-4}.

In addition to the criterion for convergence the numerical accuracy is affected by the interpolation scheme. By default Fluent v4.4 approximates the convective fluxes by the power-law differencing scheme. However, this scheme is only first-order accurate and hence diffusive in the presence of flow-to-grid skewness (Hogg and Leschziner, 1989). A widely applied higher-order differencing scheme is the quadratic upstream-weighted scheme (QUICK), which is relatively stable, but is not bounded and therefore may lead to non-physical solutions. A bounded version of the QUICK-scheme is obtained by using a piecewise linear limiter function such as the UMIST flux-limiter (see *e.g.* Hadzić (1999) for a discussion of flux limiters). All final solutions were obtained by using this scheme.

The turbulence quantities were uniformly imposed at the inlet by using the following correlations (Fluent Inc., 1996):

$$k_{in} = \tfrac{3}{2}\left(I U_{in}\right)^2 \tag{5.9}$$

$$\varepsilon_{in} = C_\mu^{\frac{3}{4}} k_{in}^{\frac{3}{2}} / l_m \tag{5.10}$$

where the turbulence intensity, I, was taken 0.10, C_μ is an empirical constant equal to 0.09, and the characteristic turbulence length scale $l_m = 0.07\,b$. The computed value of k is used to estimate the Reynolds stresses at the inlet from the assumption of isotropic turbulence, *i.e.* the normal stresses are set to $2\,k/3$, and all shear stresses are zero. The solutions were hardly sensitive to the exact inlet values for k_{in} and ε_{in}.

5.3 RESULTS AND DISCUSSION

In this section, results are presented on the modelling and calculation of the gas flow field in cyclones. Laser-Doppler velocity measurements were used to assess the performance of several turbulence models for (modifications of) the Stairmand cyclone. The performance of turbulence models on the prediction of the gas flow field in the tangential swirl tube separator was discussed by Hoekstra et al. (1999b). The geometrical lay-out of the cyclones and the co-ordinate system were shown schematically in Fig. 3.5. The numerical results shown for industrial gas cyclones are based on steady-state modelling of the Reynolds averaged Navier-Stokes (RANS) equations; a comparison between RANS modelling and Large Eddy simulation (LES) is done for the flow field in a laboratory scale vortex chamber.

5.3.1 Tangential velocity

The radial swirl distribution in a cyclone separator is generally described by a combined vortex, where the centre of the flow known as the core region is dominated by a solid-body rotation and the outer region is of a free-vortex rotation type. From the investigation of several confined swirling flow applications, eddy viscosity models are known for their inability to predict the combined forced-free vortex motion (see *e.g.* Jones and Pascau (1989)). This also accounts for the swirl flow in a standard Stairmand cyclone as is shown in Fig. 5.3. In this figure, LDA measurements of the mean tangential velocity component are compared to three simulations using different turbulence closure models, *i.e.* the $k-\varepsilon$ model, the RNG-$k-\varepsilon$ model, and the Reynolds stress transport model (RSTM). Note that the calculated velocity profiles are symmetric with respect to the centreline. It is seen that only the Reynolds stress transport model is capable of predicting the combined vortex in accordance with the experimental data.

The $k-\varepsilon$ model predicts a solid-body type of rotation over the entire cyclone radius, which is related to the scalar nature of the eddy viscosity. Jakirlić (1997) explains this by simplifying the transport equation for the mean tangential velocity (Eq. 5.4) for the case of a fully developed axially rotating pipe flow ($\partial/\partial x = 0$, $\partial/\partial\theta = 0$, and $V = 0$). The reduced transport equation for the swirl velocity results in a solid-body rotation ($W \propto r$) for eddy viscosity models. This explanation could be applied to cyclone flow too, although cyclone flow can not be considered fully developed in the axial direction. The swirl modification of the eddy viscosity in case of the RNG-$k-\varepsilon$ model shows some improvement compared to the standard $k-\varepsilon$ model with respect to the existence of two vortex types. A disadvantage of the model is that this swirl dependency is modelled in a rather ad-hoc manner (see Fluent Inc. (1996)).

For the standard Stairmand cyclone the RSTM is well capable of predicting the combined vortex, although the predicted swirl velocity magnitude in the free-vortex region is slightly underestimated. However, the model deviates more significantly from the measurements for the two modified Stairmand geometries as is shown in Fig. 5.4. Due to the exit pipe contraction the vortex core is reduced in size and the magnitude of the maximum tangential velocity is increased. The Reynolds stress model also predicts this trend, but clearly the correspondence between the calculation and the experimental data is limited to the outer flow region. In the same figure, a second calculation of the mean tangential velocity is presented, which shows a much closer overall agreement to the measurements. In this case, the Reynolds stress transport model was modified by disregarding the wall-reflection term in the model for the pressure-strain

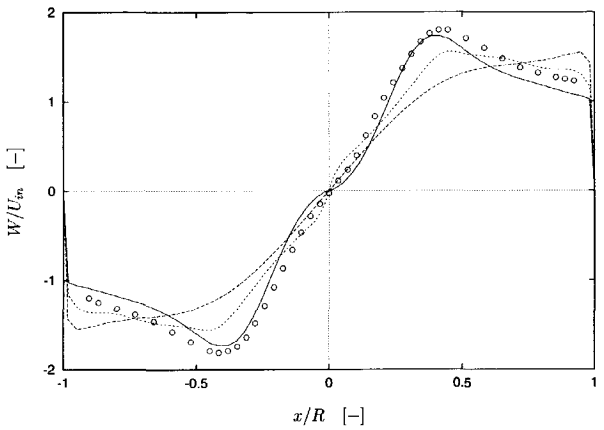

FIGURE 5.3: *Radial profile of the mean tangential velocity for the Stairmand cyclone at $z/D = 0.75$. Comparison of measurements and model predictions: (o) LDA measurements, (–) Reynolds stress transport model with wall-reflection term, (- -) $k-\varepsilon$ model, and (...) RNG $k\varepsilon$ model.*

correlation (see Sec. 5.2.1).

Although the need for the wall-reflection term can be justified by the exact equation for the pressure-strain interaction, the damping of the Reynolds stress component normal to the wall was originally done by tuning the complete model for Φ_{ij} to satisfy experimental data. Hadzić (1999) compared the Reynolds stress transport model with and without wall-reflection term to DNS data for fully developed channel flow. It was shown that the RSTM without wall-reflection term does not predict sufficient anisotropy of the Reynolds stress, particularly close to the wall. By including the wall-reflection term in the model the near-wall stress distribution is predicted much better, however, the level of Reynolds stress anisotropy away from the wall is too high. This comparison shows that the effect of the wall-reflection term on the Reynolds stress tensor is not limited to the near-wall region. Clearly, in case of cyclones the mean tangential velocity distribution is affected significantly by the wall-reflection term. We will elaborate more on this in Sec. 5.3.4, where the distribution of the Reynolds stresses is discussed.

The radial distribution of the mean tangential velocity exhibits a strong similarity along the axial co-ordinate as is shown in Fig. 5.5 for the Stairmand cyclone separator. The size of the vortex core is approximately equal at all axial measurement stations, which implies that the free-vortex region of the flow is reduced in the conical part of the cyclone. As a result the wall circumferential velocity is not reduced due to wall friction, but the velocity magnitude is increased due to the reduction of the cross sectional area of the cyclone. This is advantageous, because particles are transported by the wall boundary layer towards the cyclone base, and the conical section reduces the probability of getting them dispersed into the flow field again. For the standard Stairmand geometry, a disadvantage of the cone is that the size of the particle outlet at the base is smaller than the vortex core diameter. Hence, the edge of the vortex core with its high tangential velocities will reach the cyclone wall. This could enhance the entrainment of particles from the boundary layer into the vortex core.

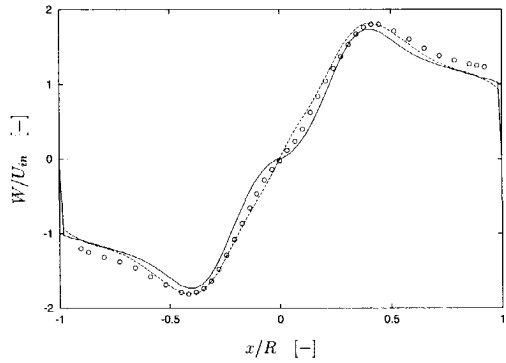

(a)

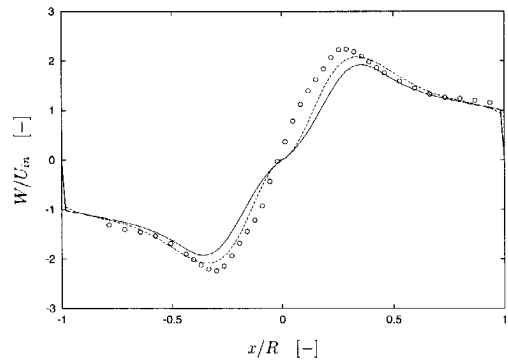

(b)

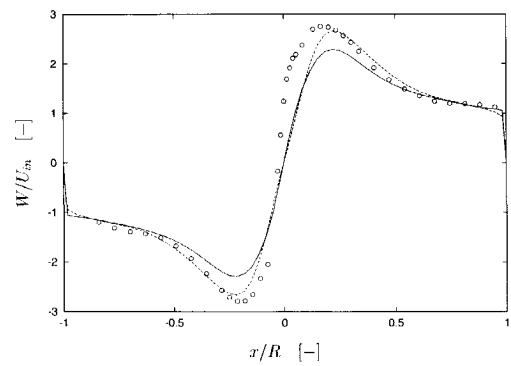

(c)

FIGURE 5.4: *Radial profile of the mean tangential velocity at $z/D = 0.75$ for the Stairmand cyclone with D_e/D equal to (a) 0.50, (b) 0.40, and (c) 0.30. LDA measurements (○), (–) RSTM with wall-reflection term, and (- -) RSTM without wall-reflection term.*

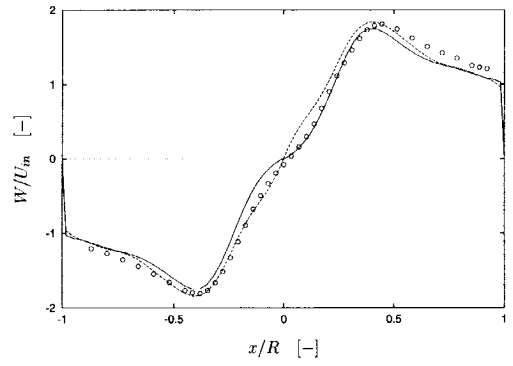

(a)

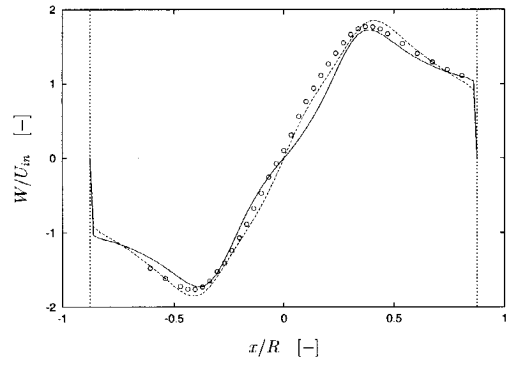

(b)

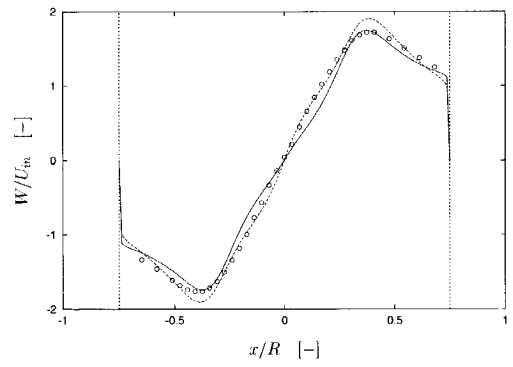

(c)

FIGURE 5.5: *Radial profile of the mean tangential velocity at (a) $z/D = 0.625$, (b) 2.0, and (c) 2.5 for the standard Stairmand cyclone. LDA measurements (○), ( ) RSTM with wall-reflection term, and (- -) RSTM without wall-reflection term.*

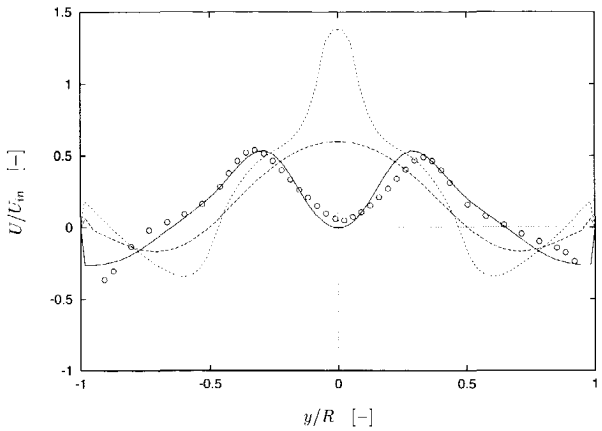

FIGURE 5.6: *Radial profile of the mean axial velocity for the standard Stairmand cyclone at* $z/D = 0.75$. *Comparison of measurements and model predictions: (○) LDA measurements, (–) Reynolds stress transport model with wall-reflection term, (- -) $k-\varepsilon$ model, and (...) RNG $k\varepsilon$ model.*

5.3.2 Axial velocity

The mean axial velocity component of the cyclone flow field can be decomposed in three characteristic regions, *i.e.* a downward directed flow close to the cyclone wall, an upward directed flow at smaller radii, and a region of axial velocity deficit or even flow reversal near the centreline. The calculated velocity profiles and the LDA measurements of the mean axial velocity for the standard Stairmand cyclone at $z/D = 0.75$ are shown in Fig. 5.6. Only the Reynolds stress transport model is capable of predicting the characteristic radial distribution of the axial velocity component, and the correspondence between the measurements and the RSTM calculation is good. The shape of the velocity profile obtained with the RNG-$k-\varepsilon$ model results from a circulation region near the cyclone wall, *i.e.* instead of the expected downward flow at the wall the mean axial velocity component is directed upwards. The results near the centreline particularly deviate from the measurements. The $k-\varepsilon$ model too does not predict the reduced axial velocity magnitude near the centreline.

For the Stairmand geometry with $D_e/D = 0.30$ the numerical prediction of the axial velocity benefits from disregarding the wall-reflection term of the Reynolds stress model as is demonstrated in Fig. 5.7. There is no clear benefit of choosing the RSTM without the wall-reflection term in case of a larger exit pipe diameter. For $D_e/D = 0.30$ the RSTM with wall-reflection term predicts a jet-like shape of the axial velocity component at the centreline, which clearly contradicts the experimental results. Without the wall-reflection term the axial velocity magnitude at the core region is reduced, although for both cyclones the flow is reversed at the centreline, which is not observed in the LDA data. It should be noted, however, that this could be due to the spatial averaging effect of the precessing vortex core (PVC), *i.e.* the velocity profile is smoothed due to the precessing motion and the finite size of the LDA measuring volume (see also discussion in Sec. 4.3.3).

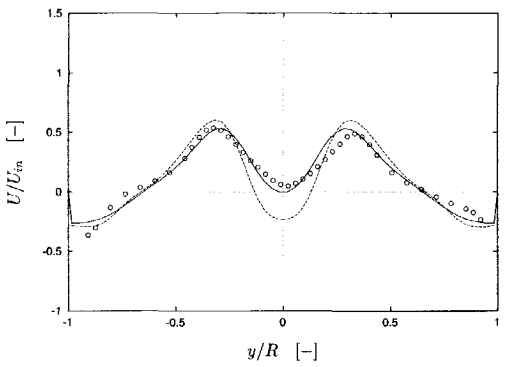

(a)

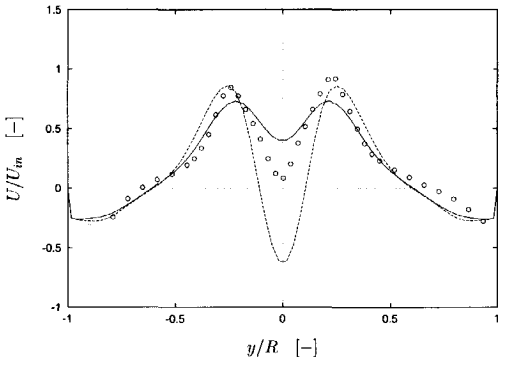

(b)

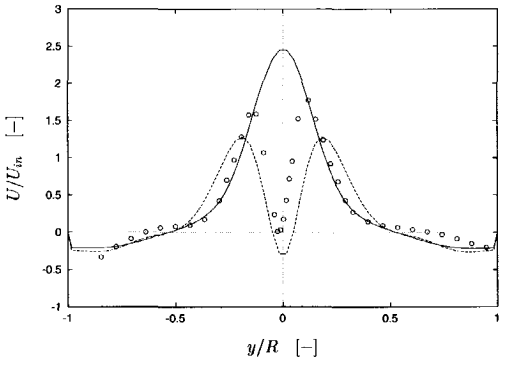

(c)

FIGURE 5.7: *Radial profile of the mean axial velocity at $z/D = 0.75$ for the Stairmand cyclone with D_e/D equal to (a) 0.50, (b) 0.40, and (c) 0.30. LDA measurements (o), (-) RSTM with wall-reflection term, and (- -) RSTM without wall-reflection term.*

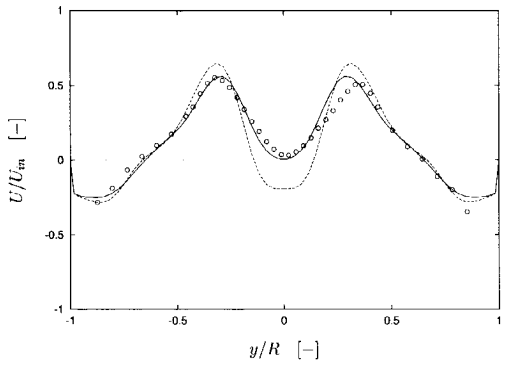

(a)

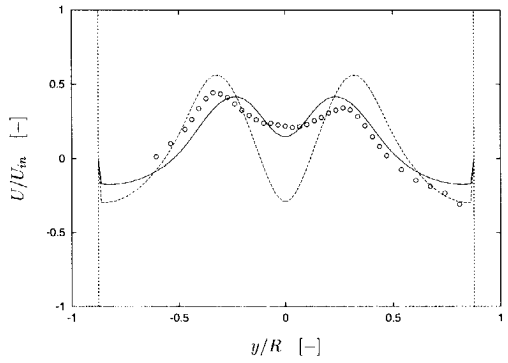

(b)

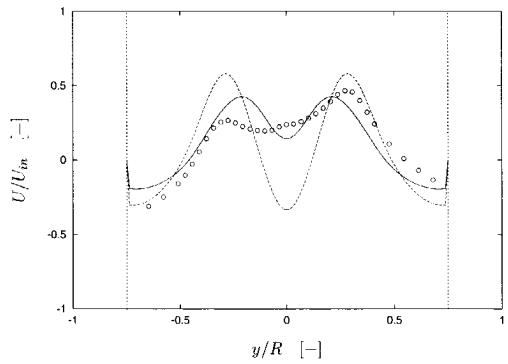

(c)

FIGURE 5.8: *Radial profile of the mean axial velocity at (a) $z/D = 0.625$, (b) 2.0, and (c) 2.5 for the Stairmand cyclone. LDA measurements (∘), (–) RSTM with wall-reflection term, and (- -) RSTM without wall-reflection term.*

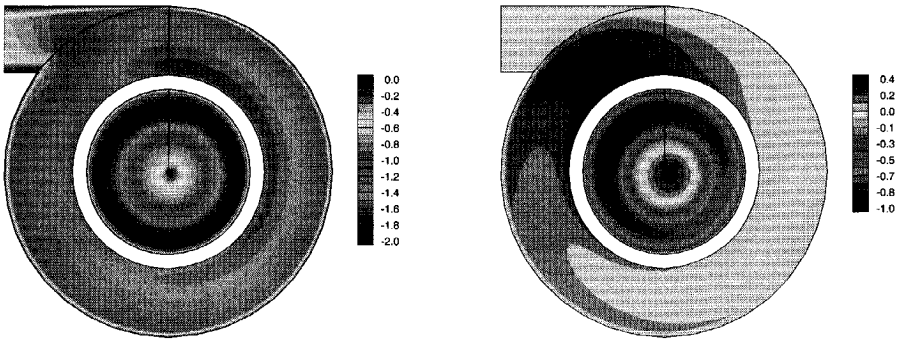

(a) (b)

FIGURE 5.9: *Countour plot in a horizontal $(x, y$-$)$ plane at $x/D = 0.5$ of the (a) tangential and (b) axial velocity magnitude normalised by the linear inlet velocity.*

The radial distribution of the mean axial velocity component is presented in Fig. 5.8 for different measurement stations along the cyclone height. The velocity profiles exhibit a velocity deficit near the centreline, although its magnitude is diminished while moving towards the cyclone base. In addition, the axial flux is reduced as a result of the radial inflow of gas towards the vortex core. The figure shows that no improvement is obtained by disregarding the wall-reflection term in the RSTM. An explanation for the low axial velocity magnitude in the vortex core near the exit pipe entrance is found by the strong coupling of the swirl velocity and the dynamic pressure component (see Eq. 2.1).

5.3.3 3D flow characteristics

A limitation of the axisymmetric flow predictions is that the geometry of the tangential inlet section is not taken into account. This effect is commonly assumed to be of limited importance for the flow field in the separation zone of the cyclone, *i.e.* the region below the vortex finder annulus (see *e.g.* Boysan et al. (1982)). To investigate the validity of this assumption, a three-dimensional simulation was done of the standard Stairmand cyclone separator. In this simulation, the inlet conditions were imposed on a plane in the direction normal to the entrance of the inlet box. The axisymmetric grid was used to define the grid resolution in the radial and axial direction. In the tangential direction the grid cells extended over $\pi/18$ radians. The particle collection bin attached to the cyclone base was not included in the 3D model to reduce the computational effort. The final model consisted of $38 \times 38 \times 93$ grid cells in the radial, tangential and axial direction, respectively, and a converged solution with the power-law scheme was obtained after $10,000$ iterations.

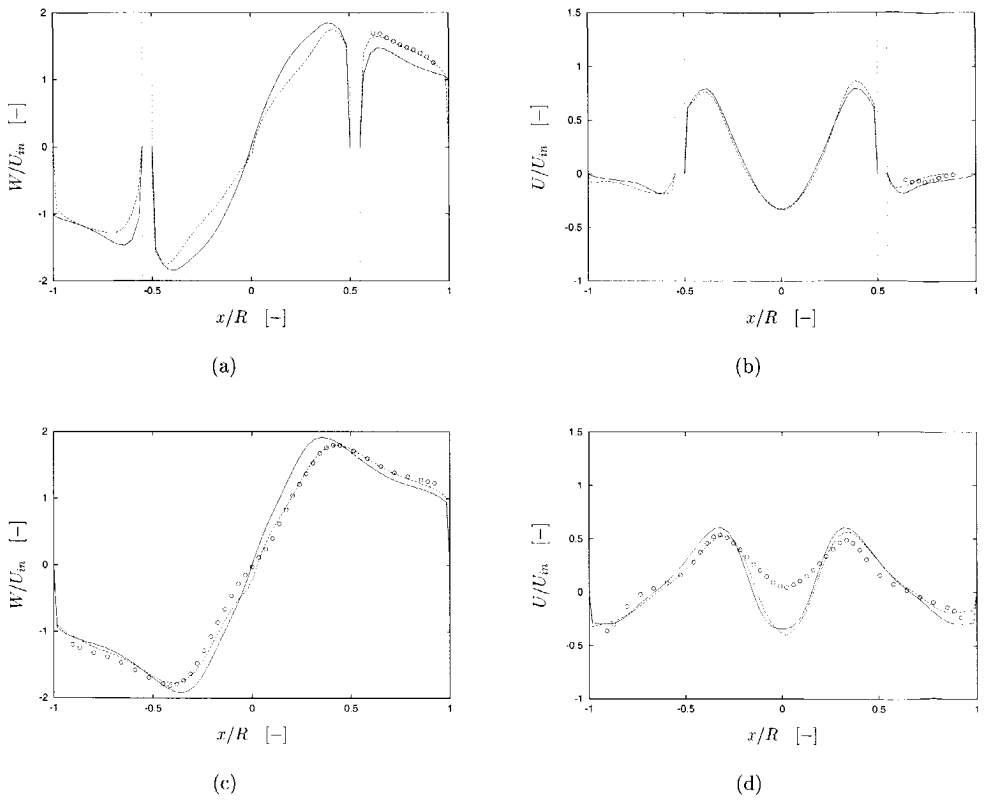

FIGURE 5.10: *Comparison of 2D and 3D calculation of the Stairmand cyclone separator: RSTM without wall-reflection term and no collection bin included. Radial profiles of the tangential and axial mean velocity at (a,b) $z/D = 0.25$, and (c,d) $z/D = 0.75$. LDA measurements (∘), (–) 2D RSTM without wall-reflection term, and (- -) 3D RSTM without wall-reflection term.*

In Figs. 5.9a and b, contour plots of the mean tangential and axial velocity components are presented for the axial position at the lower rim of the exit pipe ($x/D = 0.50$). The solid line from the centre to the cyclone wall represents $\theta = 0$. For both components the velocity magnitude in this cross section depends on the azimuthal angle θ, because the gas in the annulus is joined by the flow entering the cyclone from the inlet. At this position, the flow is accelerated in the tangential direction, which results in an increased level of the mean tangential velocity near the exit pipe wall. The contour lines for the axial velocity component show that the annular flow is forced downwards, especially near the exit pipe wall, just before it joins the inlet flow. This results in a locally increased level of short-cut flow, *i.e.* fluid from the annulus that is exhausted directly through the exit pipe. The contour lines of the axial velocity in the exit pipe confirm this effect, and also demonstrate a small axi-asymmetry of the flow with respect to the centreline of the geometry.

Although the three-dimensional results of the annular flow between the cyclone wall and the exit pipe deviate considerably from axisymmetry, the radial distribution of the mean axial and tangential velocity components in the cyclone body is largely similar for the 2D and 3D simulation. This is shown for two axial measurement stations in Fig. 5.10. As a comparison, 2D results are presented that were calculated for the same geometry as applied by the 3D simulation, so without the particle collection bin. The velocity profiles half way the inlet annulus ($z/D = 0.25$) show that the azimuthal flow dependency predicted by the 3D simulation is similar to the LDA measurements. For both the axial and tangential velocity components the 3D simulation corresponds well with the experimental data as opposed to the axisymmetric results. At $z/D = 0.75$, the 2D and 3D velocity profiles are quite similar, which implies that very few axi-asymmetry is left as a result of the tangential inlet. Hence, it is reasonable to assume axisymmetry while modelling the gas flow field in a cyclone separator.

5.3.4 Reynolds stresses

The normal stress components of the Reynolds stress tensor, $\rho\overline{u_i u_i}$, are commonly represented in terms of the root mean square (rms) of the velocity fluctuations, $u_{i,rms}$. The radial distribution of the rms velocity components at a characteristic measurement station for the standard Stairmand cyclone is shown in Fig. 5.11. The experimental data are compared to calculated velocity profiles that were obtained by use of the RSTM with and without wall-reflection term. For the radial rms velocity no experimental data were available. The other velocity components show that there is a fair correspondence between the predicted and measured rms levels except for the core region of the flow. The mutual difference between the two Reynolds stress models is small, where the RSTM without wall-reflection term predicts lower rms levels.

In the core region, the measured rms levels increase significantly, although the tangential rms velocity is reduced again at the centreline and the axial rms velocity flattens. It was argued in Ch. 3 and 4 that this characteristic distribution of the rms velocity in the core region is due to pseudo-turbulent fluctuations, which result from the precessing vortex core (PVC). The magnitude of the PVC contribution to the measured rms velocity is in a first approximation proportional to the mean velocity gradient, *e.g.* the tangential rms velocity near the centreline is reduced as a result of the lower mean velocity gradient at $r = 0$ (see Fig. 5.3). Since the PVC is not taken into account in the RANS model, the predicted rms profiles involve only turbulent motion.

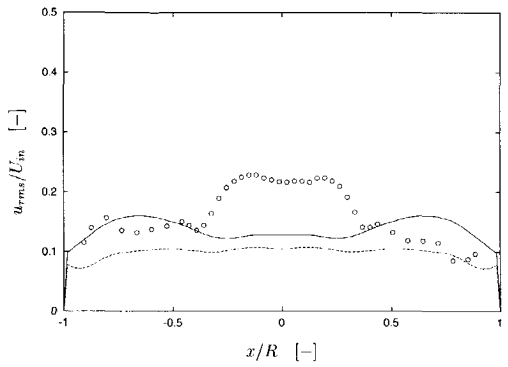

(a)

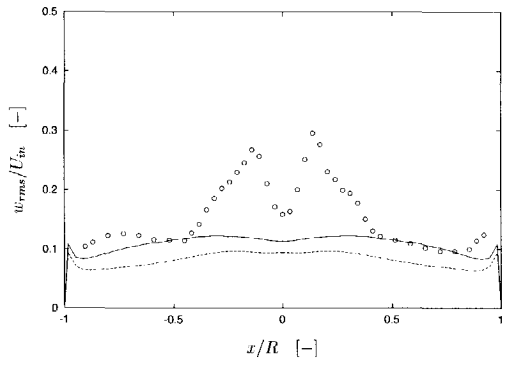

(b)

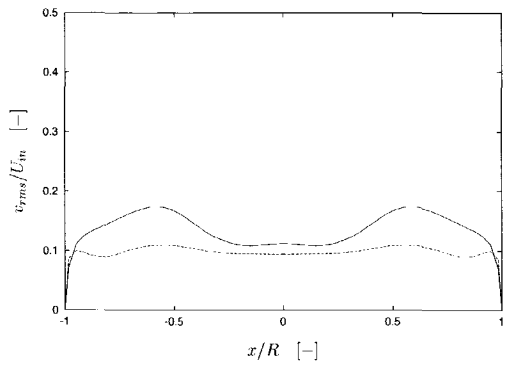

(c)

FIGURE 5.11: *Radial profiles of the (a) axial, (b) tangential and (c) radial rms velocity for the Stairmand cyclone at $z/D = 0.75$. LDA measurements (○), (–) RSTM with wall-reflection term, and (- -) RSTM without wall-reflection term.*

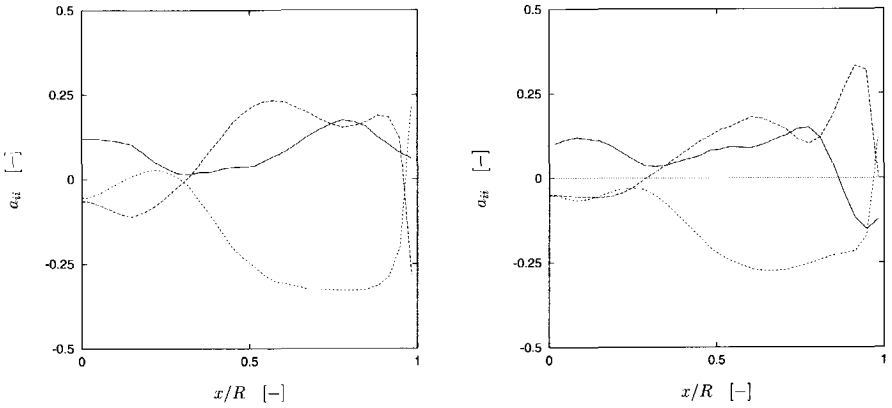

FIGURE 5.12: *Radial profile of the normal components of the anisotropy tensor, (–) a_{uu}, (- -) a_{vv}, (...) a_{ww}, for the Stairmand cyclone separator at $z/D = 0.75$: (a) RSTM with wall-reflection term, (b) RSTM without wall-reflection term.*

The turbulent character is expected to be different among the core and outer regions because of the centrifugal stabilising or destabilising effect in the swirling flow (Rayleigh criterion, see Sec. 2.1). The calculated rms velocity profiles for the radial and axial component exhibit some suppression of the fluctuating motion in the core region when the wall-reflection term is included in the RSTM. However, this effect is not observed for the RSTM without wall-reflection term. In addition to the stabilising effect of forced vortex, there is the production of kinetic energy in the axial direction, which makes the situation more complex than two-dimensional curved flow (Kitoh, 1991).

Strongly swirling flow is usually associated with Reynolds stress anisotropy. The anisotropy of the Reynolds stress can be represented by the anisotropy tensor a_{ij}, defined as (Hadzić, 1999):

$$a_{ij} = \frac{\overline{u_i u_i}}{k} - \frac{2}{3}\delta_{ij} \tag{5.11}$$

In Fig. 5.12, the diagonal components of the anisotropy tensor are shown for the Stairmand cyclone at $z/D = 0.75$. The effect of disregarding the wall-reflection term in the Reynolds stress transport model is clearly shown for the near-wall region. Due to the wall-reflection term the normal stress in the radial direction is suppressed at the wall, which results in a large value for the difference $a_{ww} - a_{vv}$. Both RSTM calculations predict significant normal stress anisotropy in the free-vortex region of the flow, while at the forced vortex region the anisotropy is reduced. The near-isotropic distribution of the normal stresses in the forced vortex region

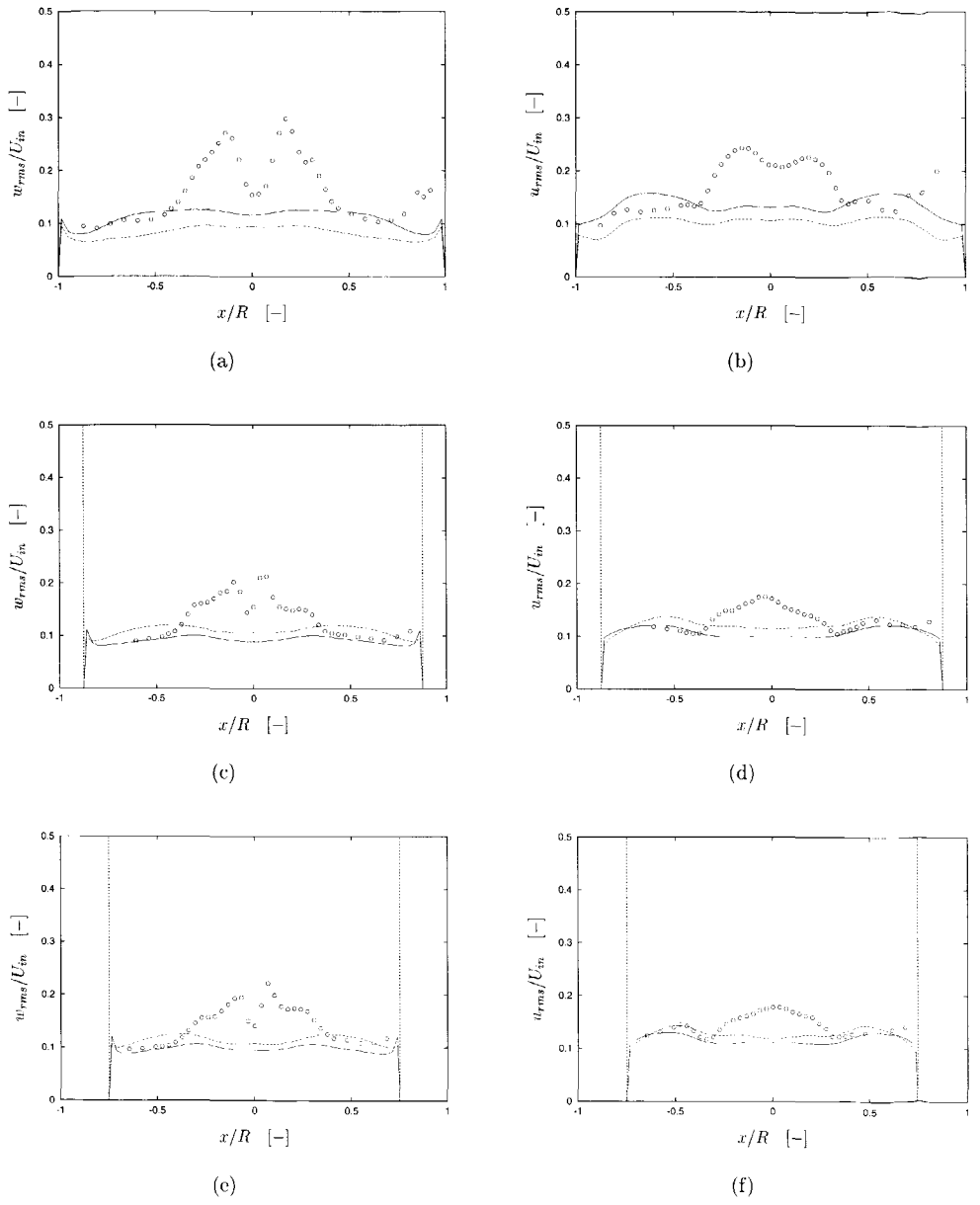

FIGURE 5.13: *Radial profiles of the tangential and axial rms velocity for the Stairmand cyclone at (a,b) $z/D = 0.625$, (c,d) 2.0, and (e,f) 2.5. LDA measurements (○), ( ) RSTM with wall-reflection term, and (- -) RSTM without wall-reflection term.*

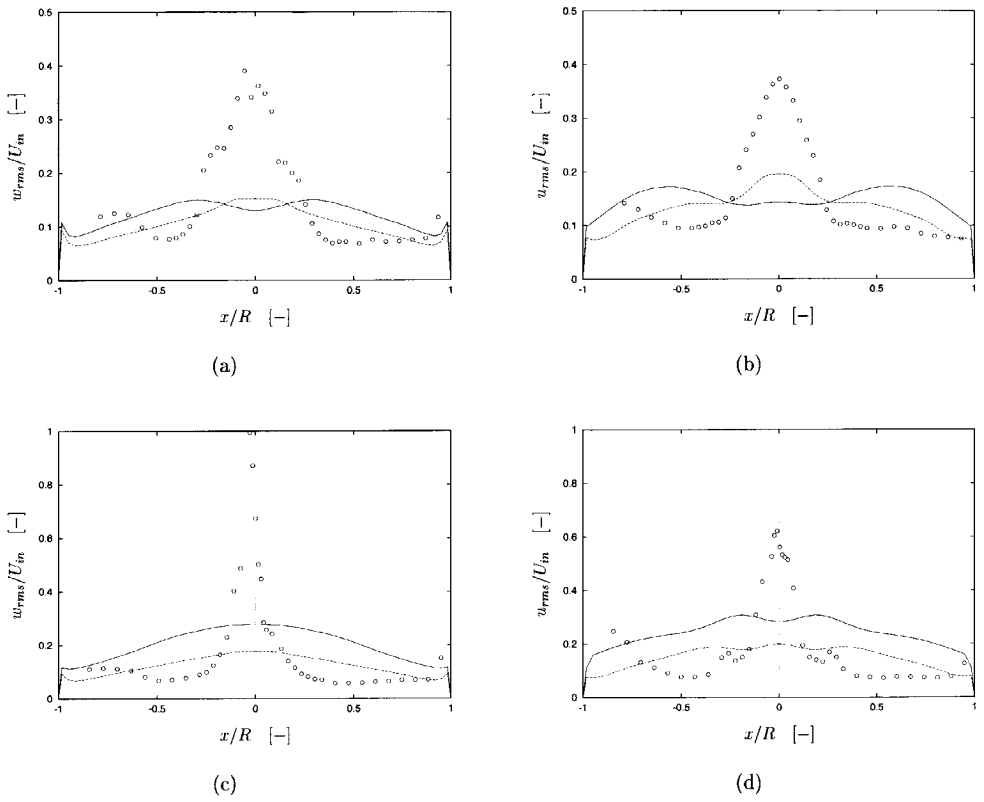

FIGURE 5.14: *Radial profiles of the (a,c) tangential and (b,d) axial rms velocity for the Stairmand cyclone at $z/D = 0.75$ with from top to bottom $D_e/D = 0.40$ and $D_e/D = 0.30$. LDA measurements (○), (–) RSTM with wall-reflection term, and (- -) RSTM without wall-reflection term.*

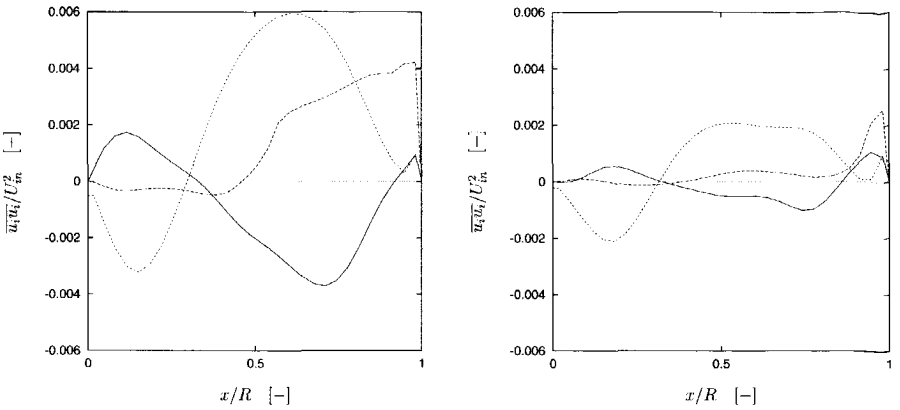

FIGURE 5.15: *Radial profile of the Reynolds shear stresses, (–) $\overline{uv}$, (- -) $\overline{vw}$, (...) $\overline{uw}$, for the Stairmand cyclone separator at $z/D = 0.75$: (a) RSTM with wall-reflection term, (b) RSTM without wall-reflection term.*

is consistent with the observations of Hogg and Leschziner (1989), Kitoh (1991) and Jakirlić (1997) for confined swirling flow. In these studies, the phenomenon is attributed to the model for the pressure-strain interaction used in the RSTM. Kitoh (1991) argues that the magnitude of the fit coefficient in the rapid term Φ_{ij}^2 is too low; a more elaborate version of the RSTM improved the prediction of the a_{uu} magnitude.

The measured and predicted rms velocity profiles at other axial stations are shown in Fig. 5.13 for completeness. There is a fair agreement between the measured and calculated rms levels, while the RSTM with wall-reflection term generally agrees better with the experimental data. The precessing vortex core affects the measured rms velocity in the core region at all measurement stations by introducing pseudo-turbulent fluctuations (see Ch. 4). The level of rms velocity is fairly constant along the axial co-ordinate for both components.

The model calculations for the modified Stairmand cyclones do not agree very well with the experimental data as is shown in Fig. 5.14. The RSTM predicts an increased level of both tangential and axial rms velocity with reduced exit pipe diameter. This contradicts with the LDA measurements in the free vortex that show a similar rms velocity level independent of the exit pipe diameter. In the Reynolds stress model the mean velocity gradient affects the production of turbulent kinetic energy, *i.e.* the production of $\overline{u^2}$ and $\overline{w^2}$ is proportional to the mean axial and tangential velocity gradient in the radial direction, respectively (see also Kitoh (1991)). These gradients are significantly higher for cyclones with a smaller exit pipe diameter, and, consequently, a smaller vortex core size, hereby resulting in high tangential and axial rms levels. Again, the precessing motion of the vortex core strongly affects the flow field near the centreline. Its contribution to the fluctuating velocity is largest for the geometry with

$D_e/D = 0.30$, since the level of pseudo-turbulence is also related to the mean velocity gradient.

The distribution of the off-diagonal components of the Reynolds stress tensor is shown in Fig. 5.15 for the standard Stairmand geometry. Since no LDA data on the shear stresses were available, only calculated profiles are given. The inclusion of the wall-reflection term in the RSTM affects the magnitude of the shear stresses considerably, although the shape of its radial distribution is rather similar for both calculations. Near the wall the magnitude of $\overline{vw}$ is approximately two times larger if the wall-reflection term is included, which is due to the damping of the radial normal stress and, consequently, increase of the tangential normal stress. This results in a higher wall shear stress. The radial distribution of $\overline{vw}$ also affects the vortex shape by its strong interaction with the mean tangential velocity gradient in the radial direction. This was demonstrated in Fig. 5.4, where the radial gradient of the swirl profile in the free-vortex region was shown to be different for the RSTM calculations with and without wall-reflection term.

5.3.5 RANS models versus Large Eddy Simulation

To obtain a fair degree of accuracy in predicting the gas flow field of cyclones, a RANS model needs at least second moment closure as was illustrated earlier. One typical feature of the flow field was, however, not predicted, *i.e.* the precessing motion of the vortex core. A suitable way to resolve this hydrodynamic instability both spatially and temporarily is by means of a Large Eddy Simulation (LES). This was already demonstrated for the confined vortex flow in a laboratory scale cyclone (see Sec. 4.5, Derksen and Van den Akker (2000)). In this section, the prediction of the mean and fluctuating velocity components is assessed by means of Laser-Doppler measurements. In addition, the LES results are compared to a three-dimensional RANS prediction of the flow field.

Experimental

The flow geometry is shown schematically in Fig. 5.16. Air is introduced tangentially into a cylinder at a flow rate of $16.3\,m^3\,h^{-1}$. The exit pipe is a straight tube, allowing the air to leave the cyclone through the top. From the geometrical dimensions a geometric swirl number equal to 2.1 can be calculated (see Eq. 2.4). Based on the linear inlet velocity and the cyclone body diameter ($D = 0.1\,m$) the Reynolds number of the flow amounted to 15,000.

A two-component Laser-Doppler anemometer was used to measure the tangential and axial velocity components. The laser beams were focused with a 250 mm lens to obtain a measurement volume of approximately 0.78 mm in length and 0.078 mm in width. Due to the cyclone wall thickness of 5.0 mm, the two measurement volumes did not exactly coincide at all radial positions. The measurement positions were corrected for the optical distortion. The air flow was seeded with water/glycerol droplets to obtain a data rate varying from 300 Hz in the outer vortex region to just a few Hz near the centreline (for a description of the seeding system the reader is referred to Sec. 3.2.3).

Velocity profiles were measured along the cyclone radius at four axial measurement stations. These stations were located in the separation section between the vortex finder and the flat bottom plate, *i.e.* at $x/D = 0.89$, 1.39, 1.89, and 2.39 (where the $x/D = 0$ position was chosen at the bottom of the cyclone, and x points upwards). At each axial location, the measurement

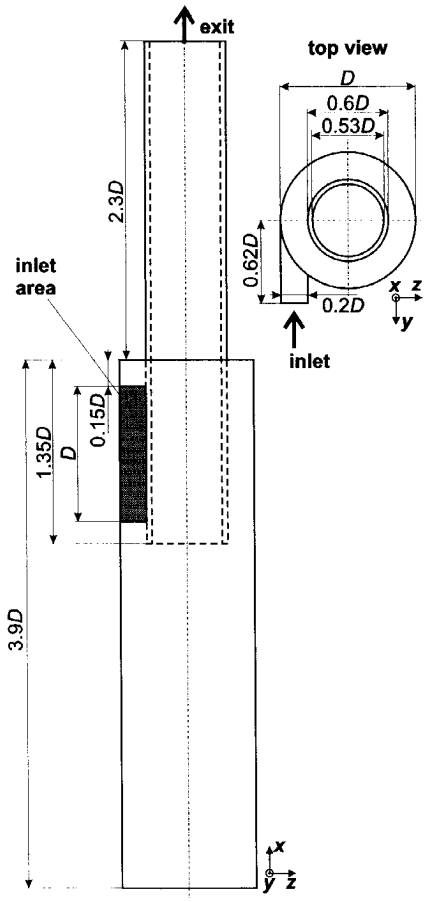

FIGURE 5.16: *Schematic representation of the vortex chamber.*

volume was traversed in the z-direction (see the coordinate system defined in Fig. 5.16), over a line through the cyclone body's geometrical centre, starting close to the wall (*i.e.* at $z/R \approx 0.9$, with $R = D/2$) and ending at, or slightly opposite to the centre. From the measured velocity time series, average velocities and RMS velocity values were derived. All statistics were derived from $10^3 - 10^4$ data points per channel, depending on the radial position.

Numerical

Within a Large Eddy Simulation (LES), the largest scales of the flow are fully resolved while the smaller scales are modelled by a so-called subgrid-scale model. In this simulation, the standard Smagorinsky model was employed, which is an eddy viscosity model with a subgrid-scale eddy viscosity (ν_e) depending on the local, resolved deformation rate:

$$\nu_e = \lambda_{mix}^2 \sqrt{S^2} \tag{5.12}$$

where λ_{mix} represents the mixing length of subgrid-scale motion and S^2 the squared resolved deformation rate (Smagorinsky, 1963). In the standard Smagorinsky model, the ratio between the mixing length λ_{mix} and the lattice spacing Δ is constant:

$$\lambda_{mix} = c_s \Delta \tag{5.13}$$

For c_s a value of 0.10 was adopted. Note that the subgrid-scale eddy viscosity in the LES is dissimilar to the eddy viscosity used in RANS turbulence closure models.

Compared to a RANS simulation, LES requires much higher spatial resolution in order to do physically sound subgrid-scale modelling. This asks for a fast discretisation scheme. Derksen and Van den Akker (2000) used a lattice-Boltzmann scheme, since its efficiency is hardly hampered by the complexity of the flow domain (this in contrast to *e.g.* spectral methods), and due to its straightforward and efficient parallelisation properties. A disadvantage of the lattice-Boltzmann scheme is its uniform, cubic lattice, which excludes local grid refinement. Due to the moderate Reynolds number of the flow studied here, the uniform grid could however, adequately resolve the boundary layers.

The flow geometry was mapped onto a cubic grid of 499 lattice cells in the axial direction, and 99 cells in the two lateral directions. At the inlet plane a uniform inlet velocity was set, and at both the inlet and outlet planes a zero flow gradient condition was applied in the flow direction. The simulation was run on four parallel processors of a HP Convex S-Class computer. The total memory requirements were about 0.6 Gbyte. The wall-clock time per time step for the code running on a single processing element typically was $30\,s$. Simulation of a single integral time scale (here defined as D/U_{in}) therefore requires 10 hours wall clock time. Parallel implementation, however, can reduce this number drastically. Running the code on the four processing elements gave a wall clock time reduction with a factor 3.8.

In contrast, the three-dimensional RANS simulation employed an O-type of grid consisting of $38 \times 41 \times 78$ cells in the tangential, radial and axial direction, respectively. The standard Reynolds stress transport model with wall reflection terms was used as a closure model for the Reynolds stresses. The simulation was performed on a single HP S-class processor, which took

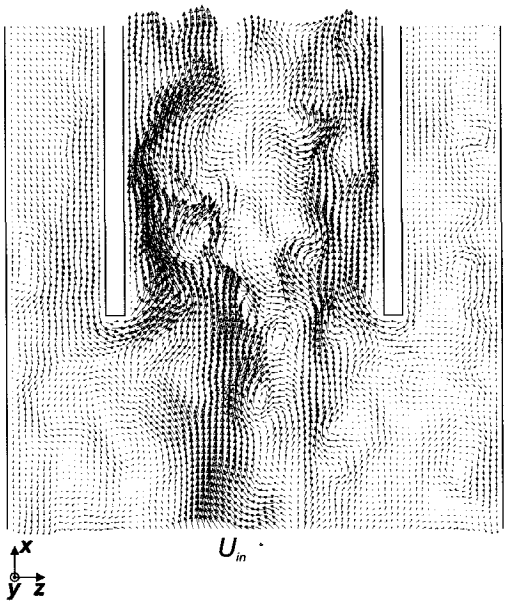

FIGURE 5.17: *Single flow field realisation calculated by a Large Eddy Simulation of a part of the vortex chamber interior.*

approximately 21 s for one iteration. To avoid instabilities to occur during the calculation, low values for the underrelaxation factors were set. A fully converged solution was obtained after 20,000 iterations. Since the LES results were gathered over a run that covered 80 integral time scales, its time requirements are approximately one order of magnitude larger than that of the 3D RANS simulation.

Flow field predictions

An illustrative example of the turbulent nature of the flow is presented in Fig. 5.17, where a single LES realisation is shown of the region close to the inlet of the exit pipe. This image gives the full resolution of the simulation. After averaging a large number of flow realisations the mean and fluctuating velocity components could be calculated.

In Fig. 5.18, the measured average velocity values are shown along with the corresponding simulation results. The agreement of both the RANS and LES simulations with the experimental data regarding the tangential velocity is quite good. The RANS simulation performs slightly better in predicting the solid body rotation in the central region of the profile. The maximum levels of tangential velocity, and their radial location are predicted very well. This also is true for the development in axial direction in the free vortex region; closer to the bottom of the cyclone, the decay of tangential velocity in the free vortex region is much stronger than higher up in the cyclone.

For the axial velocity profiles (Fig. 5.18b), quite a different picture applies. The maximum

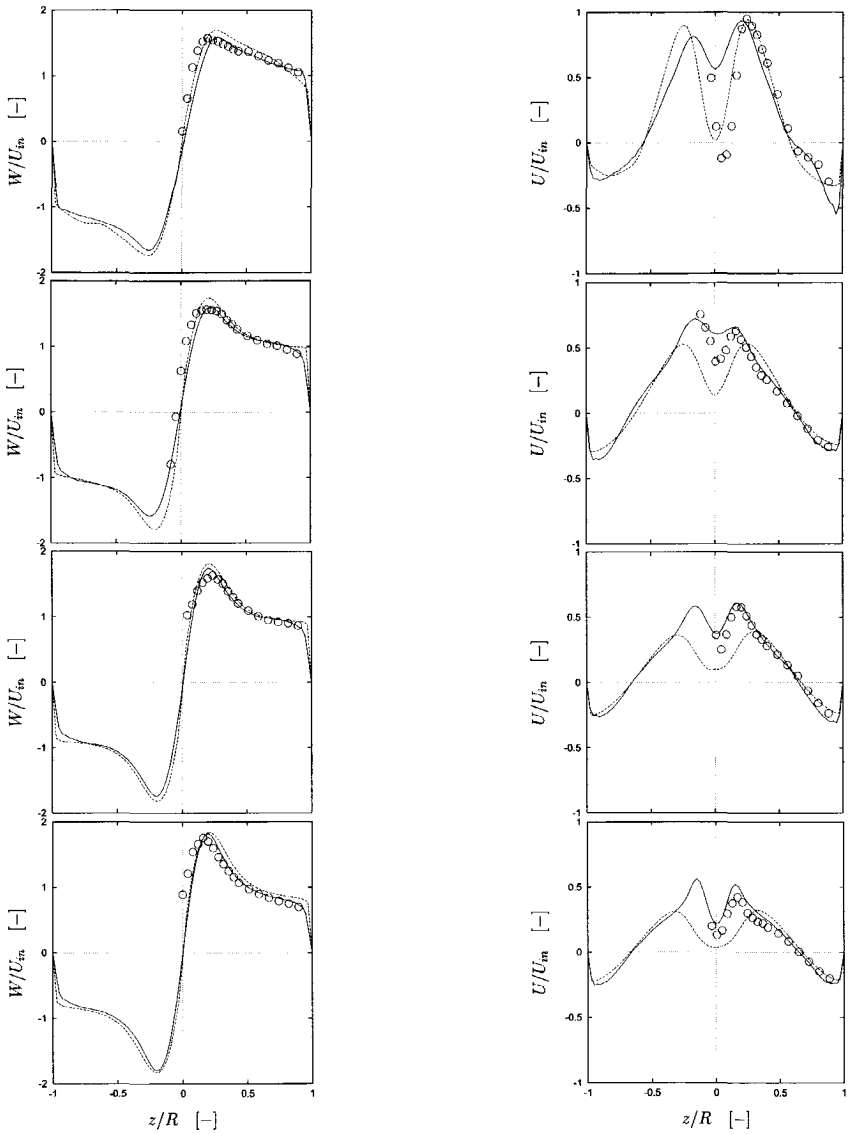

FIGURE 5.18: *Radial profiles of the average tangential (a) and axial (b) velocity at four axial positions; from bottom to top:* $x/D = 0.89$, 1.39, 1.89, *and* 2.39. *LDA measurements* (○), *Large Eddy Simulation* (–), *and 3D RANS simulation* (- -).

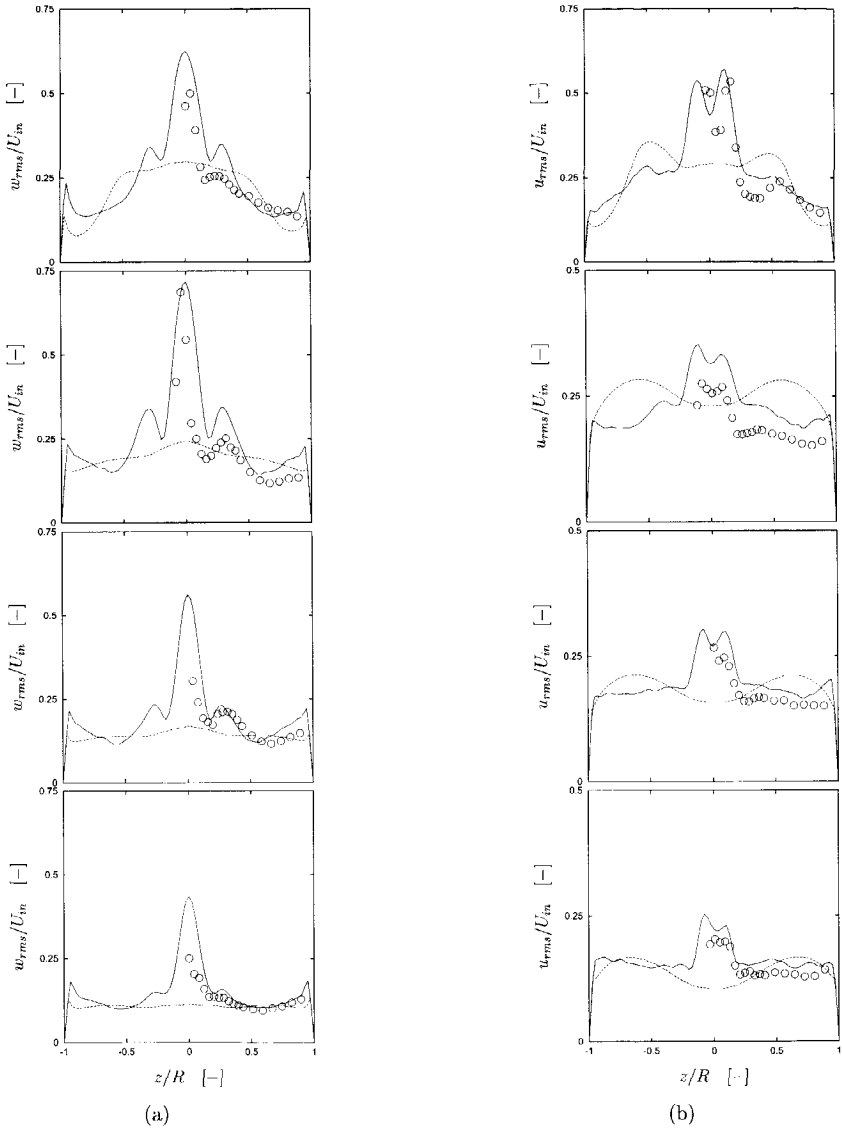

FIGURE 5.19: *Radial profiles of the tangential (a) and axial (b) rms velocity at four axial positions; from bottom to top: x/D = 0.89, 1.39, 1.89, and 2.39. LDA measurements (○), Large Eddy Simulation (–), and 3D RANS simulation (- -).*

levels of axial velocity are well predicted by LES, whereas the RANS simulations underestimate them (except for the profile located highest). The experimentally observed very strong velocity deficit near the centre, just below the entrance of the vortex finder (at $x/D = 2.39$) is clearly present in the RANS simulation, but much too weak in the LES. This applies in a less pronounced way also for the lower x-level profiles.

The rms profiles (Fig. 5.19) show complicated features, that can be largely ascribed to the precessing vortex core (PVC, see Sec. 4.5). The strong peak of the tangential rms velocity near the cyclone's center is due to the combined effect of the motion of the vortex core, and a steep profile of the average tangential velocity, causing high fluctuation levels. These are obviously not present in the RANS simulations. On either side of the peak in the LES data is a local minimum that is a result of the zero gradient in the average tangential profile there. In the free vortex region, the turbulent fluctuations (this in contrast to the fluctuations induced by the PVC, that contain a great deal of coherence) dominate the rms velocities. The trends described above for the LES profiles are to some extent also present in the experiments. Due to the steady-state nature of the RANS simulation, its prediction regarding tangential rms velocities deviates strongly from the experiment. It should be noted, however, that in the free vortex the RANS rms level is approximately correct.

Basically the same remarks as made for the tangential rms profiles apply for the axial rms profiles (Fig. 5.19b). In the centre, the combined effects of the PVC and the average velocity profile dominate the rms levels (here we have a local minimum at the centre due to the zero gradient in the average profile) of the experiment and in the LES. The rms levels of the RANS simulations are acceptable, the shape of its profiles, however, does not relate to the experiments.

5.4 Closure

One of the first numerical predictions of the flow field in a cyclone separator was presented by Boysan et al. (1982). Although the limitations on the computational mesh were much more severe in those times, the modelling framework has been the basis for a number of CFD studies of cyclones since then. Basically, the approach of solving the steady-state, axisymmetric RANS equations together with a second moment closure model for the turbulent stresses has been applied for most of the results presented in this thesis.

Why does this approach still yield acceptable results? We need to recall the original model assumptions put forward by Boysan et al. (1982):

- Turbulence closure models based on the assumption of isotropy (*e.g.* the $k - \varepsilon$ model) are inapplicable in the case of highly swirling flows.
- The flow (in a cyclone) loses its three-dimensional character at a short distance from the tangential inlet, *i.e.* it is permissible to neglect all the derivatives with respect to the tangential direction.

Both assumptions have been confirmed by the results presented in this chapter. The assessment of turbulence models was possible by the extensive experimental data set obtained for a number of cyclone geometries. Three-dimensional aspects of the flow field could be studied by means of the 3D simulation of the Stairmand cyclone, and its comparison with the 2D simulation and the LDA measurements.

The availability of a parallel computer cluster enabled the prediction of the vortex flow in a laboratory cyclone by means of a Large Eddy Simulation (LES). The LES approach has the inherent advantage of reducing the modelling effort to the subgrid level, and, hence, avoiding the model assumptions cited earlier. The LES is capable of predicting the precessing motion of the vortex core, which has not been reported in the literature before. However, the computational demand of a Large Eddy Simulation currently limits its application to moderate Reynolds number flows. In addition, a comparison of the mean gas flow field in a vortex chamber predicted by both the LES and a conventional RANS simulation did not favour the Large Eddy Simulation in terms of prediction accuracy.

CHAPTER 6

SIMULATION AND MEASUREMENT OF COLLECTION EFFICIENCY

An experimental facility was built to measure the overall collection efficiency of the Stairmand cyclone operating at low solids loading. The cyclone performance was studied as a function of the inlet velocity and the exit pipe diameter. The efficiency measurements were fit to a response surface model by means of least-mean-squares regression. The grade efficiency curve of the cyclone was predicted by tracking a large number of particles for different particle size classes through the computational domain. The effect of the turbulent flow field of the gas on the particle trajectories was included by means of a particle dispersion model. The predicted overall collection efficiency is compared to the experimental results for the different test conditions.

6.1 INTRODUCTION

Cyclone performance is usually assessed in terms of its pressure drop and its collection efficiency. The pressure drop of cyclone separators of industrial size is readily estimated by means of a conventional manometer, although some caution is required when the experimental data are compared to (semi-)empirical model predictions (see discussion of Sec. 2.2). Experimental data on the collection efficiency, however, are generally more difficult to obtain. This is due to the fact that the overall collection efficiency is dependent upon the cyclone separation capability and the particle size distribution of the incoming powder. The separation capability of a cyclone is characterised by the grade efficiency curve, which describes the collection efficiency as a function of the particle size.

Whereas the overall collection efficiency can be estimated relatively easy based on the weight balance of incoming and collected solids (Hoffmann et al., 1992; Ontko, 1996), more advanced experimental techniques are needed to measure the grade efficiency curve. In most of the studies reported in the literature, an isokinetic sampling probe is used to obtain a particle size distribution of the exhausted solids (Stairmand, 1951; Mothes, 1982; Bernard, 1992). By means of a size analysis of the inlet and exit samples, a grade efficiency curve can be derived. A prerequisite for obtaining a representative sample is to minimise flow field disturbances caused

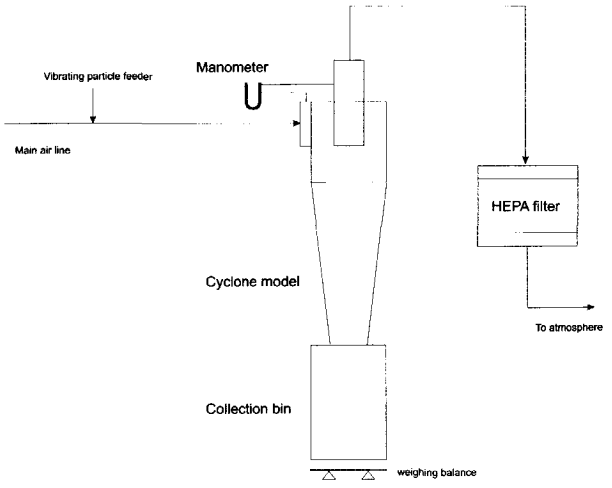

FIGURE 6.1: *Schematic representation of the experimental set-up. The solids are dosed by a vibrating particle feeder and introduced in the main air duct. After each run the catch bin is disconnected from the cyclone and weighed.*

by the finite size of the sampling probe. More recently, in-line optical techniques are employed to obtain the particle size distribution at the inlet and exit pipe directly (Gottschalk and Bohnet, 1998; Wanker et al., 1998).

In principle, for a given set of physical properties of the fluid and the particulate phases, the collection efficiency can be predicted by means of Computational Fluid Dynamics. In turbulent flow, the particle trajectories are stochastic by nature, so collection statistics need to be based on a large number of (computational) particles. The CFD model for the simulation of the fluid phase in a Stairmand cyclone was already discussed in Ch. 5.

In this chapter, the numerical treatment of the particulate phase is discussed, and predictions of the collection efficiency are presented. The simulations are compared to experimental data. The experimental programme was limited to measurements of the overall collection efficiency of the Stairmand cyclone operating at low solids loading.

6.2 EXPERIMENTAL SET-UP

In Fig. 6.1, the experimental facility is schematically shown. The experimental test rig that was used for the LDA measurements was extended with a particle injection system and a high-efficiency particulate air (HEPA) filter. The injection system comprises a vibrating particle feeder positioned in an airtight box, and a funnel. Pressurised air is injected into the airtight box to prevent clogging of particles in the funnel, and to ensure a small overpressure in the system. The powder is conveyed pneumatically into a nozzle or eductor, which is inserted in a small pipeline. After acceleration of the injected particles by the nozzle the flow is injected into the main duct, and consecutively into the cyclone model.

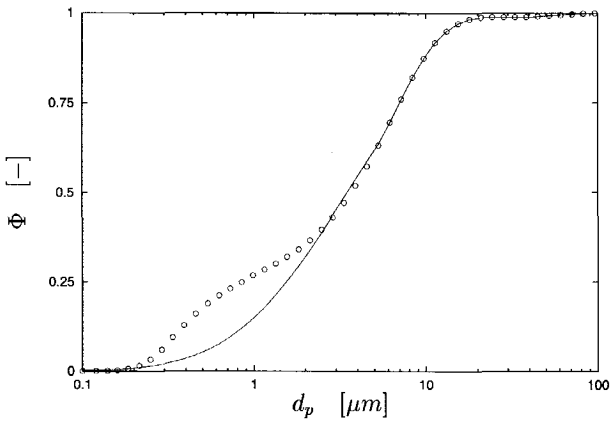

FIGURE 6.2: *Volume density distribution of test particles ($CaCO_3$) measured by the Malvern Mastersizer used in the collection efficiency measurements. Imaginary part of particle refractive index equal to (o) 0.1 and (-) 1.0.*

A catch bin at the particle exit of the separator collects powder that is separated from the air by the cyclone. The gas flow is exhausted through the vortex finder together with uncollected particles, and passes the HEPA filter before emission into the atmosphere. According to the manufacturer, the HEPA filter is capable of collecting 99.999% of particles exceeding 0.3 μm in diameter.

The test powder used for the collection efficiency measurements is chalk dust or calcite ($CaCO_3$) ex Rhone-Poulenc with a particle density of $2,740\, kg\, m^3$. The powder was premixed with 1 w/w % of Aerosil ex Degussa, which acts as a dispersing aid to improve flow behaviour. A similar powder was applied in a collection efficiency study by Hoffmann et al. (1992). The volume density distribution of the test powder was measured by means of a Malvern Mastersizer (Malvern Instruments Ltd., UK), and is shown in Fig. 6.2. Each data point represents the averaging of two samples.

The analysis technique is based on laser diffraction and Mie theory. The particle refractive index was set to 1.5295, however, for light-absorbing the refractive index is complex. The imaginary part of the refractive index affects in particular the lower tail of the size distribution as is illustrated in Fig. 6.2. For further analysis the imaginary part of the particle refractive index was assumed equal to 0.10. The distribution is characterised by a mean volume diameter $d_{4,3}$ of 4.23 μm, and a geometric standard deviation of 5.92 μm.

The overall collection efficiency was measured by weighing the collected powder in the catch bin and dividing it by the particulate mass fed during each individual run. An alternative way to estimate the collection efficiency is to measure the exhausted particle mass that is collected by the filter. However, inspection of the ducts between the cyclone and the HEPA filter revealed that these were partly covered with exhausted powder, which implies that the exhausted powder is not completely captured by the filter.

To reduce electrostatic build-up at the cyclone wall, the geometry was shielded with thin sheet of copper, which was attached to the frame. The apparatus was cleaned between each

experiment. The measurement accuracy of the weighing balance was 0.1 g, whereas the total mass of test powder fed to the cyclone during a run was at least 1 kg. During each experiment the cyclone was operated at a constant solids loading, C, of $2.8\,10^{-3}$ kg solids/kg gas. This was obtained by changing the frequency of the vibrating particle feeder with inlet velocity level. The cyclone pressure drop was only slightly reduced by the presence of solids in the flow field, which is consistent with the observations of Hoffmann et al. (1992). During the efficiency measurements the pressure drop was not recorded. Pressure drop measurements of the Stairmand cyclone at unloaded conditions were presented in Ch. 3, and will be used to assess numerical predictions at a later stage.

In this study, the effect of the linear inlet velocity and the exit pipe diameter on the collection efficiency was investigated. These variables are known to strongly affect the gas velocity field, and, hence, the collection efficiency of the cyclone. The Stairmand high-efficiency cyclone was used as the benchmark design. The functional relationship between the two independent variables (factors) and the dependent variable (response) was approximated by means of a response surface design (Montgomery, 1984). An experimental design for fitting a second-order model has to consist of at least three levels of each factor, so that the model parameters can be estimated. The factor levels were chosen to accommodate the industrial conditions at which the Stairmand cyclone is commonly operated, *i.e.* an inlet velocity varying between 10 and $30\,m\,s^{-1}$, and a normalised exit pipe diameter of $0.30 - 0.50$. The central composite design was based on a 2D projection of a face centred cubic. The method of least-squares was used to estimate the parameters of the corresponding polynomial. The model adequacy was determined by means of analysis of variance (ANOVA). In the next section, the numerical model for the particulate phase is discussed first.

6.3 Numerical model

6.3.1 Equation of particle motion

The gas-particle flow field in the cyclone is modelled in an Eulerian-Lagrangian frame of reference, *i.e.* the (vector) velocity of the fluid is defined as a function of position relative to the cyclone geometry, whereas the particles are treated as discrete elements. The trajectory of a particle in the gas flow field is determined by solving its equation of motion. In turbulent flows, the presence of particles complicates the calculation of the particle trajectories, because two important mechanisms need to be taken into account, which are the dispersion of discrete particles due to the fluid turbulence, and the modification of turbulence properties caused by the presence of particles.

Elghobashi (1994) has mapped the interaction between particles and turbulence by means of two characteristic dimensionless quantities, *viz.* the volume fraction of particles, Φ_p, and the ratio of the particle response or relaxation time, τ_p, and the Kolmogorov time scale, τ_K. For very low values of Φ_p ($\leq 10^{-6}$) the particles have negligible effect on turbulence, and the interaction between the particles and turbulence reduces to one-way coupling. This means that particle dispersion, in this regime, depends on the state of turbulence, but due to the negligible concentration of the particles the momentum transfer from the particles to the turbulence has an insignificant effect on the flow. For higher values of Φ_p ($\leq 10^{-3}$), the momentum transfer

from the particles is large enough to alter the turbulence structure. This interaction is called two-way coupling. In this regime, the magnitude of the ratio τ_p/τ_K determines whether the fluid turbulence is damped or enhanced by the particulate phase. For $\Phi_p > 10^{-3}$ particle-particle interaction becomes important in addition to the two-way momentum exchange between the fluid and particulate phases.

In the experimental set-up discussed in the previous section, the gas cyclones are operated at low-solids loading. The solids loading for each experiment was equal to 2.8 10^{-3} kg solids/kg gas. This corresponds to the upper limit of regime 1 in terms of the volume fraction of particles ($\Phi_p \approx 10^{-6}$), which is defined as the product of the solids loading C and the density ratio ρ_g/ρ_p. Hence, only one-way coupling needs to be taken into account in the model, which is a significant reduction of the computational effort.

In the Lagrangian approach, the particulate phase is represented by a number of computational particles whose trajectories $x_p(t)$ are computed by simultaneously integrating (Elghobashi, 1994):

$$\frac{d\mathbf{x}_p}{dt} = \tilde{\mathbf{u}}_p \tag{6.1}$$

in each coordinate direction ($\tilde{\mathbf{u}}_p$ being the particle velocity), and the equation of motion for a rigid spherical particle, which is also known as the Basset-Boussinesq-Oseen equation. Since the density of the particles injected into the cyclone is much larger than the gas density, the equation of particle motion can be simplified by neglecting the Basset force, the added mass force and the displaced mass force (Hajji et al., 1996). For particle-laden cyclone flow, all other external forces except the drag force are usually neglected as well (Boysan et al., 1982), resulting in:

$$\frac{d\tilde{\mathbf{u}}_p}{dt} = \frac{1}{\tau_p}(\tilde{\mathbf{u}} - \tilde{\mathbf{u}}_p) \tag{6.2}$$

where τ_p is the particle response time, and $\tilde{\mathbf{u}}$ is the instantaneous fluid velocity. The particle response time is given by:

$$\tau_p = \frac{\rho_p}{\rho_g}\frac{d_p^2}{18\nu}\frac{24}{C_D Re_p} \tag{6.3}$$

where C_D is the drag coefficient and Re_p is the particle Reynolds number:

$$Re_p = \frac{d_p|\tilde{\mathbf{u}} - \tilde{\mathbf{u}}_p|}{\nu} \tag{6.4}$$

At very small Reynolds numbers ($Re_p \approx 0.1$), the flow is known as Stokes flow and under these conditions: $C_D = 24/Re_p$. For higher Reynolds numbers, the drag coefficient can be approximated by means of an empirical relation given by Morsi and Alexander (1972).

In order to integrate Eq. 6.2, the instantaneous velocity of the carrier flow needs to be known at the particle position. Since the time-averaged velocity of the fluid is only known at fixed

points of the computational grid, an assumption must be made to obtain the instantaneous fluid velocity at the particle position from its time-averaged value and the turbulent quantities. MacInnes and Bracco (1992) discuss two different approaches to approximating the fluid velocity experienced by a particle, *viz.* random walk and Langevin models.

6.3.2 Particle dispersion models

The random walk models are subdivided into continuous and discontinuous or eddy-lifetime models. The eddy-lifetime model has been widely applied due to its simplicity and moderate computational demands (see *e.g.* Weber et al. (1984), Milojevic (1990), Sommerfeld (1990)). The instantaneous velocity of the gas at the particle position is estimated by adding to the calculated mean velocity a fluctuating component ($\tilde{u} = U + u$), which obeys a Gaussian probability distribution having zero mean and a variance corresponding to the local rms velocity ($\sqrt{\overline{u^2}}$). A sampled velocity fluctuation remains fixed until the eddy-lifetime has elapsed, *i.e.* during this eddy-lifetime the particle is assumed to interact with a single fluid phase eddy.

The Lagrangian autocorrelation function describes how the values of the fluid velocity $\tilde{u}(t)$ are temporally related along the particle trajectory. It is characterised by a Lagrangian integral time scale, T_L, which is a rough measure of the interval over which $u(t)$ is correlated with itself. In most discontinuous random walk models, the eddy-lifetime is taken equal to $2T_L$, and the auto-correlation function has a linear shape. An alternative way is to sample the eddy-lifetime at random from a Poisson distribution based on the integral time scale T_L, hereby assuming a decreasing exponential shape of the autocorrelation function. This is a more realistic approach in view of the experimental data available of the Lagrangian autocorrelation function in homogeneous turbulence (MacInnes and Bracco, 1992; Berlemont et al., 1998).

The continuous random walk models proposed by Berlemont et al. (1990) and Zhou and Leschziner (1991) employ a correlation function, which comprises the covariance matrix, computed from the flow field turbulence model, and an assumed shape of the temporal correlation function. Whereas the fluid velocity fluctuation in the eddy-lifetime concept is taken constant during a specific time interval, the continuous random walk models calculate a new velocity fluctuation at each numerical time step δt based on the velocity covariance matrix of the Eulerian solution and one or more previous time steps. Although the continuous variant is more sophisticated than the eddy-lifetime concept, MacInnes and Bracco (1992) show that both models predict a unphysical accumulation of particles in regions of low turbulence intensity for strongly inhomogeneous, diffusion-dominated flows. Note that this model evaluation was done for the tracer-particle limit, *i.e.* the particles were not exposed to the drag force.

A Langevin model employs a Lagrangian stochastic differential equation to compute the instantaneous fluid velocity. The advantage of this approach is that the Langevin model for particle motion can be made consistent with the Eulerian prediction obtained with a turbulence closure model (Haworth and Pope, 1985). Written as a stochastic differential equation, the Langevin equation is (Pope, 1994):

$$d\tilde{u}(t) = -\frac{\tilde{u}}{T}dt + \left(\frac{2\overline{u^2}}{T}\right)^{1/2} dW(t) \tag{6.5}$$

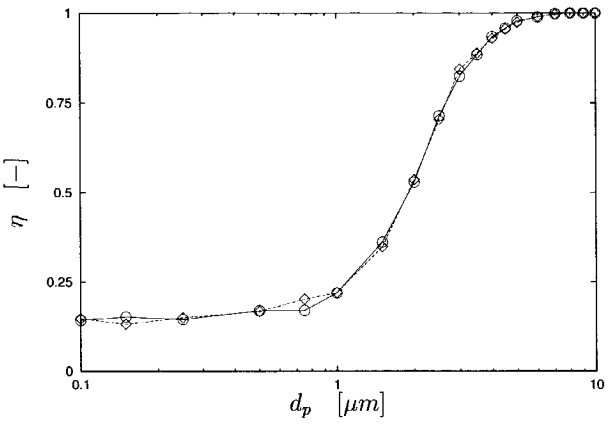

FIGURE 6.3: *Grade efficiency curves calculated by using the (○) Langevin model according to Eq. 6.5, and the (◇) eddy-lifetime model. The inlet velocity, cyclone diameter, and particle density were equal to* $15\,m\,s^{-1}$, $0.29\,m$, *and* $2,000\,kg\,m^{-3}$, *respectively. The Reynolds stress model with wall-reflection term was used to predict the gas flow field.*

where $W(t)$ is a Wiener process, and the increment in the Wiener process, $dW(t)$, can be thought of as a Gaussian random variable with mean zero, and variance dt. For this model the Lagrangian correlation function is $\exp(-t/T)$ and so T is the Lagrangian integral time scale T_L. Note that Eq. 6.5 is derived for homogeneous, stationary, one-dimensional situations with no mean flow (Thomson, 1987), and that it exhibits similar weaknesses as random walk models in the tracer-particle limit (MacInnes and Bracco, 1992).

Random walk as well as Langevin models require an expression for the Lagrangian integral time scale T_L in terms of known flow properties. This time scale is usually hard to determine experimentally, but it is suggested to take $T_L = k/3\varepsilon$ based on spectral similarity considerations (Tennekes and Lumley, 1972). Based on the Langevin equation, Pope (1994) presented several modifications and extensions for inhomogeneous flows, where the time scale T is expressed in terms of local mean velocity gradients, Reynolds stresses and dissipation of turbulent kinetic energy.

In Fluent v.4.4, two particle dispersion models are implemented, *viz.* the eddy-lifetime model and the Langevin model according to Eq. 6.5. For the latter model, the Lagrangian integral time scale is corrected for the 'crossing-trajectories' effect: a heavy particle continuously changes its fluid-particle neighbourhood so that its velocity correlation drops more rapidly with time than that of a diffusing fluid particle (Csanady, 1963). The Lagrangian time scale is reduced by a factor that is a function of the particle drift velocity $(\tilde{u} - \tilde{u}_p)$ and the turbulent kinetic energy. The particle drift velocity is averaged over a period $3T_L$.

In Fig. 6.3, grade efficiency curves obtained by using the eddy-lifetime and the Langevin model are mutually compared. The curve calculated by the Langevin model exhibits a somewhat smoother shape, but both model predictions do not differ significantly. The grade efficiency curves presented in the remainder of this chapter were all calculated by using the Langevin model. For sub-micron sized particles, the model predictions deviate from the the-

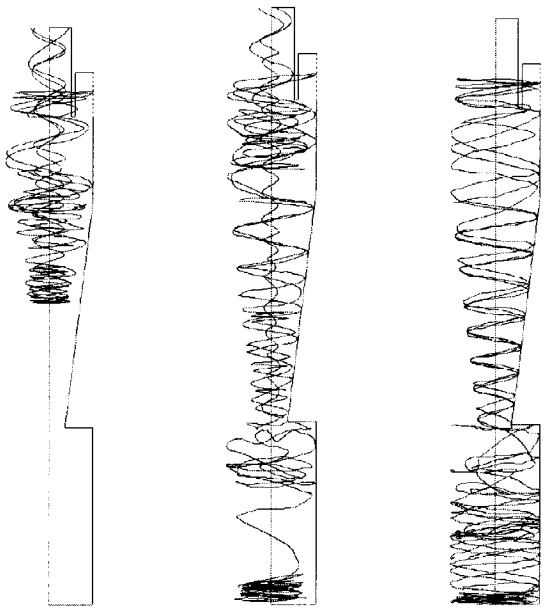

FIGURE 6.4: *Three predicted trajectories in the flow field of a Stairmand cyclone corresponding to particles with a diameter equal to (a) 0.10, (b) 2.0, and (c) 10 μm. The particles are injected halfway the cyclone inlet. Particle dispersion was predicted by the Langevin model according to Eq. 6.5. For details on the gas flow field see caption of Fig. 6.3.*

oretical shape of the grade efficiency curve; a small fraction of the particles is still collected irrespective of particle size. This could be attributed to the model weaknesses in the tracer-particle limit described earlier, *i.e.* small particles tend to accumulate in low-turbulence regions of the flow domain (*e.g.* the collection bin). Hence, a fraction of these particles injected into the cyclone could end up in the collection bin, and reach the lower side of the catch.

6.3.3 Boundary conditions

The grade efficiency curve of a cyclone is estimated by calculating the collection efficiency of a number of particle size classes. It was found out that accurate collection statistics could be obtained by calculating 1,000 trajectories for each particle size class. The stochastic nature of the particle motion is illustrated in Fig. 6.4, where trajectories are shown for three different particle size classes. Particles 10 μm in diameter migrate towards the cyclone wall immediately after injection into the cyclone, and are transported by the wall-boundary layer into the collection bin. The approximate cut-size of the cyclone is represented by the particle trajectories

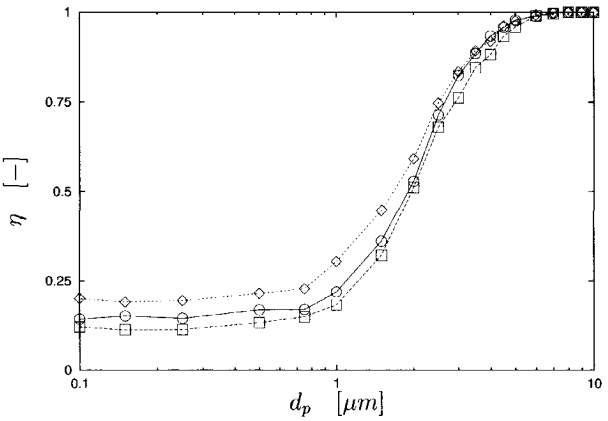

FIGURE 6.5: *The effect of collection boundary conditions on the calculated grade efficiency curve of a Stairmand cyclone: (○) lower side of the catch, (◇) lower side and side wall of the catch, and (□) lower side of the cone (no catch included).*

calculated for $d_p = 2.0\,\mu m$. Here, the figure shows that some particles are not collected, but move along with the gas in the vortex core towards the cyclone exit. Trajectories calculated for particles $0.10\,\mu m$ in diameter are not likely to reach the lower side of the collection bin.

The termination of a particle trajectory is determined by boundary conditions. At the inlet, ten particle injection points were equally spaced along its height to simulate the lateral dispersion of particles across the inlet duct. The initial particle velocity was set equal to the local mean velocity of the gas. When a particle migrates into a cell corresponding to one of the boundaries of the domain of integration, or an internal wall, one of the following boundary conditions are applied (Boysan et al., 1982; Griffiths and Boysan, 1996):

- After collision with the top wall, the inlet zone boundaries, the vortex finder, and the side wall of the cyclone and the collection bin, the particle is reflected assuming a coefficient of restitution of one. Although in practice no perfectly elastic collision of the particle with a wall will occur, it was observed that the calculated grade efficiency was not affected by using a restitution coefficient equal to 0.5.

- After collision with the lower side of the collection bin, collection is assumed.

- When the particle reaches the outlet plane of the vortex finder it is considered lost.

The lower side of the collection bin was used as a boundary condition for particle collection. Fig. 6.5 shows that the collection boundary condition mainly affects the lower tail of the grade efficiency curve. Hoffmann et al. (1996) observed a more dramatic effect of disregarding the catch in the simulation of the cyclone flow field, although for a different cyclone geometry and numerical model.

A small number of particle trajectories ($< 5\%$) do not reach a final state by reaching the collection boundary at the lower side of the collection bin or the exhaust boundary at the

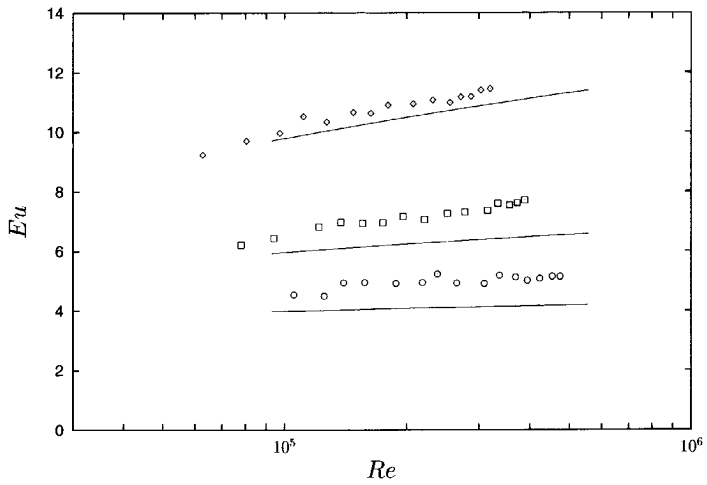

FIGURE 6.6: *Measured dimensionless pressure drop or Euler number versus Reynolds number for the Stairmand cyclone with D_e/D equal to (○) 0.50, (□) 0.40, and (◇) 0.30. The solid lines represent CFD predictions of these geometries.*

exit plane of the vortex finder within a maximum number of time steps. These particles were disregarded in the collection statistics. The maximum number of time steps was set to 10^6.

For the integration of Eq. 6.2, the time step was set to 1/20th of the cell transit time, which represents the time that it would take for a particle to cross the control volume. The mean velocity of the gas at the particle position was obtained by interpolation of the fluid velocity at the cell vertices. To improve the accuracy of the Langevin model (Eq. 6.5) an upper limit was imposed on the integration time step. This upper limit was defined as a fraction of the integral time scale ($\delta t_{max} = 0.3T$).

6.4 RESULTS AND DISCUSSION

6.4.1 Pressure drop

The pressure drop of the Stairmand geometry was measured as a function of the inlet velocity for different values of the exit pipe diameter. These results were already presented in Fig. 3.6 and compared to the theoretical pressure drop model of Stairmand (1949). It was shown that the cyclone pressure drop is strongly affected by the inlet velocity. The pressure drop is usually normalised by the inlet velocity head $\frac{1}{2}\rho_g U_{in}^2$ to obtain a dimensionless quantity known as the Euler number Eu. In Fig. 6.6, the Euler number is shown versus the Reynolds number for the Stairmand cyclone with D_e/D equal to 0.30, 0.40, and 0.50, respectively. The Reynolds number Re was calculated according to Eq. 2.6.

The measurements show that the Euler number is linearly dependent to the logarithm of the

D_e/D [−]	U_{in} $[ms^{-1}]$	$\overline{\eta}$ [−]
0.30	10	0.7450
0.50	10	0.5861
0.30	30	0.8133
0.50	30	0.7308
0.30	20	0.7842
0.50	20	0.6377
0.40	10	0.6730
0.40	30	0.7754
0.40	20	0.7264
0.40	20	0.6944
0.40	20	0.7083
0.40	20	0.6908
0.40	20	0.7326

TABLE 6.1: *Measurement results of the overall collection efficiency ($\overline{\eta}$) for different levels of the normalised exit pipe diameter (D_e/D) and the linear inlet velocity (U_{in}).*

Reynolds number for the range of inlet velocities and exit pipe diameters studied. A contraction of the exit pipe aperture results in a significantly higher Euler number. There is a combined effect of the Reynolds number and the exit pipe diameter, *i.e.* the effect of Re on Eu is larger for smaller values of D_e/D.

In the same figure, the experimental data are compared to numerical predictions obtained with the Reynolds stress model without wall-reflection term (see Ch. 5). The cyclone pressure drop was calculated as the pressure difference between the inlet and the average pressure across the vortex finder exit. The CFD model generally predicts a lower value of the Euler number or lower cyclone pressure drop. For the standard Stairmand cyclone this amounts to approximately one inlet velocity head. The simulations are consistent with the measurements, *i.e.* the CFD model predicts the combined effect of the Reynolds number and the exit pipe diameter on the Euler number, too.

6.4.2 Collection efficiency

Measurements

The linear inlet velocity and the exit pipe diameter were set at three different levels. The experimental results of the overall collection efficiency are presented in Table 6.1. The measurements were carried out in random order. The inlet velocity and exit pipe diameter were suitably coded in order to equalise their scale and minimise variance inflation. The experimental design allowed the estimation of linear and quadratic effects. The response surface model was evaluated using the statistical software tool Minitab v.12. For more detail on the aspects of response surface methodology, the reader is referred to Montgomery (1984) or Sec. 7.4 of this thesis.

The first four measurements shown in Table 6.1 represent the vertices of the experimental

Coef	Value	Rms
β_0	0.7113	0.0064
β_1	-0.06465	0.0063
β_2	0.05257	0.0063
β_{11}	-0.00237	0.0092
β_{22}	0.01088	0.0092
β_{12}	0.01910	0.0077

TABLE 6.2: *Estimated regression coefficients and their standard deviation of the response surface model for the cyclone collection efficiency.*

design or the full factorial part. The next four measurements correspond to the axial design points. The five remaining data are measurements at the centre point of the central composite design, which are used to estimate the experimental error.

The response surface model for the cyclone collection efficiency is given by

$$\overline{\eta} = \beta_0 + \beta_1 x_1 + \beta_2 x_2 + \beta_{11} x_1^2 + \beta_{22} x_2^2 + \beta_{12} x_1 x_2 \tag{6.6}$$

where

$$x_1 = \frac{D_e/D - 0.4}{0.1} \tag{6.7}$$

and

$$x_2 = \frac{U_{in} - 20}{10} \tag{6.8}$$

are the coded factors.

The parameters of Eq. 6.6 were estimated by means of least-squares regression of the experimental data. The statistical significance of the model terms was evaluated by means of an analysis of variance (ANOVA). The regression coefficients of the second-order model are summarised in Table 6.2. A statistical test showed that the square terms of the model can be disregarded at the 5% significance level.

The measurement results and the response surface predictions are shown in Fig. 6.7. The results show that the overall collection efficiency of the Stairmand cyclone increases with increasing inlet velocity and decreasing normalised exit pipe diameter. Both factors affect the maximum tangential velocity of the gas flow field, and, hence, cause a shift of the cut-size d_{50} towards smaller particle sizes. Consequently, the overall collection efficiency is improved.

There are other factors that could affect the measured collection efficiency, *e.g.* it was observed that particles were prone to stick at the interior of the cyclone for low gas velocities and large exit pipe apertures, hereby resulting in wall build-up. Since only solids deposited into the collection hopper were weighed, the overall collection efficiency was slightly underestimated under these conditions. At high gas velocities, particle attrition may affect the overall collection

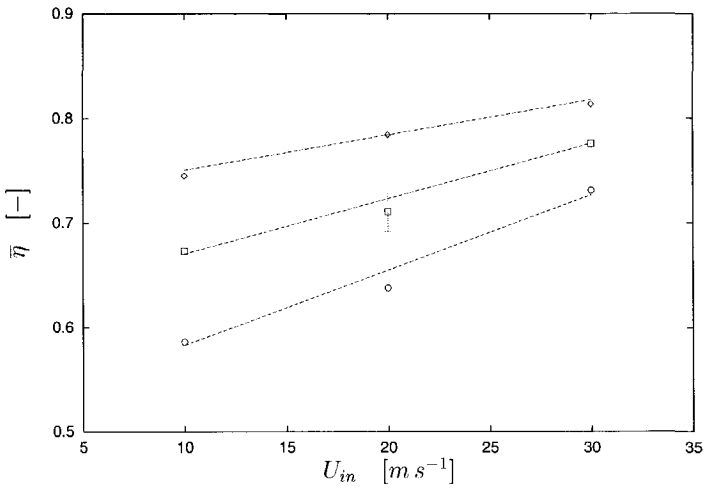

FIGURE 6.7: *Measured overall collection efficiency as a function of the linear inlet velocity for the Stairmand cyclone with D_e/D equal to (○) 0.50, (□) 0.40, and (◇) 0.30. The dashed lines are response surface model predictions (only linear and interaction terms). The error bar represents two standard deviations of the measurement error.*

efficiency due to the in-situ production of fines according to Reppenhagen and Werther (1998), although the catalyst particles studied by these authors are likely more sensitive to attrition than the calcite particles used in this study.

Simulations

The experimental data obtained for the collection efficiency of the Stairmand cyclone were used to assess CFD simulations. The grade efficiency curve was calculated for each experimental test condition by using the Langevin model (Eq. 6.5). The Reynolds stress transport model was applied as a closure model for the turbulent gas flow field. No wall-reflection terms were included. For details on the numerical model the reader is referred to Ch. 5. Collection statistics were based on tracking computational particles through the domain for a number of particle size classes, where each class was represented by 1,000 particles. The calculated grade efficiency curves are presented in Fig. 6.8.

The grade efficiency curve is usually characterised by two parameters, *viz.* a characteristic size and a slope parameter. In the literature, the shape of the grade efficiency curve is usually approximated by means of a Rosin-Rammler cumulative distribution function, or a logistic function. In this study, the logistic function was used. It has the advantage that the cut-size is equal to the size parameter used in the logistic equation, whereas for the Rosin-Rammler equation it is a function of both the size and the slope parameter.

The logistic equation is given by:

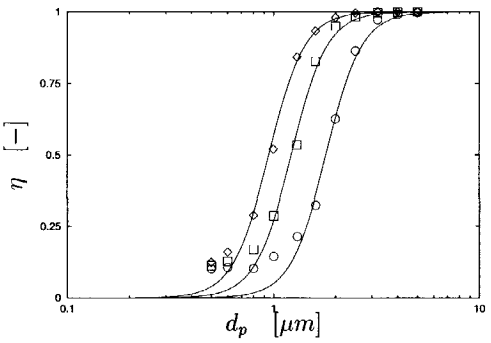

(a)

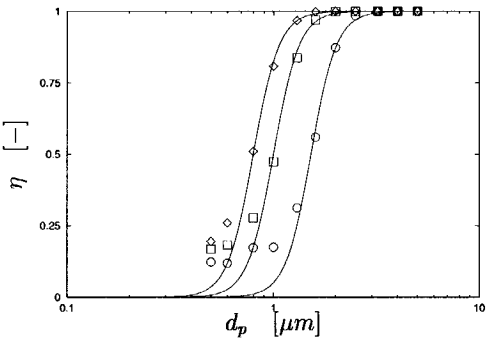

(b)

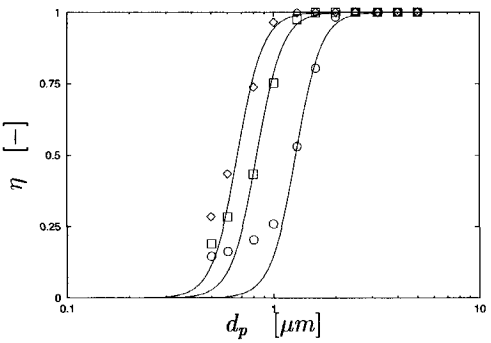

(c)

FIGURE 6.8: *Calculated grade efficiency curves for the Stairmand cyclone with D_e/D equal to (a) 0.50, (b) 0.40, and (c) 0.30. The particle density was equal to $2,740\,kg\,m^{-3}$. The data were calculated for an inlet velocity U_{in} equal to (○) 10, (□) 20, and (◇) 30 m/s. The solids lines represent the grade efficiency given by the logistic function.*

	$D_e/D = 0.50$		$D_e/D = 0.40$		$D_e/D = 0.30$	
U_{in}	d_{50}	β	d_{50}	β	d_{50}	β
10	1.80	5	1.52	7	1.28	7
20	1.22	5	1.00	7	0.83	7
30	0.95	5	0.80	7	0.67	7

TABLE 6.3: *Parameters of the logistic function used to characterise the grade efficiency curve of the Stairmand cyclone. The inlet velocity, U_{in}, and cut-size, d_{50}, are given in $m\,s^{-1}$ and μm, respectively.*

$$\eta(d_p) = 1/\left[1 + \left(\frac{d_{50}}{d_p}\right)^{\beta}\right] \qquad \beta > 0 \tag{6.9}$$

where d_{50} is the cut-size, and β the shape parameter of the grade efficiency curve. This equation is also known as the generalised Lapple equation (Overcamp and Mantha, 1998). Instead of using a least-squares fit to the data, the logistic function was determined as follows. The cut-size was estimated by interpolation of the calculated values near $\eta = 0.5$. The slope parameter of the logistic equation was chosen such that the gradient of the curve at d_{50} and the high-efficiency tail were resembled.

Fig. 6.8 shows that at the lower tail of the grade efficiency curve, the calculated efficiency deviates from the logistic fit equation. For small particle sizes, the efficiency levels off, where the level depends on the size of the exit pipe diameter. This was also observed in Fig. 6.3; this could be related to the unphysical behaviour of the model for small particle sizes.

The cut-size d_{50} and slope parameter β for the calculated grade efficiency curves are summarised in Table 6.3. The results show that a lower cut-size is obtained by increasing the inlet velocity and/or reducing the exit pipe diameter. The shape of the grade efficiency curve is slightly steeper for the cyclones with D_e/D equal to 0.30 and 0.40 compared to the standard Stairmand cyclone.

The grade efficiency η is related to the overall collection efficiency $\overline{\eta}$ by (Ontko, 1996):

$$\overline{\eta} = \int_0^1 \eta \, d\Phi \tag{6.10}$$

where Φ is the cumulative volume density distribution of the particles (see Fig. 6.2). Eq. 6.10 is illustrated for the standard Stairmand cyclone in Fig. 6.9. In this figure, the grade efficiency is shown versus the cumulative volume density distribution measured by the Malvern Mastersizer (imaginary part equal to 0.10). The area under the curve represents the overall collection efficiency of the cyclone.

Using Eq. 6.10, the overall collection efficiency was calculated for the Stairmand geometries at three different inlet velocities. The results are shown in Fig. 6.10. In Table 6.4, the predicted and measured collection efficiencies are mutually compared. For the Stairmand cyclone with $D_e/D = 0.40$, the calculated and measured collection efficiencies correspond reasonably well.

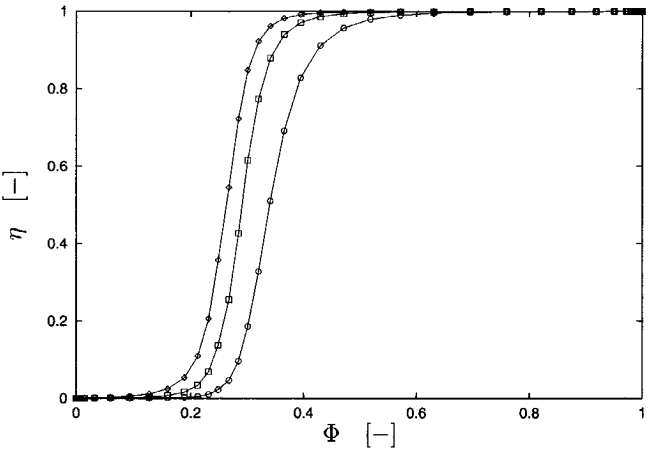

FIGURE 6.9: *Calculated grade efficiency, η, versus cumulative volume density distribution, Φ, for the standard Stairmand cyclone ($D_e/D = 0.50$) with an inlet velocity equal to (○) 10, (□) 20, and (◇) 30 $m\,s^{-1}$. The grade efficiency was approximated by a logistic function. Each symbol represents a measured particle size (see Fig. 6.2. The area under a curve represents the overall collection efficiency $\overline{\eta}$.*

	$D_e/D = 0.50$		$D_e/D = 0.40$		$D_e/D = 0.30$	
U_{in}	Exp	CFD	Exp	CFD	Exp	CFD
10	0.586	0.651	0.673	0.680	0.745	0.703
20	0.638	0.707	0.711	0.732	0.784	0.755
30	0.731	0.739	0.775	0.759	0.813	0.783

TABLE 6.4: *Comparison between the calculated and measured overall collection efficiency, $\overline{\eta}$, for the Stairmand cyclone. The inlet velocity, U_{in}, is given in $m\,s^{-1}$.*

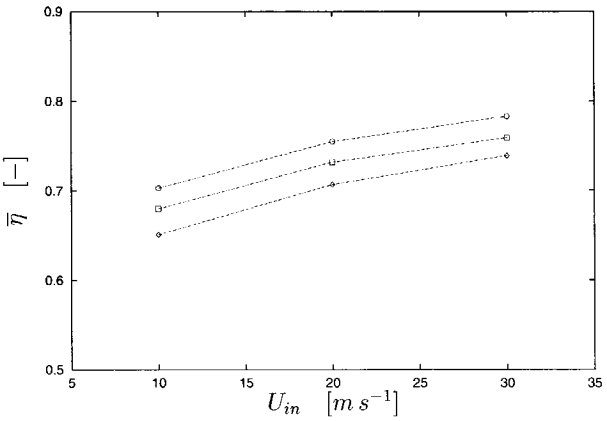

FIGURE 6.10: *Calculated overall collection efficiency as a function of the linear inlet velocity for the Stairmand cyclone with D_e/D equal to (○) 0.50, (□) 0.40, and (◇) 0.30.*

The calculated collection efficiency of the standard Stairmand geometry is somewhat higher than measured, in particular at moderate inlet velocities. For the cyclone with $D_e/D = 0.30$, the CFD model underestimates the efficiency by a few per cent. The simulations do not predict the combined effect of the inlet velocity and the exit pipe diameter that was observed experimentally.

6.5 CLOSURE

Although the measured and calculated efficiencies agree reasonably well and demonstrate similar trends with respect to the inlet velocity magnitude and the exit pipe diameter, some restrictions should be made by using collection efficiency measurements to assess CFD predictions. First, the measured volume density distribution has a large influence on the calculated efficiency data. In Fig. 6.2, it was shown that the imaginary part of the particle refractive index has a significant effect on the lower tail of the size distribution. Using the size distribution derived with an imaginary part of 1.0 instead of 0.1 (see Fig. 6.2), the calculated efficiencies are typically $5 - 12\%$ higher than the values listed in Table 6.4. Second, the CFD model does not take the build-up of particles at the cyclone wall into account. In the measurements, the accumulation of particles at the wall was clearly observed at moderate values of the inlet velocity. This does, however, not explain the combined effect of the inlet velocity and exit pipe diameter on the overall efficiency as was observed in the experiments.

The effect of the precessing vortex core on particle collection is not included in the RANS simulations or in the particle dispersion model. The experimental study on vortex precession (see Ch. 4) showed that the time scale associated with the PVC is similar or even larger than the macro time scale of the flow. Due to their size and corresponding (small) relaxation time, the calcite particles are capable of following their changing surroundings, *i.e.* the precessing vortex core would not contribute to particle dispersion. The mean gas velocity distribution,

however, would be affected by the PVC as was revealed by the adaptive filtering of LDA data (see Sec. 4.3), which implies that the particle trajectories would periodically move to and away from the cyclone wall. In addition, the PVC would likely affect the wall-boundary layer flow near the particle exit at the lower end of the cyclone. These aspects could be studied by combining particle tracking and a Large Eddy Simulation (Derksen and Van den Akker, 2000).

CHAPTER 7

DESIGN OPTIMISATION BASED ON CFD PREDICTIONS

For a number of cyclone geometries, CFD predictions are obtained of both the pressure drop and the collection efficiency. These predictions are subsequently used to obtain an algebraic equation that relates the performance of a cyclone to its operating conditions and its geometrical dimensions. The equation is derived by means of a least-mean-squares regression, while an analysis of variance was performed to assess the significance of first-order and second-order effects. By means of a non-linear optimisation procedure, optimal cyclone designs are determined that yield the lowest particle cut-size at a required flow rate and pressure drop. The application of this approach to the practical design of cyclone separators is demonstrated by an example.

7.1 INTRODUCTION

The performance of a cyclone separator is determined by a limited number of dimensionless quantities such as the Reynolds number, the Stokes number, and the relative dimensions of the cyclone. During the years, research has been carried out on the subject of *optimal* cyclones, *i.e.* the design of cyclone separators that yield the highest performance at a given duty and operating conditions. Barth (1956) argued that the performance of a cyclone is mainly determined by the ratio of the maximum swirl velocity to the mean axial velocity in the exit pipe. The value of this velocity parameter affects both the cyclone pressure drop and the collection efficiency in terms of the cut-size.

This velocity parameter was also used by Muschelknautz (1972), who proposed a diagram of optimal cyclone geometries of equivalent size and, consequently, of equal manufacturing costs, since these costs are determined by the amount of material needed for construction, and the number of cyclones. The diagram is used to select the cyclone geometry that yields the required efficiency at minimum operating costs, *i.e.* energy or pressure loss. Rumpf et al. (1968) derived model equations that relate cyclone performance to a set of geometrical and flow parameters. These equations were subsequently used in a mathematical optimisation procedure. In all these approaches the main issue of concern is the applicability of the underlying model equations,

a/D	b/D	D_e/D	S/D	h/D	H/D	c/D
0.50	0.20	0.50	0.50	1.50	4.0	0.375

TABLE 7.1: *Characteristic dimensions of the Stairmand high efficiency cyclone.*

and their validity in the range of geometries and conditions studied.

More recently, Iozia and Leith (1989) performed an experimental study of a number of cyclone test designs to derive a functional relationship between cyclone performance and input parameters. They characterised the gas flow field of a number of cyclones by measuring the maximum tangential velocity and the diameter of the vortex core. These parameters were used to estimate the cut-size by balancing the centrifugal and drag forces acting on a particle. By using regression techniques, the cyclone cut-size could be described as a function of its dimensions. A similar study was performed to approximate the grade efficiency curve by a logistic function, which depends on the cut-size and a slope parameter (Iozia and Leith, 1990).

Although of a less generic nature, empirical models that are obtained by fitting experimental data usually provide better estimates of cyclone performance than models based on a theoretically derived flow pattern. Ramachandran et al. (1991) derived empirical model equations that relate the pressure drop and cut-size to cyclone design and operation. This model was subsequently used in a mathematical optimisation study.

In this study, CFD calculations are used instead of experiments to relate the pressure drop and the collection efficiency to the dimensions of a cyclone separator. An evident advantage of CFD calculations with respect to experiments is that a large number of flow and geometry variables can be varied at relative low costs. By means of a response surface methodology, an equation is derived that relates these variables to cyclone performance. This model can be used for optimising the design given a required performance level. An example will be given to illustrate this approach.

7.2 CYCLONE SIMILARITY PARAMETERS

In the literature, most cyclones designed for gas-solids separation emanate from the high-efficiency cyclone proposed by Stairmand (1951). The high-efficiency cyclone separator is defined by seven design ratios, which relate the dimensions of the cyclone to the barrel diameter. In Fig. 7.1, the geometrical lay-out of the high-efficiency Stairmand cyclone is shown. Its characteristic dimensions are summarised in Table 7.1. The particle loaded gas flow is injected into the cyclone by means of a tangential inlet. To supply a larger flow rate, a scroll type of inlet is usually preferred to prevent gas and particles colliding with the exit pipe in the cyclone interior. This design is referred to as a high-gas rate cyclone (Stairmand, 1951). The particles are collected in the catch bin, which has a diameter equal to and a length of twice the cyclone body diameter to prevent re-entrainment of particles already separated.

The performance of a cyclone is usually assessed in terms of its collection efficiency and pressure drop. The overall collection efficiency, $\overline{\eta}$, is the captured fraction of the particulate mass entering the cyclone, and therefore depends, among others things, on the particle size distribution of the feed. The fractional or grade efficiency, $\eta(d_p)$, describes the variation of the collection efficiency with particle size, d_p, and is related to the overall efficiency by:

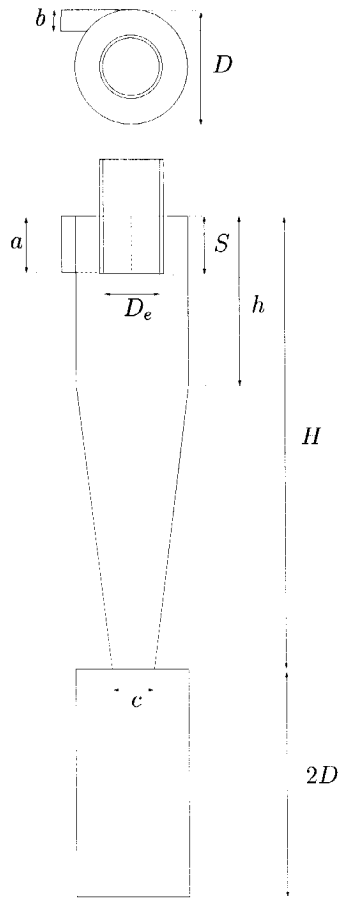

FIGURE 7.1: *Schematic representation of the high-efficiency cyclone after Stairmand (1951).*

$$\overline{\eta} = \int_{d_{min}}^{d_{max}} \eta(d_p)\ \phi(d_p)\ \mathrm{d}\, d_p \tag{7.1}$$

where $\phi(d_p)$ represents the particle size distribution at the inlet. In Eq. 7.1, the fractional efficiency is assumed to be independent of the particle size distribution. The cut-size, d_{50}, represents the particle size that corresponds to 50% collection efficiency, and is often used to characterise the cyclone performance rather than the overall efficiency.

Cyclone studies presented in the literature (*e.g.* Bernard (1992)) have identified that the grade efficiency is affected by the properties of gas and particles, *viz.* the gas density ρ_g, the gas dynamic viscosity μ, the particle density ρ_p, and the particle size d_p. The gas-particle flow is characterised by the volumetric flow rate, ϕ_v, which is the product of inlet velocity and inlet cross sectional area, and by the particulate mass loading, C. Here, the effects of mass loading on pressure drop and collection efficiency are not considered, because only one-way interaction between the phases was taken into account by the CFD model. Hence, the results presented are valid for cyclones operating at low-solids loading only (see Sec. 6.3). Other factors associated with the particulate phase, such as attrition and friability, are disregarded, too. The centrifugal force field in the cyclone is determined by the flow velocity at the inlet, U_{in}, the diameter, D, of the cyclone, and the remaining geometrical dimensions.

Provided that these variables are sufficient to describe the separation of gas and particles in a cyclone, the cut-size for a Stairmand high-efficiency cyclone can be expressed as a function of these dimensional variables:

$$d_{50} = f\left(U_{in}, \rho_p, \rho_g, \mu, D, a, b, D_e, h, H, S, c\right) \tag{7.2}$$

in which f is an unknown function (Overcamp and Scarlett, 1993). Since there are 13 dimensional variables and three independent dimensions, the number of dimensionless quantities that can be identified by using Buckingham's Π theorem is 10 (Bird et al., 1960). Eq. 7.2 can be written in a dimensionless form as

$$\frac{d_{50}}{D} = f'\left(Re, \frac{\rho_p}{\rho_g}, \frac{a}{D}, \frac{b}{D}, \frac{D_e}{D}, \frac{h}{D}, \frac{H}{D}, \frac{S}{D}, \frac{c}{D}\right) \tag{7.3}$$

in which f' is an unknown function, and the Reynolds number, Re, is defined as:

$$Re = \frac{\rho_g U_{in} D}{\mu} \tag{7.4}$$

The characteristic dimensions of the Stairmand cyclone were listed in Table 7.1. A dimensionless quantity conventionally taken to be a similarity parameter for the cyclone cut-size is the Stokes number, Stk_{50} (Ontko, 1996). For cyclone flow, the Stokes number is defined as the ratio of the particle relaxation time and a macro time scale of the flow, and may be written as a product of three dimensionless variables:

$$Stk_{50} = \left(\frac{\rho_p d_p^2}{18\mu}\right)\left(\frac{U_{in}}{D}\right) = \frac{1}{18}\left(\frac{\rho_p}{\rho_g}\right)\left(\frac{d_p}{D}\right)^2 Re \tag{7.5}$$

Combining Eq. 7.3 and Eq. 7.5, the cyclone cut-size is only a function of the Stokes number, Stk_{50}, for geometrically similar geometries at low solids loading. Provided that the density ratio, ρ_p/ρ_g, scales linearly with the Stokes number, Eq. 7.3 can be reduced to:

$$Stk_{50} = f''\left(Re, \mathbf{geometry}\right) \tag{7.6}$$

where **geometry** represents the characteristic geometrical dimensions of the cyclone normalised by the cyclone body diameter.

In the CFD model, cyclone pressure drop is assumed to be independent of the properties of the particulate phase. The pressure drop is conventionally normalised by the velocity head $\frac{1}{2}\rho_g U_{in}^2$ yielding for the dimensionless pressure drop or Euler number:

$$Eu = g\left(Re, \mathbf{geometry}\right) \tag{7.7}$$

in which g is an unknown function.

A parameter often used to characterise swirling flow is the swirl number, which is a measure of the ratio of angular to axial momentum fluxes. For cyclones, the geometric swirl number is a function of cyclone body diameter, exit pipe diameter, and inlet cross sectional area. The swirl number is known to affect the gas flow field in the cyclone significantly (Gupta et al., 1984). In this study, the number of cyclone dimensions considered in Eq. 7.6 and Eq. 7.7 was limited to the normalised height, a/D, and width, b/D, of the inlet section, and the diameter of the exit pipe, D_e/D. The other four cyclone dimensions are generally expected to affect the body volume of the cyclone, and, consequently, the residence time of gas and particles. The effect of the length of the cyclone was studied by varying the length of the cylindrical part of the cyclone body, or $(h - S)/D$ in terms of the geometrical dimensions listed in Fig. 7.1. At the same time, the length of the exit pipe in the interior of the cyclone was kept equal to the inlet height, $S = a$, while the conical section was not modified.

7.3 Model set-up

7.3.1 Response surface design

Experiments are usually carried out to investigate the relationship between input parameters (factors) and output parameters (responses). This relationship is often approximated quantitatively by using design of experiment (DOE) and regression techniques. Methods that are directed towards this kind of investigation are usually referred to as response surface methodology (RSM) (Box and Draper, 1987). The response surface represents the way a variable of interest depends on two or more factors. The basic idea of RSM is the following: suppose that a response surface is sufficiently smooth for a particular domain of interest and, hence, can be

approximated by a low-order polynomial of, *e.g.* , first or second order. The coefficients of the polynomial are then estimated from an appropriate experimental design; on this basis, the response can be predicted at any point in the domain of interest. The preferred factor settings are indicated if an optimum exists on the response surface. For the simultaneous investigation of more than one response, a multiple optimisation procedure is needed.

Provided that the response surface is adequately fit by a second-order model, the estimated response y for k input variables is given by (Hinkelmann and Kempthorne, 1994):

$$y(X_1, X_2, ..., X_k) = \beta_0 + \sum_{i=1}^{k} \beta_i X_i + \sum_{i=1}^{k} \beta_{ii} X_i^2 + \sum_{i<j} \beta_{ij} X_i X_j + e(X_1, X_2, ..., X_k) \qquad (7.8)$$

where X_i is the level setting of factor i, β_i, β_{ii} and β_{ij} represent regression coefficients for the linear, quadratic and interaction terms, and e is the error. Note that Eq. 7.8 is a *linear* model, because the response is a linear function of the model parameters. There are two sources of error, *viz.* an experimental error, and a lack-of-fit error; the latter incorporates higher order terms or interactions. It was not possible to estimate the experimental error due to the deterministic character of the CFD model applied in this study; as a result, the error term only relates to the model capability.

It was argued in the previous section that the performance of a cyclone separator is affected by at least five factors. A way to estimate the parameters of Eq. 7.8 is to study the response for all (combinations of) factors set at three different levels. This full factorial design would require $3^5 = 243$ different CFD simulations. However, the number of degrees of freedom (df) of the second-order model is only $2k + \frac{1}{2}k(k-1)$, which is equal to 20 for a five factor design. A more suitable design to estimate the regression coefficients with a limited number of points is the central composite design (Box and Draper, 1987). For this study, the design points of the central composite design were located on a face centred hypercube, which is composed of three parts: (1) a full factorial part of 2^k vertices, (2) an axial part of $2k$ points at the origin of each factor axis, and (3) a centre point. This set-up results in a central composite design of five factors demanding only 43 CFD calculations, which is a considerable reduction compared to the three level factorial design.

The regression coefficients of Eq. 7.8 are estimated by use of a least squares method. Since the variance of the model parameters depends on both the mean square error (MSE) and the factor magnitude, it is convenient to scale the factor level as follows:

$$x_i = \frac{X_i - \overline{X_i}}{\frac{1}{2}(X_{iH} - X_{iL})} \qquad (7.9)$$

where X_{iH} and X_{iL} denote the high and low level of the ith factor, respectively, and $\overline{X_i}$ is the mean level. In coded units, the high and low levels become $x_{iH} = 1$ and $x_{iL} = -1$, respectively, and the mean factor level, $\overline{x_i}$, is equal to zero. Coded factor levels are used in the so-called design-model matrix, which represents all points needed in the central composite design.

The significance of the regression coefficients is determined by means of an analysis of variance (ANOVA) of the linear model. The idea of ANOVA is to partition the total sum of

squares, SS_{total}, into components that are related to the model terms, SS_{model}, and the residual error, SS_{res}. The significance of the model terms can then be tested by means of an F-test. For the design and evaluation of the cyclone performance model, the statistical software program Minitab V12 was used (Minitab Inc., 1998).

7.3.2 CFD model

The CFD calculations of the gas-particle flow in a number of cyclone geometries were performed by the flow solver Fluent V4.4 in an Eulerian-Lagrangian framework with one-way coupling between the phases, *i.e.* the particulate phase did not affect the fluid phase. The steady-state, axi-symmetric Reynolds averaged Navier-Stokes (RANS) equations were solved with an additional turbulence closure model. It was shown in Ch. 5 that the Reynolds stress transport model (RSTM) is capable of predicting the turbulent vortex flow in a cyclone at a fair degree of accuracy. No wall reflection terms were included in the RSTM, because it was observed that the RSTM without these terms yields an improved prediction of the cyclone flow field, especially for designs with a small exit pipe diameter.

Whereas, for a 3D simulation, the boundary conditions can be naturally imposed at the inlet cross section of the cyclone by the linear inlet velocity, this is more complicated for the axisymmetric case. The inlet conditions for the axisymmetric case are modelled by imposing a mean radial and tangential velocity component along the inlet height, which define the volumetric flow rate, ϕ_V, and the angular momentum at the inlet, WR, respectively. In the simulations it is assumed that the tangential velocity component W at the cyclone radius R is equal to the linear inlet velocity, U_{in}. The turbulent quantities at the inlet were uniformly imposed and estimated from a turbulence intensity set to 10%, and a characteristic length scale equal to the inlet width. The boundary conditions at the outlet of the cyclone were prescribed by zero streamwise gradients for all flow variables. In all simulations, the convective fluxes were approximated by a bounded QUICK-scheme. Converged solutions were obtained at numerical grid up to 14,000 grid cells.

The grade efficiency curve was estimated by calculating the trajectories of 1,000 computational particles in the cyclone flow field for a range of particle-size classes. The particles were injected into the computational domain at ten equally spaced positions along the inlet height. The dispersion of particles due to the turbulent fluid motion is taken into account by a stochastic process that depends on the turbulent properties of the fluid flow. Collection statistics were obtained by assuming that particles colliding with the lower side of the catch bin are collected while those that leave through the exit will escape. Collisions between particles and the cyclone wall, the top wall, and the walls of the inner and outer exit pipe are assumed to be perfectly elastic with a coefficient of restitution equal to one. For more details on the model, the reader is referred to Ch. 5 and Ch. 6.

7.3.3 Responses and factors

The response surface model requires a prediction of the performance parameters, *i.e.* the pressure drop and grade efficiency curve. The pressure drop is estimated from the difference between the total pressure head averaged at the inlet and the outlet planes. The Euler number is subsequently obtained by normalising the pressure drop with the inlet velocity head. The

factor	coded	min	max
D_e/D	x_1	0.30	0.70
a/D	x_2	0.30	0.80
b/D	x_3	0.15	0.35
$(h-S)/D$	x_4	0.50	2.50
$\ln(Re)$	x_5	10.4	15.0

TABLE 7.2: *Low and high level settings of the factors used in the response surface model.*

grade efficiency curve is approximated by the logistic function (Eq. 6.9), which is described by a cut-size and a slope parameter (see Sec. 6.4). The estimated value for the cut-size is used to calculate the Stokes number, Stk_{50}.

The high and low levels of the geometrical design ratios were chosen to include a wide range of both high-efficiency and high-throughput industrial cyclones. In Table 7.2, these level settings are presented. The coded factor levels correspond to -1, 0, and 1 according to Eq. 7.9, and the factors are denoted by x_i.

The geometric swirl number of the investigated cyclone geometries varied between ≈ 1 and 12. The levels chosen for the Reynolds number are based on the operating window for the inlet velocity, $U_{in} = 2 - 30\,m\,s^{-1}$, and a size range for industrial cyclones, $D = 0.25 - 1.5\,m$, at ambient conditions ($\nu = \mu/\rho_g \approx 1.5\ 10^{-5}\,m^2\,s^{-1}$). The effect of the Reynolds number was considered on a logarithmic scale. In the CFD simulations, the Reynolds number was set by varying the dynamic viscosity, μ, from $3.16\ 10^{-4}\,N\,s\,m^{-2}$ to $3.16\ 10^{-6}\,N\,s\,m^{-2}$, while the other flow parameters were kept constant, *viz.* $U_{in} = 10\,m\,s^{-1}$, $D = 1.0\,m\,s^{-1}$, and $\rho_g = 1.0\,kg\,m^{-3}$. The density ratio of solids to gas was equal to 1,000.

7.4 RESULTS AND DISCUSSION

The results of the CFD predictions on cyclone performance are summarised in Sec. 7.7 for all geometries studied. The results were used to fit the response surface for three performance parameters, *viz.* the Euler number, Eu, the Stokes number related to the cut-size, Stk_{50}, and the slope parameter of the logistic function, β. The response surface models for the pressure drop and the collection efficiency are consecutively presented and discussed. In the next section, the responses are applied in an optimisation study.

7.4.1 Pressure drop

The 21 coefficients of the second-order model (Eq. 7.8) for the Euler number were estimated by linear regression. The analysis was done using coded units. In Table 7.3, the analysis of variance of the response surface model is presented. The sum of squares related to the model is subdivided into contributions due to the linear, square and interaction terms. The mean sum of squares (MS) of the model and error term is obtained by dividing the sum of squares (SS) by its corresponding number of degrees of freedom (*df*'s). The overall fit is assessed by an F-test of the hypothesis H_0 : All regression coefficients, except β_0, are zero. The test statistic F_0 is

Source	df	SS	MS	F_0	p
Model	20	756.5	37.82	49.71	0.000
Linear	5	595.7	119.1	155.6	0.000
Square	5	28.80	5.759	7.568	0.000
Interaction	10	132.0	13.20	17.35	0.000
Error	22	16.80	0.761		
Total	42	773.2			

TABLE 7.3: *ANOVA for full quadratic model for the Euler number.*

Source	df	SS	MS	F_0	p
Model	11	751.0	68.28	95.35	0.000
Linear	5	595.7	119.1	166.4	0.000
Square	1	28.63	28.63	39.98	0.000
Interaction	5	126.7	25.35	35.40	0.000
Error	31	22.20	0.716		
Total	42	773.2			

TABLE 7.4: *ANOVA for reduced quadratic model for Euler number.*

obtained by dividing the model and error mean sum of squares. Similar test statistics were obtained for the linear, square, and interaction terms from the sequential sums of squares. The calculated p-values for the model terms are all smaller or equal to 10^{-3}. These values indicate that there is sufficient evidence that the quadratic model is adequate for likely Type I error rates (Hinkelmann and Kempthorne, 1994).

The null hypothesis was also tested for each regression coefficient of Eq. 7.8 by means of a T-test. The ratio of a coefficient and its standard deviation is used as a test statistic. The full quadratic model for the Euler number was reduced by evaluating the calculated p-value for each regression coefficient against a 99% confidence level ($\alpha = 0.01$). The ANOVA for the reduced quadratic model is presented in Table 7.4.

It is seen that the number of model coefficients can be reduced considerably. Only one square term is significant, while the number of interaction terms is reduced by a factor of two. In addition, the mean square error due to lack-of-fit is slightly decreased. The non-zero coefficients of the reduced quadratic model are listed in Table 7.5. The coefficient of determination adjusted for the appropriate number of df's, $R^2(adj)$, was 96.1%.

The response surface for the Euler number can be visualised as a function of two different factors. This is presented in Fig. 7.2 for all combinations of factors with significant interaction. The response surface exhibits a considerable curvature due to the interaction of the factor D_e/D with the other factors. The curvature of the response surface for the inlet height and width is very small.

The coefficients for the main effects (see Table 7.5) show that the Euler number increases linearly with increasing inlet height (a/D), inlet width (b/D) and the logarithm of the Reynolds number ($\ln(Re)$). Both the height and the width of the inlet section affect the flow rate injected

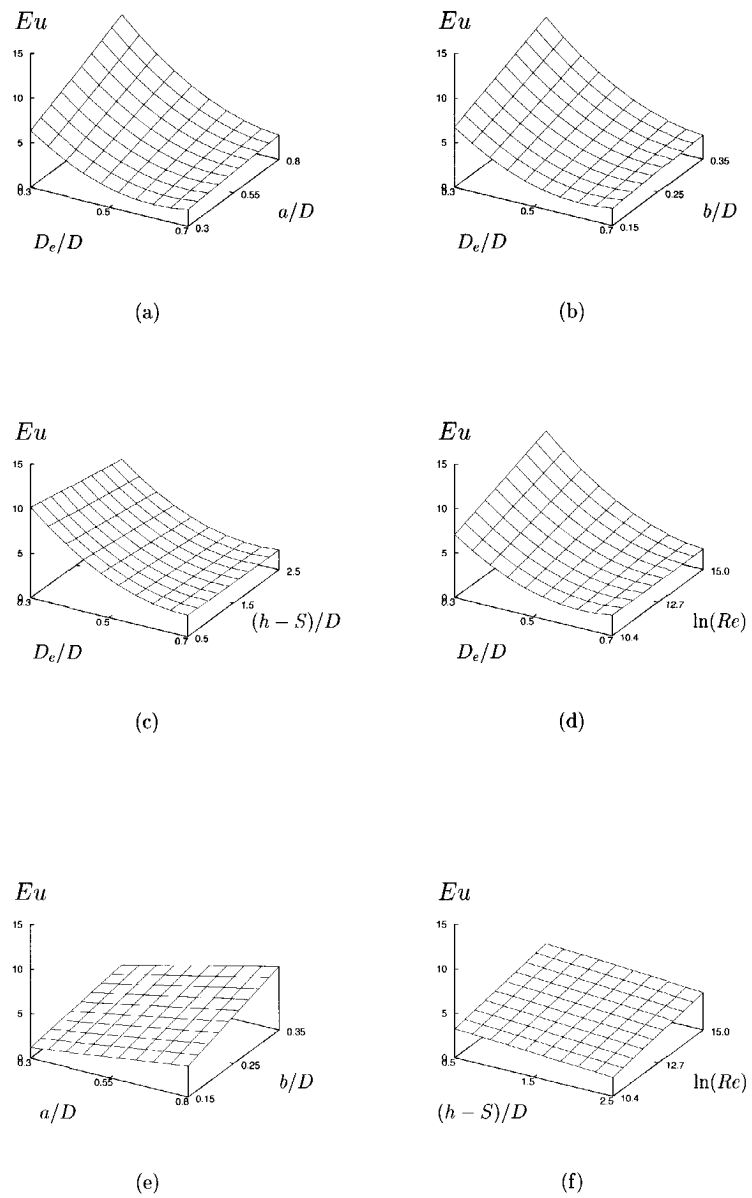

FIGURE 7.2: *Response surfaces as a function of two different factors for the Euler number. The reduced quadratic model was used to represent the interactions (see Table 7.5).*

Term	Coef	Value	Rms
Const	β_0	3.71	0.28
D_e/D	β_1	-3.41	0.15
a/D	β_2	1.61	0.15
b/D	β_3	1.39	0.15
$(h-S)/D$	β_4	-0.56	0.15
$\ln(Re)$	β_5	1.03	0.15
$D_e/D * D_e/D$	β_{11}	2.01	0.32
$D_e/D * a/D$	β_{12}	-1.19	0.15
$D_e/D * b/D$	β_{13}	-1.02	0.15
$D_e/D * (h-S)/D$	β_{14}	0.47	0.15
$D_e/D * \ln(Re)$	β_{15}	-1.04	0.15
$a/D * b/D$	β_{23}	0.46	0.15

TABLE 7.5: *Regression coefficients and their standard deviation (rms) of the response surface model with coded factors for the Euler number.*

into the cyclone. This is consistent with the pressure drop equations of Stairmand (1949) and Barth (1956), which both predict a larger Euler number if the inlet area is increased.

The effect of the Reynolds number on the Euler number is explained qualitatively in terms of the wall friction factor, *i.e.* for a turbulent boundary layer the friction factor is a linear function of the logarithm of the Reynolds number (*cf.* Blasius formula or the experimental work of Muschelknautz and Krambrock (1970)). A reduction of the friction factor results in a higher maximum tangential velocity, and, consequently, a larger velocity head of the vortex. Since the formation of the vortex contributes significantly to the total pressure drop, the Euler number is increased as well.

Increasing the cyclone length results in a higher loss of momentum due to wall friction, which is proportional to the interior wall surface. However, the Euler number is reduced due to its attenuating effect on the velocity head of the vortex. The only square effect in the model is related to the diameter of the exit pipe, *i.e.* Eu is a concave function of D_e/D. The strong effect of the exit pipe diameter on the maximum tangential velocity and the pressure drop is well known and was confirmed by experiments (see Ch. 3).

The advantage of the response surface approach is its ability to identify relevant interactions between input parameters. It is shown that especially the interaction between the exit pipe diameter and the other factors has a significant effect on the pressure drop. The interaction between the height and width of the inlet suggests a small effect of the inlet section aspect ratio on the pressure drop. One CFD prediction deviates $> 3\sigma$ from the response surface model; it corresponds to the upper bound of the variable range.

7.4.2 Collection efficiency

For each point in the central composite design, the grade efficiency curve was calculated by means of tracking particle trajectories. The grade efficiency curve is approximated by the logistic function of Eq. 6.9 to yield an estimate of the cut-size, d_{50}, and the slope parameter,

Source	df	SS	MS	F_0	p
Model	14	69.60	4.971	74.63	0.000
Linear	5	50.85	10.17	152.7	0.000
Square	2	4.290	2.145	32.20	0.000
Interaction	7	14.45	2.065	31.00	0.000
Error	28	1.865	0.067		
Total	42	71.46			

TABLE 7.6: *ANOVA for the reduced quadratic model of the Stokes number,* $\ln(Stk_{50})$.

β. In Fig. 7.3, calculated grade efficiency curves and their corresponding fits are presented for three different normalised inlet areas ($a/D * b/D$). The exit pipe diameter, D_e/D, was varied between the low and high level. The other factors were set at the lowest level.

The exit pipe diameter strongly affects the grade efficiency curve with respect to the cut-size and the slope parameter. By increasing the flow rate, the curve is also transposed towards smaller particle size, except if the inlet height and width are at their respective maximum magnitude. Some efficiency calculations are not readily fit by the logistic function, in particular the low efficiency tail of the curve for cyclones with $D_e/D = 0.3$. For the largest inlet area, the calculated curve too shows a stronger deviation from the logistic equation. The procedure of fitting the logistic function to the calculated fractional efficiency data was already mentioned in Sec. 6.4, The fitted values of the cut-size, d_{50}, and the slope parameter, β, are listed in Sec. 7.7 for all points of the response surface design.

The cut-size is used to calculate the Stokes number, Stk_{50}, according to Eq. 7.5. Analysis of the response surface model showed that the regression benefits from a logarithmic transformation of the Stokes number. At a confidence level of 95% the full quadratic model of $\ln(Stk_{50})$ could be reduced by omitting a number of square and interaction terms. The ANOVA table for the reduced model with $R^2(adj) = 96.1\%$ is given in Table 7.6. The regressions coefficients in coded units are presented in Table 7.7.

In Fig. 7.4, the response surface for Stk_{50} is presented for different combinations of factors. The regression coefficients show that the Stokes number is a concave function of the inlet area by varying the inlet height a/D or the inlet width b/D. Similar to the model for the Euler number, the interaction between the inlet height and width is significant, *i.e.* the aspect ratio of the inlet cross section affects cyclone performance. The model predicts a smaller Stokes number or cut-size for a higher Reynolds number. This is consistent with the results reported by Overcamp and Scarlett (1993). Furthermore, there is a significant interaction between the Reynolds number and the four geometrical factors.

Increasing the exit pipe diameter results in a larger value for the cut-size, which is explained by the effect of the exit pipe diameter on the vortex in the cyclone. By increasing the cylindrical section of the cyclone, a smaller mean radial velocity directed inwards results in a smaller cut-size. The response surface model also predicts this effect. The negative coefficient for the interactions $a/D * (h - S)/D$ and $b/D * (h - S)/D$ is related to the mean residence time of gas and particles in the cyclone. Injecting a large flow rate (high $a/D * b/D$ level) into a cyclone with a small volume (low $(h - S)/D$ level), or vice versa, affects the cut-size negatively. Again, one point at the edge of the variable range has a large residual error.

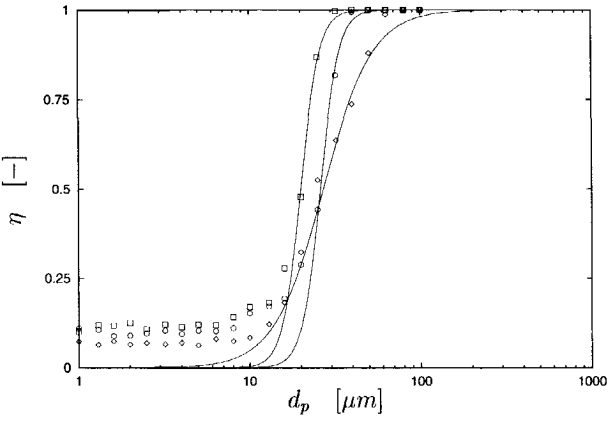

(a) $D_e/D = 0.30$

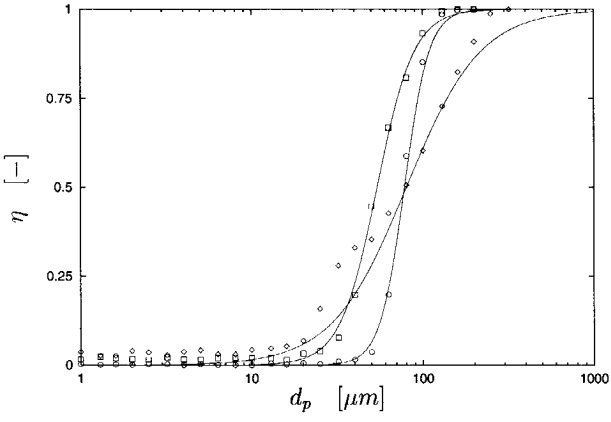

(b) $D_e/D = 0.70$

FIGURE 7.3: *Calculated grade efficiencies for different particle size as a function of the normalised inlet area, where $a/D * b/D$ equals (○) 0.045, (□) 0.12, (◇) 0.28. The solid curves represent fits using the Eq. 6.9.*

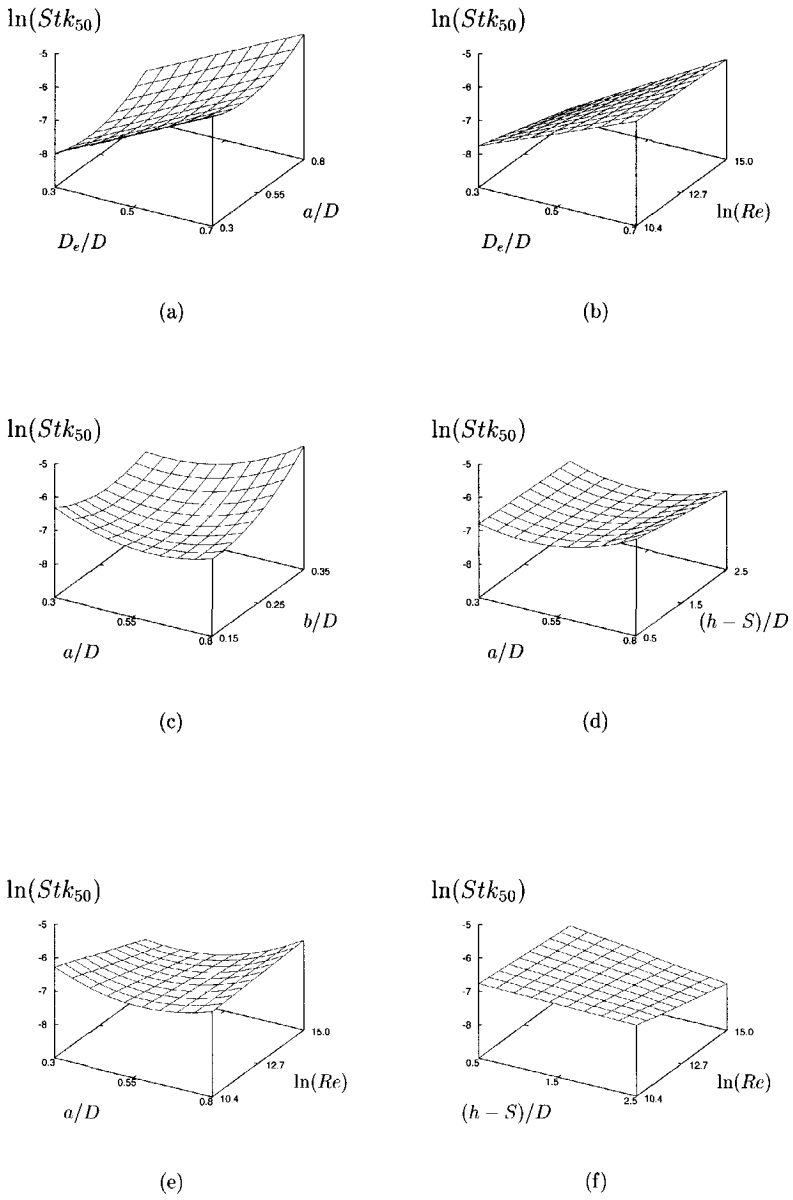

FIGURE 7.4: *Response surfaces as a function of two different factors for the Stokes number* ($\ln(Stk_{50})$). *A reduced quadratic model was used (see Table 7.7).*

Term	Coef	Value	Rms
Const	β_0	-7.072	0.091
D_e/D	β_1	1.129	0.044
a/D	β_2	0.239	0.044
b/D	β_3	0.268	0.044
$(h-S)/D$	β_4	-0.167	0.044
$\ln(Re)$	β_5	-0.252	0.044
$a/D * a/D$	β_{22}	0.456	0.14
$b/D * b/D$	β_{33}	0.381	0.14
$D_e/D * \ln(Re)$	β_{15}	0.189	0.046
$a/D * b/D$	β_{23}	0.422	0.046
$a/D * (h-S)/D$	β_{24}	-0.102	0.046
$a/D * \ln(Re)$	β_{25}	0.323	0.046
$b/D * (h-S)/D$	β_{34}	-0.110	0.046
$b/D * \ln(Re)$	β_{35}	0.313	0.046
$(h-S)/D * \ln(Re)$	β_{45}	-0.116	0.046

TABLE 7.7: *Regression coefficients and their standard deviation of the response surface model with coded factors for the Stokes number,* $\ln(Stk_{50})$.

Although the cut-size is a good indicator for the collection efficiency of a cyclone, an additional model is needed for the shape parameter β of the logistic function. The ANOVA of the full quadratic model for β showed that only the linear terms are significant for a confidence level of 95%. However, the linear model is a rather poor fit with a $R^2(adj)$ of only 58.5%. The regression coefficients of the linear model are listed in Table 7.8.

It is shown that increasing the inlet area of the cyclone affects the sharpness of the grade efficiency curve negatively. This was already demonstrated in Fig. 7.3 for the highest level of a/D and b/D. A contraction of the exit pipe diameter and a higher Reynolds number result in a larger value for the slope parameter. The effect of the factor $(h-S)/D$ on the sharpness of the grade efficiency curve is small and has a low p-value. The low value of $R^2(adj)$ suggests that a linear or quadratic model is inadequate for modelling the β response surface.

Term	Coef	Value	Rms
Const	β_0	4.79	0.21
D_e/D	β_1	-0.60	0.24
a/D	β_2	-1.24	0.24
b/D	β_3	-1.09	0.24
$(h-S)/D$	β_4	0.19	0.24
$ln(Re)$	β_5	-0.68	0.24

TABLE 7.8: *Coefficients of linear response surface model for the slope parameter,* β, *of the logistic function (Eq. 6.9) obtained by regression of coded factors.*

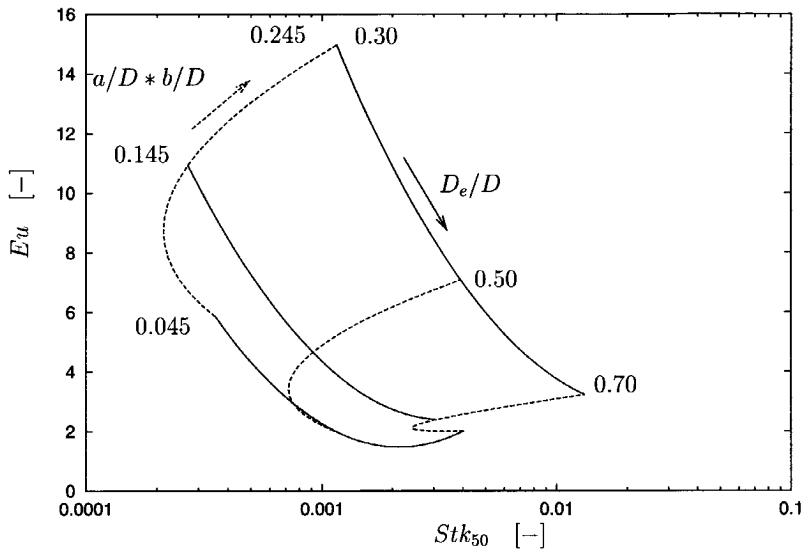

FIGURE 7.5: *Performance diagram based on Stairmand cyclone with* $(h - S)/D = 1.0$ *and* $Re = 10^6$. *Curves are given for constant normalised (–) inlet area, and (- -) exit pipe diameter.*

7.5 MULTIPLE RESPONSE OPTIMISATION

7.5.1 Cyclone performance diagram

The response surface models derived in the previous section can be used to estimate the performance of a specific cyclone separator design. Cyclone capability can be visualised by means of a performance diagram, which is a two-dimensional representation of the responses in parameter space. An example of a performance diagram is given in Fig. 7.5. In this figure, the Euler number, Eu, is presented versus the Stokes number related to the cut-size, Stk_{50}, for the baseline design of the Stairmand cyclone with $(h - S)/D = 1.0$. The Reynolds number was equal to 10^6, which corresponds to a cyclone of industrial size operating under ambient conditions.

The curves represent three levels of the normalised inlet area, $a/D * b/D$ and the exit pipe diameter, D_e/D. Since the interaction between the inlet height and width is significant in the response surface model of both Eu and Stk_{50}, the aspect ratio of the inlet area was kept constant $(a/b = 2.0)$. The performance diagram exhibits a complicated shape. Increasing the inlet area results in a larger Euler number, whereas the Stokes number can be minimised for a specific inlet cross sectional area. Fig. 7.5 is useful to identify alternative geometrical layouts if one of the performance parameters is bounded by the operating conditions, *e.g.* the pressure drop may not exceed a specified level, or environmental regulations prohibit the emission of a specific particle size.

From a practical point of view, the reverse approach would be preferred, *i.e.* designing the

optimal cyclone design with respect to the cut-size at a given pressure drop. This requires a mathematical optimisation procedure of the response surface. Since the model equations for the Euler number and the Stokes number are of second order, we are dealing with a so-called *nonlinear programming* problem (see *e.g.* Hillier and Lieberman (1995)). The application of nonlinear programming to cyclone design optimisation is illustrated in the following section.

7.5.2 Optimal cyclone separators

Cyclones are commonly designed to handle a required throughput of gas, loaded with particles. The gas flow rate determines the number of cyclone separators needed, and their size. The aim is to design a cyclone with superior performance characteristics, *e.g.* a geometry that yields the highest collection efficiency at a given pressure drop. Using the cut-size as an indicator for the collection efficiency, the nonlinear programming problem is to find $\mathbf{x} = (x_1, x_2, x_3, x_4, x_5)$ that minimise the cut-size d_{50} at a specified volumetric flow rate, ϕ_v, and overall pressure drop, Δp. The factors are constrained by the lower and upper levels presented in Table 7.2.

Since the cut-size minimum is only reached if the flow rate and the pressure drop are equal to their specified levels, the problem is also known as a constrained optimisation with equality constraints (Hillier and Lieberman, 1995). In addition to the variable costs of the cyclone separation represented by the pressure drop, the manufacturing costs can be used to put an additional constraint on the optimisation procedure. Muschelknautz (1972) propose the body cross section ($\sim D^2$) or the cyclone weight ($\sim HD^2$) as a ground for comparison.

Consider a Stairmand high efficiency cyclone separator of industrial size ($D = 1.0\,m$) operating at ambient conditions ($\rho_g = 1.185\,kg\,m^{-3}$, $\mu = 1.85\ 10^{-5}\,N\,s\,m^{-2}$). Air is injected into the cyclone at a linear inlet velocity of $15.0\,m\,s^{-1}$, or a flow rate ϕ_v of $1.5\,m^3\,s^{-1}$. The particle density, ρ_p, is set to $2370\,kg\,m^{-3}$, which corresponds to a density ratio of particles to air of 2,000. This value is typical for industrial powders such as FCC catalyst. Using the response surface models for Eu and Stk_{50} derived in Sec. 7.4, we can calculate the cut-size and the pressure drop of the Stairmand cyclone: $d_{50} = 2.58\,\mu m$ and $\Delta p = 467 Pa$.

If the Stairmand geometry corresponds to the optimal cyclone design under these conditions, the objective function for d_{50} is at its minimum. The cyclone manufacturing costs are taken into account as an additional constraint by holding the cylindrical body height and the cyclone diameter at $(h - S)/D = 1.0$ and $D = 1.0m$, respectively. Another constraint from design practice was applied for the inlet height to width aspect ratio ($a/b \leq 3.0$).

The nonlinear programming problem can then be summarised as follows:

$$\text{Minimise} \quad d_{50} = d_{50}(D_e, a, b, U_{in}) \tag{7.10}$$

subject to equality constraints

$$\begin{aligned} \phi_v \equiv \quad & a\,b\,U_{in} && = 1.5 m^3/s \\ \Delta p \equiv \quad & f(D_e, a, b, U_{in}) && = 467 Pa \end{aligned}$$

and variable constraints

$$\begin{aligned} 0.30 \leq\ & D_e & \leq 0.70 \\ 0.30 \leq\ & a & \leq 0.80 \\ 0.15 \leq\ & b & \leq 0.35 \\ 1.0 \leq\ & U_{in} & \leq 40.0 \\ 1.0 \leq\ & a/b & \leq 3.0 \end{aligned}$$

where the response surface models for Stk_{50} and Eu are used to calculate d_{50} and Δp, respectively. Eq. 7.10 was solved by means of the generalised reduced gradient (GRG2) method (Frontline Systems, Inc., 1995). The optimal cyclone design at the given duty and pressure drop is close to the Stairmand geometry with $D_e/D = 0.44$, $a/D = 0.54$, $b/D = 0.23$, and $U_{in} = 12.0\, m\, s^{-1}$. The performance of the optimal cyclone in terms of the cut-size is $2.51\, \mu m$, which is only slightly better than the Stairmand high-efficiency design.

The analysis shows that the optimal cyclone prefers to handle the flow rate by a larger inlet at a reduced inlet velocity compared to the Stairmand cyclone. The exit pipe diameter is reduced concurrently, *i.e.* the ratio of inlet to outlet cross-sectional area is changed from 0.51 for the Stairmand to 0.83 for the optimal cyclone.

The optimisation procedure of Eq. 7.10 is now used to define a range of optimal cyclone geometries that handle a fixed duty. These cyclones obtain the highest performance or smallest cut-size at a given pressure drop. The performance diagram of the optimal cyclone designs is presented in Fig. 7.6. In this figure, two curves are presented, which correspond to a flow rate of 1.5 and $3.0\, m^3\, s^{-1}$, respectively. Both curves show that a lower cut-size is achieved at the cost of a considerable increase of cyclone pressure drop.

Along the performance curves the cyclone geometry and the inlet velocity magnitude are varied to meet the required flow rate and pressure drop. In Fig. 7.7, similar curves are presented that represent the magnitude of D_e/D for optimal cyclones versus their cut-size. It is shown that a lower cut-size is obtained by means of a contraction of the exit pipe. The curves for both flow rates have a similar shape, and are shifted along the cut-size axis with respect to each other due to their mutual difference in Reynolds number. The shift is not constant along the curves as a result of the interaction between the exit pipe diameter and the Reynolds number in the response surface model for Stk_{50} (see Table 7.7). Due to the constraints imposed on the normalised exit pipe diameter ($0.30 \leq D_e/D \leq 0.70$), the performance outside these boundaries is only obtained by varying the inlet velocity and inlet cross sectional area. The positions corresponding to the exit pipe diameter constraints were indicated in the performance diagram of Fig. 7.6 by symbols.

The inlet cross sectional area and the inlet velocity are modified concurrently while reducing the exit pipe diameter. It was seen that the aspect ratio (a/b) of the inlet box was equal to ≈ 2.3 for all optimal cyclone designs. Hence, it is adequate to disregard the interaction between the inlet width and inlet height, and only consider the variation of the normalised inlet cross sectional area ($a/D * b/D$). In Fig. 7.8a, the inlet area is shown versus the exit pipe diameter at the volumetric flow rates studied. Both curves are quite similar and exhibit a convex shape. They do not overlap completely due to the interaction term between the Reynolds number and the inlet dimensions in the response surface model for Stk_{50}. In Fig. 7.8b, the inlet velocity is

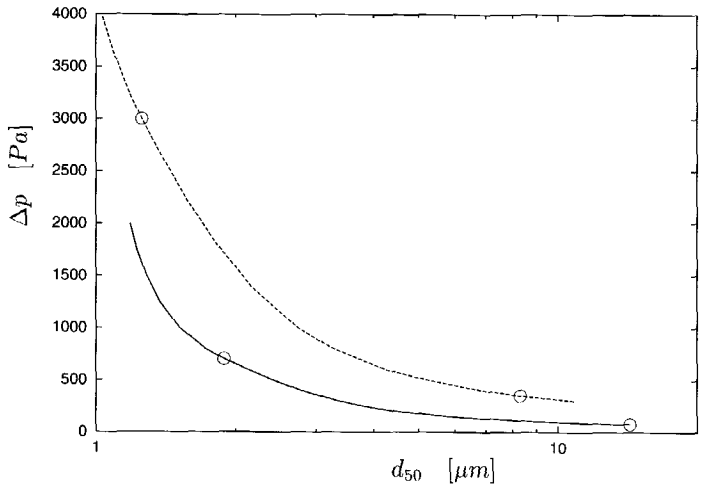

FIGURE 7.6: *Performance diagram of optimal Stairmand designs with* $(h - S)/D = 1.0$ *and* $D = 1.0\,m$. *The flow rate is equal to (-)* $1.5\,m^3\,s^{-1}$ *and (- -)* $3.0\,m^3\,s^{-1}$. *The labelled positions (o) represent the constraints of the normalised exit pipe diameter.*

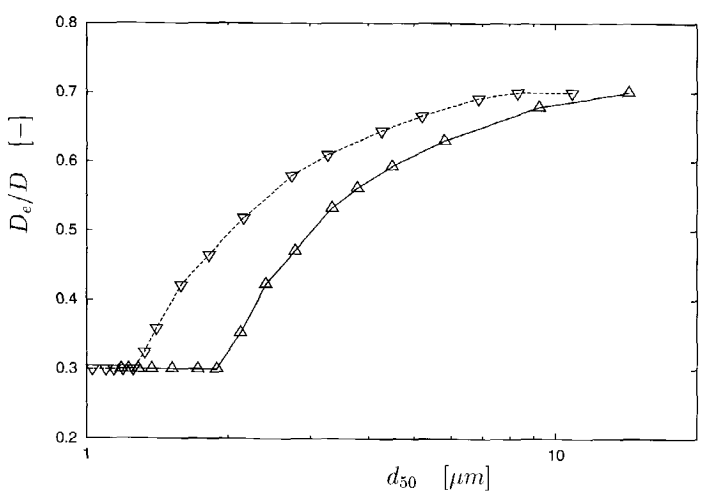

FIGURE 7.7: *Normalised exit pipe diameter versus cut-size for optimal cyclones. The flow rate is equal to (-)* $1.5\,m^3\,s^{-1}$ *and (- -)* $3.0\,m^3\,s^{-1}$.

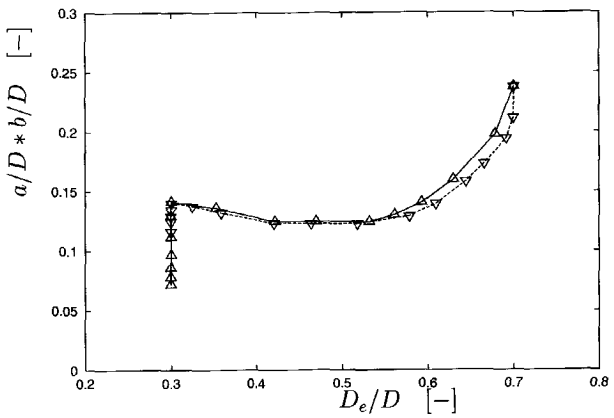

(a)

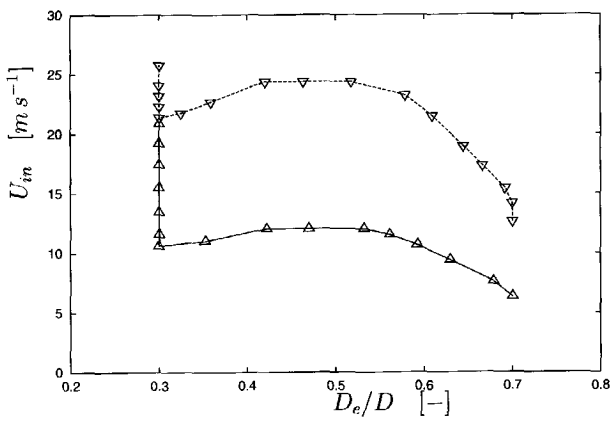

(b)

FIGURE 7.8: *Optimal cyclone characteristics: (a) inlet cross sectional area versus exit pipe diameter, and (b) inlet velocity versus exit pipe diameter. The flow rate is equal to (–)* $1.5\,m^3\,s^{-1}$ *and (- -)* $3.0\,m^3\,s^{-1}$.

presented as a function of the exit pipe diameter. These curves exhibit a concave functional relationship, since the inlet velocity is inversely proportional to the inlet area at a given flow rate.

Comparing Figs. 7.8a and b reveals that the performance of an optimal cyclone design outside the constraints for D_e/D is affected by modifying the inlet velocity and the inlet area. At the lower bound of the curve ($D_e/D = 0.30$) a smaller cut-size is obtained by increasing the inlet velocity and concurrently decreasing the inlet cross sectional area. At the upper bound ($D_e/D = 0.70$) it is the other way round. Its implication is that there is only one degree of freedom left in Eq. 7.10.

The performance diagram for optimal cyclone designs (Fig. 7.6) can be used to study alternative choices of cyclone design. This is illustrated by the following example. The optimal cyclone geometry discussed earlier was capable of handling a gas flow rate of $1.5\,m^3\,s^{-1}$, while yielding a cut-size $d_{50} = 2.51\,\mu m$ at a pressure drop $\Delta p = 467\,Pa$. Let's assume that the flow rate offered to this cyclone is increased by a factor of two ($\phi_v = 3.0\,m^3\,s^{-1}$) due to for instance an improved utilisation of the process capacity. The required performance in terms of the cut-size stays the same, or $d_{50} \leq 2.51\,\mu m$.

The following design options are now available:

- **Increasing the inlet velocity by a factor of two**
  Using the response surface model the cut-size d_{50} will be reduced to $1.69\,\mu m$. However, the cyclone pressure drop is considerably increased up to $\Delta p = 2010\,Pa$.

- **Re-design of the cyclone to obtain an optimal geometry**
  This corresponds to the position at the upper curve of Fig. 7.6, where the cut-size is equal to $2.51\,\mu m$. The pressure drop of this optimal cyclone design is now $1122\,Pa$, but the diameter of the exit pipe has to be increased from $D_e/D = 0.44$ to 0.56. It is not necessary to modify the height and width of the inlet box.

- **Application of a second cyclone separator**
  By presenting the flow to a configuration of two parallel cyclones of similar design, the collection efficiency remains constant, whereas the total pressure drop is increased with a factor of two: $\Delta p = 934\,Pa$.

Choosing one of these options is a trade-off between operating costs in terms of pressure drop, and manufacturing costs associated with the modification of the cyclone or the construction of a second cyclone. Injecting the higher flow rate in the existing cyclone separator without any adjustments is the easiest option, but has its price in terms of pressure drop. In addition, this option is not feasible if the inlet velocity would exceed a high-level constraint. The lowest pressure drop is obtained by splitting the flow and using two parallel cyclones of similar design. In this case, it has to be determined whether the low operating costs outweigh the construction of a second cyclone and the additional space requirements. Re-designing the cyclone geometry offers an intermediate solution, *i.e.* a small modification of the cyclone geometry results in an optimal design for the new conditions. Its investment costs are moderate compared to the third option, whereas the operating costs in terms of the pressure drop are considerably lower than that of the first option.

7.6 Closure

The optimisation study presented in this chapter showed that the performance of gas cyclones operating at low solids loading can be approximated by means of a combined application of CFD calculations and response surface methodology. It was shown that the performance of the Stairmand cyclone can be modelled using a limited set of dimensionless quantities, such as the Reynolds, Euler, and Stokes numbers. This approach towards predicting cyclone design and performance has not been reported before.

The CFD model applied in this study has been assessed by using an experimental data set for the Stairmand cyclone with varying exit pipe diameter. In this respect, the applicability of the regression equations is limited to this type of geometry, whereas a large number of industrial cyclones are employed that strongly deviate from the Stairmand design. The optimisation technique discussed here for the Stairmand design could, however, be easily adapted to an alternative design and variable range; it was shown that a limited number of CFD simulations will do.

For the optimisation study presented in this thesis, the variable range was intentionally chosen quite large to include a wide range of industrial operating conditions and cyclone designs. The model results for the shape parameter β of the grade efficiency curve already showed that the accuracy of the regression equations would certainly benefit from using a smaller variable range. For practical situations, the variable range for the operating conditions (*i.e.* the Reynolds number) would be much smaller than used in the present study.

7.7 Appendix

Central composite design of cyclone performance

Node	D_e/D	a/D	b/D	h/D	$\ln(Re)$	Eu	$\ln(Stk_{50})$	β
1	0.3	0.3	0.15	0.5	10.4	3.69	-6.74	8
2	0.7	0.3	0.15	0.5	10.4	1.64	-4.54	6
3	0.3	0.8	0.15	0.5	10.4	8.42	-7.26	8
4	0.7	0.8	0.15	0.5	10.4	2.27	-5.27	4
5	0.3	0.3	0.35	0.5	10.4	7.20	-7.16	8
6	0.7	0.3	0.35	0.5	10.4	2.14	-5.31	4
7	0.3	0.8	0.35	0.5	10.4	12.6	-6.66	3
8	0.7	0.8	0.35	0.5	10.4	3.52	-4.49	2
9	0.3	0.3	0.15	2.5	10.4	2.37	-6.38	8
10	0.7	0.3	0.15	2.5	10.4	1.40	-4.56	8
11	0.3	0.8	0.15	2.5	10.4	5.80	-7.16	7
12	0.7	0.8	0.15	2.5	10.4	2.02	-5.64	5
13	0.3	0.3	0.35	2.5	10.4	5.31	-7.07	7
14	0.7	0.3	0.35	2.5	10.4	1.92	-5.47	6
15	0.3	0.8	0.35	2.5	10.4	10.4	-6.90	4
16	0.7	0.8	0.35	2.5	10.4	3.18	-5.06	2

17	0.3	0.3	0.15	0.5	15.0	6.69	-8.46	6
18	0.7	0.3	0.15	0.5	15.0	1.81	-5.73	8
19	0.3	0.8	0.15	0.5	15.0	11.2	-8.37	4
20	0.7	0.8	0.15	0.5	15.0	2.24	-5.17	2.5
21	0.3	0.3	0.35	0.5	15.0	10.9	-8.05	5
22	0.7	0.3	0.35	0.5	15.0	2.12	-5.24	2
23	0.3	0.8	0.35	0.5	15.0	20.4	-5.06	4
24	0.7	0.8	0.35	0.5	15.0	3.62	-3.37	3
25	0.3	0.3	0.15	2.5	15.0	5.10	-8.37	5
26	0.7	0.3	0.15	2.5	15.0	1.63	-5.82	10
27	0.3	0.8	0.15	2.5	15.0	9.69	-8.65	4
28	0.7	0.8	0.15	2.5	15.0	2.10	-5.87	2.5
29	0.3	0.3	0.35	2.5	15.0	8.58	-8.46	5
30	0.7	0.3	0.35	2.5	15.0	2.00	-6.14	2.5
31	0.3	0.8	0.35	2.5	15.0	17.2	-6.81	3
32	0.7	0.8	0.35	2.5	15.0	3.37	-3.85	2.5
33	0.3	0.5	0.25	1.5	12.7	9.76	-8.12	4
34	0.7	0.5	0.25	1.5	12.7	2.22	-5.75	2.5
35	0.5	0.3	0.25	1.5	12.7	3.07	-6.94	6.5
36	0.5	0.8	0.25	1.5	12.7	4.31	-6.74	2.5
37	0.5	0.5	0.15	1.5	12.7	3.23	-7.02	7
38	0.5	0.5	0.35	1.5	12.7	4.15	-6.81	3
39	0.5	0.5	0.25	0.5	12.7	4.07	-6.85	2.5
40	0.5	0.5	0.25	2.5	12.7	3.49	-7.21	5
41	0.5	0.5	0.25	1.5	10.4	3.50	-6.55	6
42	0.5	0.5	0.25	1.5	15.0	3.85	-7.37	4
43	0.5	0.5	0.25	1.5	12.7	3.73	-7.21	4

Face-centred response surface design of five factors. Results are presented for three responses, *viz.* the Euler number, Eu, the Stokes number, $\ln(Stk_{50})$, and the slope parameter of the logistic equation, β. The responses were derived from CFD predictions.

CHAPTER 8

CONCLUSIONS AND RECOMMENDATIONS

8.1 MAIN CONCLUSIONS

Gas flow field

- Laser-Doppler Anemometry (LDA) measurements of the cyclone flow field confirmed once more that the swirl velocity distribution is characterised by a combined vortex, where a solid body rotation prevails in the vortex core, and a free-type of vortex exists between the core boundary and the cyclone wall. The shape of the combined vortex strongly depends on the exit pipe diameter. A contraction of the exit pipe aperture results in a higher maximum tangential velocity, and, consequently, in an increase of the cyclone pressure drop.

- The mean axial velocity is characterised by a reverse flow pattern, where near the wall the flow is directed downwards, while in the centre region the flow is directed towards the exit pipe. Near the centre of the vortex core the mean axial velocity is suppressed. Due to an adverse pressure gradient, the axial velocity deficit becomes more pronounced while proceeding towards the exit pipe.

- The origin of the vortex deviates only slightly from the geometrical centre of the cyclone. The gas flow field can be considered axisymmetric, *i.e.* the mean velocity gradient in the tangential direction is negligible.

Vortex core precession

- In the core region, the LDA measurements are dominated by low-frequency oscillations, which can be attributed to the precessing vortex core (PVC). The frequency of the PVC is linearly dependent on the inlet velocity.

- By means of an adaptive filtering technique the low-frequency component due to the PVC could be estimated from the LDA signal. On the basis of the PVC signal and the

shape of the auto- and cross-correlation functions, phase-resolved velocity profiles were reconstructed that correspond to the approximate 'apogee' and 'perigee' position of the vortex core origin.

- The time-averaged tangential and axial velocity profiles are smoothed by the precession motion of the vortex core. Moreover, a significant part of the measured rms velocity in the core region is not related to turbulence, but is due to the PVC.

Turbulence modelling

- Based on a comparison with LDA measurements, it can be concluded that cyclone modelling is best done by means of second-moment closure, *i.e.* a Reynolds stress transport model (RSTM). Eddy-viscosity models are by no means capable of predicting the combined vortex.

- The wall-reflection term of the pressure-strain model has a significant effect on the predicted vortex shape as well as on the low axial velocity region near the centreline. For cyclones with a small exit pipe diameter the simulation benefits from disregarding the wall-reflection term in the RSTM.

- Compared to an axisymmetric simulation, a three-dimensional model does not yield an improved prediction of the flow field in the separation zone of the Stairmand cyclone. Three-dimensional effects are limited to the inlet section of the cyclone and the short-cut flow near the exit pipe entrance.

- The distribution of Reynolds stresses is strongly anisotropic in the outer region of the flow, while in the vortex core the Reynolds stress model predicts less anisotropy. This could not be confirmed by the LDA measurements; a large part of the rms velocity in this region is due to the PVC.

- A Large Eddy Simulation (LES) is capable of predicting the precessing motion of the vortex core in a laboratory scale cyclone. The effect of the PVC on the rms velocity in the vortex core is well captured. Compared to a three-dimensional RANS simulation with second-moment closure, however, the mean flow field is not predicted better by the LES.

Particle collection

- The effect of the inlet velocity and the exit pipe diameter on the overall collection efficiency was measured for (modifications of) the Stairmand cyclone. The measurement results are consistent with cyclone theory, but due to build-up of particles at the cyclone wall, the overall efficiency was likely underestimated at moderate inlet velocities.

- By means of a particle tracking model, the grade efficiency curve of the Stairmand cyclone was predicted. The overall collection efficiency was obtained by integration of the grade efficiency curve and the measured particle size distribution of the test particles. The agreement between the calculated and measured overall efficiencies was reasonable,

although the calculated values were rather sensitive to the shape of the particle size distribution.

Optimising cyclone design

- The performance of the Stairmand cyclone separator can be modelled by using a limited set of dimensionless quantities, such as the Reynolds, Euler, and Stokes numbers. By means of CFD simulations, the response surface could be obtained for a range of geometries and operating conditions. The predicted trends for pressure drop and cut-size are consistent with results reported in the literature, although the model accuracy would benefit by reducing the variable range of the model.

- By means of a non-linear optimisation procedure, optimal cyclone geometries were sorted out that yield the lowest particle cut-size at a required flow rate and available cyclone pressure drop. It was seen that, at a given volumetric flow rate, the collection efficiency of a Stairmand cyclone is improved by simultaneously reducing the exit pipe diameter and the cross-sectional area of the inlet. This optimisation technique can also be applied to study alternative cyclone designs for practical engineering problems.

8.2 Suggestions for further work

- Although the Reynolds stress transport model is capable of predicting the gas flow field of cyclones at a fair degree of accuracy, the model could still be improved, especially with respect to the wall-reflection term used in the pressure-strain model. It was shown that this term affects the predicted mean flow field significantly, *i.e.* the simulation of the standard Stairmand cyclone benefits from the inclusion of the wall-reflection term, whereas omitting this term improved the flow field predictions for cyclones with a reduced exit pipe diameter. There are several alternative models for the pressure-strain correlation available in the literature, one example being the SSG model (Speziale et al. (1991)), which does not employ the wall-reflection term. This should enable the simulation of the flow field in different Stairmand geometries by a single model.

- For a laboratory-scale cyclone, Large Eddy Simulations showed the potential of capturing all flow features including the precessing vortex core. More insight in this phenomenon could be gained by pursuing this route for other cyclone geometries as well. More research is needed to determine why the LES fails to predict the mean axial velocity profile near the exit pipe aperture. A straightforward extension of the present LES study would be the inclusion of particles to calculate the grade efficiency curve. Since the LES predicts an instantaneous, three-dimensional fluid velocity along the particle trajectory, a particle dispersion model is not needed, except when the particle relaxation time and the cut-off frequency of the LES are of the same order. Moreover, the effect of the PVC on the particle trajectory is covered as well, although due to its low frequency the PVC does not likely increase particle dispersion (Derksen and Van den Akker (2000)). Within the RANS framework, the prediction of particle trajectories may be improved by applying more

advanced particle dispersion models, *e.g.* the generalised Langevin model of Haworth and Pope (1985).

- The design optimisation procedure described in this thesis has illustrated that the combination of CFD simulations and response surface techniques could well be applied to practical cyclone engineering. The gas and particle flow in a cyclone can be characterised by a small number of dimensionless quantities, and the optimisation procedure is straightforward. The model accuracy, however, could be improved by reducing the variable range. For practical engineering purposes, the process towards optimisation of the cyclone design could involve two steps, *viz.* defining the direction for improvement by using the response surface model presented in this thesis, and subsequently predicting the performance of a small number of cyclones by means of the CFD model.

DANKWOORD

De voltooiing van dit proefschrift is een definitieve afsluiting van mijn Delftsche tijd, die zo'n elf jaar geleden is begonnen. Ik kijk naar zowel mijn studententijd als mijn OIO-tijd met veel genoegen terug. Een groot deel ervan heb ik doorgebracht aan het Kramers Laboratorium voor Fysische Technologie, wat me inmiddels op elk uur van de dag vertrouwd doet voorkomen. In de eerste plaats wil ik daarom mijn promotor, Harrie van den Akker, bedanken voor de mogelijkheid om het promotieonderzoek bij dit lab uit te voeren. Ik heb onze (al dan niet frequente) gesprekken over het werk altijd zeer stimulerend ervaren, vooral door zijn positieve instelling en uitgesproken vertrouwen.

Jos Derksen ben ik als mijn dagelijkse begeleider veel dank verschuldigd. Niet alleen voor de vele correcties op het geschrevene, maar vooral voor zijn eigen (numerieke) werk aan cyclonen, dat voor mij een extra inspiratiebron is geweest. Daarnaast natuurlijk voor het aangename gezelschap tijdens ons bezoek aan Lissabon, dat een uitstekende locatie bleek te zijn voor diepzinnige discussies over den wetenschap.

De halfjaarlijkse vergaderingen van de gebruikerscommissie zijn van groot belang geweest voor de voortgang van het onderzoek en hebben mijn inzicht in de weerbarstige realiteit van cyclonen verbeterd. Ik ben Huub Dries (Shell), Henk Geljon (Van Tongeren Kennemer), Cor Waringa en Johan Bernard (Hoogovens) zeer erkentelijk voor hun bijdrage en interesse.

I would like to express my gratitude in particular to Ferit Boysan (Fluent Inc.) for his contribution to the work and his efforts to join the committee's meetings in spite of his busy travelling schedule. It has been very stimulating to discuss my work with the person who did his pioneering Ph.D. work on cyclone modelling already in 1982. The comments on the draft thesis put forward by Prof. M. Escudier are also greatly acknowledged.

Bij verschillende delen van het werk heb ik hulp gehad van studenten, van wie ik hier met name Eelco van Vliet en Thijs Israël wil noemen. Zij hebben een jaar van hun studie gewijd aan experimenteel cyclononderzoek en kunnen de resultaten van hun werk terugvinden in met name hoofdstuk IV van het proefschrift. Eelco, succes met het afronden van jouw promotieonderzoek!

Voor het experimentele werk heb ik regelmatig een beroep gedaan op de expertise van de werkplaats van het Kramers Lab. Graag noem ik hier Jaap van Raamt, Jaap Kamminga, Jan Groeneveld en Cees Vermeulen voor hun werk aan de diverse cycloonopstellingen; Ab Schinkel en Jaap Beekman voor hun hulp aan laser-gerelateerde problemen.

Een niet onbelangrijk deel van het werkplezier werd bepaald door mijn collega-promovendi van het Kramers Lab. Mijn kamergenoten van het eerste uur Helmar van Santen, Robert van den Berg en Bart Venneker verdienen lof voor het tolereren van mijn soms wat nadrukkelijke aanwezigheid. Dit gaat uiteraard ook op voor mijn latere kamergenoten Ridwan Oeij en Koji Kuramoto. Daarnaast wil ik alle andere promovendi bedanken voor het veraangenamen van

mijn verlengde verblijf in Delft in de vorm van (niet-) wetenschappelijke discussies tijdens het werk en natuurlijk de wekelijks terugkerende vakgroepborrels in dat kleine cafe bij de Aula (en nog een paar in de binnenstad van Delft).

Jack Ramaker heeft mij gewezen op de mogelijkheden van Design of Experiment, wat een belangrijk onderdeel is geworden van het onderzoek. Jack, zonder jouw inbreng had dit er heel anders uitgezien. Mijn paranimfen, Edo Hoekstra en Pieter Jonker, wil ik vanaf deze plaats alvast bedanken voor hun morele steun tijdens de verdediging. Ik draag het proefschrift op aan mijn ouders als dank voor hun betrokkenheid en vriendschap gedurende de afgelopen jaren en de vele jaren die nog komen gaan.

Het schrijven van een proefschrift heeft zo z'n eigen realiteit; er zijn momenten dat het al je gedachten en al je tijd in beslag kan nemen. Nu is het proefschrift klaar, einde oefening. Vanaf dit moment zal ik mijn tijd kunnen delen met jou, Caren, en zullen ook mijn gedachten weer onvoorwaardelijk naar jou uitgaan.

Delft, 19 oktober 2000.

About the Author

Arjen Hoekstra was born on June 4, 1970 in Leiden, but was raised in a picturesque village called Warmond. In 1988, he obtained his 'VWO' certificate at the Christelijke Scholengemeenschap 'Dr. W. A. Visser 't Hooft' Leiden. He started his studies at Leiden University, where he obtained his 'Propaedeutics' certificate in Chemistry in 1989. He then decided to continue his studies at Delft University of Technology, where he earned a M.Sc. degree in Chemical Technology in August 1995. During his stay in Delft, he participated in a symphony orchestra, climbed mountains in the Alps, and enjoyed a three months working visit in Manila at the invitation of Unilever. The topic of his Master's thesis, written at the 'Kramers Laboratorium voor Fysische Technologie', was the experimental and numerical study of the mould filling process under supervision of Dr. R. van Tol and Prof. Dr. H. E. A. Van den Akker. In October 1995, he started his Ph.D. research under the supervision of Professor Van den Akker at the Kramers Laboratorium, the result of which is presented in this dissertation. Part of the work was presented at conferences in Saint-Jean Cap Ferrat (France, 1998), Lisbon (Portugal, 1998), Newport Beach (CA, U.S.A., 1998), Danvers (MA, U.S.A., 1999), Boston (MA, U.S.A., 1999), Bremen (Germany, 1999) and Warwick (U.K., 2000). Since 1 January 2000, he has been working at Unilever Research in Vlaardingen.

BIBLIOGRAPHY

Absil, L. H. J. (1995). *Analysis of the Laser Doppler measurement technique for application in turbulent flows.* PhD thesis, Delft University of Technology, Faculty of Aerospace Engineering.

Adrian, R. (1991). Particle-imaging techniques for experimental fluid mechanics. *Annu. Rev. Fluid Mech.*, 23:261–304.

Alexander, R. M. (1949). Fundamentals of cyclone design and operation. *Proc. Aust. Inst. Min. Met.*, 152-153:203–228.

Alonso, M. and Finn, E. J. (1980). *Fundamental university physics*, volume 1. Addison-Wesley.

Barth, W. (1956). Berechnung und Auslegung von Zyklonabscheidern auf Grund neuerer Untersuchungen. *Brennst. Wärme Kraft*, 8:1–9.

Beeckmans, J. M. and Kim, C. J. (1977). Analysis of the efficiency of reverse flow cyclones. *Can. J. Chem. Engng*, 55:640–643.

Berlemont, A., Chang, Z., and Gouesbet, G. (1998). Lagrangian scheme for particle tracking in non-isotropic turbulence. *ERCOFTAC Bulletin*, 36:7–10.

Berlemont, A., Desjonqueres, P., and Goucsbet, G. (1990). Particle Lagrangian simulation in turbulent flows. *Int. J. Multiphase Flow*, 16(1):19–34.

Bernard, J. G. (1992). *Experimental investigation and numerical modelling of cyclones for application at high temperatures.* PhD thesis, Delft University of Technology, Delft University Press.

Bernard, J. G., Andries, J., and Scarlett, B. (1989). Cyclone research for application at high temperatures and pressures. In *1st European Symposium Separation of Particles from Gases*, pages 399–412. PARTEC 89.

Bird, R. B., Stewart, W. E., and Lightfoot, E. N. (1960). *Transport phenomena.* John Wiley and Sons, New York.

Bloor, M. I. G. and Ingham, D. B. (1987). The flow in industrial cyclones. *J. Fluid Mech.*, 178:507–519.

Bohnet, M. (1982). Zyklonabscheider zum Trennen von Gas/Feststoff-Strömungen. *Chemie-Ing.-Techn.*, 54(7):621–630.

Bohnet, M. (1984). Optimalauslegung von Aerozyklonen. *Chemie-Ing.-Techn.*, 56(5):416–417.

Bohnet, M. (1995). Influence of the gas temperature on the separation efficiency of aerocyclones. *Chem. Eng. Process.*, 34:151–156.

Box, G. E. P. and Draper, N. R. (1987). *Empirical model building and response surfaces.* John Wiley and Sons, New York.

Boysan, F., Ayers, W. H., and Swithenbank, J. (1982). A fundamental mathematical modelling approach to cyclone design. *Trans. Inst. Chem Engng*, 60:222–230.

Broer, L. J. F. (1961). Flow phenomena in cyclones. In *Cyclones in Industry*, pages 33–45. Elsevier Publishing Company.

Chanaud, R. C. (1965). Observations of oscillatory motion in certain swirling flows. *J. Fluid Mech.*, 21(1):111–127.

Clift, R., Ghadiri, M., and Hoffmann, A. C. (1991). A critique of two models for cyclone performance. *A.I.Ch.E. J.*, 37(2):285–289.

Comas, M., Comas, J., Chetrit, C., and Casal, J. (1991). Cyclone pressure drop and efficiency with and without an inlet vane. *Powder Technol.*, 66:141–148.

Csanady, G. T. (1963). Turbulent diffusion of heavy particles in the atmosphere. *J. Atmos. Science*, 20:201–208.

Daly, B. J. and Harlow, F. H. (1970). Transport equations of turbulence. *Phys. Fluids*, 13:2634–2649.

Derksen, J. J. and Van den Akker, H. E. A. (1999). Large eddy simulations on the flow driven by a rushton turbine. *A.I.Ch.E. J.*, 45(2):209–221.

Derksen, J. J. and Van den Akker, H. E. A. (2000). Simulation of vortex core precession in a reverse-flow cyclone. *A.I.Ch.E. J.*, 46(7):1317–1331.

Dietz, P. W. (1981). Collection efficiency of cyclone separators. *A.I.Ch.E. J.*, 27(6):888–892.

Dirgo, J. and Leith, D. (1985). Cyclone collection efficiency: comparison of experimental results with theoretical predictions. *Aerosol Sci. Technol.*, 4:401 415.

Dirkzwager, M. (1996). *A new axial cyclone design for fluid-fluid separation.* PhD thesis, Delft University of Technology, Faculty of Mechanical Engineering.

Drain, L. E. (1980). *The Laser-Doppler technique.* John Wiley and Sons, New York.

Durst, F., Melling, A., and Whitelaw, J. H. (1976). *Principles and practice of Laser Doppler Anemometry.* Academic Press, London.

Dyakowski, T. and Williams, R. A. (1993). Modelling turbulent flow within a small-diameter hydrocyclone. *Chem. Engng Sci.*, 48(6):1143–1152.

Dyson, J. (1992). Vacuum cleaner apparatus. United States Patent No. 5,160,356.

Elghobashi, S. (1994). On predicting particle-laden turbulent flows. *Applied Sci. Res.*, 52:309 329.

Enliang, L. and Yingmin, W. (1989). A new collection theory of cyclone separators. *A.I.Ch.E. J.*, 35(4):666–669.

Escudier, M. P. (1987). Confined vortices in flow machinery. *Ann. Rev. Fluid Mech.*, 19:27–52.

Escudier, M. P., Bornstein, J., and Zehnder, N. (1980). Observations and LDA measurements of confined turbulent vortex flow. *J. Fluid Mech.*, 98:49–63.

Ferziger, J. H. and Perić, M. (1996). *Computational methods for fluid dynamics.* Springer-Verlag, Berlin Heidelberg.

Fluent Inc. (1996). *Fluent User's Guide Release 4.4.* Lebanon (NH). info at http://www.fluent.com.

Fokke, M. G. D., Liem, T. L., Derksen, J. J., and Van den Akker, H. E. A. (1994a). LDA and LIF experiments on the quasi-periodic and complex flow in a cyclone. In *7th International Symposium on Applications of Laser techniques to Fluid Mechanics*, volume 1, pages 16.4.1–6, Lisbon, Portugal.

Fokke, M. G. D., Liem, T. L., and Van den Akker, H. E. A. (1994b). Imaging vortex precession in cyclones. In *Optical methods and data processing in heat and fluid flow*, volume 1, pages 193–196, IMechE London, UK.

Fraser, S. M. and Abdullah, M. Z. (1995). LDA measurement on a modified cyclone. In *ASME-FED Laser Anemometry*, page 395, American Society of Mechanical Engineers.

Frontline Systems, Inc. (1995). *Solver.* info at http://www.frontsys.com.

Garg, A. K. and Leibovich, S. (1979). Spectral characteristics of vortex breakdown flow fields. *Phys. Fluids*, 22(11):2053–2064.

Gibson, M. M. and Launder, B. E. (1978). Ground effects on pressure fluctuations in the atmospheric boundary layer. *J. Fluid Mech.*, 86:491–511.

Gorton-Hülgerth, A. and Staudinger, G. (1996). Geschwindigskeitsmessungen mit LDA und Lichschnittbilder aus einem Staubzyklon. In *Zyklonabscheider in der Energie- und Verfahrenstechnik*, pages 113–126. VDI Verlag.

Gottschalk, O. and Bohnet, M. (1998). Calculation of grade efficiency and pressure drop of aerocyclones with suction of a partial gas stream. In *4th European Symposium Separation of Particles from Gases*, pages 95–109. PARTEC 98.

Greif, V. (1996). Druckverlust und Druckverlustreduzierung bei Zyklonabscheidern. In *Zyklonabscheider in der Energie- und Verfahrenstechnik*, pages 65–79. VDI Verlag.

Griffiths, W. D. and Boysan, F. (1996). CFD and empirical modelling of the performance of a number of cyclone samplers. *J. Aerosol Sci.*, 98:281–304.

Grosjean, N., Graftieaux, L., Michard, M., Hübner, W., Tropea, C., and Volkert, J. (1997). Combining LDA and PIV for turbulence measurements in unsteady swirling flows. *Meas. Sci. Technol.*, 8:1523–1532.

Gupta, A. K., Lilley, D. G., and Syred, N. (1984). *Swirl flows.* Abacus Press.

Hadzić, I. (1999). *Second-moment closure modelling of transitional and unsteady turbulent flows.* PhD thesis, Delft University of Technology, Faculty of Technical Physics.

Hajji, L., Pascal, P., and Oesterlé, B. (1996). Lagrangian simulation of particle dispersion in a turbulent shear flow. In *ASME-FED Vol. 236*, pages 27–32, American Society of Mechanical Engineers.

Hanjalić, K. (1994). Advanced turbulence closure models: a view of current status and future prospects. *Int. J. Heat and Fluid Flow*, 15(3):178–203.

Haworth, D. C. and Pope, S. B. (1985). A generalized Langevin model for turbulent flows. *Phys. Fluids*, 29(2):387–405.

Hillier, F. S. and Lieberman, G. J. (1995). *Introduction to operations research.* McGraw-Hill, New York.

Hinkelmann, K. and Kempthorne, O. (1994). *Design and analysis of experiments. Volume 1: Introduction to experimental design.* John Wiley and Sons, New York.

Hoekstra, A. J., Derksen, J. J., and Van den Akker, H. E. A. (1999a). A CFD study on the performance of a high-efficiency gas cyclone. In *Int. Symp. Computational Technologies for Fluid/Thermal/Chemical Systems with Industrial Applications*, volume 397 2, pages 219–226. ASME-PVP.

Hoekstra, A. J., Derksen, J. J., and Van den Akker, H. E. A. (1999b). An experimental and numerical study of turbulent swirling flow in gas cyclones. *Chem. Engng Sci.*, 54:2055–2065.

Hoekstra, A. J., Derksen, J. J., and Van den Akker, H. E. A. (1999c). Simulation of unsteady confined vortex flow. Proceedings of the 8th International Symposium on Computational Fluid Dynamics, 5-10 Sept 1999, Bremen, Germany.

Hoekstra, A. J., Derksen, J. J., and Van den Akker, H. E. A. (2000). Cyclone optimisation based on cfd predictions. Proceedings of the 5th International Conference on Cyclone Technologies, 31 May-2 June 2000, Warwick, UK.

Hoekstra, A. J., Israël, A. T., Derksen, J. J., and Van den Akker, H. E. A. (1998a). The application of laser diagnostics to cyclonic flow with vortex precession. In *9th International Symposium on Applications of Laser techniques to Fluid Mechanics*, volume 1, pages 4.3.1–8, Lisbon, Portugal.

Hoekstra, A. J., van Vliet, E., Derksen, J. J., and Van den Akker, H. E. A. (1998b). Vortex core precession in a gas cyclone. In *Advances in Turbulence VII*, pages 289–293, Dordrecht. Kluwer Academic Publishers.

Hoffmann, A. C., de Groot, M., and Hospers, A. (1996). The effect of the dust collection system on the flow pattern and separation efficiency of a gas cyclone. *Can. J. Chem. Engng*, 74:464–470.

Hoffmann, A. C., Van Santen, A., Allen, R. W. K., and Clift, R. (1992). Effects of geometry and solid loading on the performance of gas cyclones. *Powder Technol.*, 70:83–91.

Hoffmann, D., Gorton-Hülgerth, A., and Staudinger, G. (1998). Influence of boundary layer flow and vortex finder length on separation behaviour of cyclones. In *4th European Symposium Separation of Particles from Gases*, pages 26–34. PARTEC 98.

Hogg, S. and Leschziner, M. A. (1989). Computation of highly swirling confined flow with a Reynolds stress turbulence model. *AIAA J.*, 27:57–63.

Hsieh, K. T. and Rajamani, R. K. (1991). Mathematical model of the hydrocyclone based on physics of fluid flow. *A.I.Ch.E. J.*, 37(5):735–746.

Iozia, D. L. and Leith, D. (1989). Effect of cyclone dimensions on gas flow pattern and collection efficiency. *Aerosol Sci. Technol.*, 10:491 500.

Iozia, D. L. and Leith, D. (1990). The logistic function and cyclone fractional efficiency. *Aerosol Sci. Technol.*, 12:598–606.

Ito, T., Suematsu, Y., Kanda, N., and Hayase, T. (1983). On the oscillatory phenomena in a swirling pipe flow. *Bulletin of the JSME*, 26(218):1348–1356.

Jakirlić, S. (1997). *Reynolds-Spannungs-Modellierung Komplexer Turbulenter Strömungen*. PhD thesis, Universität Erlangen-Nürnberg, Herbert Urtz Verlag, München.

Jones, W. P. and Pascau, A. (1989). Calculation of confined swirling flows with a second moment closure. *Trans. ASME J. Fluids Engng*, 111:248–255.

Kim, W. S. and Lee, J. W. (1997). Collection efficiency model based on boundary-layer characteristics for cyclones. *A.I.Ch.E. J.*, 43(10):2446–2455.

Kitamura, O. and Yamamato, M. (1999). Proposal of a Reynolds stress model for gas-particle turbulent flows and its application to cyclone separators. In *Engineering Turbulence Modelling and Experiments 4*, pages 893–902. Elsevier.

Kitoh, O. (1991). Experimental study of turbulent swirling flow in a straight pipe. *J. Fluid Mech.*, 225:445–479.

Launder, B. E. (1991). Current capabilities for modelling turbulence in industrial flows. *Applied Sci. Res.*, 48:247–269.

Launder, B. E., Reece, G. J., and Rodi, W. (1975). Progress in the development of a Reynolds-stress turbulence closure. *J. Fluid Mech.*, 68(3):537–566.

Leith, D. and Jones, D. L. (1997). Cyclones. In *Handbook of Powder Science and Technology*, pages 727–752. Chapman and Hall, New York.

Leith, D. and Licht, W. (1972). The collection efficiency of cyclone type particle collectors - A new theoretical approach. *A.I.Ch.E. Symp. Series*, 68(126):196–206.

Liem, T. L. and Van den Akker, H. E. A. (1992). LDV measurements of the turbulent flow in gas cyclones. In *13th Symposium on Turbulence*, page B.12, University of Missouri-Rolla, USA.

Lien, F. S. and Leschziner, M. A. (1993). Second-moment modelling of recirculating flow with a non-orthogonal collocated finite-volume algorithm. In *Turbulent Shear Flows*, volume 8, pages 205–222.

MacInnes, J. M. and Bracco, F. V. (1992). Stochastic particle dispersion modelling and the tracer-particle limit. *Phys. Fluids A*, 4(12):2809–2824.

Milojevic, D. (1990). Lagrangian stochastic-deterministic predictions of particle dispersion in turbulence. *Part. Part. Syst. Charact.*, 7:181–190.

Minitab Inc. (1998). *User's guide Minitab 12.* info at http://www.minitab.com.

Molerus, O. and Glückler, M. (1996). Development of a cyclone separator with new design. *Powder Technol.*, 86:37–40.

Montgomery, D. C. (1984). *Design and analysis of experiments.* John Wiley and Sons, New York.

Morsi, S. A. and Alexander, A. J. (1972). An investigation of particle trajectories in two-phase flow systems. *J. Fluid Mech.*, 55:193–208.

Mothes, H. (1982). *Bewegung und Abscheidung der Partikeln im Zyklon.* PhD thesis, Technische Hochschule Karlsruhe.

Mothes, H. and Löffler, F. (1984). A model for particle separation in a cyclone. *Chem. Eng. Process*, 18:323.

Muschelknautz, E. (1972). Die Berechnung von Zyklonabscheidern für gase. *Chemie-Ing.-Techn.*, 44(1):63–71.

Muschelknautz, E. and Brunner, K. (1967). Untersuchungen an Zyklonen. *Chemie-Ing.-Techn.*, 39(9):531–538.

Muschelknautz, E. and Krambrock, W. (1970). Aerodynamisch Beiwerte des Zyklonabscheiders auf grund neuer und verbesserter Messungen. *Chemie-Ing.-Techn.*, 42(5):247–255.

Ogawa, A. (1984). *Separation of particles from air and gases*, volume 2. CRC Press, Boca Raton.

Ontko, J. S. (1996). Cyclone separator scaling revisited. *Powder Technol.*, 87:93–104.

Overcamp, T. J. and Mantha, S. V. (1998). A simple method for estimating cyclone efficiency. *Environmental Progress*, 17(2):77 79.

Overcamp, T. J. and Scarlett, S. E. (1993). Effect of reynolds number on the stokes number of cyclones. *Aerosol Sci. Technol.*, 19:362–370.

Patterson, P. A. and Munz, R. J. (1996). Gas and particle flow patterns in cyclones at room and elevated temperatures. *Can. J. Chem. Engng*, 74:213–221.

Pope, S. B. (1994). Lagrangian PDF methods for turbulent flows. *Annu. Rev. Fluid Mech.*, 26:23–63.

Ramachandran, G., Leith, D., Dirgo, J., and Feldman, H. (1991). Cyclone optimization based on a new empirical model for pressure drop. *Aerosol Sci. Technol.*, 15:135–148.

Reppenhagen, J. and Werther, J. (1998). Particle attrition influences cyclone performance. In *4th European Symposium Separation of Particles from Gases*, pages 63–72. PARTEC 98.

Reydon, R. F. and Gauvin, W. H. (1981). Theoretical and experimental studies of confined vortex flow. *Can. J. Chem. Engng*, 59:14–23.

Rietema, K. (1961). The mechanism of the separation of finely dispersed solids in cyclones. In *Cyclones in Industry*, pages 46–63. Elsevier Publishing Company.

Rumpf, H., Borho, K., and Reichert, H. (1968). Optimale Dimensionierung von Zyklonen mit Hilfe vereinfachender Modellrechnungen. *Chemie-Ing.-Techn.*, 40(21):1072 1082.

Shepherd, C. B. and Lapple, C. E. (1939). Flow pattern and pressure drop in cyclone dust collectors. *Ind. Eng. Chem.*, 31:972–984.

Slack, M. D. and Boysan, F. (1998). Advances in cyclone modelling using unstructured grids. Presented at the Scandinavian Fluent Users' Group Meeting, Gothenborg.

Sloan, D. G., Smith, P. J., and Smoot, L. D. (1986). Modeling of swirl in turbulent flow systems. *Prog. Energy Combust. Sci.*, 12:163–250.

Smagorinsky, J. (1963). General circulation experiments with the primitive equations: 1. The basic experiment. *Mon. Weather Rev.*, 91:99.

Smith, J. L. (1962). An experimental study of the vortex in the cyclone separator. *J. Basic Engr*, 84:602–608.

So, R. M. C., Ahmed, S. A., and Mongia, H. C. (1985). Jet characteristics in confined swirling flow. *Exp. Fluids*, 3:221–230.

Sommerfeld, M. (1990). Particle dispersion in turbulent flow: the effect of particle size distribution. *Part. Part. Syst. Charact.*, 7:209–220.

Sowter, J. K. (1986). Cyclones in industrial processes. Van Tongeren International Ltd.

Speziale, C. G., Sarkar, S., and Gatski, T. B. (1991). Modelling the pressure-strain correlation of turbulence: an invariant dynamical systems approach. *J. Fluid Mech.*, 227:245–272.

Stairmand, C. J. (1949). Pressure drop in cyclone separators. *Engineering*, 168:409–412.

Stairmand, C. J. (1951). The design and performance of cyclone separators. *Trans. Instn Chem. Engrs*, 29:356–383.

Svarovski, L. (1984). *Hydrocyclones.* Technomic Publishing Co Inc, London.

Talman, J. A. (1998). *Characterisation of a downflow reactor for fluid catalytic cracking.* PhD thesis, ETH Zurich, Institute of Process Engineering.

Tennekes, H. and Lumley, J. L. (1972). *A first course in turbulence.* The MIT Press, Cambridge (MA).

Ter Linden, A. J. (1949). Investigations into cyclone dust separators. *Proc. Inst. Mech. Eng.*, 160:233–240.

Thomson, D. J. (1987). Criteria for the selection of stochastic models of particle trajectories in turbulent flows. *J. Fluid Mech.*, 180:529–556.

TSI Inc. (1988). *Instruction manual IFA 750.* St. Paul (MN).

Tummers, M. J., Passchier, D. M., and Narayama, P. A. A. (1994). Three-component LDA measurements of mean turbulence quantities, time- and spatial correlation functions in the wake of a flat plate in an adverse pressure gradient. In *7th International Symposium on Applications of Laser techniques to Fluid Mechanics*, volume 2, pages 25.1.1–7, Lisbon, Portugal.

Van den Akker, H. E. A. and De Kort, C. J. M. (1989). Swirl tube separator. European Patent 0 360 360 B1.

Van der Velde, H. (1996). *On turbulent reacting dilute gas-particle flows in cyclones.* PhD thesis, Twente University.

Viollet, P. L., Simonin, O., Olive, J., and Minier, J. P. (1992). Modelling turbulent two-phase flows in industrial equipments. In *Computational Methods in Applied Sciences*, pages 213–224. Elsevier Science Publishers.

Volkert, J., Tropea, C., Domann, R., and Hübner, W. (1996). Combined application of PIV and LDA to swirling flow under compression. In *8th International Symposium on Applications of Laser techniques to Fluid Mechanics*, volume 1, pages 19.1.1–8, Lisbon, Portugal.

Wanker, R., Hartner, P., Hoffmann, D., and Staudinger, G. (1998). Agglomeration in connection with separation experiments in a cyclone. In *4th European Symposium Separation of Particles from Gases*, pages 55–62. PARTEC 98.

Watrasiewicz, B. M. and Rudd, M. J. (1976). *Laser Doppler measurements.* Butterworths, London.

Weber, R., Boysan, F., Ayers, W. H., and Swithenbank, J. (1984). Simulation of dispersion of heavy particles in confined turbulent flows. *A.I.Ch.E. J.*, 30(3):490–492.

Widrow, B. and Stearns, S. D. (1985). *Adaptive signal processing.* Prentice-Hall.

Wong, Y. K. E. and Sharif, M. A. R. (1995). Evaluation of the performance of three turbulent closure models in the prediction of confined swirling flows. *Computers and Fluids*, 24(1):81 - 100.

Wunenburger, R., Andreotti, B., and Petitjeans, P. (1999). Influence of precession on velocity measurements in a strong laboratory vortex. *Exp. Fluids*, 27(2):181–188.

Yazdabadi, P. A., Griffiths, A. J., and Syred, N. (1994). Characterization of the PVC phenomena in the exhaust of a cyclone dust separator. *Exp. Fluids*, 17:84–95.

Zhou, L. X. and Soo, S. L. (1990). Gas-solids flow and collection of solids in a cyclone separator. *Powder Technol.*, 63:45 53.

Zhou, Q. and Leschziner, M. A. (1991). A Lagrangian particle dispersion model based on a time-correlated stochastic approach. In *ASME-FED Gas-Solids Flows Vol. 121*, pages 255 260, American Society of Mechanical Engineers.